Aus dem Institut für Physikalische Chemie der
Universität Freiburg (Schweiz)

RADIOLYSIS OF [1.1.1]PROPELLANE AND OF AZIRIDINES: FATE OF THEIR MOLECULAR IONS

INAUGURAL - DISSERTATION

zur Erlangung der Würde eines *Doctor rerum naturalium*
der Mathematisch-Naturwissenschaftlichen Fakultät
der Universität Freiburg in der Schweiz

vorgelegt von
BEAT CHRISTOPH MÜLLER
aus Zofingen (AG)

Diss. Nr. 1299

Imprimerie St-Paul, Freiburg

2000

Von der Mathematisch-Naturwissenschaftlichen Fakultät der Universität Freiburg in der Schweiz angenommen, auf Antrag der Herren

Prof. Dr. Albert Gossauer, Universität Freiburg, Präsident der Jury

Prof. Dr. Thomas Bally, Universität Freiburg, Dissertationsleiter

Prof. Dr. Robert J. McMahon, University of Wisconsin, Madison, Experte

Prof. Dr. Edwin Haselbach, Universität Freiburg, Experte

Freiburg, den 14. Juni 2000

Der Dissertationsleiter   Der Dekan

Prof. Dr. Thomas Bally   Prof. Dr. Béat Hirsbrunner

"The most exciting phrase to hear in science, the one that heralds new discoveries, is not 'Eureka!' (I've found it!), but 'That's funny…'"

Isaac Asimov

Table of Contents

Abbreviations

‡	radical cation
A	Aziridine
B3LYP	method of Becke, Lee, Yang, and Parr
BDPA [a]	*cis*-C,C'-diphenyl-N-*n*-butylaziridine
BPA [a]	C-phenyl-N-*tert.*-butylaziridine
Bq	Bequerel
CASSCF	complete active space self consistent field
CASPT2	complete active space 2nd order perturbation theory
cc	coupled-cluster
CCSD(T)	coupled-cluster single, double and contr. of triple excitation
CI	configuration interaction
CP	cyclopentadiene
CPA [a]	C-phenylaziridine
DFT	density functional theory
DIA	dimethyleneallene
DMA	N,N-dimethylaniline
DMC	dimethylenecyclopropane
DPA [a]	*cis*-C,C'-diphenylaziridine
EA	electronic absorption
ESR	electron spin resonance
FT	Fourrier transformation
HF	Hartree-Fock
HOMO	highest occupied molecular orbital
IRC	intrinsic reaction coordinate
LST	linear synchronous transit
LUMO	lowest unoccupied molecular orbital
MBB	methylenebicyclobutyl
MCB	methylenecyclobutene
MCC	methylenecyclobutylidene
MDPA [a]	*cis*-C,C'-diphenyl-N-methylaziridine
MO	molecular orbital
MP2	Møller Plesset 2nd order perturbation theory (method)
MPA [a]	C-phenyl-N-methylaziridine
NBMO	non-bonding molecular orbital
NCPA [a]	C,N-diphenylaziridine

NCPA-CN [a]	C,N-(*para*-cyanophenyl)aziridine
NCPA-OMe [a]	C,N-(*para*-methoxyphenyl)aziridine
NIR	near infrared
NMA [a]	N-methylaziridine
NMR	nuclear magnetic resonance
NPA [a]	N-phenylaziridine
NPA-CN [a]	N-(*para*-cyanophenyl)aziridine
PDMA [a]	*trans*-C,C'-dimethyl-N-phenylaziridine
PDY	pentadienylidene (radical cation)
PES	photoelectron spectrum
PMA [a]	C-methyl-N-phenylaziridine
PRP	[1.1.1]propellane
pVDZ	polarized valence double zeta (basis set)
pVTZ	polarized valence triple zeta (basis set)
QCISD	quadratic config. interact. involv. single and double excit.
rms	root mean square
ROHF	restricted open shell Hartree-Fock
SCF	self consistent field
SOMO	singly occupied molecular orbital
Sv	Sievert
td	time dependent
TPA [a]	trans-triphenylaziridine
TS	transition state
UHF	unrestricted Hartree-Fock
UV	ultraviolet
VCP	vinylidenecyclopropane
VIA	*E*- or *Z*- vinylallene
Vis	visible
VUV	vacuum ultraviolet
Y [a]	azomethine ylid
ZPVE	zero point vibrational energy

[a] Most of the abbreviations ending with **A** denote aziridines. The abbreviations for the corresponding ring-opened azomethine ylids are obtained by substituting the **A** by a **Y**.

Summary

On ionization of [1.1.1]propellane (PRP^{+}) in cryogenic matrices a photo-labile species with a broad, weak NIR band (λ_{max} = 1440 nm) and an ESR spectrum consisting of a 14.8 G quintet of 5.4 G triplets is formed. On NIR irradiation this species is converted into the radical cation of vinylidenecyclo-propane (VCP^{+}), which was generated independently by ionization of VCP. Quantum chemical calculations show that the spectroscopic features of the photolabile intermediate are compatible with its assignment to the radical cation of dimethylene allene (DIA^{+}). DIA^{+} is also formed on ionization of dimethylene-cyclopropane (DMC) which suggests that DMC^{+} is an intermediate in the for-mation of DIA^{+} from PRP^{+}. The potential energy surface connecting DIA^{+} and PRP^{+} is explored and fully characterized at the CCSD(T)/cc-pVDZ//B3LYP/6-31G* level. Thereby it is found that vibronic interactions play an important role in determining the mechanism for the spontaneous decay of ionized PRP to DIA^{+}.
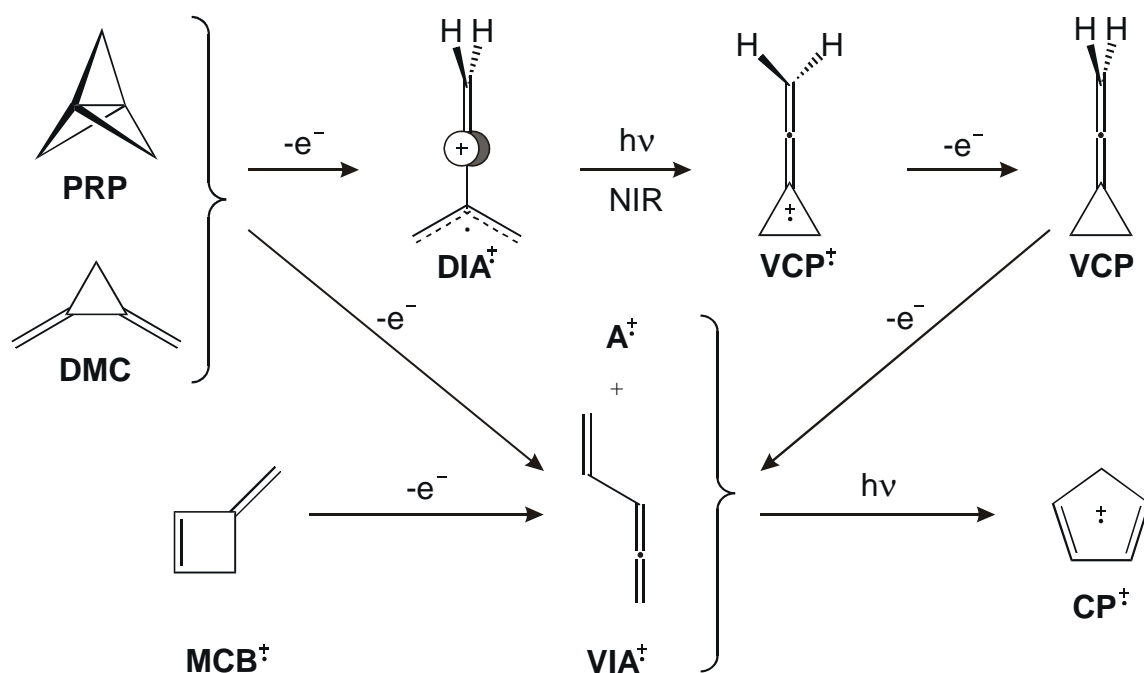
Optical spectra indicate the formation of additional products on ionization of PRP, DMC, or VCP in Freon and Argon matrices, notably the radical cation of vinylallene (VIA^{+}), which was also generated independently by ionization of VIA. Argon matrix experiments reveal also the presence of an intermediate A^{+} which can be transformed photochemically into the radical cation of cyclopenta-

diene ($\mathbf{CP}^{+}$). Intermediate **A** could not be identified, but several species which could be responsible for the corresponding spectroscopic manifestations are proposed. Further work will also be needed to shed more light on some other species which were observed during the above transformations.

The second part of this work describes the generation of azomethine ylid, **Y**, and its radical cation. It is of theoretical interest to investigate experimentally the force constants for the symmetric and asymmetric stretching deformation of the C-N bonds of **Y** and to compare them to those of the allyl radical. By investigating also $\mathbf{Y}$-d_1 and the $\mathbf{Y}$-d_4 it should be possible to determine these force constants by fitting the force field of the three isotopomers.

Furthermore we showed that substituents - particularly phenyl groups - play a very important role in determining the behavior of aziridines under photo-induced electron transfer (PET) conditions. N-phenyl rings stabilize the aziridine radical cation, whereas C-phenyl rings stabilize preferentially the ring-opened azomethine ylid cation. The extent of this stabilization can be assessed by calculating the energy increase on rotating the phenyl ring to a perpendicular position, so that resonance between the phenyl and the aziridine or the azomethine ylid moieties, respectively, is suppressed. Experiments and calculations showed that N-phenylaziridine radical cation, $\mathbf{NPA}^{+}$, is so strongly stabilized that it cannot undergo ring-opening on ionization (nor on subsequent electronic excitation of the radical cation). Methyl groups on the C atoms of **NPA** cause some lowering of the ring-opening transition state but the effect is too weak to allow a thermal crossing of the barrier.

In contrast, C-phenyl substitution leads to a pronounced stabilization of the ring-opening TS, whereas the stabilization of the reactant and of the product are quite similar. Therefore N-H and N-alkyl-C-phenylaziridines undergo immediate ring-opening on ionization. The question which effect "wins" in ionized *C,N*-diphenyl aziridine could not be answered satisfactorily. However for triphenyl-aziridine, **TPA**, short photolysis suffices to induce ring-opening.

Thus, the use of aziridines, opened by ionization to perform [3+2]cycloadditions with dipolarophiles **A=B**, is limited to derivatives where substituents do not stabilize the ring-closed form too much.

Zusammenfassung

Bei der Ionization von [1.1.1]Propellan (**PRP**$^{+}$) in Tieftemperaturmatrizen entsteht eine photolabile Spezies, die eine breite, schwache Bande im NIR Bereich (λ_{max} = 1440 nm) und ein Triplett von 5.4 G eines Quintetts von 14.8 G im ESR Spektrum aufweist. Nach Bestrahlung mit NIR Licht wird diese Spezies in das Radikalkation von Vinylidencyclopropan (**VCP**$^{+}$) umgewandelt, welches unabhängig durch Ionisation von **VCP** nachgewiesen wurde. Quantenchemische Rechnungen zeigen, dass die spektroskopischen Eigenschaften des photolabilen Zwischenproduktes vergleichbar sind mit jenen des Radikalkations von Dimethylenallen (**DIA**$^{+}$). **DIA**$^{+}$ wird auch bei der Ionisation von Dimethylen-cyclopropan (**DMC**) gebildet was darauf hinweist, dass **DMC**$^{+}$ bei der Bildung von **DIA**$^{+}$ aus **PRP**$^{+}$ ein Intermediat darstellt. Die Potentialfläche, welche **DIA**$^{+}$ und **PRP**$^{+}$ verbindet, wurde untersucht und auf dem CCSD(T)/cc-pVDZ// B3LYP/6-31G* Niveau vollständig charakterisiert. Dabei wurde festgestellt, dass vibronische Wechselwirkungen beim Mechanismus des spontanen Zerfalls von ionisiertem **PRP** nach **DIA**$^{+}$ eine wichtige Rolle spielen.
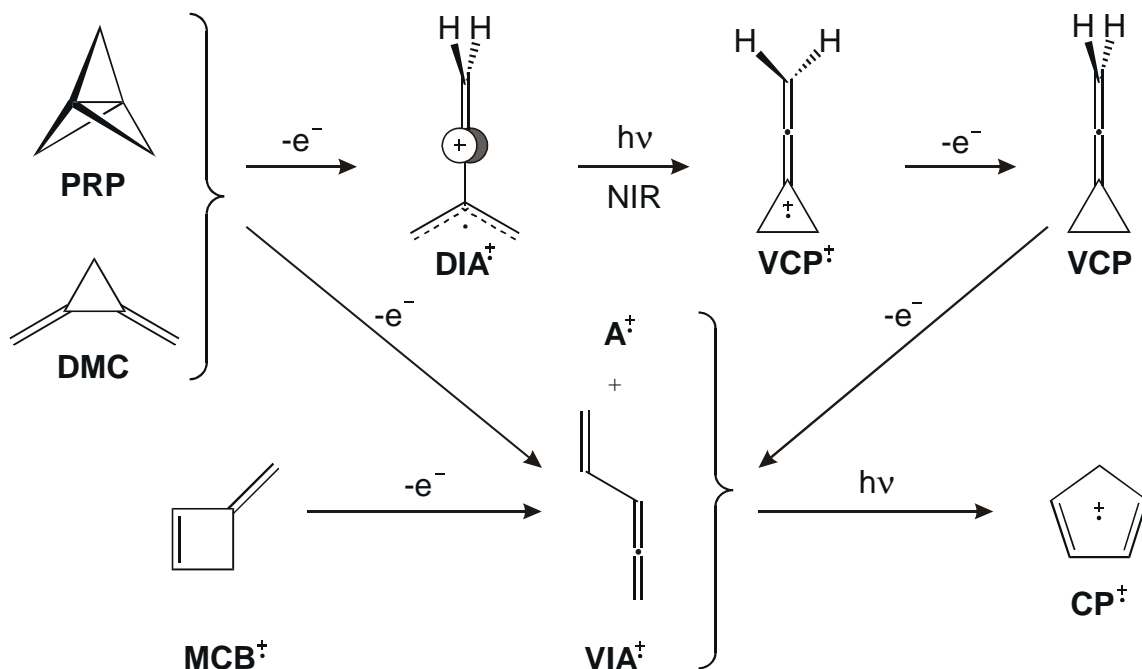
Optische Spektren weisen auf die Bildung zusätzlicher Produkte bei Ionisation von **PRP**, **DMC** oder **VCP** in Freon- and Argonmatrizen hin; insbesondere jene von Vinylallen (**VIA**$^{+}$), das ebenfalls durch Ionisation von **VIA** hergestellt

und charakterisiert werden konnte. Experimente in Argonmatrizen zeigten ein weiteres Zwischenprodukt **A**, welches photochemisch zum Radikalkation von Cyclopentadien (**CP**$^{+\cdot}$) umgelagert werden konnte. **A** konnte nicht identifiziert werden, aber verschiedene Spezies, welche für die beobachteten Spektren verantwortlich sein könnten, wurden vorgeschlagen. Weiterführende Arbeiten werden nötig sein, um die unbekannten Intermediate, welche bei den erwähnten Umlagerungen auftreten, zu identifizieren.

Der zweite Teil dieser Arbeit beschreibt die Bildung von Azomethinylid, **Y**, und des entsprechenden Radikalkations. Die experimentelle Untersuchung der Kraftkonstanten der C-N Bindungen in **Y** und der Vergleich mit jenen des Allylradikals sind von theoretischem Interessen. Durch das Hinzuziehen von **Y**-d_1 und **Y**-d_4 sollte es durch Skalierung des Kraftfeldes der drei Isotopomere möglich sein, diese Kraftkonstanten zu ermitteln.

Weiter wird gezeigt, dass Substituenten - im besonderen Phenylgruppen - beim Verhalten der Aziridine unter Bedingungen von photoinduziertem Elektronentransfer (PET) eine wichtige Rolle spielen. N-Phenylringe stabilisieren das Aziridin-Radikalkation während C-Phenylringe bevorzugt das ringgeöffnete Azomethinylid Kation stabilisieren. Das Mass dieser Stabilisierung kann ermittelt werden indem der Energiebedarf für die Rotation der Phenylgruppe in eine senkrechte Position berechnet wird, in der die Resonanz zwischen der Phenylgruppe und dem Aziridinring bzw. dem Azomethinylid unterdrückt wird. Experimente und Berechnungen zeigten, dass das N-Phenylaziridin Radikalkation, **NPA**$^{+\cdot}$, derart stark stabilisiert wird, dass es weder durch Ionisation noch durch anschliessende elektronische Anregung des Radikalkations zur Ringöffnung gebracht werden kann. Methylgruppen an den C-Atomen von **NPA** bewirken ein gewisses Absenken des Übergangszustandes der Ringöffnung, aber der Effekt ist zu gering, um die Überwindung der thermischen Barriere zu ermöglichen.

Im Gegensatz dazu bewirkt C-Phenylsubstitution eine ausgeprägte Stabilisierung des Übergangszustandes der Ringöffnung relativ zum Edukt (und dem Produkt). Damit erleiden N-H- und N-Alkyl-C-Phenylaziridine unmittelbar nach Ionisierung Ringöffnung. Die Frage, welcher der beiden Effekte im Falle des *C,N*-Diphenylaziridins "gewinnt", konnte nicht befriedigend beantwortet wer-

den. Jedoch genügte im Falle von ionisiertem Triphenylaziridin, **TPA**, eine kurze Photolyse, um eine Ringöffnung zu induzieren.

Damit ist der Gebrauch von Aziridinen, die durch Ionisierung geöffnet werden, um mit **A=B** Dipolarophilen [3+2]Cycloadditionen einzugehen, auf jene Derivate beschränkt, bei denen die ring-geschlossene Form nicht zu stark von den Substituenten stabilisiert wird.

1. Introduction

To study reactive intermediates such as radical cations, $M^{+\cdot}$, on a long time scale, as it was done in this thesis, they need to be immobilized and separated from any potential reaction partners. One way to achieve this is to embed the reactive intermediate (or, more often, a stable precursor for it) into an inert solid medium, such as a frozen noble gas.

The first experiments on radical ions in noble gas matrices were conducted in the mid 1960's by Pimentel and Andrews who found that, after reaction of Li with NO_2 *during* deposition, the IR bands of $NO_2^{-\cdot}$ could be observed [1]. However, the main drawback of this type of experiment is that, due to coulombic attraction, the counterions reside in close proximity to the $M^{-\cdot}$ which are thus subjected to strong mutual interactions. This problem can be largely resolved if electron transfers occurs *after* matrix isolation of neutral substrates and alkali metal atoms (at distant sites of the matrix). Kasai et al. found that this can be effected by mercury arc photolysis [2]. A similar approach led Milligan and Jacox to the observation of $C_2^{-\cdot}$ which they obtained by photoinitiated electron transfer from triethylamine or Cs to C_2 produced by VUV photolysis of acetylene [3].

Although Jacox and Milligan observed already in 1971 that VUV photolysis of $CHCl_3$ leads to the formation of the closed shell cations CCl_3^+ or $HCCl_2^+$ (depending on the wavelength of photolysis) [4], it was not until 1975 that Andrews et al. provided the first evidence for the formation of a *radical cation* in noble gas matrix. Bombardment of matrix isolated CCl_4 with 2 keV protons (*proton radiolysis* [5]) resulted in a very complex mixture of products, whose infrared spectrum showed three bands at 927, 502, and 374 cm^{-1} which could be assigned to $CCl_4^{+\cdot}$ (viewed as a $[CCl_2 \cdot Cl_2]^{+\cdot}$ complex [6, 7].

Using a slightly different approach, Bondybey and Miller initiated in 1978 a program for the study of the electronic structure of organic $M^{+\cdot}$. They elected to expose samples isolated in Neon matrices to ionizing radiation (usually the 10.2 eV photons of the Lyman α hydrogen line) through a LiF window. This permitted the independent variation of the host material and the exciting radiation and furthermore excluded bimolecular reactions of the $M^{+\cdot}$ prior to their immobilization in the noble gas matrix.

The scope of $M^{+\cdot}$ whose electronic structure could be probed in noble gas matrices widened considerably when, starting in 1980, the groups of Bondybey and Andrews began to measure *electronic absorption* (EA)spectra in Neon (Bondybey et al.) and Argon (Andrews et al.), respectively. Since the concentration of $M^{+\cdot}$ obtained by the VUV photolysis technique proved insufficient to measure their absorption spectra *perpendicularly* to the matrix, Bondybey and Miller resorted to an optical waveguide technique [8, 9] in which the light is coupled *laterally* via an entrance slit into the matrix and propagates through it by internal reflection.

In the mid 1980s Bally and Roth elaborated a new technique for producing radical cations in Argon matrices by X-irradiation [10, 11]. This allowed for the first time to measure also *vibrational* spectra of $M^{+\cdot}$ with this technique [12]. 10 - 15% of the neutral precursor can be converted to radical cations which makes it possible to measure spectra perpendicularly to the matrix. This results in a considerable simplification of the experimental setup.

A different technique to immobilize reactive species is to generate them in frozen glasses. In 1955, Evans [13] found that boric acid glasses [14] containing aromatic hydrocarbons become colored upon UV irradiation. He ascribed these changes to the formation of free radicals, but later Hoijtink at al. showed that spectra of these radicals were identical to those of the corresponding $M^{+\cdot}$ obtained in solution [15] and extended the boric acid glass studies to a broader range of aromatic hydrocarbons. However, the main limitation of this technique is that the substrate to be studied must survive the 400°C needed to produce a boric acid melt, and it is probably for this reason that such studies have remained confined to the investigation of polycyclic aromatic hydrocarbon cations which are often difficult to dissolve in organic solvents.

The majority of spectroscopic studies on organic radical ions is done by dissolving a neutral substrate in a suitable organic solvent which turns solid upon cooling to liquid nitrogen temperature, whereupon immobilized substrate ions can be formed by photolysis or radiolysis. The choice of solvent is dictated by two requirements which it much fulfill simultaneously: Firstly, it must be suitable for the spectroscopic technique to be used. Thus it should form a transparent glass for optical studies while ESR spectra can also be obtained in opaque polycrystalline matrices. Secondly, it should be able to serve as a

scavenger for ejected electrons (if $M^{+\cdot}$ are to be obtained) or positive charges (if $M^{-\cdot}$ are to be obtained), respectively.

While many of the early studies were done in CCl_4 [16, 17] which, however, shows strong absorptions of its own after radiolysis. Therefore CCl_4 was later replaced by Freons. CCl_3F (F-11) [18] has become the most popular of these for ESR investigations of $M^{+\cdot}$ [19], whereas its application in optical studies has remained limited because it forms highly scattering matrices. However, if CCl_3F is mixed with an equal amount of CF_2Br-CF_2Br (F-114B2), transparent glasses are easily obtained and this Freon mixture, which is often referred to as the Grimison-Simpson matrix after the authors who first reported its use in the literature [20], has become the standard medium for $M^{+\cdot}$ optical studies.

Depending on the species which should be investigated, the Argon or the Freon matrix isolation technique are preferred: an advantage of Ar is the transparency of the matrix over a wide range of the electromagnetic spectrum from 50 to 50'000 wavenumbers. Another advantage is the low temperature of 12 K where most chemical reactions are prevented. A disadvantage is that M has to be brought into the gas phase to mix it with the gaseous Ar before both condense on the crystal window. Furthermore, the high excess energy of the charge transfer from Ar to the substrate could lead to decay of metastable primary radical cations which otherwise might survive the ionization process.

An advantage of the Freon glass technique is that the precursor does not have to be brought into the gas phase but it is dissolved in the Freon mixture. This can also turn to be a disadvantage because Freons are not very good solvents for many substance classes. A further advantage is that the excess energy imparted onto the incipient $M^{+\cdot}$ lower and that this excess energy is rapidly dissipated by the solvent molecules. Disadvantages are the rather high temperature of 77 K and the fact that. Freons are opaque in the IR and in the far UV region.

2. Methods

In the field of reactive intermediates, to which radical cations ($M^{\dotplus}$) also belong, special techniques must be applied to probe their properties. If the goal is to characterize these molecules spectroscopically, either very fast methods (such as laser flash photolysis), or the matrix isolation technique can be used. The latter technique has the advantage to allow the observation of these challenging species over longer periods of time (days), and consequently several different measurements (UV/Vis, IR and ESR) can be performed on the same sample. However, the resulting spectra are not always straightforward to interpret. Many observations, including some of those presented in this Ph.D. thesis, would have had to be put aside unexplained without the help of quantum chemical models. Modern methods nowadays allow rather accurate quantitative predictions of the energetics of reactions. Furthermore IR-, UV/Vis and ESR spectra can often be predicted with enough precision to permit unambiguous assignments.

In this chapter a short introduction to the experimental and theoretical methods used in the present work will be given, focussing mainly on problems related to radical cations.

2.1 Experimental methods

2.1.1 Introduction

In the most general sense, matrix isolation comprises a range of experimental techniques in which guest molecules or atoms are trapped in rigid host materials. The trapped species are prevented from diffusing and can therefore not undergo any bimolecular reactions, except with the host material. This material can be a crystalline solid, a polymer, or a glass formed by freezing a liquid or by solidifying a gas. The term matrix isolation is, however, most commonly used in a narrower sense: to refer to the technique or trapping molecules or atoms in solidified inert (or occasionally reactive) gases - a technique that requires very low temperatures.

2.1.2 Argon matrix isolation

Matrix isolation in argon is a valuable tool to stabilize reactive intermedia-tes, such as the radical cations studied in this thesis, by isolating them from other molecules in an atomic lattice of noble gas atoms, hereafter called matrix. In this way bimolecular reactions are prevented. Additionally, the low temperatures (<20 K) used to solidify Ar (m.p. 83.8 K) suppress many unimolecular thermal reactions.

The cryogenic refrigeration and vacuum systems used in this study have been described in some detail elsewhere [10, 11]. To form the matrices, the gaseous constituents, argon (Argon 57 Carbagas: 99.9997% pure) and an electron scavenger such as methylene chloride (Fluka, for IR-spectroscopy) are mixed with the substrates of interest in a specially designed vacuum system. This so-called premixing of M is possible whenever its equilibrium vapor pressure is larger than ~14 Pa at room temperature. Liquid constituents (CH_2Cl_2 and possibly M) are degassed using three consecutive freeze-pump-thaw cycles. The ratio of the gas mixture is set to ~1000:1:1.5 ($Ar:CH_2Cl_2:M$). In the next step the moveable cryostat system is connected to the vacuum line and the mixture is released from the 2000 ml recipient through a flow-tube until the pressure has dropped by ~10 kPa. The mixture is sprayed onto a polished CsI window which leads to the buildup of a more or less transparent, several µm thick layer of solid argon doped with electron scavenger and the substrate. After this process the cryostat is separated from the vacuum line and wheeled to the spectrometer, to the X-ray source, or to the lamps.

In case of substrate molecules with lower vapor pressures only CH_2Cl_2 and Ar are premixed in the 2000 ml recipient and the substrate is placed into a U-tube which is inserted between the vacuum line and the cryostat inlet. The gas flow of the Ar/CH_2Cl_2 mixture streaming through the U-tube sweeps the substrate molecules along whereby the concentration of M can be controlled by the temperature of the bath into which the U-tube is immersed.

2.1.2.1 Generation of radical cations by X-irradiation in Argon

The X-irradiation technique is one of the main reasons why we use argon, rather than any other noble gas, because it has just the right cross section for interaction with keV photons (resulting mostly in core ionization which happens

to be resonant with the energy of the bremsstrahlung emanating from a tungsten target).

The radical cations were generated by irradiating the matrix through a 1 mm Suprasil window for 90 min. A Philips high voltage generator (model PW 1720/ 25) together with the corresponding tungsten X-ray tube PW 2234/20 were used as a source. An acceleration voltage of 40 kV and a tube current of 38 mA were the usual settings.
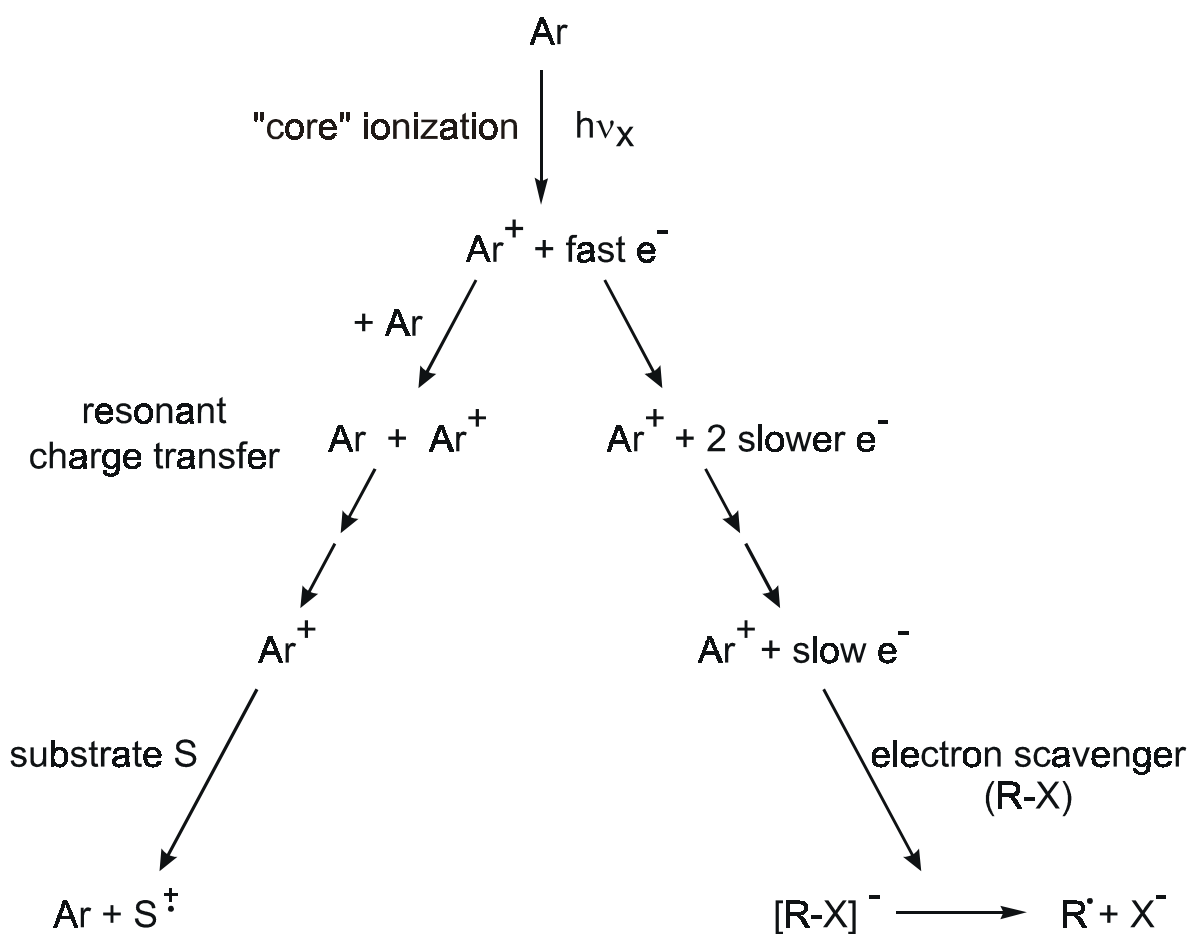
Figure 2-1: Schematic representation of the processes leading to the generation of radical cations ($S^{+\cdot}$) in Ar-matrices.

The processes leading eventually to the generation of radical cations in Ar-matrices are depicted in Figure 2-1. Initially an X-photon core-ionizes an Ar-atom generating a positive "hole" and a fast electron. The positive "hole" can move through the lattice by a mechanism called resonant charge transfer, until a molecule with a lower ionization potential (such as S) is encountered on which the positive charge gets trapped. On the other hand, the primary ejected electron

may have enough energy to ionize other Ar-atoms before its kinetic energy is sufficiently low to move through the Ar lattice by resonant charge transfer and eventually becomes attached to the electron scavenger. The electron scavenger, in our case CH_2Cl_2, traps the electron by dissociative electron attachment leading to a CH_2Cl radical and a Cl anion trapped in the same matrix cage. This complex has a flat absorption band at 600 nm which can, however, be readily bleached by visible light.

2.1.2.2 Use of X-rays to distinguish radical cations from neutrals
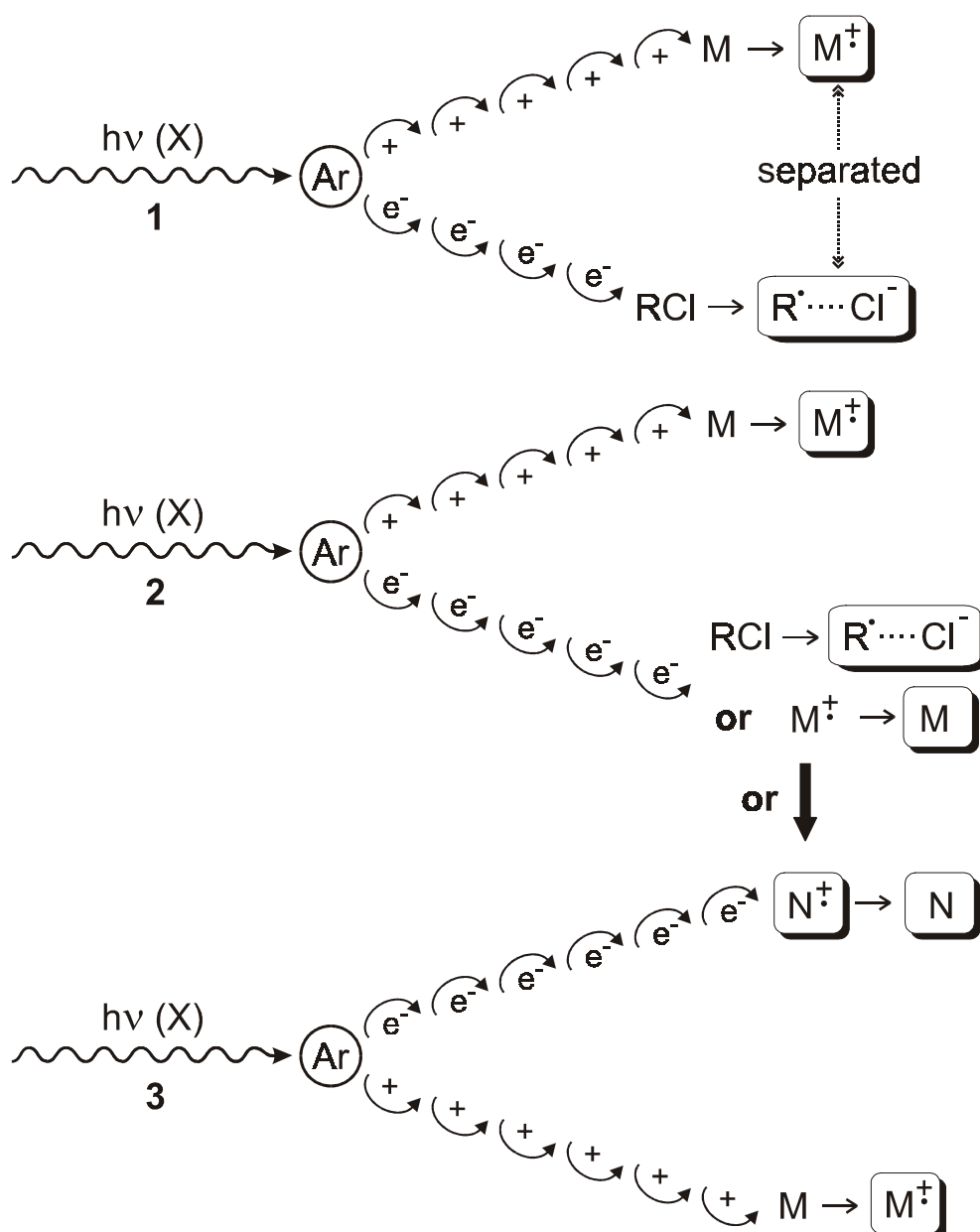
Figure 2-2: Different chain reactions in Argon matrices on X-irradiation.

On X-irradiation of an Argon matrix, different processes can occur as depicted in Figure 2-2: (1) An Ar atom is ionized by an X photon where the ejected electron travels away in one direction, from one Ar to the next, and the "hole", i.e. the positive charge, travels in another direction. When the electron meets a scavenger molecule, e.g. methylene chloride CH_2Cl_2, it gets trapped. If the positive charge encounters a substrate molecule, that molecule is ionized to its radical cation. The radical anion and the radical cation are separated in the Ar lattice, so they cannot easily recombine.

After a certain concentration of $M^{+\cdot}$ has built up, an electron moving through the matrix may encounter a $M^{+\cdot}$, and they combine to re-generate a neutral M. After around 90 min. of X-irradiation, $M^{+\cdot}$ are created and re-neutralized at the same rate and therefore the amount of $M^{+\cdot}$ levels off. Consequently, absorption bands of $M^{+\cdot}$ do not continue to grow after about 90 min. of X-irradiation.

In certain cases the $M^{+\cdot}$ rearrange or fragment spontaneously, forming new radical cations, say $N^{+\cdot}$, which also reach an "equilibrium" concentration after about 90 min. of X-irradiation. But now these new radical cations $N^{+\cdot}$ are in turn reneutralized by the ejected electron, whereby a new neutral molecule N is formed whose concentration may in principle continue to grow with irradiation time until all of the original substrate M is converted to N.

Thus, any primary radical cations that are formed on X-irradiation are visible in the spectra already after 15 min. of radiolysis. Their absorption bands grow until ca. 90 min. and then stay constant on longer radiolysis. However, reneutralized isomers (or fragments) N show up only very weakly after short periods of radiolysis but they keep growing steadily on prolonged irradiation. The limiting factor here is the availability of the original substrate M which of course decreases also in the course of this process. This difference in behavior allows us to distinguish peaks of radical cations from peaks of new neutral molecules that occur in many cases on prolonged radiolysis.

It is worthwhile to note that, especially in the electronic absorption (EA) spectra, a continuous increase of certain bands can be observed which arise even in the absence of any added substrate M and which must therefore originate from Ar or from the electron scavenger. An experiment with only methylene chloride in Ar shows after long X-irradiation two bands at 746 nm and at 720 nm together with a broad band at around 600 nm (see Figure 2-3). This set of bands can be bleached by photolysis at >715 nm (160 min.). Another broad band

with a pronounced vibrational structure peaking at 507 nm can be bleached partially, together with a strong band at 236 nm, on photolysis at >515 nm (160 min.). Two sharp bands at 279 nm and at 229 nm which also arise on long X-irradiation do not show any pronounced photosensitivity. They increase slightly on the first and decrease slightly on the second photolysis. Unfortunately, no peaks with a corresponding behavior could be observed in the IR-spectra hence the species formed on prolonged X-irradiation of CH_2Cl_2 could not be identified.
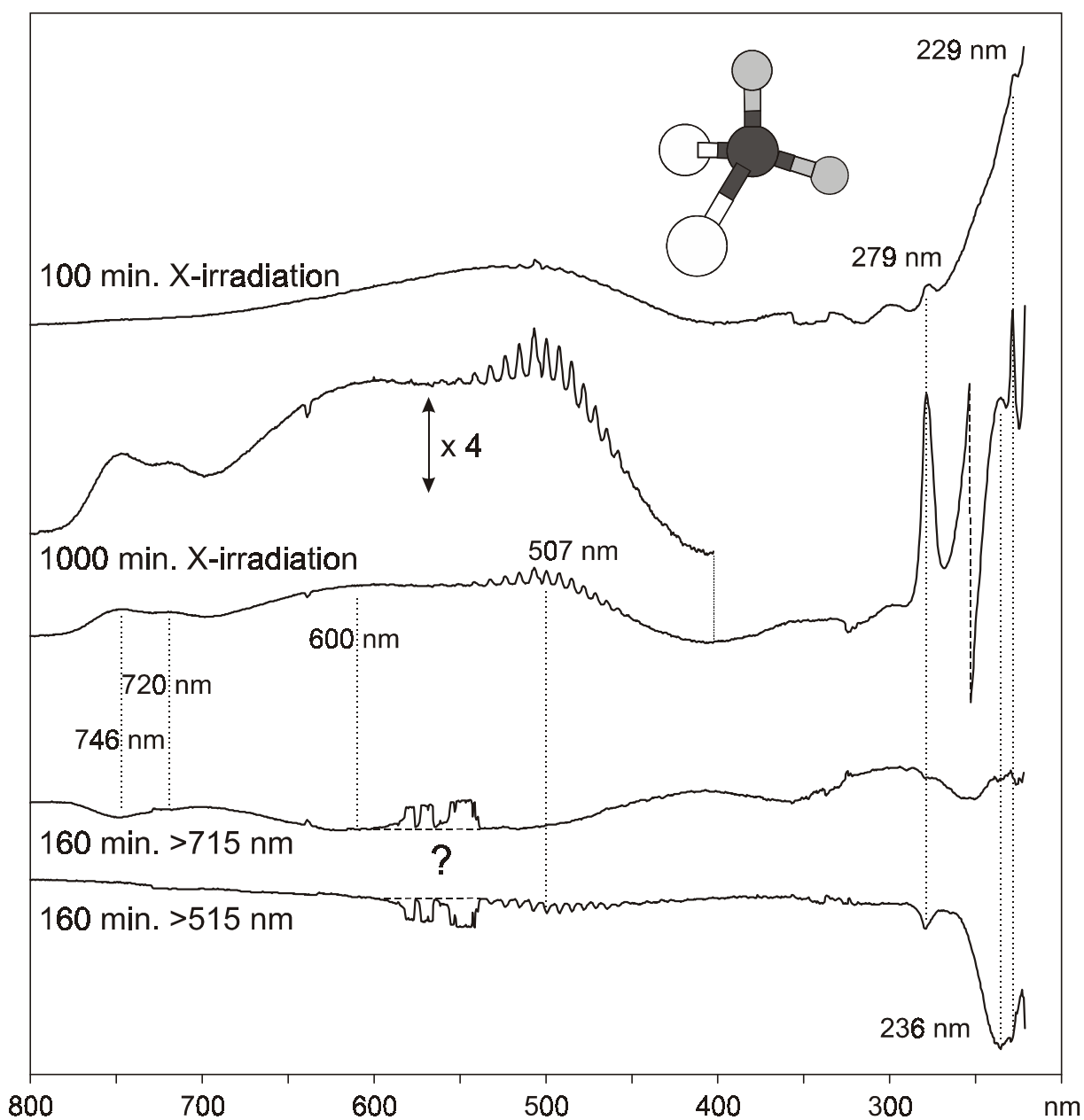
Figure 2-3: EA difference spectra of methylene chloride after long radiolysis and after photolyses.

2.1.3 Freon matrix isolation

It was Hamill et al. [21] who first demonstrated the formation of radical cations in organic glasses by γ-irradiation. The electrons ejected by radiolysis are trapped by the solvent and the "holes" are travelling through the matrix by a mechanism which is believed to involve resonant charge transfer between adjacent RX moieties.[1] When a substrate molecule M of lower oxidation potential than RX is encountered by the migrating "hole" it becomes attached permanently, as in the case of Ar matrices.

$$
\begin{array}{llllll}
\text{R-X} & & \rightarrow & \text{R-X}^{+\cdot} & + \quad e^- & \text{(ionization)} \\
\text{R-X} & + \quad e^- & \rightarrow & \text{R-X}^{-\cdot} & & (e^- \text{ attachment}) \\
\text{R-X}^{-\cdot} & & \rightarrow & \text{R}^{\cdot} & + \quad \text{X}^- & \text{(dissociation)} \\
\text{R-X}^{+\cdot} & + \quad \text{R-X} & \rightarrow & \text{R-X} & + \quad \text{R-X}^{+\cdot} & \text{(resonant CT)} \\
\text{R-X}^{+\cdot} & + \quad \text{M} & \rightarrow & \text{M}^{+\cdot} & + \quad \text{R-X} & \text{(hole attachment)}
\end{array}
$$
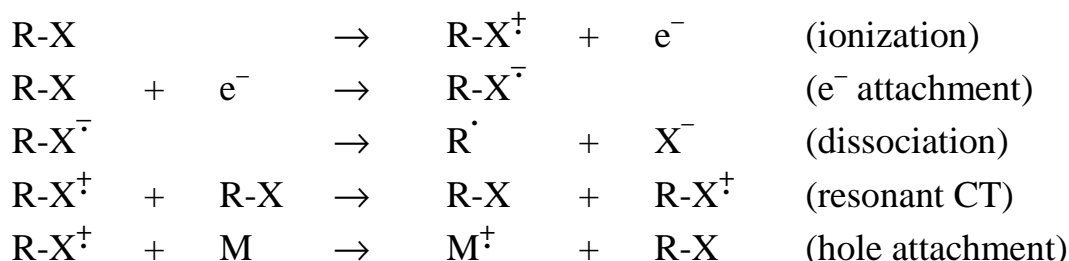
However, in the contrast to Ar matrices, the ejected electrons do not travel very far, but are trapped dissociatively by the matrix material as soon as their energy has decreased below a certain threshold. Consequently, re-neutralization of $M^{+\cdot}$ (or secondary $N^{+\cdot}$) does not come into play under these conditions.

It turns out that a substrate concentration of 10^{-3} M suffices to scavenge most of the positive charges generated during ionization of RX. As a solvent we normally use a 1:1 mixture of the Freons $CFCl_3$ (FC-11) and BrF_2C-$CBrF_2$ (FC-114B2). Freons are not very good solvents for many organic compounds, therefore the solubility is often a limiting factor for this technique. At low concentrations of the substrate a very broad band is observed around 600 nm (solvated electrons?) which can, however, be bleached by visible light within 3 min., thus leaving behind the absorptions due to $M^{+\cdot}$.

For γ-irradiation we used a Gammacell 220 ^{60}Co unit (Atomic Energy of Canada Ldt.). ^{60}Co emits γ photons of 1.173 MeV and 1.332 MeV (λ = 1.057 and $1.075 \cdot 10^{-2}$ Å) next to electrons of 93 keV average (314 keV maximal) energy, with a half life of 5.27 years. A first unit had been charged in 1970 with

---

[1] Note that, in contrast to the case of an Ar matrix, this hole transfer is associated with a (Frank-Condon) barrier in a polyatomic solvent, hence it requires (excess) thermal energy to occur.

$7 \cdot 10^{14}$ Bq (= 18'900 Ci) of ^{60}Co which yielded originally a measured dose rate of 16 kSv/h (1.6 Mrad/h) at the center of the sample chamber. During the time span when the unit was used for the present work, the activity was about $2 \cdot 10^{13}$ Bq leading to a dose rate of 450 Sv/h. The irradiation times were correspondingly adjusted to obtain the desired total dose (usually between 5 and 10 kSv $\rightarrow$ ~15 h of irradiation). The unit was replaced in 1998 and the activity of the new source was of $4.64 \cdot 10^{14}$ Bq (464 TBq) at the 22nd of January 1998. Consequently the irradiation time to reach the required dose decreased to around 45 minutes.

2.1.4 Photolyses

Photolyses in the visible domain were performed with a 1600W high-pressure Ar plasma arc lamp of Gamma Analysen Technik (GAT), model PB 1500. This lamp has a high continuum emission with additional intense lines around 800 and 400 nm. Additionally a 1000W low pressure xenon arc lamp, (Oriel model 6269) was used for the visible and NIR range. A medium pressure 150W mercury/xenon arc lamp, (Oriel model 6137) was employed for irradiations in the UV region. Next to a relatively intense continuum, this lamp exhibits strong mercury emission lines at 313 nm and 363 nm which were selected with appropriate interference filters. A set of suitable cutoff- (Andover Corporation) and interference filters was used in combination with the above mentioned lamps to select the needed energy range of the light used for the photolyses.

2.1.5 Spectrometers

In the course of this work electronic and vibrational absorption spectroscopy was used to characterize the generated reactive intermediates. The UV/Vis/NIR spectra were recorded on a Perkin-Elmer Lambda 19 (later Lambda 900) spectrometer which is capable of measurements between 190 and 3200 nm. The instrument was initially driven by a PC-computer program developed in our laboratories (SWO) which was later replaced by a commercial program from Perkin-Elmer (UVWIN LAB).

IR spectra were measured using an evacuable Bomem DA3 FT-IR spectrometer. In the 450-5000 cm^{-1} domain an MCT detector was used together with a KBr beamsplitter. In October 1995 a liquid He cooled Si bolometer and a Mylar broadband beamsplitter were acquired, thus permitting measurements

also in the 200-700 cm^{-1} range with CsI windows mounted on the vacuum shroud of the cryostat. Although the spectrometer has a maximum resolution of 0.02 cm^{-1}, IR spectra were generally recorded with a resolution of 1 cm^{-1} which proved to be sufficient. 256 scans were accumulated before the Fourier transformation. The spectrometer is entirely controlled by a computer which is connected to a front-end PC by an Ethernet link.

2.2 Theoretical methods

2.2.1 Introduction

In the course of this thesis, I spent about half of my time performing quantum chemical calculations on the species of interest. Mainly *ab initio* and density functional methods were used to shed light onto the problems under investigation. It would certainly exceed the scope of this thesis to present all these methods in due detail. The reader is therefore referred to textbooks [22, 23, 24]. In order to explain some of the results we have obtained, brief introductions to the methods used will be given in the respective context.

Three quantum-chemical program packages were used for the reported calculations: Gaussian94/98 [25], MOLPRO96 [26] and MOLCAS-4 [27]. These programs were installed on UNIX workstations of the Institute (Power Challenge, 4 x R10000, 1 GB RAM & 4 Pentium II/III, 8 x 400 - 550 MHz, 4 x 512 MB RAM), of the science faculty (DEC EV 6, 6 x Alpha, 4 GB RAM) or on those of the Centro Svizzero di Calcolo Scientifico (CSCS) in Manno (4 HP N-Class systems, 24 PA8500 360 MHz, 2 GB RAM).

2.2.2 Koopmans' theorem

UV photoelectron spectroscopy is an important tool to understand the properties of radical cations [28]. This is mainly owing to Koopmans' theorem [29] which provides a transparent link between this experiment and theory. The following ionization process is considered:

$$M(^1\Psi_0) \; + \; h\nu \; \rightarrow \; M^{+\cdot}(^2\Psi_j) + e^-$$
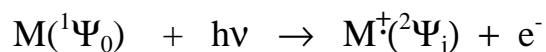
where M is a neutral molecule in its singlet ground state, $^1\Psi_0$, whereas $^2\Psi_j$ is a doublet state of the radical cation $M^{+\cdot}$. The ionization potential (IP_j) is the energy difference between $M(^1\Psi_0)$ and $M^{+\cdot}(^2\Psi_j)$.

Koopmans has shown that in Hartree-Fock calculations of the Roothaan-Hall type which yield canonical molecular orbitals $\{\psi_n\}$, the IP is equal to the negative energy of the orbital from which an electron is removed, provided that the ground state of the neutral molecule and the doublet state of the radical cation obtained by ionization can be described by the same set of molecular orbitals (MOs), i.e.,

$$IP_j = E(^2\Psi_j) - E(^1\Psi_0) = -\varepsilon_j$$

Koopmans' theorem has proven to be very successful in explaining and understanding photoelectron spectra, even though it contains some approximations. This success is due to the cancellation of two errors (see Figure 2-4).
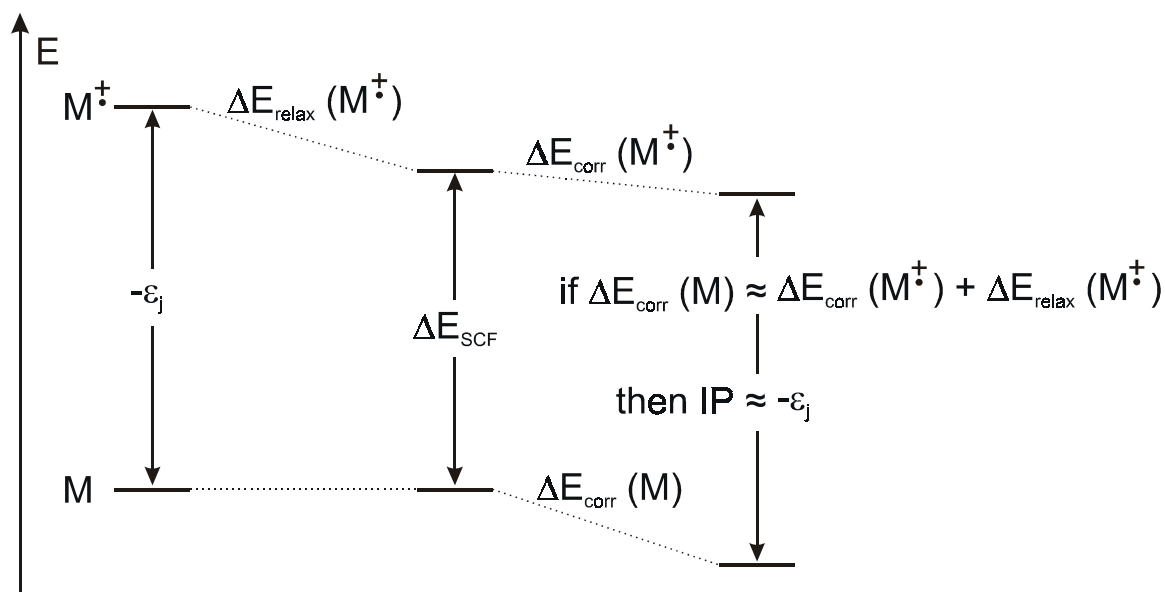
Figure 2-4: Canceling of errors in Koopmans' theorem.

Frozen core approximation: As the same MOs are used to build the Slater determinants for the neutral molecule and the radical cation, the orbital relaxation on ionization is neglected and therefore $M^{+\cdot}$ / M energy difference is *overestimated*.

Neglect of correlation energy: The correlation energy is the energy difference between the 'correct' energy and the Hartree-Fock energy of the system. In

Hartree-Fock calculations, the motion of each electron is evaluated in an average charge field, and most of the correlation energy is intrinsically omitted, which leads to an *underestimation* of the energy difference between M and M^{+}, because the correlation energy scales with the number of electrons. As it were, the two above errors tend to cancel very well for valence ionization.

Koopmans configuration: Koopmans' theorem applies only to electronic configurations of radical cations (see Figure 2-5) where electron promotion takes place among occupied orbitals. Such configurations are therefore called *Koopmans configurations*. The corresponding states are observed in the PE spectrum because they arise from simple ejection of electrons from doubly occupied molecular orbitals of neutral M. Configurations arising by promotion of electrons into virtual MOs (called *Non-Koopmans configurations*) describe states which do not appear in the PE spectra because on formation from M such states require the simultaneous ejection of one electron and the promotion of another one, a process which is forbidden by the PE selection rules. Non-Koopmans configurations may, however, be very important in the optical spectra of radical cations, as we will see in the section of experimental results.
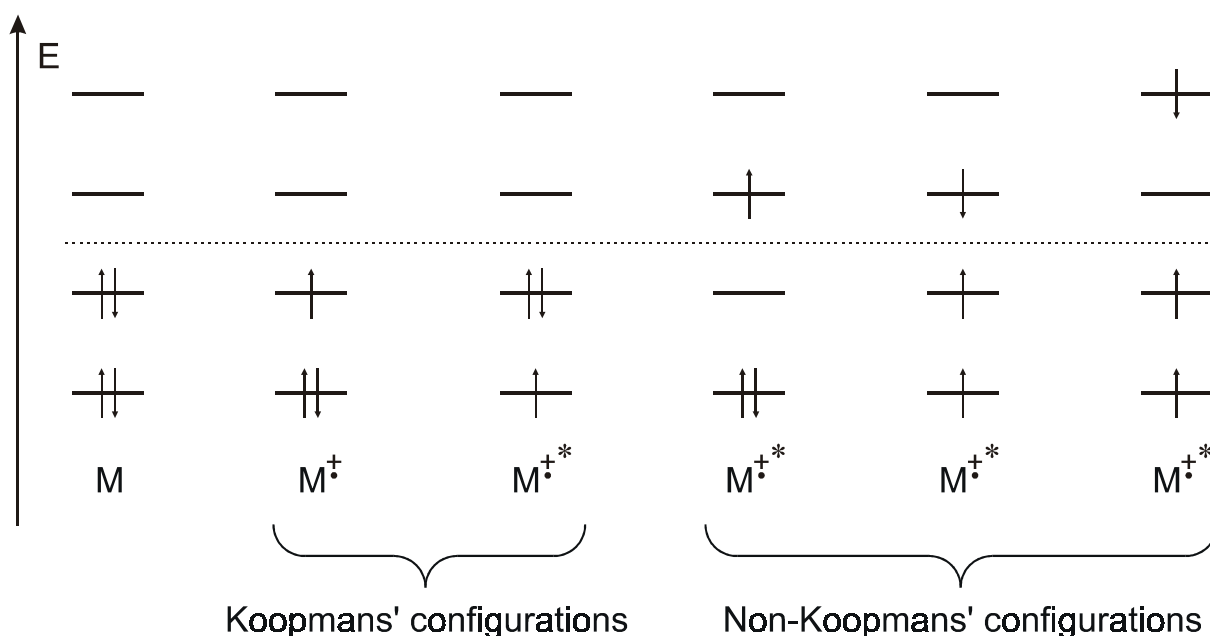
Figure 2-5: Electron configurations of radical cations.

2.2.3 Ab initio methods

With the development of highly efficient algorithms and high speed computers, ab initio methods can nowadays be applied to rather large molecules. However, electronic structure calculations including electron correlation are still a formidable task. In order to get a good electronic wavefunction, it is important to select an appropriate model. Different approximations may considerably affect the validity of the results.

2.2.3.1 The self-consistent field (SCF) method

Within Hartree-Fock theory, each electron is considered to move in an effective potential field corresponding to that of the nuclei supplemented by an average distribution of all the other electrons. Using the molecular orbital concept and the variational principle, the following equations derived by Roothaan [30] and Hall [31] are applied in order to describe the molecular orbital expansion coefficients.

$$\sum_{\nu=1}^{N} (F_{\mu\nu} - \varepsilon_i S_{\mu\nu}) c_{\nu i} = 0 \qquad \mu = 1,2,..., N$$

$$F_{\mu\nu} = H_{\mu\nu}^{core} + \sum_{\lambda=1}^{N}\sum_{\sigma=1}^{N} P_{\lambda\sigma} [(\mu\nu|\lambda\sigma) - \frac{1}{2}(\mu\lambda|\nu\sigma)]$$

$$P_{\lambda\sigma} = 2\sum_{\mu}^{occ} c_{\mu\lambda} c_{\mu\sigma}$$

Here $F_{\mu\nu}$ are elements of Fock matrix, $S_{\mu\nu}$ are elements of the overlap matrix and the ε_i are the one-electron energies of the molecular orbitals. $P_{\lambda\sigma}$ are the elements of the one-electron density matrix. By solving these equations, one can acquire a complete set of orbitals (occupied and virtual) and their energies. On that basis, one can compute the total electronic energy which, after adding the nuclear repulsion energy, gives the total energy of a system.

For open-shell systems, the above equations can be modified in two ways. One is the spin-unrestricted Hartree-Fock method (UHF). Thereby two distinct sets of molecular orbitals associated with α-spin and β-spin electrons are calculated. This allows to account for spin correlation, i.e. the fact that electrons

of equal spin maintain on the average a higher distance than those of the same spin (a consequence of the Pauli exclusion principle). Account of spin correlation is required to model the effect of spin polarization in radicals which makes that spin density with the opposite sign to that of the unpaired electron may occur, e.g. at hydrogen atoms attached to planar π-systems. However, because UHF wavefunctions are not eigenfunctions of the total spin operator $\hat{S}^2$, they contain a measure of so called spin contamination due to the admixture of states with higher spin multiplicity. In some cases, this can be so large that UHF results become practically meaningless. The spin contamination of the UHF wavefunction can be measured by the difference of the expectation value of the wavefunction with $\hat{S}^2$ from the correct value for a given spin state (0.75 for a doublet) [32]:

$$\langle \hat{S}^2 \rangle_{UHF} = \langle \hat{S}^2 \rangle_{exact} + N^\beta - \sum_i^{N^\alpha} \sum_j^{N^\beta} \langle \varphi_i^\alpha | \varphi_j^\beta \rangle^2$$

In the other method, ROHF, a single set of molecular orbitals is used to describe the distribution of α- and β-electrons. Unlike in the UHF case, the ROHF wavefunction is an eigenfunction of the total spin operator $\hat{S}^2$, but it does not allow for spin polarization, which can constitute a serious problem, e.g. if one wants to model ESR spectra. In addition ROHF wavefunctions are prone to symmetry breaking which can cause problems in the evaluation of derivatives. Figure 2-6 illustrates the comparison of these two methods.
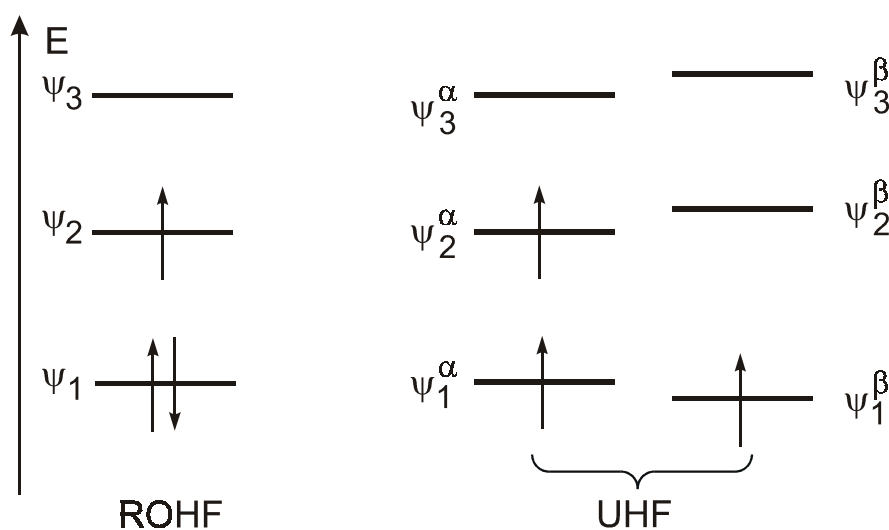
Figure 2-6: Comparison between UHF and ROHF.

2.2.3.2 Electron correlation by post-SCF methods

As we have seen above, the Hartree-Fock model is inadequate for treating the motion of electrons in many-electron systems. In cases like potential energy surfaces for bond dissociations where electron correlation plays a key role, the Hartree-Fock method often fails to give meaningful results.

Electron correlation effects may be subdivided into non-dynamic (or structural) and dynamic correlation. The latter refers to the correlation between the movements of different electrons arising through their Coulomb repulsion. An extensive configuration interaction (CI, see below) must be performed in order to take this effect into account properly. Dynamic correlation usually favors delocalization of electrons. Non-dynamic correlation refers to other deficiencies of the wavefunction such as the inability to describe dissociation or near degeneracy correctly and it can normally be rectified with a relatively limited CI treatment. The correlation energy is, by convention, defined as

$$E_{corr} = E_{exact} - E_{HF}$$

Here E_{exact} is a non-relativistic energy; E_{HF} is energy obtained at the Hartree-Fock level.

2.2.3.2.1 Full configuration interaction (CI)

Configuration interaction is an expansion of a many-electron wavefunction as a linear combination of Slater determinants:

$$\Psi = C_0 \Psi_0 + \sum_{L>0} C_L \Psi_L$$

where the Ψ_L are known as configuration state functions (CSFs); the coefficients C_L can be obtained from a variational calculation of the total electron energy E,

$$E = \frac{\int \Psi \hat{H} \Psi d\tau}{\int \Psi \Psi d\tau} \geq E_{exact}$$

If all possible Slater determinants within a set of occupied and virtual MOs are included (a so called full CI), then the electron correlation which is neglected in HF method can be fully recovered within the limits imposed by the choice of

the AO basis set. However, a full CI is very expensive and impractical except for very small systems. Therefore, other methods have been developed to limit the length of CI expansion and give a reasonable description for electron correlation.

2.2.3.2.2 Limited configuration interaction

In a practical CI calculation, the Hartree-Fock wavefunction for the ground state Ψ_0 is taken as a zero-order wavefunction to which one adds a set of excitations whereby the CI expansion is truncated at a limited level. If only single and double excitations are taken into account, this leads to the CISD method where the wavefunction can be expressed as follows:

$$\Psi_{CISD} = C_0 \Psi_0 + \sum_i^{occ} \sum_a^{virt} C_i^a \Psi_i^a + \sum_{i<j}^{occ} \sum_{a<b}^{virt} C_{ij}^{ab} \Psi_{ij}^{ab}$$

In closed-shell systems, singly excited configurations cannot mix with the ground state wavefunction, but this is not the case in open-shell systems.

Let us take the allyl radical as an example to illustrate the effect of a limited CI calculation [11] in treating non-dynamic correlation (see Figure 2-7). In a single-determinant treatment, the $\pi_1 \to \pi_2$ and $\pi_2 \to \pi_3$ electron promotions lead to two degenerate excited configurations of B_1 symmetry. The transitions from the $^2A_2$ ground configuration to these two degenerate excited configurations have the same oscillator strength in this case. When first-order CI is taken into account, the two degenerate configurations combine and split into two states, $^2B_1^-$ and $^2B_1^+$ which contain equal contributions of the two excited configurations. As a consequence, the transition moments for the two electron excitations cancel in the $^2A_2 \to {}^2B_1^-$, whereas they add up in the $^2A_2 \to {}^2B_1^+$ transition. These correspond to two bands in the electronic absorption spectrum, one in the visible with a very weak intensity, and the other very intense in the UV, in agreement with the above qualitative model.
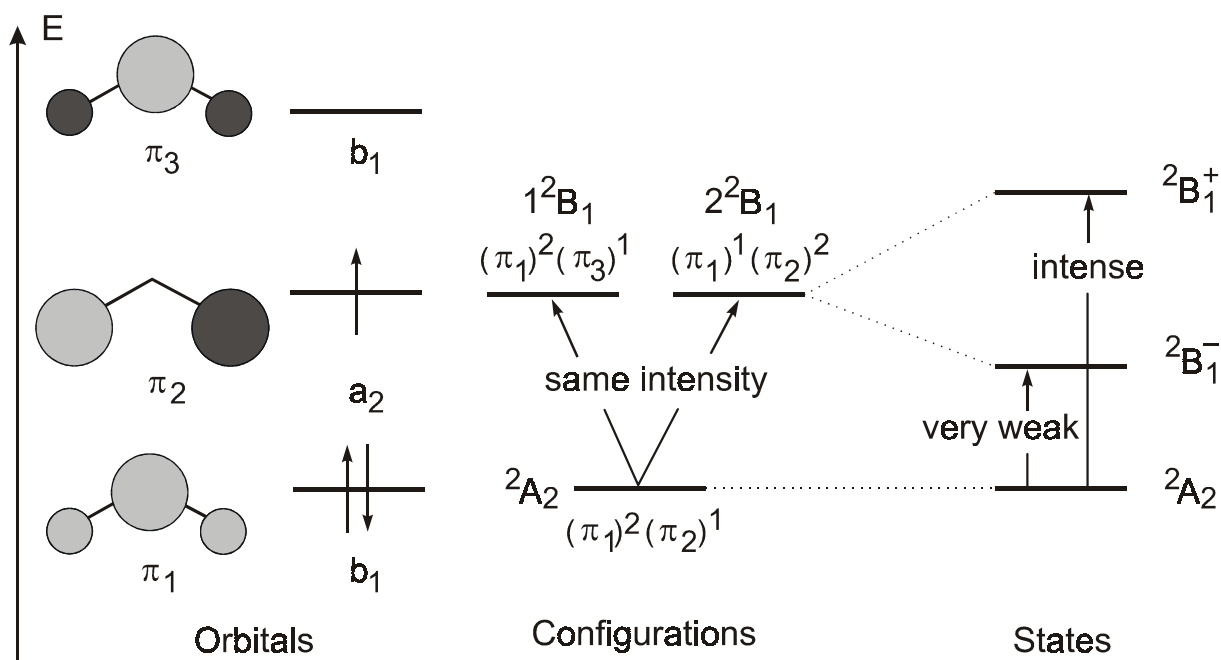
Figure 2-7: The electronic structure of the allyl radical with and without CI.

2.2.3.2.3 Many-body perturbation theory (MBPT)

The basic concept behind MBPT is to model the effects of electron correlation by treating them as a perturbation of a zero-order reference wavefunction, Ψ_0. To this end, the correlated wavefunction Ψ_0 is expanded in a series, $\Psi_0 + \Psi^{(1)} + \Psi^{(2)} + \Psi^{(3)} + \cdots$ where the superscripts in parentheses indicate the order of the perturbative expansion. Solving the resulting Schrödinger equation yields energies, $E_0 + E^{(1)} + E^{(2)} + E^{(3)} + \cdots$.

It can be shown that, provided $\langle \psi_0 | \psi^{(m)} \rangle = 0$ (i.e., all $\Psi^{(m)}$ are orthogonal to Ψ_0), $E^{(1)} = \langle \psi_0 | V | \psi_0 \rangle$, $E^{(2)} = \langle \psi_0 | V | \psi^{(1)} \rangle$, $E^{(3)} = \langle \psi_0 | V | \psi^{(2)} \rangle$ etc., where V is the electron repulsion operator, e^2/r_{12}. When perturbation theory works well, the higher the order of the correction, the smaller it is (e.g., $E^{(1)} >> E^{(2)} >> E^{(3)} \ldots$). Therefore, if perturbation theory converges rapidly, it may be unnecessary to compute most of the higher order terms in the series. Similar to the CI procedure, the wavefunctions $\Psi^{(m)}$ in MBPT are composed of excited configurations Ψ_L, formed from the filled and the virtual MOs for Ψ_0. However, the corresponding weighting coefficients, C_L, are determined by the use of perturbation theory, *not* variationally as they are in CI.

For example, in MBPT, the coefficients C_L of the excited configurations Ψ_L, that contribute to $\Psi^{(1)}$ for a reference wavefunction Ψ_0 are given by $C_L = \langle \psi_0 | V | \psi_L \rangle / (E_L - E_0)$. Thus, the C_L vary linearly with the size of the off-

diagonal matrix element that represents the interaction energy between Ψ_L and Ψ_0 and inversely with the energy difference between these two configurations.

Since the repulsion between the electrons in Ψ_0, $E^{(1)} = \langle \psi_0 | V | \psi_0 \rangle$, is already included in the energy of Ψ_0, $E^{(1)}$ can be ignored. To obtain $E^{(2)}$, $\langle \psi_0 | V | \psi_L \rangle^2 / (E_L - E_0)$ is summed over all the doubly excited Ψ_L. This requires computing the same electron repulsion integrals over the pairs of MOs, by which Ψ_0 and each Ψ_L differ, that are needed for calculating the C_L in $\Psi^{(1)}$. In a CISD calculation, the same integrals must also be computed, but they must be stored to set up the CI matrix (or, in so-called *direct* CI methods, they must be recomputed whenever they are needed). In contrast, in calculating $E^{(2)}$, once the $\langle \psi_0 | V | \psi_L \rangle$ terms have been computed, squared, divided by the energy difference $E_L - E_0$, and added to the sum of other such terms, they can be discarded. This difference obviously makes a second-order MBPT calculation, which includes the effects of singly and doubly excited configurations, much less computationally demanding than CISD.

The equations for computing $\Psi^{(2)}$, $E^{(3)}$, and the wavefunctions and energies at still higher orders of perturbation theory are quite a bit more complicated than those used for $\Psi^{(1)}$, $E^{(2)}$; and excitations beyond doubles must be included. However, conceptually, the process for including higher order terms in MBPT is similar to that used to compute $\Psi^{(1)}$ and $E^{(2)}$. [33]

2.2.3.2.4 Multi-configuration SCF (MC-SCF)

Within this method, the coefficients of the different Slater determinants Ψ_L in the CI expansion and the AO coefficients of the molecular orbital expansion are optimized simultaneously. As calculations with all the possible configurations consume too much memory and time, effective methods have been developed to reduce the need in computer resources, such as the complete active space SCF (CASSCF) method proposed by Roos et al. [34]. In CASSCF, a full CI is performed in a limited space (active space) which involves some occupied and some virtual molecular orbitals. A correct choice of the active space should include all MOs that are involved in the important configurations. Examples of active spaces are shown in Figure 2-8. After treating non-dynamic correlation effects by a CASSCF calculation, one may employ a second order perturbation method (see previous section) to include dynamic correlation effects and give a correct result without increasing the number of variationally treated con-

figurations. This method which has become increasingly popular in recent years has been given the name CASPT2.
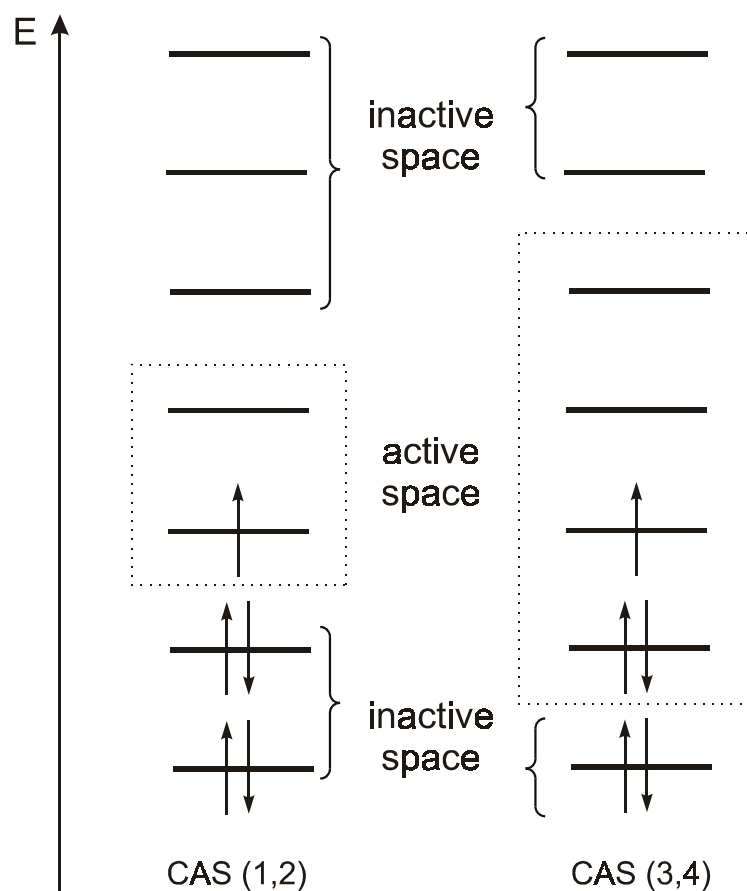
Figure 2-8: Scheme of the complete active space for a open-shell system.

The nomenclature for active spaces in this thesis indicates the number of electrons and orbitals in parentheses followed by the numbers of orbital belonging to different symmetry species in square brackets. For example, for a molecule of C_s symmetry (7,8)/[4,4] indicates seven electrons and eight orbitals in the active space, of which four of a' and four of a" symmetry.

In this work, excited state energies and transition moment of many radical cations were computed by the CASSCF/CASPT2 procedure which shows a particularly good performance in radical cations. After choosing a suitable active space, the CASSCF procedure generates a multiconfigurational wavefunction which will be used as a zero order wavefunction in the CASPT2 calculations. CASPT2 computes the first order wavefunction and the second order energy. Because radical cations are electron deficient, their molecular orbitals are more

compact than those of neutrals or anions. It is therefore not necessary to take account of Rydberg states and diffuse functions in the calculation of radical cations. Thus, simple DZ basis sets (C and O: 2s2p1d, H: 2s) are employed in all the CASPT2 calculations described in this work.

In the CASPT2 procedure, the oscillator strength for electronic transitions (f) is computed as:

$$f_{o,i} = \frac{2}{3} \times \mu_{o,i}^2 \times (E_i - E_o)$$

Here μ is the transition dipole moment which is computed by a state interaction procedure (RASSI). $(E_i - E_o)$ is the energy difference between two states obtained by CASPT2 energy calculation.

The weight, ω, of the CASSCF reference wavefunction in the first order wavefunction is an indication of the reliability of the CASPT2 result. It decreases with increasing of the numbers of electrons and can be estimated by the following equation:

$$\omega = (1 + \alpha)^{-\frac{N}{2}}$$

where N is the number of electrons and α is a constant between 0.01-0.02. If ω is significantly smaller than the above estimated value, or for one or another excited state, this is an indication that the CASSCF wavefunction is a poor approximation to the CASPT2 wavefunction and that therefore perturbation theory may fail to produce a correct result.

In chapter 2.2.3.2.3 it was shown that the coefficients C_L with which individual excited configurations enter a many-electron wavefunction Ψ are inversely proportional to the energy difference $E_L - E_0$ (where ψ_0 is the reference determinant, which may be an excited configuration in computations of excited states).

In calculations of excited states it may happen that the energies E_i and E_j of two excitations, where one virtual orbital is in the active space and the other is not, are almost degenerate. This leads to a huge coefficient $C_{ij} = \langle \psi_i | V | \psi_j \rangle / (E_i - E_j)$ because of the small denominator. A trick how one can get rid of these so-called intruder states is to shift all the virtual inactive orbitals by a constant energy value ("level shift"). Often after applying a certain level shift, one can

still find intruder states - normally involving other excitations. So one can continue to shift the virtual MOs by further increments, until one arrives at a situation where no intruder configurations occur. It is, however very important that the energies of those excited states that are not affected by intruder states remain reasonably constant throughout the series.
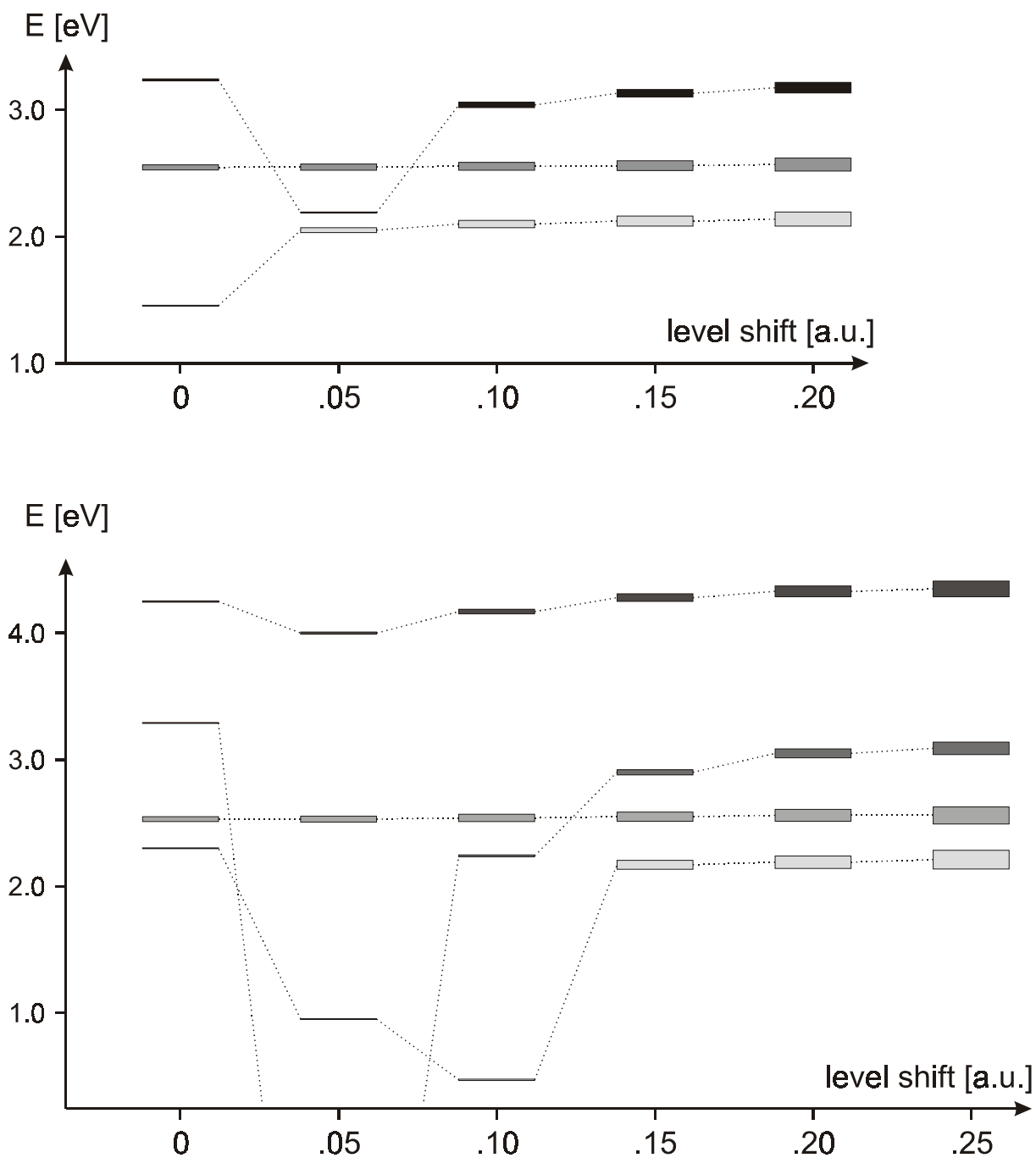
Figure 2-9: Illustration of the level shift method to eliminate intruder states at the example of *syn-* (upper graph, C_s point group) and *anti-* (lower graph, C_1 point group) C-phenyl-N-methylazomethine ylid radical cation (cf. section 4.5.3).

In Figure 2-9 two examples for such level shift calculations (*syn* and *anti* CPNMY, see chapter 4.5.3) are represented. The level of the bars show the change of the energy and the thickness show the reference weight (r.w.) which becomes constant after several level shifts. For a better visibility the thickness of the bars is not proportional to the r.w. but proportional to (0.75 - r.w.).

A small part of a Molcas output is given below where 4 roots at a level shift of 0.15 were calculated:

```
Wave function specifications:
 Number of closed shell electrons         62
 Number of electrons in active shells      9
 Max number of holes in RAS1 space         0
 Max number of electrons in RAS3 space     0
 Number of inactive orbitals              31
 Number of active orbitals                10
 Number of secondary orbitals            121
 Spin quantum number                     0.5
 State symmetry                            2
 Number of configuration state fnc.    27720
 Number of root(s) available               4
 CI root used                              1
 This is a CASSCF reference function

Orbital specifications:
 Symmetry species                          1    2
 Inactive orbitals                        30    1
 Active orbitals                           0   10
 Secondary orbitals                       90   31
 Number of basis functions               120   42

root1
Reference energy:        -401.5276257529
 Total energy:           -402.7184562079
 Reference weight:          0.72576

root2
Reference energy:        -401.4424789371
 Total energy:           -402.6405063387
 Reference weight:          0.71821

root3
Reference energy:        -401.4158875242
 Total energy:           -402.6243577362
 Reference weight:          0.71733

root4
Reference energy:        -401.3917352782
 Total energy:           -402.6034009755
 Reference weight:          0.70819
```

2.2.4 Density functional theory (DFT)

In the previous section we have discussed some methods based on Hartree-Fock theory. Density functional theory is another quantum chemical method which is now widely used because of its reliability and speed, especially in calculations of ground state properties such as the relative energies, geometries and frequencies. In this work, most geometry optimizations were performed by density functional methods. The foundation of DFT is that the total electron density may be regarded as an independent parameter of a multi-electron theory. Thus, if one knows the electron density, one can determine all ground state properties without knowing the electronic wavefunction, i.e. those properties are functionals of the density. In DFT, the critical task is to evaluate the exchange-correlation contributions of the density, and hence to the energy (see the excellent review by Ziegler [35] and other books [36, 37])

2.2.4.1 The Kohn-Sham equations

Based on the independent and non-interacting particle theory, Kohn and Sham [38] inferred the expression of the total energy:

$$E_{tot} = T_0(\rho) + \int V_{ext}\rho \, d^3r + \frac{1}{2} \iint \frac{\rho(r_1)\rho(r_2)}{r_{12}} d^3r_1 \, d^3r_2 + E_{XC}(\rho)$$

Here, T_0 is the kinetic energy of the system of non-interacting particles; the second term is the potential energy of interaction between the nuclei (V_{ext}) and electrons (ρ), the third $J(\rho)$ is the Coulomb interaction between the electron densities $\rho(r_1)$ and $\rho(r_2)$. The fourth is the exchange-correlation energy.

$$E_{XC}(\rho) = E_x + E_c$$

where E_x is evaluated by an "exchange functional" and E_c by a "correlation functional". In Kohn-Sham theory, the density ρ is modeled by a set of one-electron MOs which makes that the problem of solving the Kohn-Sham equation becomes isomorphic to that of solving the Roothaan-Hall equations (see chapter 2.2.3.1). The HF theory may be considered as a special case of DFT theory where E_c is neglected.

2.2.4.2 Local (spin) density approximation (LDA or LSDA)

Kohn and Sham introduced the local (spin) density approximation which means that the inhomogeneous system (e.g. atoms and molecules) can be treated as a uniform electron gas. In this approximation the exchange-correlation energy may be computed by the integrals

$$E_{XC}^{LSDA} = \int \varepsilon_{XC}\left[\rho_\alpha(r), \rho_\beta(r)\right]d^3r$$

Here, $\rho_\alpha(r)$ and $\rho_\beta(r)$ are the local electron spin densities.

2.2.4.3 Generalized gradient approximation (GGA)

Although the calculations at the LSDA level often give reasonable results, there are cases of large discrepancies, such as bond dissociation processes. In order to improve this deficiency, Perdew and Wang proposed the a modified approximation (GGA) which includes gradient corrections, i.e., the exchange-correlation energy is a function of the spin densities of electron and of their derivatives.

$$E_{XC}^{GGA} = \int f\left[\rho_\alpha(r), \rho_\beta(r), \Delta\rho_\alpha(r), \Delta\rho_\beta(r)\right]d^3r$$

Since then, many different correlation and exchange functionals have been developed. In practice, we can make many combinations by choosing different exchange functions and correlation functions (e.g. BeckeLYP or Becke3LYP). The general form of any model is shown below [25]:

$$aE_X^{HF} + bE_X^{local} + cE_X^{non-local} + dE_C^{local} + eE_C^{non-local}$$

Recently many studies have shown that B3LYP and BLYP models can give accurate geometries and force fields or vibrational spectra of ground state molecules.

2.2.4.4 td-B3LYP

To predict electronic transitions of molecules a recently introduced molecular density-functional method based on time-dependent response (TDR) theory [39] was used in this work. Analogous to the Hartree-Fock TDR theory, the poles and the residues of the frequency-dependent polarizability are evaluated, where the former correspond to vertical excitation energies and the

latter to oscillator strengths. Also, analogous to HF-TDR, an approximation is applied whereby excited states are described in terms of CI vectors containing single excitations from a ground state wave function (CIS), which permits a very transparent interpretation of the results. However, the treatment of electron correlation in td-DFRT goes far beyond that in a HF-based method, which means that the results are generally more accurate. We used the implementation of td-DFRT described recently by Stratmann et al. [40] and implemented in the Gaussian 98 program [25], together with the B3LYP functional. This model can also be applied to open-shell systems [41].

2.2.5 Locating transition states

Two methods were used to find transition states between two minima. The simpler one is a scan of one parameter, e.g. a bond length or an angle by well-defined increments which changes mostly in the course of a reaction and which could therefore lead to the transition state between the reactant and the product. Such a scan results in an energy profile with a structure of highest energy wherefrom a transition state (TS) search can be started (*opt=ts*). The advantage of this method is that all the geometries of the scan are optimized. Therefore the geometry of highest energy found by the scan is already very close to the TS.

Another method starts from a linear synchronous transit (LST) ansatz where the reactant is transformed into the product by a geometrical interpolation[2] [42]. In this program a weighting factor between 0.0 and 1.0 can be chosen which represents the weight of product geometry (0.0 = reactant geometry, 1.0 = product geometry). Usually single point calculations are performed for nine intermediate geometries which result in an energy profile of the reaction containing 11 points. Again, a TS search is started from the geometry of highest energy on this profile. In this procedure the geometries between reactant and product are not optimized and therefore it is recommendable to carry out a frequency calculation of the structure of highest energy before starting the TS search. The second derivatives "inform" the species about the shape of the potential surface on which it is located and in what direction is has to proceed to

---

[2]   This operation was effected with the SPARTAN program [42] which allows to introduce a
      factor between 0 and 1 that represents the weight of the product geometry (0 = reactant).

find the closest TS. In very difficult cases of small molecules on can even perform a frequency calculation after every optimization step.

A TS is characterized by a single imaginary frequency associated with a vibrational mode whose positive and the negative phases point in the direction of the product and the reactant, respectively. The full reaction pathway can be calculated by an intrinsic reaction coordinate (IRC) calculation. This procedure starts a the TS geometry and follows the imaginary vibrational mode towards the product and the reactant, respectively, by "sneaking" downwards on the potential energy surface, searching the path of the steepest descent.
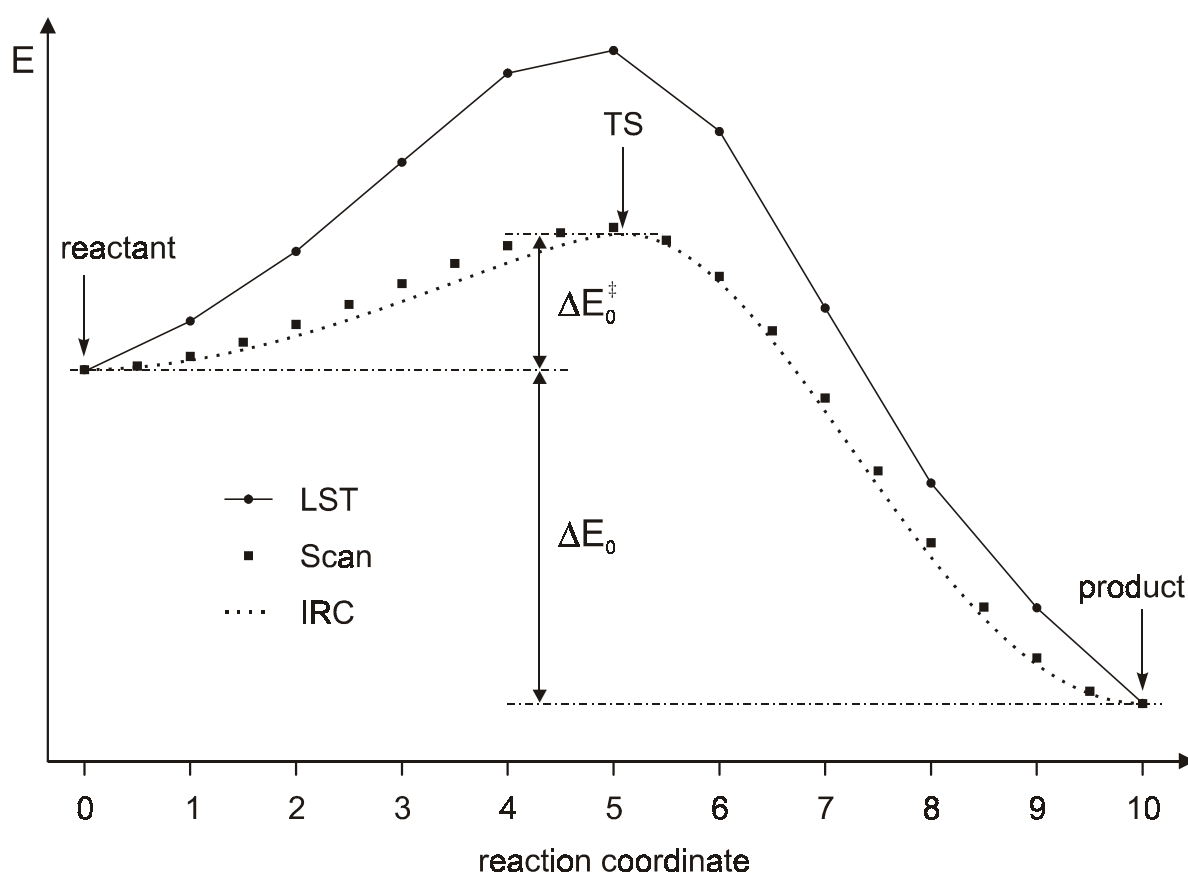
Figure 2-10: Schematic diagram of energy profiles obtained by LST, Scan and IRC calculations.

3. C$_5$H$_6$ - The Fate of Ionized [1.1.1]Propellane

3.1 Introduction

Tricyclic compounds of the structural type **1**, where three rings are connected by a common C-C bond are called [k.l.m]propellanes [43]. The indices k, l, and m represent the number of atoms forming the three bridges which span the central ethane unit. If these rings are large enough (k, l ≥ 4; m ≥ 2) the behavior of propellanes is the same as that of normal cycloalkanes [44]. Reduction of the number of ring atoms leads to a new class of substances called "small ring propellanes" [45] (k + l + m ≤ 8; m = 1 or 2). These compounds show some chemical and structural peculiarities.

1
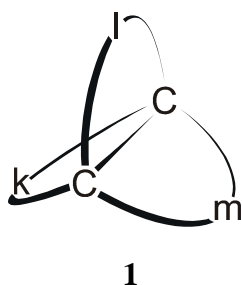
The first representative of this class, oxa[3.2.1]propellane **2**, had been synthesized in 1968 by the group of Wiberg [46] and the hydrocarbon **3a** one year later by the group of Gassman [47]. An X-ray structure analysis of the dichloro derivative, **3b**, [48] showed that all four substituents attached to each bridgehead carbon atom lie on one side of a plane containing this atom. Wiberg termed this feature "inverted tetrahedron".

2   **3a**: R = H; **3b**: R = Cl   **4**
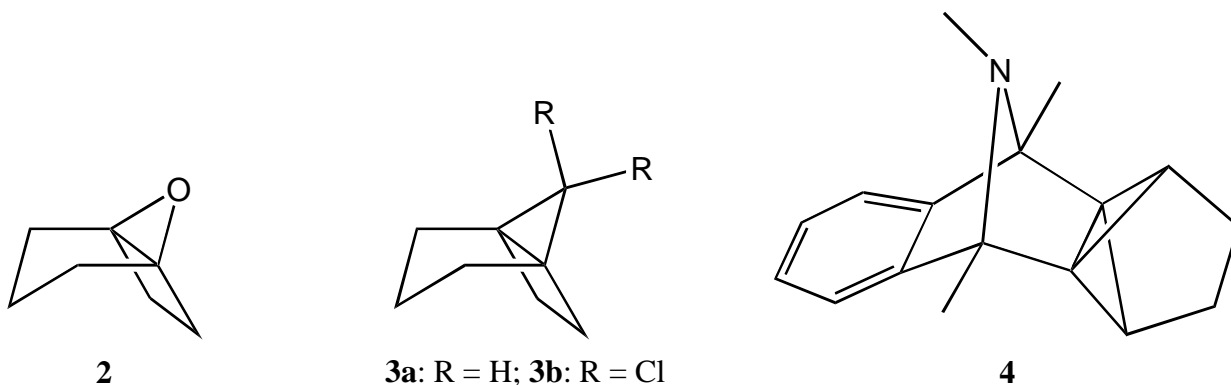
The investigation of the electron density of [3.1.1]propellane by the group of Dunitz [49] showed another anomaly: the electron density between the bridgehead atoms is close to zero. This was the first experimental proof for a

theoretical result which had been found by Newton in 1972 with the help of ab-initio calculations on [1.1.1]propellane **5** and bicyclo[1.1.1]pentane **6a** [50]. Although the distance of the bridgehead atoms in **5** is 160 pm which is not much longer than a normal C-C bond (154 pm), the central bond shows a clear deficiency of bonding electron density. Later, Wiberg [51] and Allen [52] confirmed with better basis sets the very low electron density between the bridgehead atoms - also for [2.1.1]propellane, **7** [53].

| 5 | 6a | 7 | 8 |
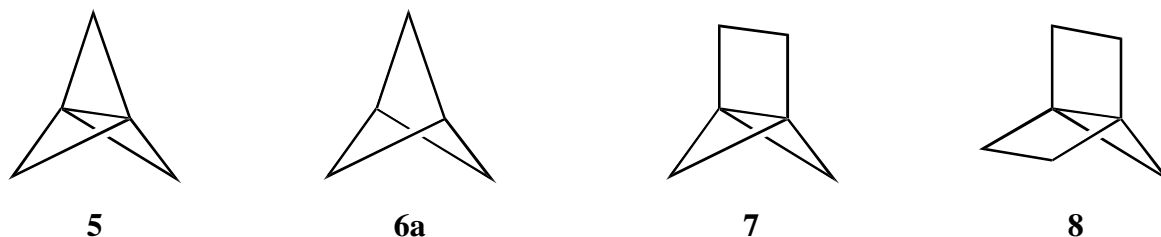
This lack of electron density *between* the bridge head carbon atoms is compensated by an increase of the density *outside* the "inverted tetrahedron" which bestows varying degrees of biradical character onto small ring propellanes. As a consequence small ring propellanes are highly reactive. Therefore [2.1.1]propellane **7** [54] and [2.2.1]propellane **8** [53] are only detectable in matrices at very low temperatures. Both compounds polymerize rapidly at higher temperatures.

14 years after the first synthesis of a small ring propellane, Wiberg et al. succeeded to synthesize **5** by reducing the dibromide **6b** with *tert.*-butyllithium [55]. Contrary to expectations and predictions, **5** turned out to be a stable compound [43, 56]. However, [1.1.1]propellane remained rather inaccessible because of a long and complicated sequence of synthetic steps leading to **6b**. Three years later, in 1985, Szeimies et al. [57] found a remedy to this problem: they synthesized the tricycle in a single step, starting from 1,1-bromo-2,2-bis-(chloromethyl)-cyclopropane **9**.

| 6b | 9 |
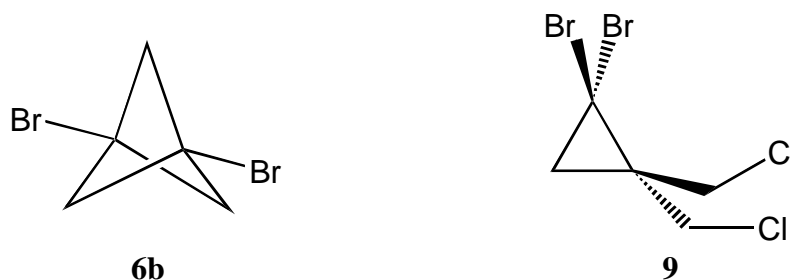
In what follows, we will use the acronym **PRP** to describe [1.1.1]propellane.

3.2 Previous results

PRP has D$_{3h}$ symmetry and therefore its radical cation could have a degenerate ground state which would be subject to Jahn-Teller distortion.
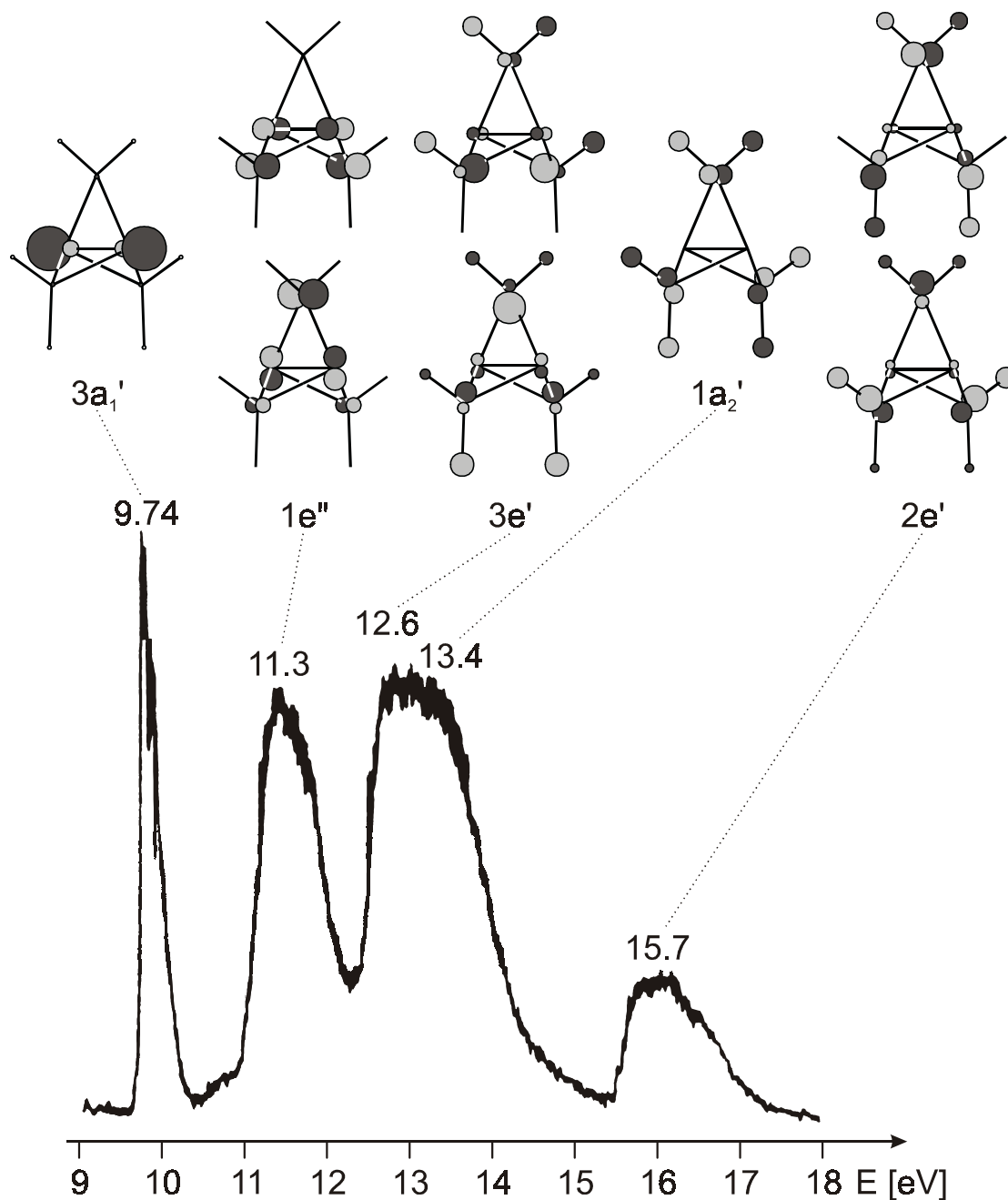
Figure 3-1: Photoelectron spectrum, ionization potentials, and SCF MOs of **PRP**.

However, the photoelectron spectrum of **PRP** (see Figure 3-1), which was measured in 1985 by the group of Heilbronner, shows a very narrow first ionization peak. This indicates that the potential energy surface of the neutral

and the ionic ground state are very similar, at least with regard to totally symmetric deformations. Moreover, all MO calculations agree in predicting a totally symmetric HOMO which is mostly localized "outside" of the central bond, whereas the density of the electron in that MO decreases almost to zero at the center of the molecule. Therefore the molecule shows a partial diradical character.

On the basis of the above features of the electronic structure we expect that the weak central bond of **PRP** gets weakened even more on ionization. However, because the propellane frame is held together by the three methylene groups which are not affected by ionization, the abstraction of one electron should not have any important influence on the structure of **PRP**. This conjecture seems to be confirmed by the Frank-Condon envelope of the first PE band indicating a very small distortion on ionization.

In the D$_{3h}$ point group the irreducible representations e' and a$_2$" transform like cartesian axes. Hence, only if the direct product of the irreducible representation of the ground state (a$_1$') with that of an excited state symmetry is e' or a$_2$", does the electronic transition have an oscillator strength different from zero. Thus, we expect that the EA spectrum of **PRP**$^{+\cdot}$ shows an absorption band around 430 nm because the PE spectrum shows an excited state of e' symmetry 2.86 eV above the a$_1$' ground state (at the neutral geometry). A td-B3LYP calculation of **PRP**$^{+\cdot}$ at the radical cation's geometry predicts this transition to occur at 380 nm (3.28 eV) but it carries a very weak oscillator strength ($f = 0.003$) which indicates that it might prove difficult to detect **PRP**$^{+\cdot}$ by electronic absorption spectroscopy.

3.3 Ionization of [1.1.1]propellane

3.3.1 Experiments in Freon glasses and in Argon matrices

After γ-irradiation of **PRP** in CF$_3$CCl$_3$, Pappas and Williams obtained an ESR spectrum which did not agree with their expectations of a heptet due to hyperfine coupling of the unpaired electron to six equivalent hydrogen atoms. It consisted instead of a 14.8 G quintet split into 5.4 G triplets (see Figure 3-2) which indicates a group of four and one of two equivalent hydrogen atoms [58].
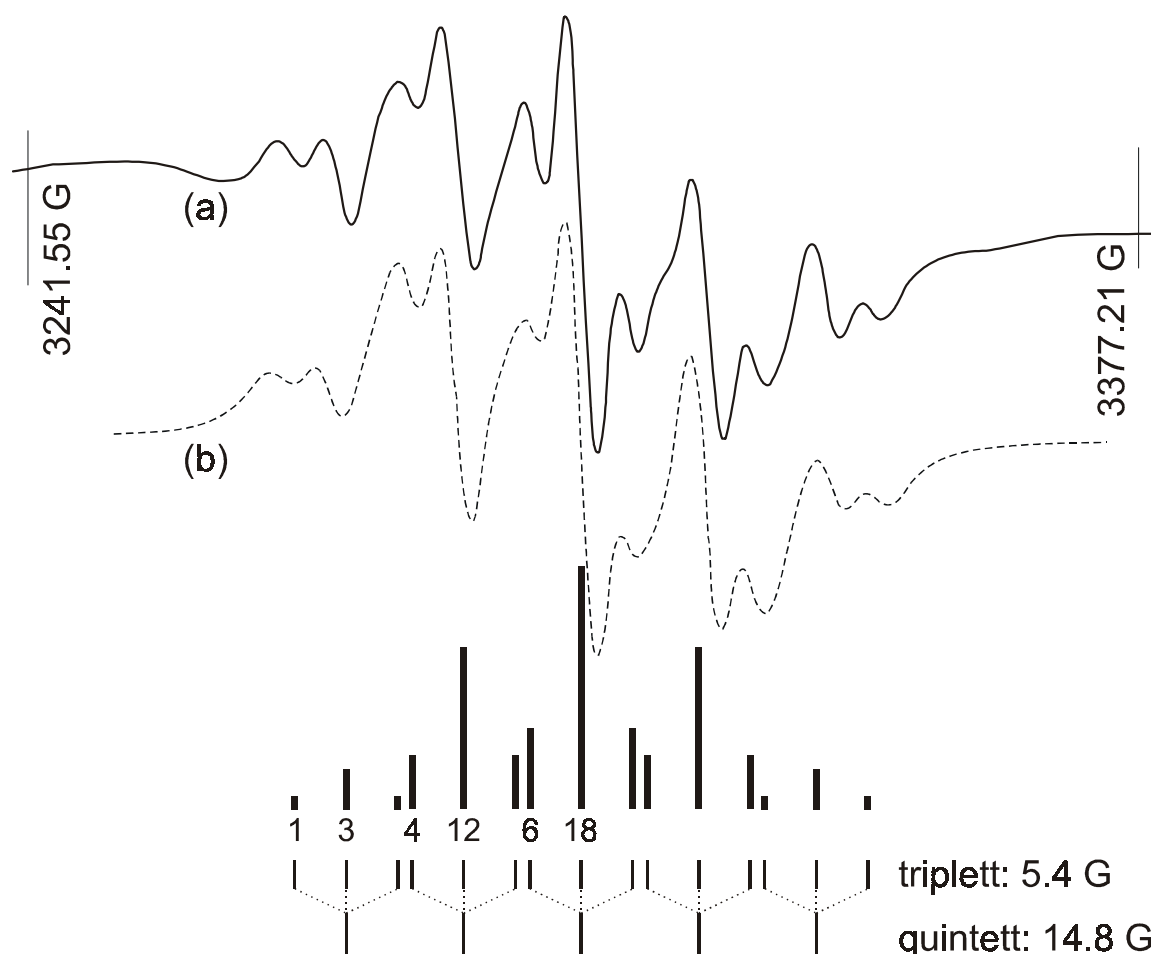
Figure 3-2: ESR spectrum of ionized **PRP** in Freon (a) and simulated spectrum (b) using the parameters a(4H) = 14.8 G, a(2H) = 5.4 G [58].

Ionization of **PRP** in a Freon glass results in a rather nondescript EA spectrum which increases gradually towards the UV. However, ionization by X-irradiation in Ar gave a spectrum with three distinct bands, a very weak, structured one in the NIR ($\lambda_{max} \cong 1400$ nm), a second, weak one around 480 nm, and an intense one at 310 nm, in addition to a few small peaks between the second and the third band (see Figure 3-3). Irradiation through a 850 nm cutoff filter led to the complete bleaching of the NIR band, whereas the other spectroscopic features remained unaffected, except for a small increase around 350 nm.

In the IR spectrum we observe after X-irradiation a decrease of the **PRP** bands (marked **P** in Figure 3-4) and an increase of several bands which are bleached again on >850 nm photolysis. The most intense peak in this set is a

band at 1870 cm^{-1} which indicates that the compound **X** which is obtained on ionization of **PRP** could contain cumulated double bonds. The IR peaks which rise and fall in concert with the NIR band in the EA spectrum are listed in Table 3-1 (p 42).

In conclusion, all experimental findings indicate that, contrary to expectations based on the nature of the HOMO from which ionization occurs, **PRP** undergoes some spontaneous rearrangement on oxidation. In order to guide our search for possible rearrangement products, and to clarify the reasons for the unexpected instability of **PRP**‡, we resorted to theoretical calculations.
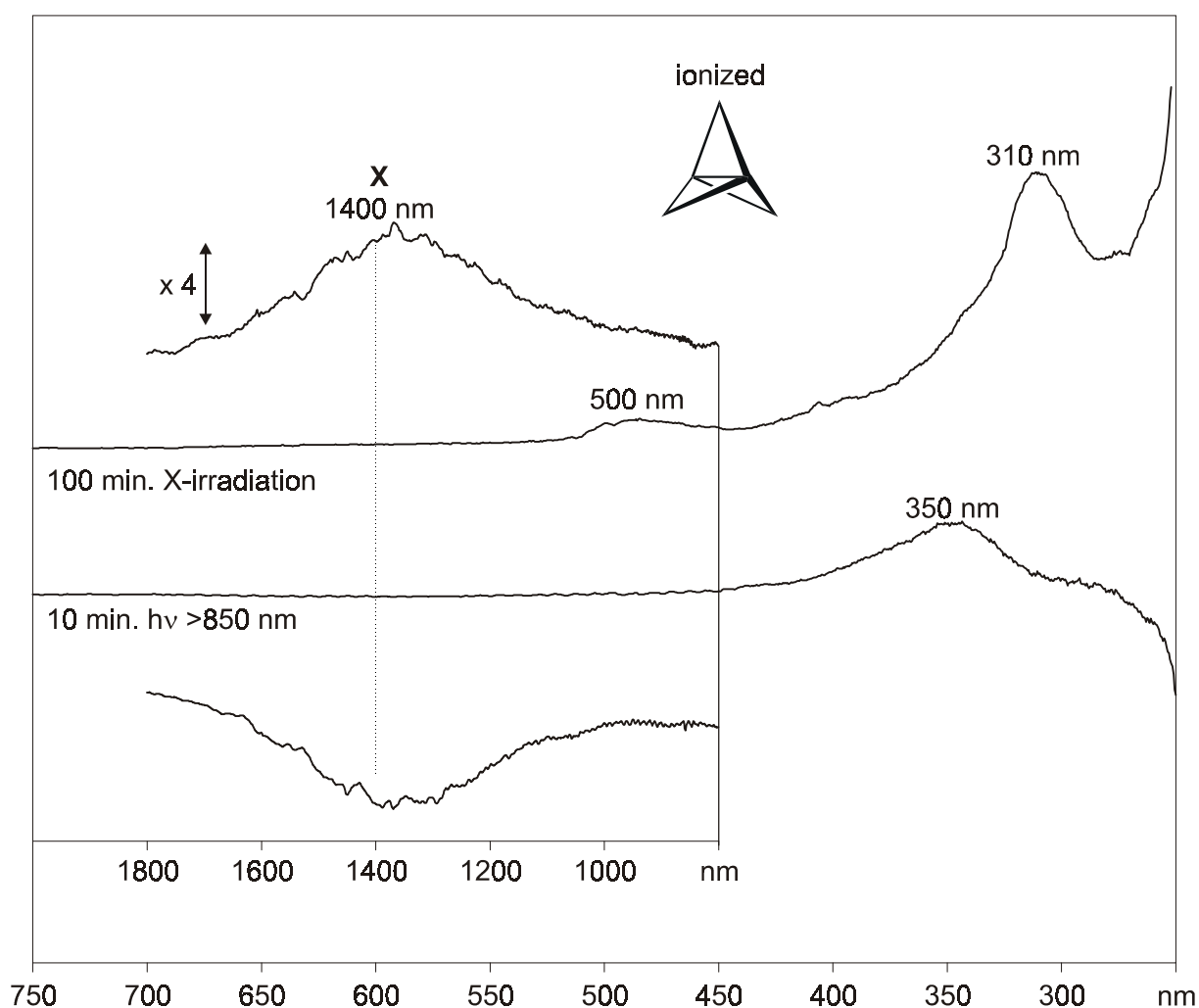
Figure 3-3: EA spectra of ionized and photolyzed **PRP** in Ar matrix.
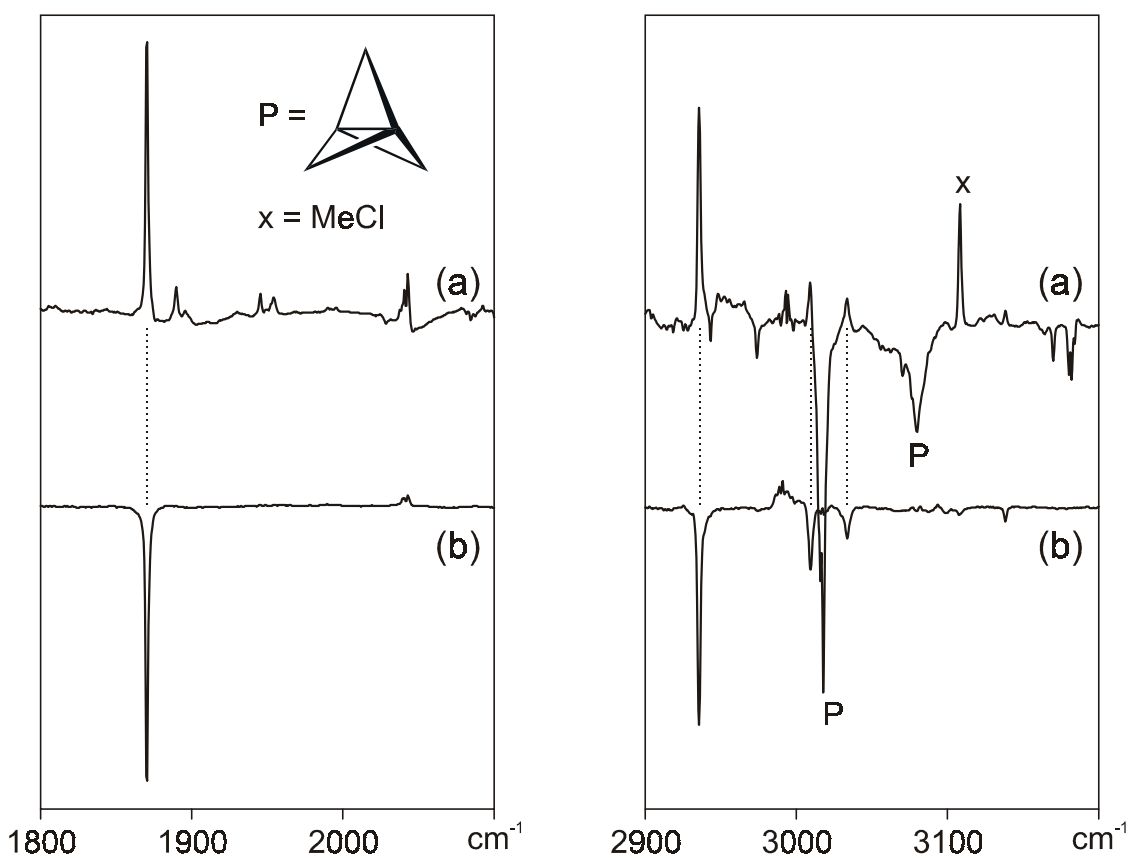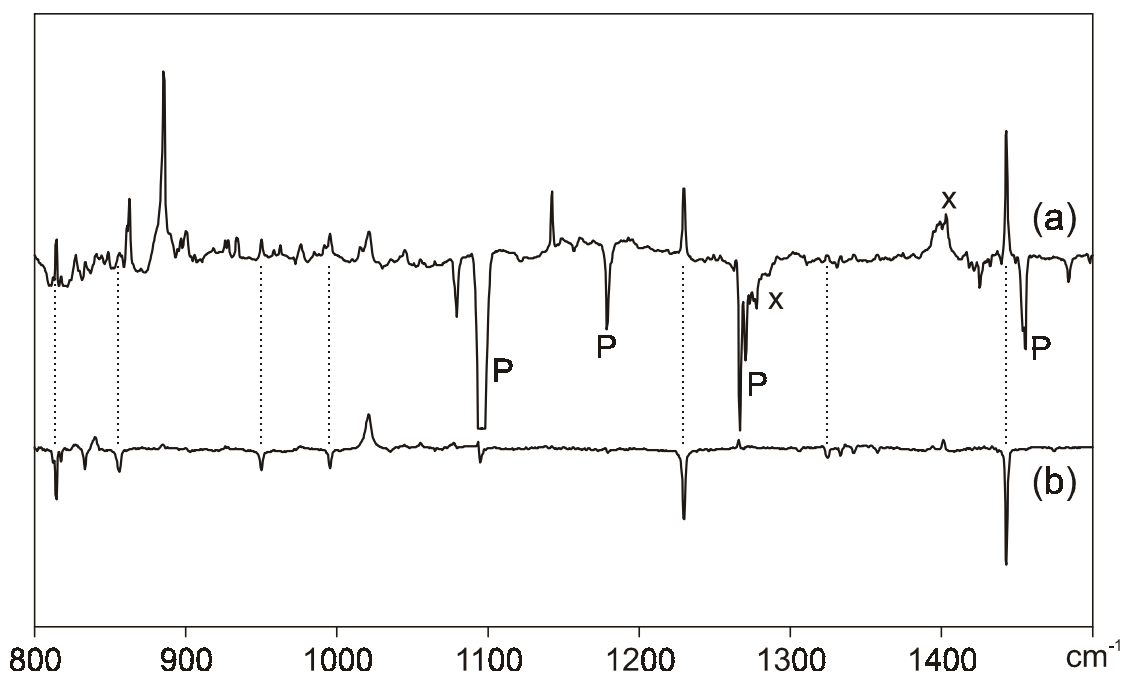
Figure 3-4: Selected regions of the IR difference spectra of **PRP** in an Ar matrix: (**a**) after X-irradiation (**b**) after subsequent bleaching at >850 nm. See Table 3-1 for a listing of the peaks which increase on X-irradiation and are bleached by NIR irradiation.

3.3.2 Theoretical investigations of [1.1.1]propellane radical cation

PRP belongs to the D$_{3h}$ point group. Since its radical cation has a totally symmetric ground state, it is appropriate to start out by calculating it also in this symmetry. As expected we found only a small geometry change on ionization (a 0.034 Å shortening of the central bond and a 0.011 Å lengthening of the lateral C-C bonds) at the B3LYP/6-31G* level. However, a force field calculation gives a vibration with a negative frequency. It corresponds to a degenerate normal mode of e" symmetry which involves, among other deformations, a lengthening of one and a shortening of the opposite lateral C-C bond (cf. Figure 3-5).

e"

-205 cm^{-1}
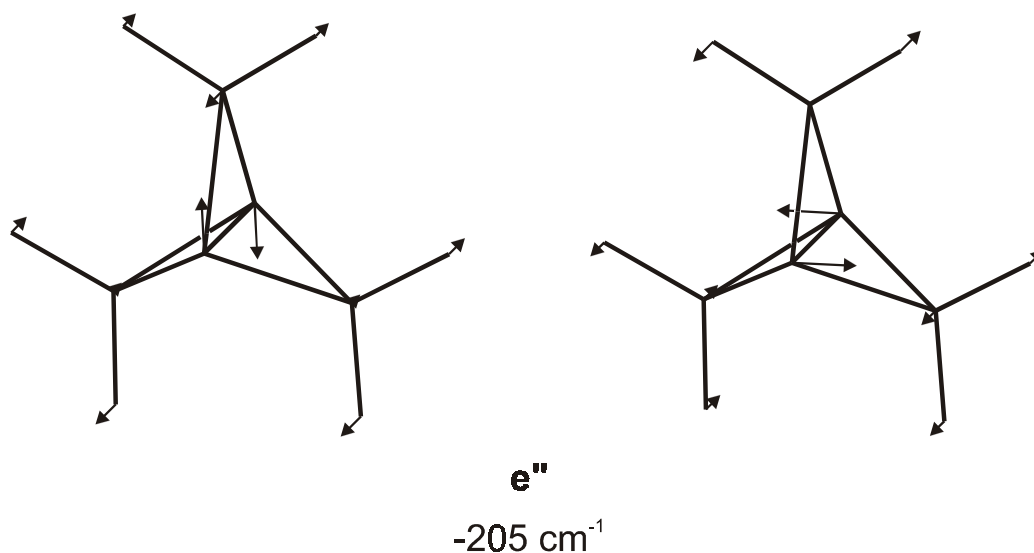
Figure 3-5: The two components of the degenerate mode of **PRP$^{+\cdot}$** in D$_{3h}$ symmetry that is associated with the negative frequency.

On following one of the components of this mode, a quite strongly distorted minimum of C$_s$ symmetry is obtained (one lateral C-C bond is lengthened by 0.12 Å, whereas the opposite one is shortened by 0.06 Å, see Figure 3-6). A force field calculation at this geometry identifies this structure as a potential energy minimum, but it shows that the two lowest frequency vibration modes still point more or less in the same direction as the two components of the e" mode in D$_{3h}$ symmetry. The lower of the two frequencies is only 146 cm^{-1} which indicates that we are close to a transition state. The change of the normal mode associated with the lowest vibrational frequency on going from D$_{3h}$ to C$_s$ symmetry is depicted in Figure 3-7.
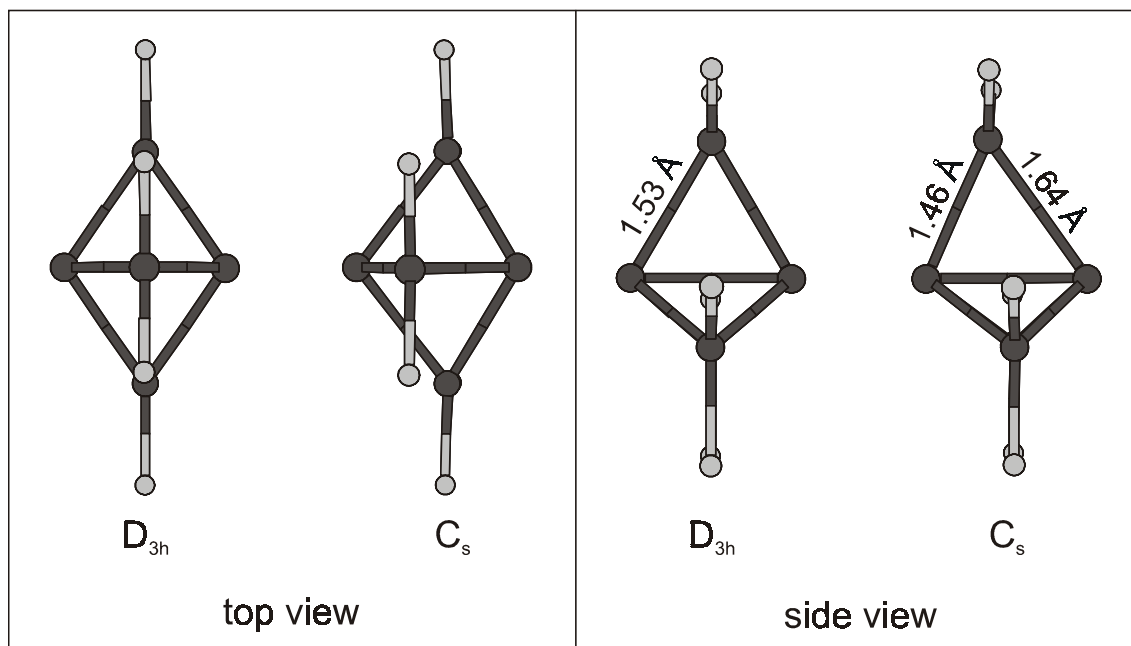
Figure 3-6: Geometries of **PRP$^{+\cdot}$** in C$_s$ symmetry (minimum) and in D$_{3h}$ symmetry (2nd order saddle point[1]).
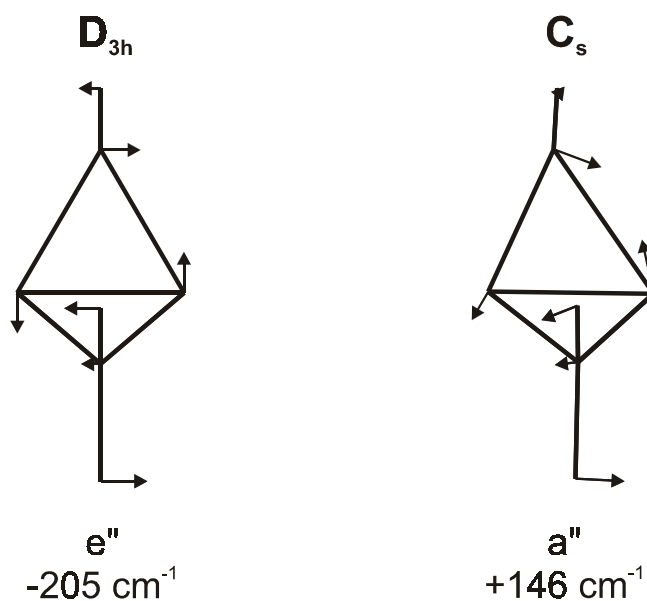
Figure 3-7: Low-frequency vibrational modes of **PRP$^{+\cdot}$** in D$_{3h}$ and in C$_s$ symmetry.

---

[1] The definition of a transition state is that all second derivatives must be positive except *one*. However, in this species shows *two* (degenerate) 2nd derivatives and it is therefore a second order saddle point.

$$\Gamma(q) = \Gamma(\Psi) \times \Gamma(\Psi^*) = e''$$
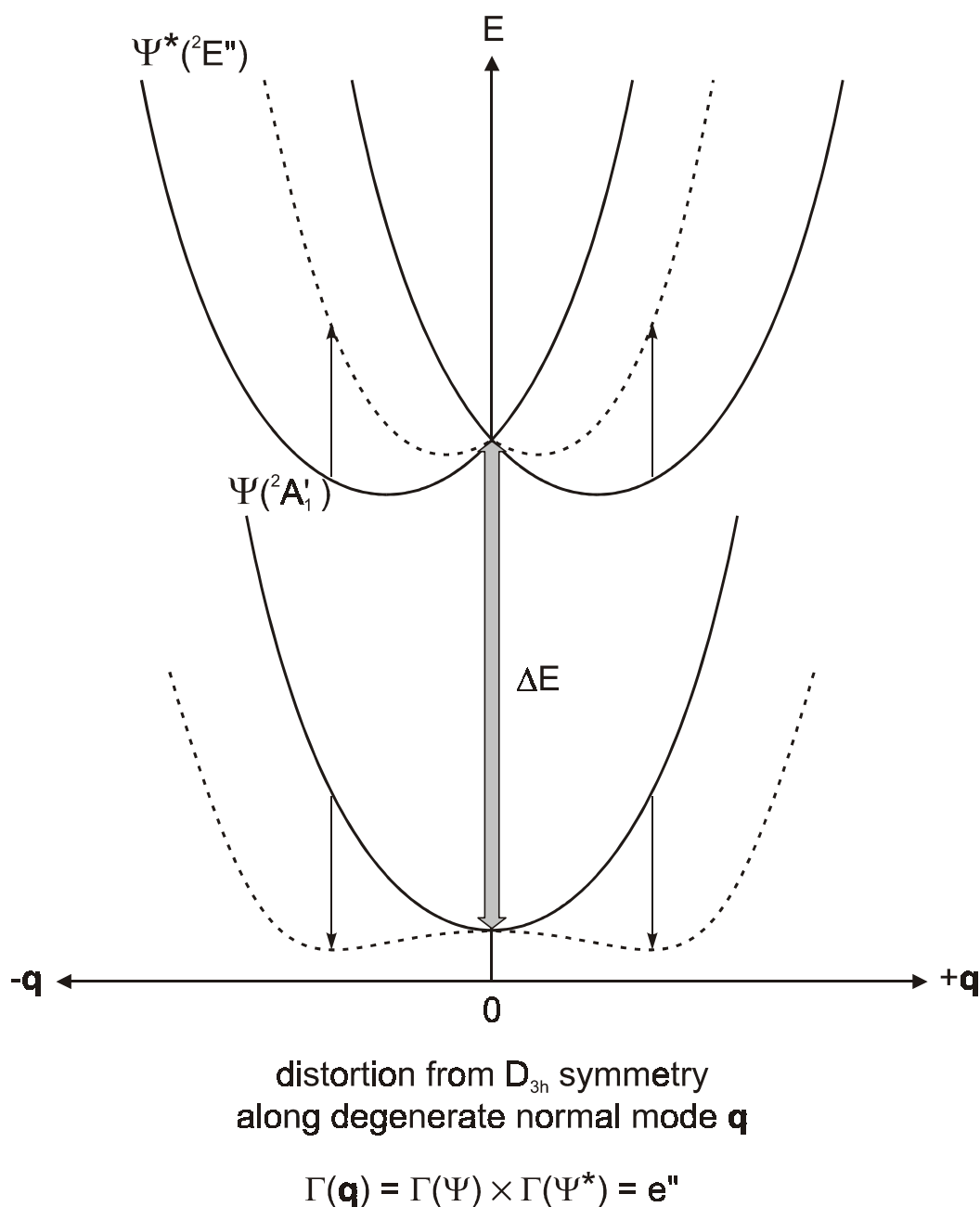
Figure 3-8: Vibronic interaction in a system of D$_{3h}$ symmetry with a totally symmetric ground state (^{2}A$_1$') and a degenerate (Jahn-Teller active) excited state (^{2}E''), e.g. **PRP**$^{+\cdot}$.

What is the reason for this unexpected distortion of ionized **PRP**? It can be explained by taking into account the interaction between the electronic and the vibrational wavefunctions (vibronic interaction).

A distortion of the molecule along a non-totally symmetric vibrational mode breaks the symmetry. Depending on the nature of this distortion the totally symmetric ground state (^{2}A$_1$') can mix with the excited state (^{2}E''). This mixing leads to "repulsion" of the potential energy curves of these two electronic states

(cf. Figure 3-8). If the interaction is sufficiently strong, the potential energy curve of the ground state may be "bent down" so that a double potential minimum is formed, as it is the case in **PRP^{+}** at the B3LYP/6-31G* level. The amount of vibronic interaction (v.i.) is proportional to the so-called derivative (or non-adiabatic) coupling term and inversely proportional to the energy gap between the two states in high symmetry

$$\text{Extent of v.i.} = \frac{\left\langle \Psi \left| \partial/\partial \mathbf{q} \right| \Psi^* \right\rangle}{\Delta E}$$

The extent to which v.i. affects the ground state potential energy surface depends additionally on the force constant f(**q**) which opposes the distortion along the symmetry-breaking normal mode **q**.

$$f(\mathbf{q}) = \left[\frac{\partial^2 E(\Psi)}{\partial \mathbf{q}^2} \right]_0$$

On the B3LYP/6-31G* potential energy surface **PRP^{+}** distorted to C$_s$ symmetry is a minimum, 0.14 kcal/mol *below* the D$_{3h}$ structure. However, upon optimization of **PRP^{+}** at the QCISD/6-31G* level, it relaxes to a geometry of (near) D$_{3h}$ symmetry, and QCISD single-point calculations at C$_s$ and D$_{3h}$ B3LYP geometries give an energy difference of 0.47 kcal/mol in favor of the latter! CCSD(T) calculations at the B3LYP geometries give an energy difference of only 0.08 kcal/mol with Dunning's correlation consistent double-zeta basis set (cc-pVDZ), whereas on going to the corresponding triple-zeta basis set (cc-pVTZ), the C$_s$ point lies 0.13 kcal/mol *below* the D$_{3h}$ structure. Furthermore, on inclusion of zero point vibrational energies (ZPVE) calculated at the B3LYP/6-31G* level the C$_s$ structure is invariably raised above the D$_{3h}$ stationary point (between 0.3 and 0.5 kcal/mol, depending on the level of calculation).

These calculations demonstrate that the potential energy surface for the distortion of **PRP^{+}** along an e" coordinate is exceedingly flat.

Returning to Figure 3-7, we continued the distortion along the low frequency mode by an additional lengthening of the lateral C-C bond. This leads to

another transition state, TS1, 1.17 kcal/mol[2] above **PRP$^{+\cdot}$**, where the lateral C-C bond length has increased to 1.86 Å and the angle between the central bond and the shortened lateral bond has increased from 66.1° to 77.7°. On the far side of TS1 this angle continues to increase smoothly to 146° while the energy decreases by 8.54 kcal/mol.[2] The bicyclic minimum thus obtained still has C$_s$ symmetry and it corresponds to methylene-bicyclobutyl radical cation (**MBB$^{+\cdot}$**) (see Figure 3-9). From the above results we concluded that **PRP$^{+\cdot}$** cannot be stabilized, even at the cryogenic temperatures preveiling in our experiments.

Figure 3-9: Thermochemistry of the first ring-opening of **PRP$^{+\cdot}$** to **MBB$^{+\cdot}$** at CCSD(T)/cc-pVTZ//B3LYP/6-31G* level, corrected for ZPVE differences.

---

[2]   CCSD(T)/cc-pVTZ energy relative to the D$_{3h}$ minimum of **PRP$^{+\cdot}$**, calculated at B3LYP/6-31G* optimized geometries and corrected for ZPVE differences at the same level. With the DZ basis set with (same geometry and the same ZPVE correction) the exothermicity of the process is 7.33 kcal/mol and the barrier is 1.40 kcal/mol.

MBB$^+$ is a distonic radical cation where 90% of the spin is located on the formally trivalent bridgehead C atom and the charge is formally located on the exocyclic CH$_2$ group. The central bond and the two lateral bonds leading to the quaternary bridgehead C atom are quite long with 1.63 and 1.57 Å, respectively. The two bonds leading to the radical center are rather short (1.44 Å). The exocyclic bond has a length of 1.34 Å which is a typical value for C=C double bonds (cf. Figure 3-10).
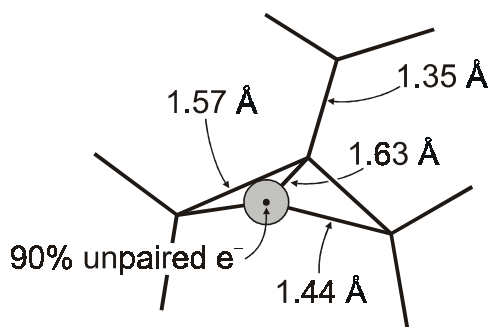
Figure 3-10: Geometry of **MBB$^+$**.

However, comparing the calculated frequencies of **MBB$^+$** (see Table 3-1) with those found experimentally shows that **MBB$^+$** is obviously not the compound that was obtained on ionization of **PRP**. In particular, it lacks the flagpole allenic band around 1870 cm^{-1}.

3.3.3 Formation of methylenecyclobutene radical cation

Since **MBB$^+$** is not the species found on ionization of **PRP** further decay paths had to be considered. An indication of a possible rearrangement is given by the central bond length of **MBB$^+$** (calculated: 1.63 Å) which is quite long for a C-C bond. When that bond breaks, a carbene radical cation, methylenecyclo-butylidene radical cation, **MCD$^+$**, is obtained. This species, which has C$_{2v}$ symmetry, proves to be the transition state for the inversion of **MBB$^+$**, lying 12.6 kcal/mol[3] above **MBB$^+$**. As expected from the carbenic valence structure of **MCD$^+$**, most of the spin and charge are located on the divalent C atom (see Figure 3-11).

---

[3]   Relative CCSD(T)/cc-pVTZ energies calculated at B3LYP/6-31G* optimized geometries and corrected for ZPVE difference at the same level.

Table 3-1: Experimental IR bands of **X**, calculated vibrational frequencies and intensities of **MBB**$^{•+}$, **MCB**$^{•+}$, and **DMC**$^{•+}$.

X$^{•+}$ (exp.)		MBB$^{•+}$ (calc.)[a]			MCB$^{•+}$ (calc.)[a]			DMC$^{•+}$ (calc.)[a]		
freq [cm^{-1}]	rel. int. [%]	mode	freq [cm^{-1}]	rel. int. [%][b]	mode	freq [cm^{-1}]	rel. int. [%][b]	mode	freq [cm^{-1}]	rel. int. [%][b]
		a'	208	8	a"	115	4	a	81	0
		a"	227	21	a'	332	2	b	149	3
		a'	416	12	a"	409	0	a	219	1
		a"	423	14	a"	445	12	b	387	6
		a'	514	22	a'	683	2	b	406	1
		a'	647	58	a"	729	20	a	418	0
814.6	12	a"	685	7	a'	842	3	b	688	1
856.5	7	a"	889	0	a'	907	13	a	831	0
950.3	4	a"	935	0	a"	926	3	a	935	2
995.7	4	a'	971	57	a'	954	11	b	940	9
		a"	1003	2	a"	963	30	a	977	0
		a'	1017	29	a"	1008	1	b	989	14
		a'	1044	8	a'	1077	7	a	1011	0
		a"	1103	32	a"	1106	0	b	1041	40
		a'	1113	0	a'	1193	2	b	1089	1
1229.7	22	a'	1145	2	a'	1230	21	a	1187	8
1324.5	3	a"	1292	0	a'	1286	100[c]	b	1321	100[c]
1333.1	1	a'	1418	48	a'	1380	42	a	1415	7
1442.8	27	a"	1421	28	a'	1437	1	a	1460	2
1474.4	1	a'	1451	16	a'	1456	18	b	1468	13
1870.5	100	a'	1615	100[c]	a'	1544	4	a	1767	3
2935.7	83	a"	2985	23	a'	2995	1	a	3013	6
3009.3	28	a'	2992	26	a'	3045	0	b	3076	5
		a'	3085	6	a'	3082	10	a	3077	1
		a"	2112	13	a'	3141	10	b	3088	2
		a'	3113	18	a'	3166	5	b	3178	2
3033.6	14	a"	3180	9	a'	3183	6	a	3179	4

[a] B3LYP/6-31G*, all frequencies scaled by 0.97. [b] In % of most intense transition. [c] Absolute intensities of the most intense peaks: 78 km/mol (**MBB**$^{•+}$), 107 km/mol (**MCB**$^{•+}$), and 226 km/mol (**DMC**$^{•+}$) respectively.

Because of the high charge density in the p-AO of the carbenic center of this species, (cf. LUMO Figure 3-11) the well-aligned hydrogen atoms on the adjacent CH$_2$ groups can easily shift to this cationic center, which leads to methylenecyclobutene radical cation, **MCB**$^{+\cdot}$. According to B3LYP calculations this reaction is exothermic by 39.7 kcal/mol[3], and the transition state, TS2, for the H-shift lies about 13.6 kcal/mol[3] above **MBB**$^{+\cdot}$.
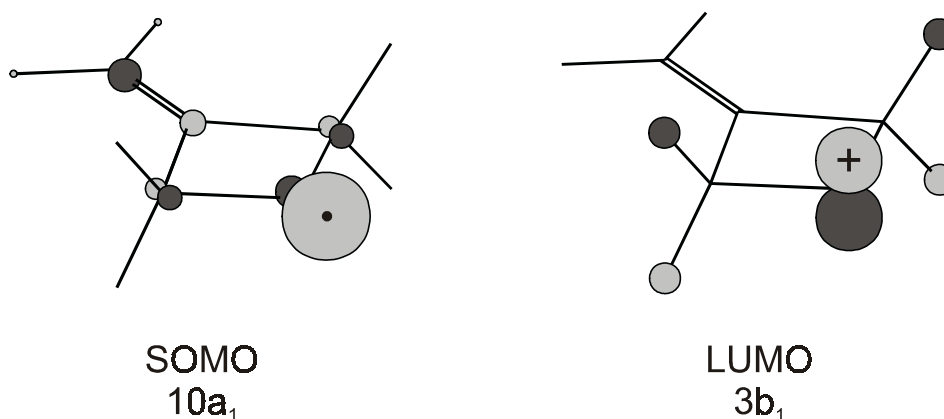
SOMO
10a$_1$

LUMO
3b$_1$

Figure 3-11: SOMO and LUMO of **MCD**$^{+\cdot}$.

As it can be seen in Figure 3-12, the transition state for the H-shift is 5 kcal/mol above that for the ring-opening of **PRP**$^{+\cdot}$, and over 6 kcal/mol above ionized **PRP**. This process is therefore not favorable because there is usually not enough excess energy from the ionization process to cross such barriers. In Table 3-1 the calculated vibrational frequencies of **MCB**$^{+}$ are compared with the experimentally observed frequencies of species **X** (see columns 1 and 2).

From this comparison it becomes once more obvious that **MCB**$^{+\cdot}$ does not correspond to species **X** obtained on ionization of **PRP**. Moreover, it is a diene radical cation with an expected particular pattern in the EA spectra [59]. Indeed, CASPT2 calculations predict such a pattern with a strong band at 320 nm (f = 0.293) and a weak one at around 600 nm (f = 0.017). Looking back at the EA spectrum of ionized **PRP** (Figure 3-3) we also observed two bands which show this diene radical cation pattern, but since they are not affected by NIR-photo-lysis they do not belong to **X**. We will come back to these bands in a later chapter, but leave now this rearrangement path which does not seem to be followed on ionization of **PRP**.
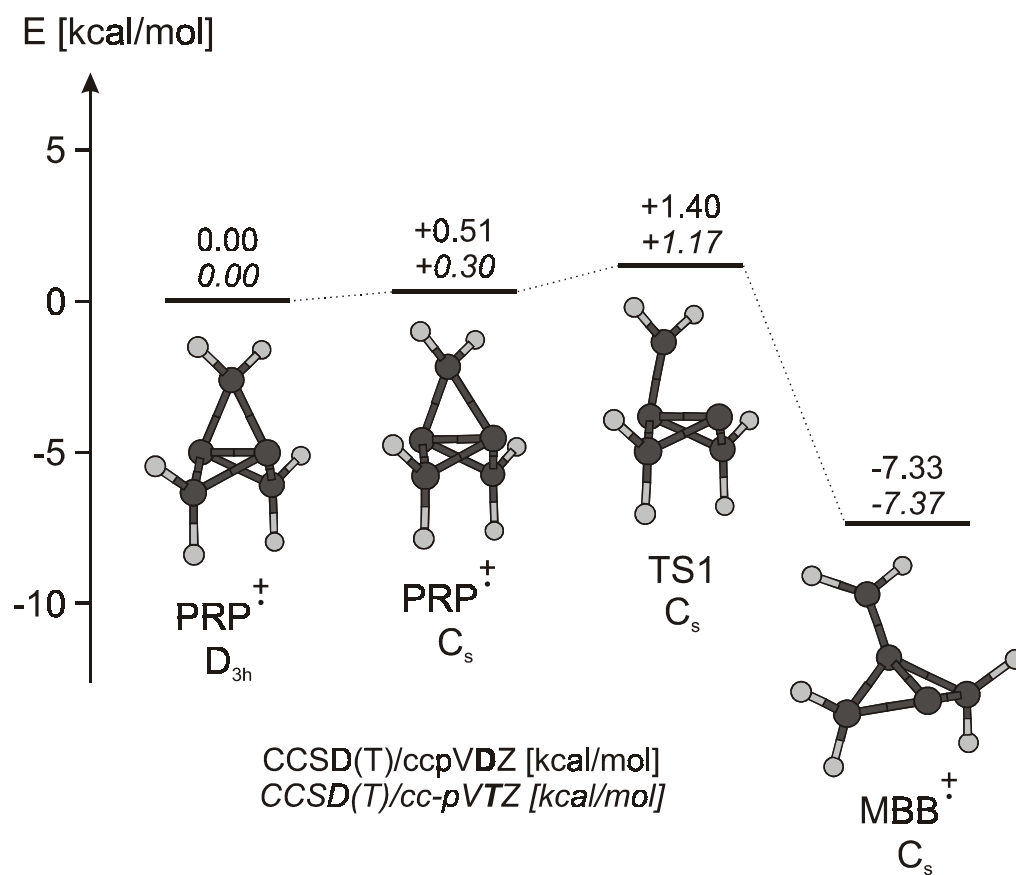
E [kcal/mol]
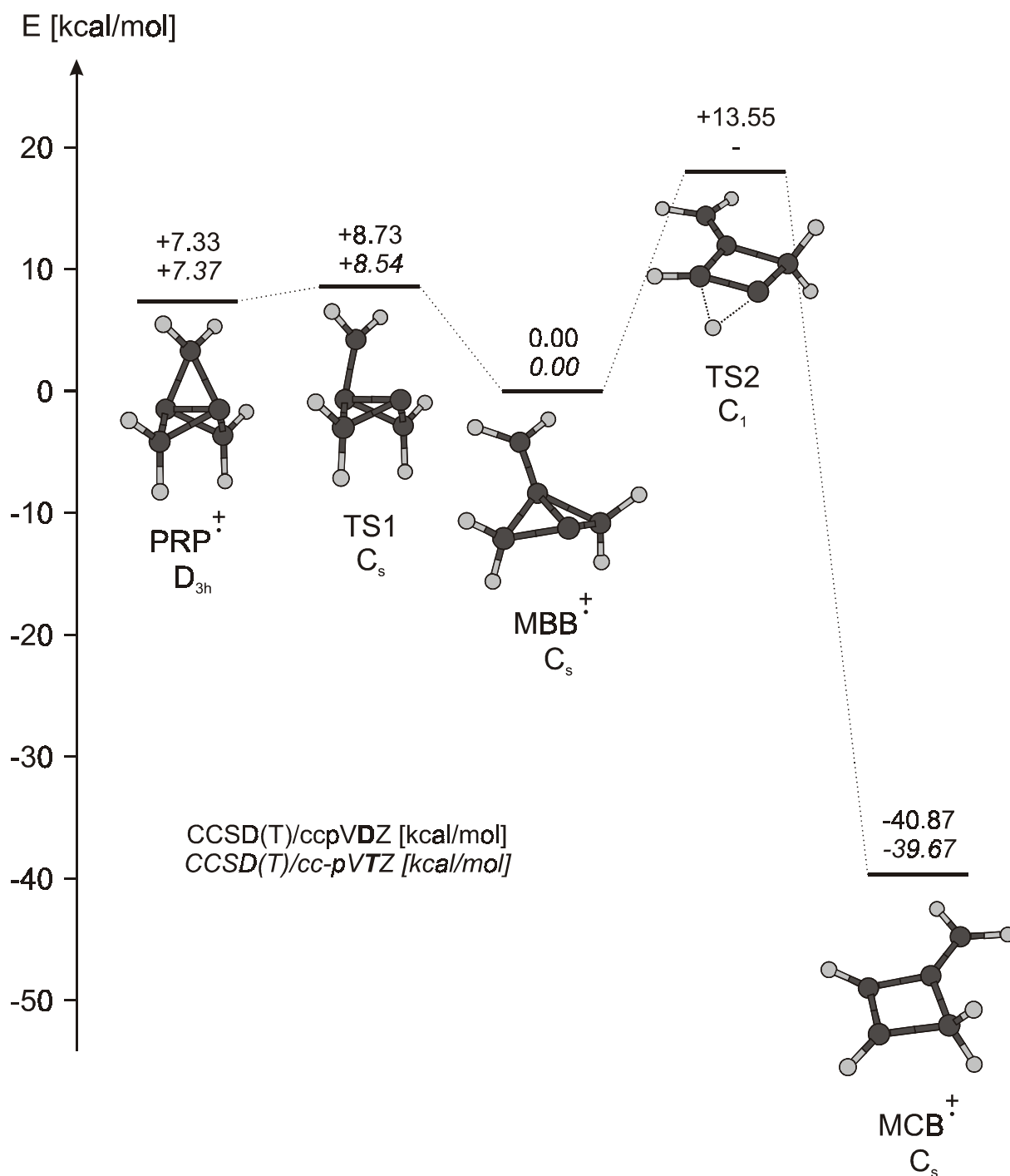
Figure 3-12: Thermochemistry of the central ring-opening of **MBB$^+$** to **MCB$^+$** at the CCSD(T)/cc-pVTZ//B3LYP/6-31G* level, corrected for ZPVE differences at B3LYP/6-31G* level (TS2 could not be calculated with the TZ basis set due to the lack of symmetry).

3.3.4 Formation of dimethylenecyclopropane radical cation

Above, the *central* C-C bond of **MBB$^{+\cdot}$** was broken but this did not lead to species **X**. Another possibility is to break one of the *lateral* bonds of **MBB$^{+\cdot}$** connected to the methylene substituted bridgehead atom which leads to the radical cation of dimethylenecyclopropane, **DMC$^{+\cdot}$**. This process is less exothermic than the rupture of the central C-C bond (-17.1 kcal/mol) but its activation barrier is much lower (3.4 kcal/mol), as depicted in Figure 3-13.

If we compare the calculated vibrational frequencies of **DMC$^{+\cdot}$** to the experimental ones of **X** (Table 3-1) it becomes obvious that this is not the same species. It has to be mentioned that in the case of **DMC$^{+\cdot}$** one frequency is close to the region where allenic vibrations are located but the intensity of the corresponding IR-transition is very weak (3% of the most intense one). It is a combination of a breathing vibration of the ring and the symmetric stretching vibration of the two methylene groups.

A CASPT2 calculation on **DMC$^{+\cdot}$** predicts a strong band ($f = 0.474$) at 330 nm in addition to a weak ($f = 0.019$) and a very weak ($f = 0.0004$) one at 770 and 560 nm respectively (Table 3-2). So, there is again no transition in the NIR.

Table 3-2: Excited states of **DMC$^{+\cdot}$** calculated by CASPT2.

states	CASPT2			CASSCF configurations [b]
	eV	nm	f^a	
1^2A_2	-	-	-	91% $(1a_2)^1$
1^2B_1	1.62	766	0.019	69% $2b_1 \rightarrow 1a_2$
				20% $1a_2 \rightarrow 3b_1$
1^2B_2	2.24	555	0.0004	86% $6b_2 \rightarrow 1a_2$
2^2B_1	3.79	328	0.474	58% $1a_2 \rightarrow 3b_1$
				21% $2b_1 \rightarrow 1a_2$
2^2A_2	5.96	208	0.003	35% $1a_2 \rightarrow 2a_2$
				33% $2b_1 \rightarrow 3b_1$
				16% $2b_1 \rightarrow 1a_2$
				$1a_2 \rightarrow 3b_1$

[a] Oscillator strength for electronic transition.

[b] Active space: 5 electrons in 1 doubly occupied + 1 virtual b$_1$, in 1 doubly occupied + 1 virtual b$_2$ and in 1 singly occupied + 1 virtual a$_2$ MOs, shown in Figure 3-14.
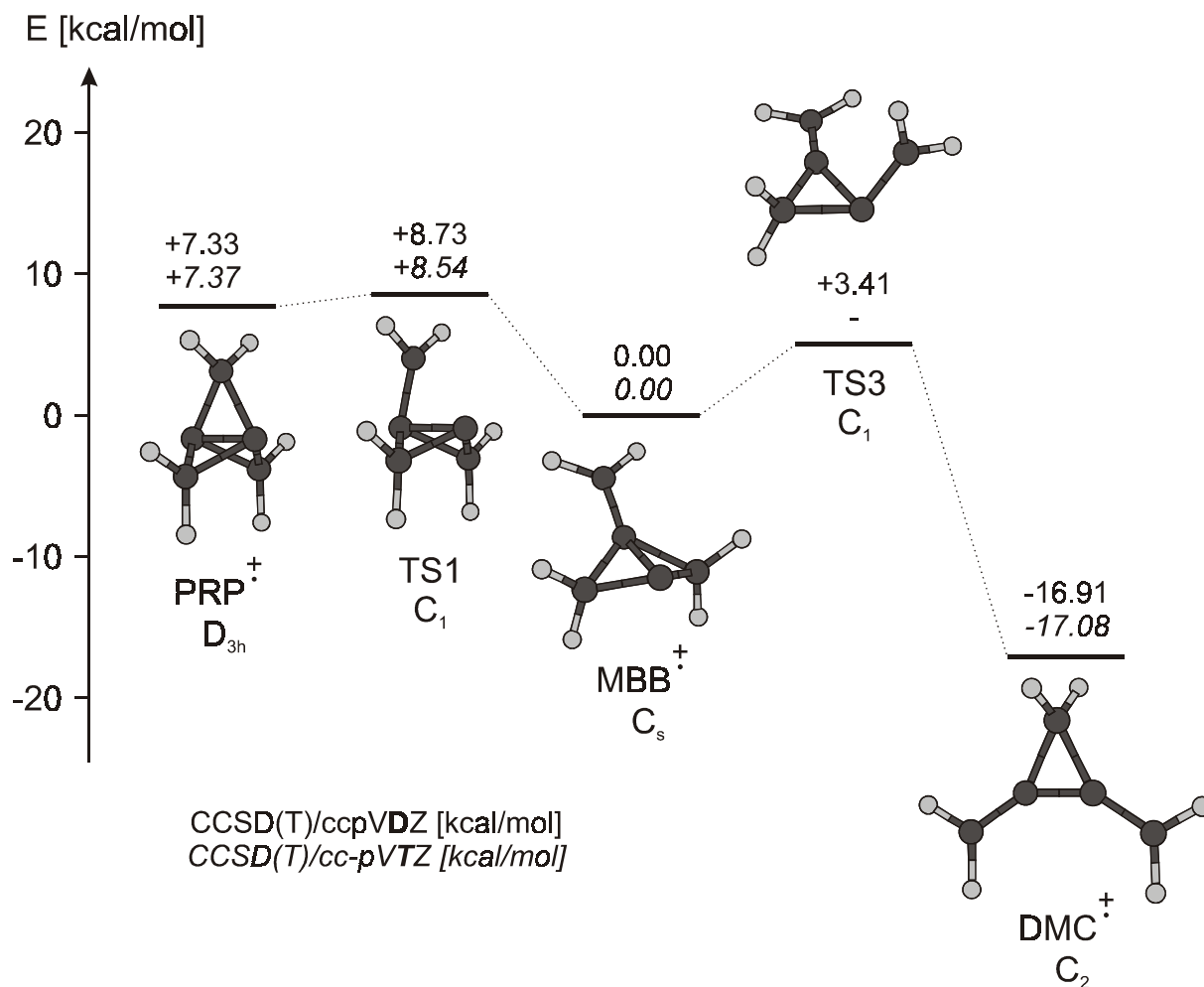
Figure 3-13: Thermochemistry of the lateral ring-opening of **MBB**$^+$ to **DMC**$^+$ at CCSD(T)/cc-pVTZ level.

To find out if the rearrangement path of ionized **PRP** is passing by **DMC**$^+$ or not, an experiment was performed starting from neutral **DMC**. If **DMC**$^+$ is an intermediate of this rearrangement path we should observe, at least in part, the same products.
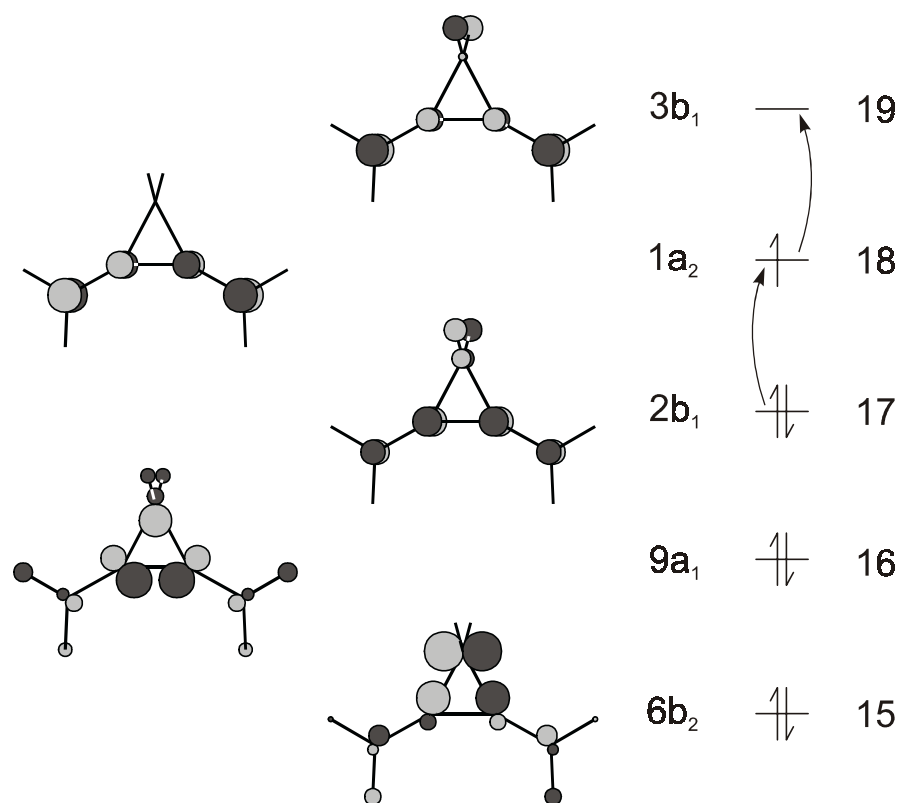
Figure 3-14: MOs of **DMC^{+}** calculated by the HF method (cf. Table 3-2).

3.4 Ionization of dimethylenecyclopropane (DMC)

To our surprise, ionization of **DMC** resulted in almost exactly the same EA spectrum (Figure 3-15) as was obtained after ionization of **PRP** (cf. Figure 3-3)! In the NIR region the weak and broad band appears even more intense. The bands at 500 and 310 nm which indicate a diene radical cation are also visible. Two or three additional small peaks - the highest one at 408 nm - which were already present in the spectrum of ionized **PRP**, but much smaller, are now more prominent.

Again, short NIR photolysis leads to the complete disappearance of the NIR band and to an increase of the asymmetric band at 350 nm (cf. Figure 3-3). Obviously exactly the same products were formed on ionization of **DMC** as they are formed under the same conditions from **PRP**. As expected, the IR spectra show also the same bands appearing on ionization and disappearing on NIR photolysis as in the experiments with **PRP** (compare Figure 3-18 to Figure 3-4. The origin of the additional bands appearing after X-irradiation which do not belong to **DIA^{+}** will be discussed later). Therefore, **DMC^{+}** must be an intermediate on the rearrangement path from **PRP^{+}** to the observed species **X**.
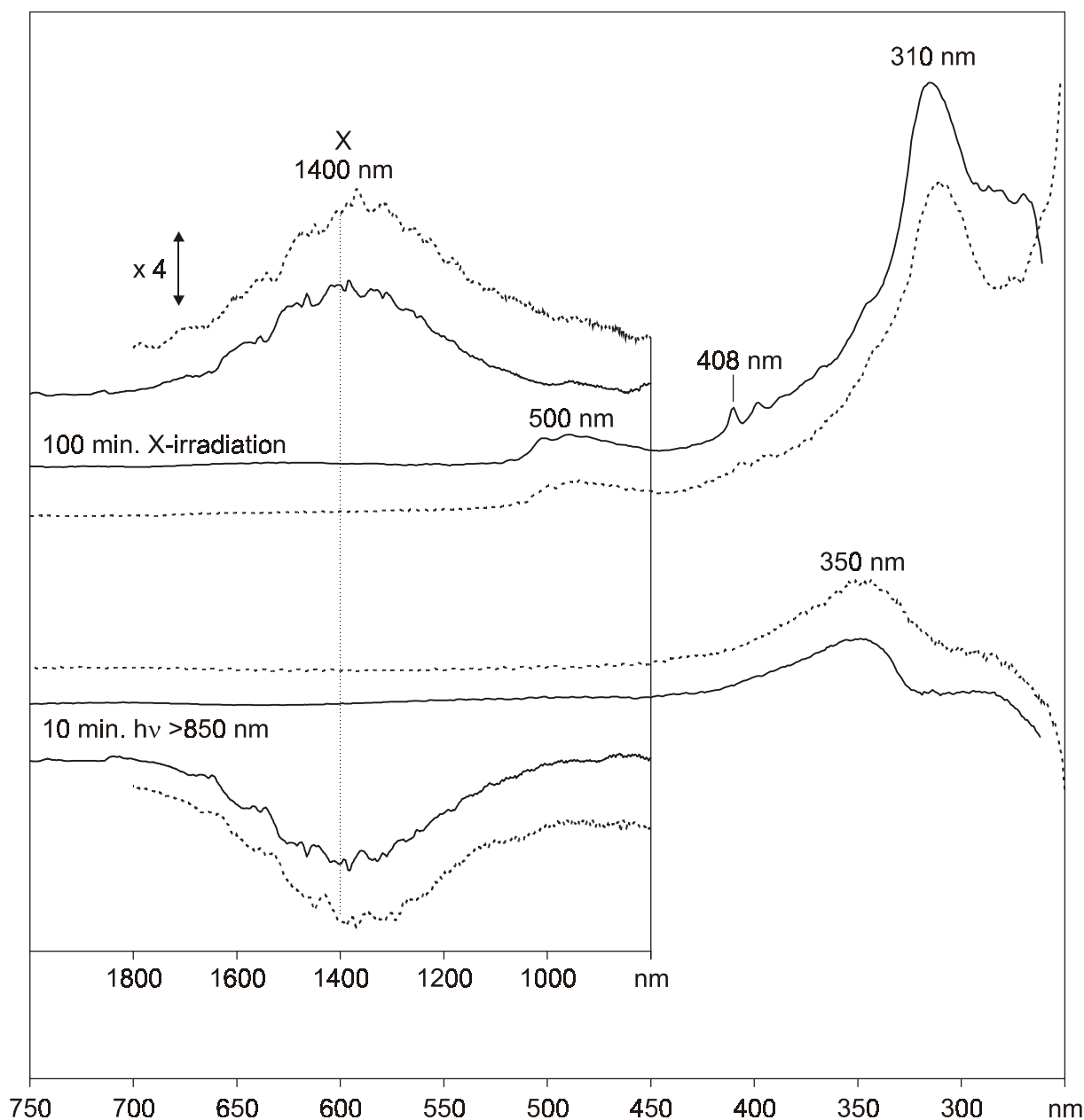
Figure 3-15: EA spectra of ionized and photolyzed **DMC** in Ar matrix compared to the EA spectra of ionized **PRP** (dotted lines, expanded by a factor of two).

Now we know that the unknown species **X** is obtained from both ionized **PRP** and ionized **DMC**, and therefore **X** must be formed from **DMC^{+}** which is 24.5 kcal/mol more stable than **PRP^{+}** in D$_{3h}$ symmetry[3]. We also know that **X** must have an allenic structure. Consequently we try to form a molecule containing a cumulated double bond from **DMC^{+}**. It turns out that this can be done by simple rupture of a lateral cyclopropane bond in **DMC^{+}** which leads to a radical cation that we will call dimethylene allene **DIA^{+}** (see Figure 3-16). This

ring-opening of **DMC**$^+$ shows a weak exothermicity of 5.96 kcal/mol[4] but a barrier of only 2.72 kcal/mol[5].

In view of the small exothermicity of the **DMC**$^+$ → **DIA**$^+$ ring-opening, and considering the fact that a C-C-σ-bond is broken in the process, the barrier for the reaction is surprisingly low. This suggests, that, once again, vibronic interaction effects are operative in shaping the potential energy surface. In the C_{2v} point group[6], deformations of b_2 symmetry lead to lengthening of one (and shortening of the other) lateral cyclopropane bond (e.g. the vibration at 710 cm^{-1} depicted in Figure 3-17. Since the SOMO of **DMC**$^+$, and hence the ground state of **DMC**$^+$, have a_2-symmetry, it must be a $^2B_1$ excited state that promotes such a distortion[7]. Indeed, the lowest excited state of **DMC**$^+$, 1.62 eV above the ground state, is of that symmetry (see Table 3-2: CASSCF/CASPT2 calculation).

Thus, we believe that it is by interaction of the lowest $^2B_1$ excited state with the $^2A_2$ ground state of **DMC**$^+$ that a distortion along a coordinate of B_2 symmetry becomes sufficiently facile to lead almost to the disappearance of the barrier separating **DMC**$^+$ from **DIA**$^+$. In the following chapter we will discuss the electronic and vibrational structure of **DIA**$^+$, the compound which is responsible for at least some of the spectroscopic features that arise on ionization of **PRP**.

---

[4] Relative CCSD(T)/cc-pVTZ energies calculated at B3LYP/6-31G* optimized geometries and corrected for ZPVE differences at the same level. The same difference but with cc-pVDT basis set is 6.38 kcal/mol

[5] Relative CCSD(T)/cc-pVDZ energies calculated at B3LYP/6-31G* optimized geometries and corrected for ZPVE differences at the same level.

[6] On full optimization, **DMC**$^+$ relaxes to a structure of C_2 symmetry due to slightly twisted CH_2 groups. However, the C_{2v} structure lies only 31 cm^{-1} (0.09 kcal/mol) above the C_2 minimum.

[7] As shown in Figure 3-8, the irreducible representation of the modes which induce mixing between two electronic states is equal to the direct product of the irreducible representation that corresponds to the symmetries of the interacting states (in our case: $b_2 = a_2 \times b_1$)

E [kcal/mol]
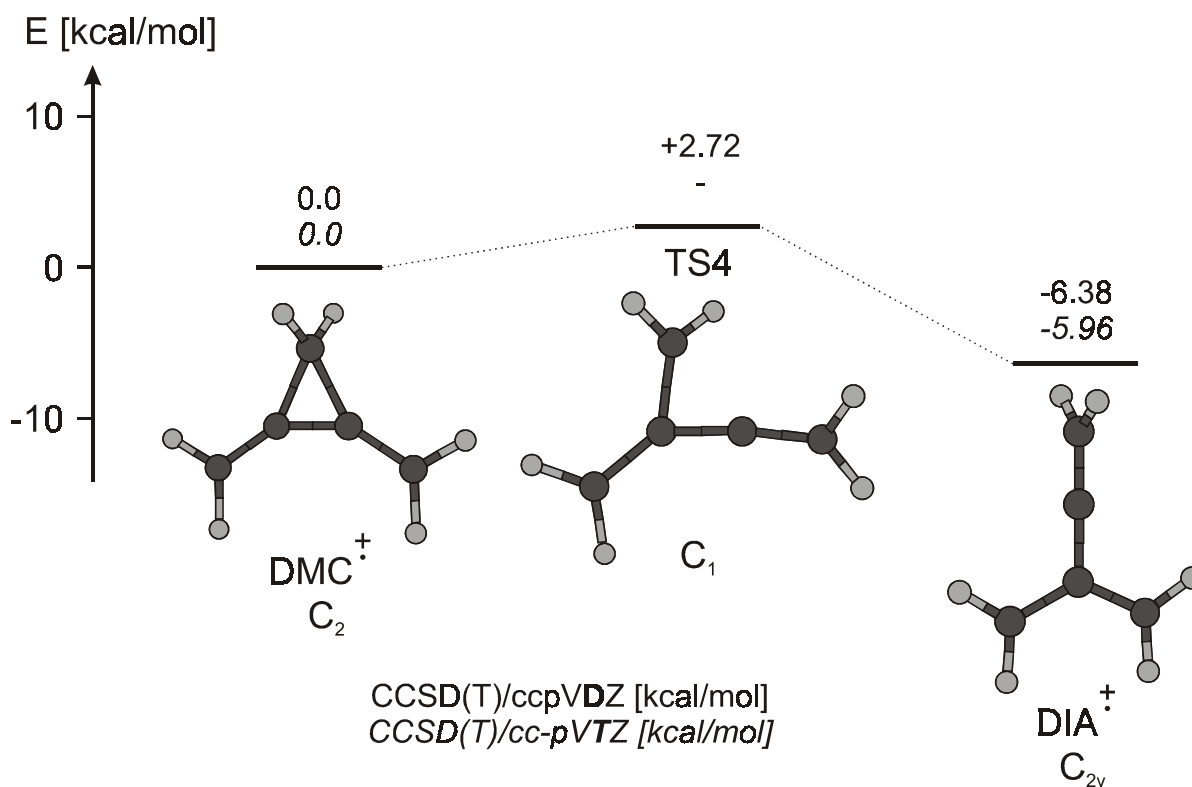
Figure 3-16: Thermochemistry of the ring-opening of **DMC$^{+\cdot}$** to **DIA$^{+\cdot}$**.
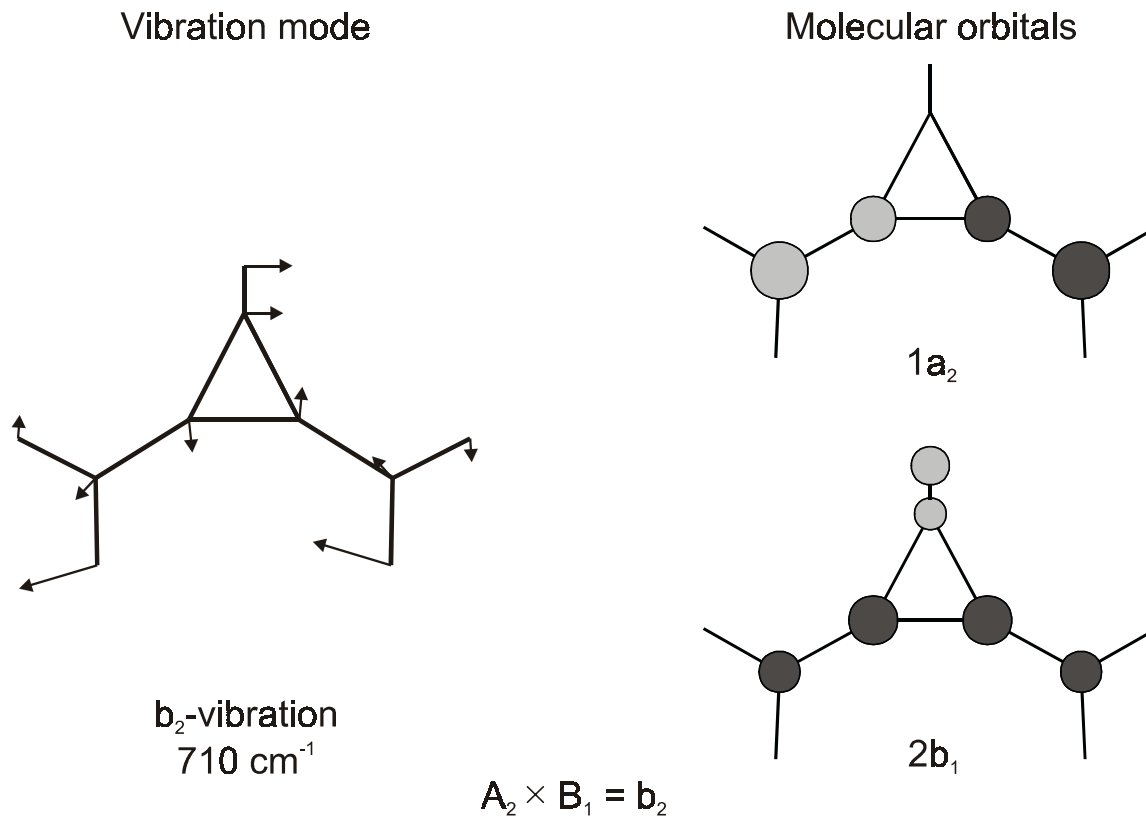
Figure 3-17: b$_2$ Vibrational mode and molecular orbitals of **DMC$^{+\cdot}$** that are singly occupied in that states which undergo vibronic interaction.
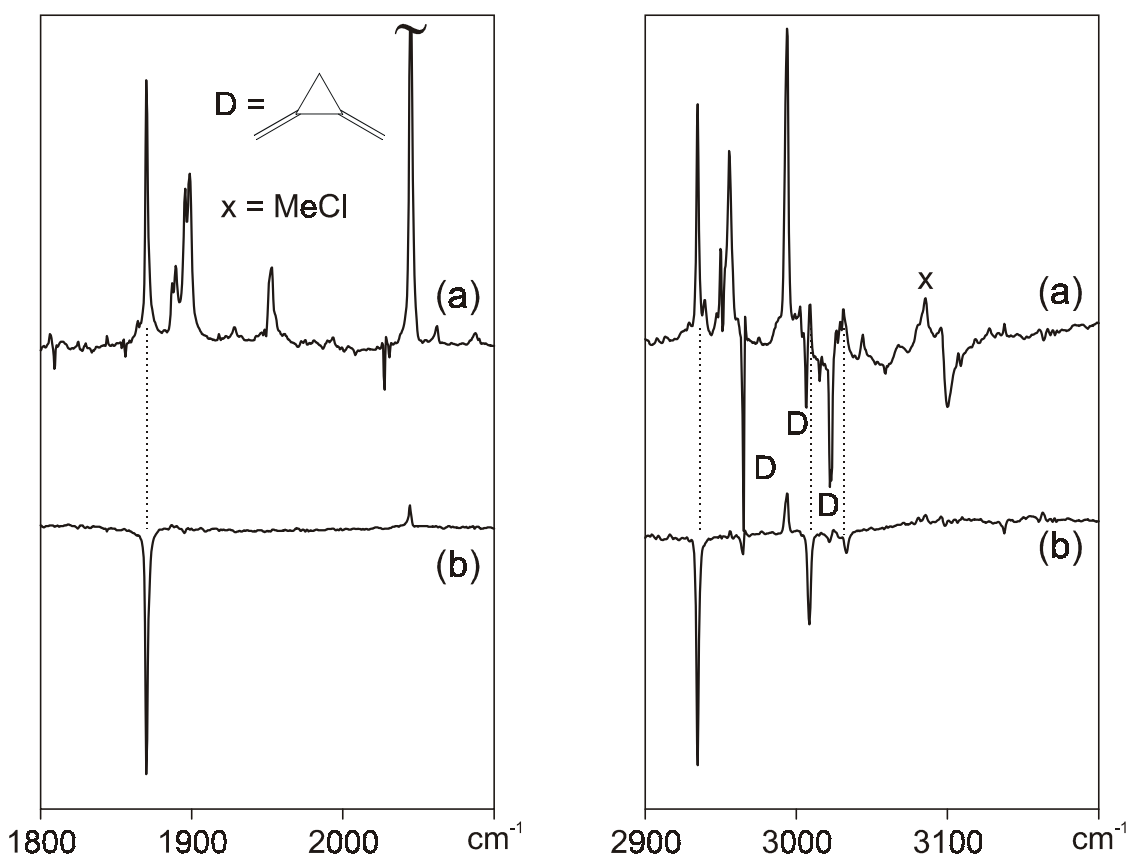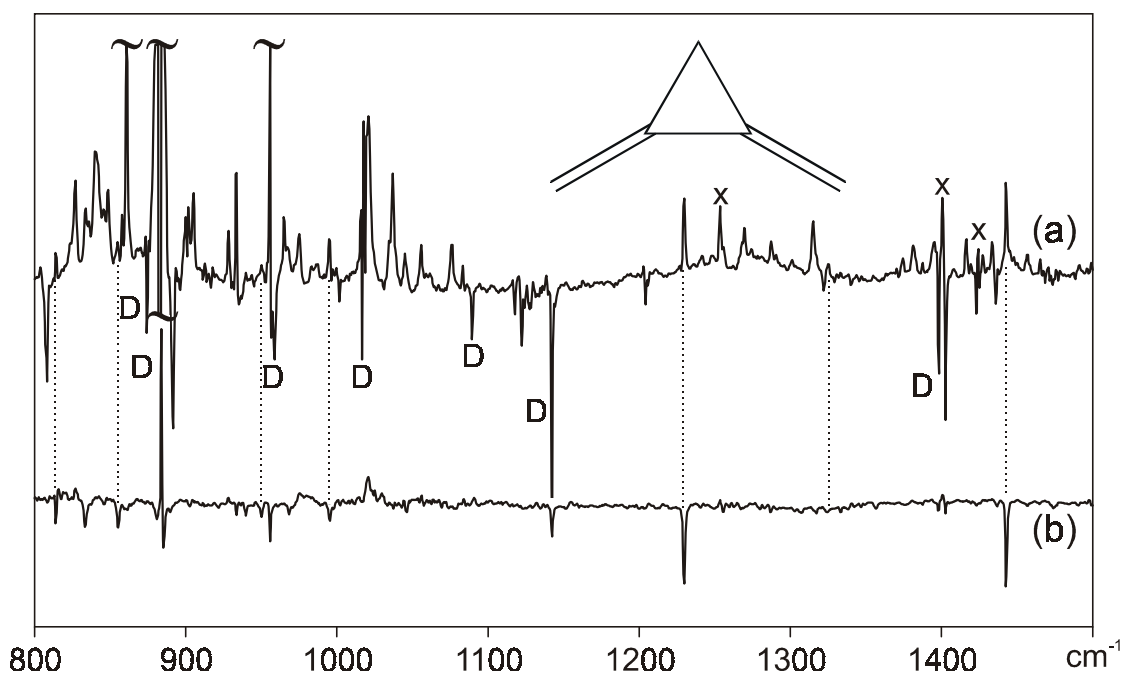
Figure 3-18: Difference IR spectra of **DMC** in Ar matrix after X-irradiation (**a**) and after photolysis at >850 nm (**b**).

3.5 Dimethylene allene radical cation (DIA$^{+\cdot}$)

Dimethylene allene radical cation, **DIA**$^{+\cdot}$, represents a minimum of C$_{2v}$ symmetry on the C$_5$H$_6$ hypersurface. The spin is located mainly in the allylic part of the molecule - mostly on the two methylene atoms C$_2$ and C$_3$. Conversely the charge is located predominantly on the central allenic carbon, C$_4$, (cf. SOMO & LUMO depicted below).
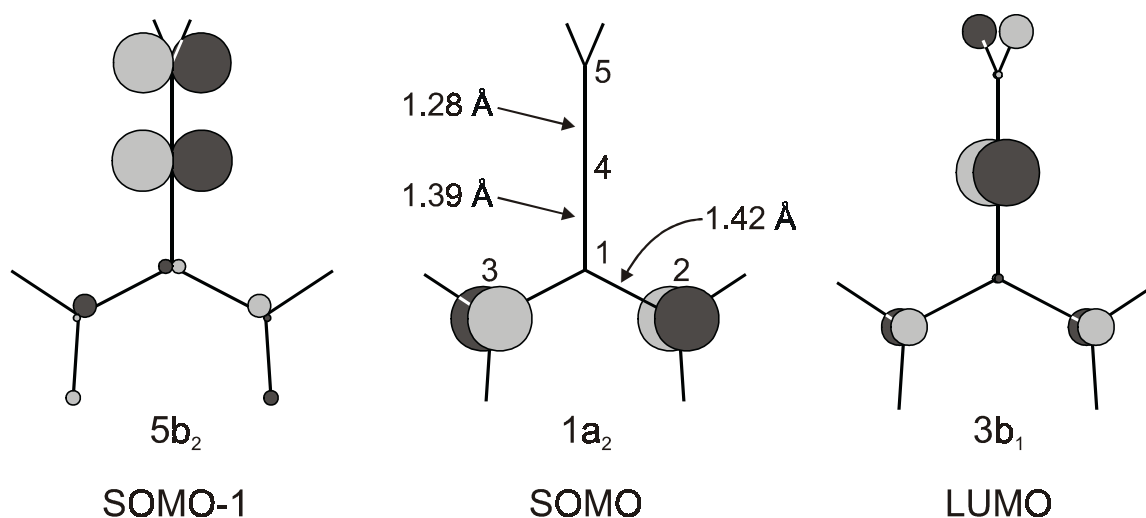
Figure 3-19: Geometry and MOs of **DIA**$^{+\cdot}$ calculated by B3LYP/6-31G*.

The two allylic C-C bonds (1.42 Å) are only 0.03 Å longer than in the allyl radical or in the allyl cation (both 1.39 Å). The length of the allenic bond between C$_1$ and C$_4$ is between that of standard single and double bonds (1.39 Å), whereas the other allenic bond length is between standard double and triple bond lengths (1.28 Å). The central C-C-C bond angle of **DIA**$^{+\cdot}$ (126.6°) is more similar to that of the allyl radical (125.1°) than to that of the allyl cation (118.7°) (all values are from B3LYP/6-31G* geometry optimizations).

CASPT2 calculations on **DIA**$^{+\cdot}$ predict an NIR transition at 1780 nm, i.e. 0.19 eV below the NIR band of **X** ($\lambda_{max} \cong 1400$ nm / 0.89 eV). The next strong transition is at 231 nm which is below other UV absorptions of ionized **PRP**. The full results of the CASPT2 calculations on **DIA**$^{+\cdot}$ are given in Table 3-3.

Table 3-3: Excited states of **DIA**$^{+\cdot}$ by CASPT2 calculations.

states	UV/Vis eV	CASPT2 eV	f^a	CASSCF configurations [b]
1^2A_2	-	-	-	90% $(1a_2)^1$
1^2B_1	0.89	0.70	0.007	84% $1a_2 \rightarrow 4b_1$
1^2B_2		3.40	0	61% $1a_2 \rightarrow 4b_1$
				$\quad\; 5b_2 \rightarrow 4b_1$
				27% $5b_2 \rightarrow 1a_2$
2^2B_1		4.90	0.009	47% $1a_2 \rightarrow 3b_1$
				31% $2b_1 \rightarrow 1a_2$
2^2B_2		5.20	0	91% $1a_2 \rightarrow 6b_2$
2^2A_2		5.36	0.413	59% $2b_1 \rightarrow 4b_1$
				17% $(1a_2)^1$
				15% $2b_1 \rightarrow 1a_2$
				$\quad\; 1a_2 \rightarrow 4b_1$
3^2B_1		5.68	0.090	55% $5b_2 \rightarrow 4b_1$
				$\quad\; 1a_2 \rightarrow 6b_2$
				14% $1a_2 \rightarrow 4b_1$
				$\quad\; 2b_1 \rightarrow 4b_1$
				10% $2b_1 \rightarrow 1a_2$
3^2A_2		5.69	0.051	59% $2b_1 \rightarrow 1a_2$
				$\quad\; 1a_2 \rightarrow 4b_1$
				22% $2b_1 \rightarrow 4b_1$
4^2B_1		5.77	0.188	30% $1a_2 \rightarrow 4b_1$
				$\quad\; 2b_1 \rightarrow 4b_1$
				27% $5b_2 \rightarrow 4b_1$
				$\quad\; 1a_2 \rightarrow 6b_2$
				16% $1a_2 \rightarrow 3b_1$
3^2B_2		6.13	0	28% $1a_2 \rightarrow 4b_1$
				$\quad\; 5b_2 \rightarrow 4b_1$
				22% $5b_2 \rightarrow 1a_2$
				18% $1a_2 \rightarrow 4b_1$
				$\quad\; 5b_2 \rightarrow 3b_1$
				16% $5b_2 \rightarrow 1a_2$
				$\quad\; 2b_1 \rightarrow 4b_1$

[a]   Oscillator strength for electronic transition.
[b]   Active space: 5 electrons in 1 doubly occupied + 2 virtual b$_1$, 1 doubly + 1 virtual b$_2$ and in 1 singly occupied a$_2$ MOs.

In Table 3-4 the calculated vibrational spectrum of **DIA$^{+\cdot}$** is compared to that observed for species **X**. Although the general matching is quite satisfactory, the predicted and observed frequencies cannot be brought into good accord with a single scaling factor (0.9513) (rms deviation: 20.8 cm^{-1}).

Table 3-4: Experimental and calculated vibration frequencies of **DIA$^{+\cdot}$**.

DIA$^{+\cdot}$ (calc.)				**X$^{+\cdot}$** (exp.)		
mode sym.	int. [%]	freq. [cm^{-1}]	scaled ^{a} [cm^{-1}]	exp. [cm^{-1}]	int. [%]	Δ^b [cm^{-1}]
b$_2$	3	178.8				
b$_1$	3	232.5				
a$_2$	0	268.8				
a$_1$	1	384.6				
b$_1$	0	479.2				
a$_2$	0	506.7				
b$_2$	7	520.8				
b$_1$	2	538.8				
a$_1$	0	822.3				
a$_2$	0	861.3				
b$_1$	25	882.9	839.8	814.6	12	25.2
b$_2$	23	883.8	840.6	856.5	7	-15.9
b$_1$	2	907.9				
b$_2$	6	979.7	931.9	950.3	4	-18.4
a$_1$	14	1023.8	973.8	995.7	4	-21.9
a$_1$	30	1300.5	1237.0	1229.7	22	7.3
b$_2$	6	1361.8	1295.3	1324.5	3	-29.2
a$_1$	2	1383.8	1316.2	1333.1	1	-16.9
b$_2$	26	1500.3	1427.1	1442.8	27	-15.7
a$_1$	2	1524.3	1449.9	1474.4	1	-24.5
a$_1$	100^c	1948.9	1853.8	1870.5	100	-16.7
a$_1$	64	3119.3	2967.0	2935.7	83	31.3
b$_2$	23	3189.7	3034.0	3009.3	28	24.7
b$_1$	25	3190.0	3034.4	3033.6	14	0.8
a$_1$	0	3196.9				
b$_2$	1	3305.2				
a$_1$	3	3306.0				

^{a} Calculated with B3LYP/6-31G*, scaled with 0.9513. ^{b} RMS deviation of observed from calculated frequencies is 20.8 cm^{-1}. ^{c} Absolute intensity of the most intense peak: 290.4 km/mol.

To improve the agreement, the force field was scaled by the Pulay SQM-force field method [60, 61] (see Table 3-5). For this, the internal coordinates depicted in Figure 3-20 were assembled into symmetry-adapted linear combinations as shown in Table 3-6. These symmetry coordinates S$_1$ - S$_{27}$ were then divided into ten groups. The diagonal force constants f$_{ii}$ for all the S$_i$ of each group were scaled jointly[8]. Then the root mean square (rms) difference between calculated and observed frequencies of **DIA‡** was minimized as a function on the ten scaling factors whereby these assumed the values shown in the last columns of Table 3-6. The vibrational frequencies corresponding to the force field that was optimized in this fashion are listed in the third column of Table 3-5. As a result of the SQM scaling procedure the rms difference between calculated and observed frequencies fell to 7.08 cm^{-1}.
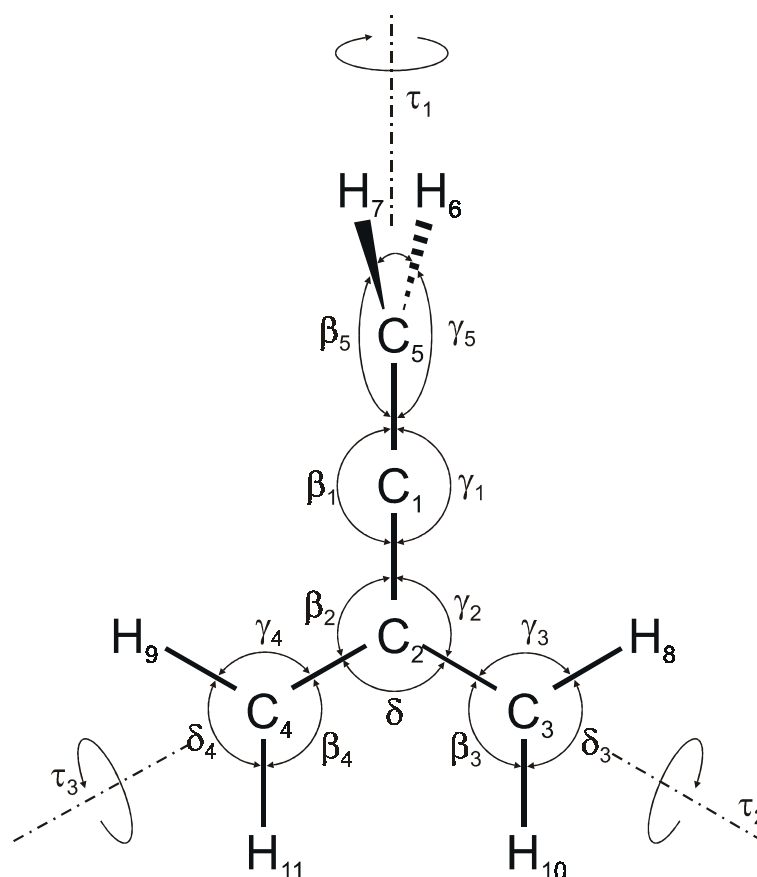
Figure 3-20: Internal coordinates of **DIA‡** (the wagging coordinates ε are not drawn).

---

[8]   The off-diagonal element f$_{ij}$ of the force constant matrix are scaled by the geometric mean of the scaling constants for f$_{ii}$ and f$_{jj}$ in the Pulay procedure.

Table 3-5: Refined SQM frequencies of **DIA^{+}** obtained from a fit over the observed peaks.

nr.	sym.	SQM [cm^{-1}]	obs. [cm^{-1}]	Δ[a] [cm^{-1}]	int.[b] [%]	int.	potential energy distribution [c]
1	a$_1$	3125.0			2.6	7.7	6(58)+5(42)
2	a$_1$	3021.9			0.1	0.4	5(58)+6(42)
3	a$_1$	2948.1	2935.0	13.1	66.2	192.3	4(99)
4	a$_1$	1870.5	1870.4	0.1	100.0	290.4	3(70)+1(28)
5	a$_1$	1468.2			1.0	2.9	8(92)+2(7)
6	a$_1$	1320.1			9.9	28.8	1(24)+10(21)+2(20)+9(12)+ 7(11)+3(10)
7	a$_1$	1227.9	1229.7	-1.8	26.5	76.9	9(87)+10(6)
8	a$_1$	994.0	995.7	-1.7	14.9	43.1	10(52)+2(40)+1(6)
9	a$_1$	795.6			0.3	0.8	1(41)+2(34)+3(14)+10(8)
10	a$_1$	376.9			0.7	2.0	7(82)+10(15)
11	a$_2$	836.8			0.0	0.0	11(99)
12	a$_2$	490.2			0.0	0.0	13(52)+12(38)+11(10)
13	a$_2$	254.4			0.0	0.0	12(52)+13(47)
14	b$_1$	3015.1	3033.6	-18.5	26.0	75.6	14(99)
15	b$_1$	863.2			3.7	10.8	16(51)+15(23)+18(13)+17(12)
16	b$_1$	853.6	856.5	-2.9	23.5	68.3	16(54)+15(33)+18(10)
17	b$_1$	523.2			2.5	7.2	19(42)+17(40)+18(8)+15(6)
18	b$_1$	459.1			0.0	0.1	19(35)+15(34)+18(16)+17(14)
19	b$_1$	223.8			2.7	7.9	18(43)+17(30)+19(19)+15(7)
20	b$_2$	3124.3			0.5	1.5	22(58)+21(41)
21	b$_2$	3015.1	3009.3	5.8	23.4	68.0	21(58)+22(41)
22	b$_2$	1441.8	1442.5	-0.7	20.8	60.5	25(94)+20(6)
23	b$_2$	1324.8	1324.7	0.1	11.9	34.5	20(80)+23(9)+26(8)
24	b$_2$	954.0	950.3	3.7	6.5	18.8	26(89)+20(11)
25	b$_2$	817.7	814.6	3.1	23.9	69.9	27(98)
26	b$_2$	506.2			6.9	20.1	23(48)+24(39)+20(7)
27	b$_2$	174.0			2.9	8.5	24(58)+23(40)

[a] RMS deviation of observed from calculated frequencies is 7.08 cm^{-1}.

[b] Intensities in % of the most intense band at 1870 cm^{-1}.

[c] Contributions in percent (in parentheses) of the symmetry coordinates listed in Table 3-6.

Table 3-6: Definition of internal and symmetry coordinates of **DIA**$^{\cdot+}$, together with their optimized scaling factors.

internal coord.[a]	description	composition	symmetry coord. a$_1$	a$_2$	b$_1$	b$_2$	scaling factors
R$_1$	ν(C-C)	r(C$_1$-C$_2$)	S$_1$				
R$_2$	"	r(C$_2$-C$_3$)	S$_2$			S$_{20}$	0.9303
R$_3$	"	r(C$_2$-C$_4$)					
R$_4$	ν(C=C)	r(C$_1$-C$_5$)	S$_3$				
R$_5$	ν(C-H)	r(C$_5$-H$_6$)	S$_4$		S$_{14}$		
R$_6$	"	r(C$_5$-H$_7$)					
R$_7$	"	r(C$_3$-H$_8$)	S$_5$			S$_{21}$	0.8936
R$_8$	"	r(C$_4$-H$_9$)					
R$_9$	"	r(C$_3$-H$_{10}$)	S$_6$			S$_{22}$	
R$_{10}$	"	r(C$_4$-H$_{11}$)					
R$_{11}$	δ(C-C-C)$_{ip}$	β$_1$-γ$_1$				S$_{23}$	
R$_{12}$	σ(C(CH$_2$)$_2$)	2δ$_2$-β$_2$-γ$_2$	S$_7$				0.9500
R$_{13}$	ρ(C(CH$_2$)$_2$)	β$_2$-γ$_2$				S$_{24}$	
R$_{14}$	σ(CH$_2$)	2δ$_3$-β$_3$-γ$_3$	S$_8$			S$_{25}$	0.9474
R$_{15}$	"	2δ$_4$-β$_4$-γ$_4$					
R$_{16}$	"	2δ$_5$-β$_5$-γ$_5$	S$_9$				0.8653
R$_{17}$	σ(CH$_2$)	β$_3$-γ$_3$	S$_{10}$			S$_{26}$	0.9474
R$_{18}$	"	β$_4$-γ$_4$					
R$_{19}$	"	β$_5$-γ$_5$			S$_{15}$		0.8653
R$_{20}$	ω(CH$_2$)	ε$_{2\text{-}3,8,10}$		S$_{11}$	S$_{16}$		0.9474
R$_{21}$	"	ε$_{2\text{-}4,9,11}$					
R$_{22}$	"	ε$_{1\text{-}5,6,7}$				S$_{27}$	0.8653
R$_{23}$	ω(C(CH$_2$)$_2$)	ε$_{1\text{-}2,3,4}$			S$_{17}$		
R$_{24}$	δ(C-C-C)$_{oop}$	β$_1$'-γ$_1$'$^{\,b}$			S$_{18}$		0.9500
R$_{25}$	τ(C=C)	τ$_1$(C$_5$H$_{6,7}$)	S$_{12}$				
R$_{26}$	τ(C-C)	τ$_2$(C$_3$H$_{8,10}$)		S$_{13}$	S$_{19}$		
R$_{27}$	"	τ$_3$(C$_4$H$_{9,11}$)					

[a] see Figure 1-20, except for wagging coordinate e$_{i\text{-}j,k,l}$ which are defined as atom i moving out of the plane defined by atoms j,k, and l.

[b] β$_1$'-γ$_1$' is perpendicular to β$_1$-γ$_1$.

The ^{1}H hyperfine couplings found in the ESR spectra of ionized **PRP** by Williams et al. (cf. Figure 3-2) were also calculated at the B3LYP/6-31G* level. For the two allenic hydrogens the predicted coupling is -9.1 G, for the allylic *endo* hydrogens -16.8 G, and for the *exo* hydrogens -17.5 G. The ESR experiment showed couplings of 5.4 G and 14.8 G respectively. The ^{1}H coupling constants for allylic Hs are slightly overestimated by B3LYP/6-31G* (allyl radical: calc.: +4.97 G (1H), -15.8 G (2H^{endo}) and -16.5 G (2H^{exo}); exp.: 4.1 G (1H), 13.9 G (2H^{endo}) and 14.8 G (2H^{exo}) [62, 63, 64]). However, the predicted coupling for the allenic hydrogen atoms is overestimated by a factor of nearly two which indicates that too much unpaired spin is placed on C$_5$ by this DFT method.

With this last step we have arrived at a full explanation of the unexpected decay of **PRP** on ionization which proceeds via two intermediate (**MBB**$^{+\bullet}$ and **DMC**$^{+\bullet}$) that are, however, only separated by small barriers from the final observed product, **DIA**$^{+\bullet}$.

The formation of **DIA**$^{+\bullet}$ on ionization of **PRP** and **DMC** being proven the next question is what happens to **DIA**$^{+\bullet}$ on NIR photolysis? The EA spectrum after photolysis shows only a weak increasing band at 350 nm which could already have been present after ionization, hidden under the intense diene cation-like band peaking at 310 nm. The IR spectrum shows several small peaks that increase after photolysis. The possibilities for photorearrangement of **DIA**$^{+\bullet}$ are not very numerous because it contains no small rings. Conversely, it could undergo an allyl-cyclopropyl ring closure leading to vinylidenecyclopropane radical cation, **VCP**$^{+\bullet}$. To investigate this possibility, **VCP** was synthesized, embedded in an Argon matrix and subjected to X-irradiation.

3.6 Ionization of vinylidenecyclopropane

The PE spectrum of **VCP** (Figure 3-21) [65] matches quite well with the results of CASSCF/CASPT2 calculations on **VCP**$^{+\bullet}$ at the neutral geometry which show that all of the states observed in the PE spectrum are quite well described by single configurations (see last column of Table 3-7).
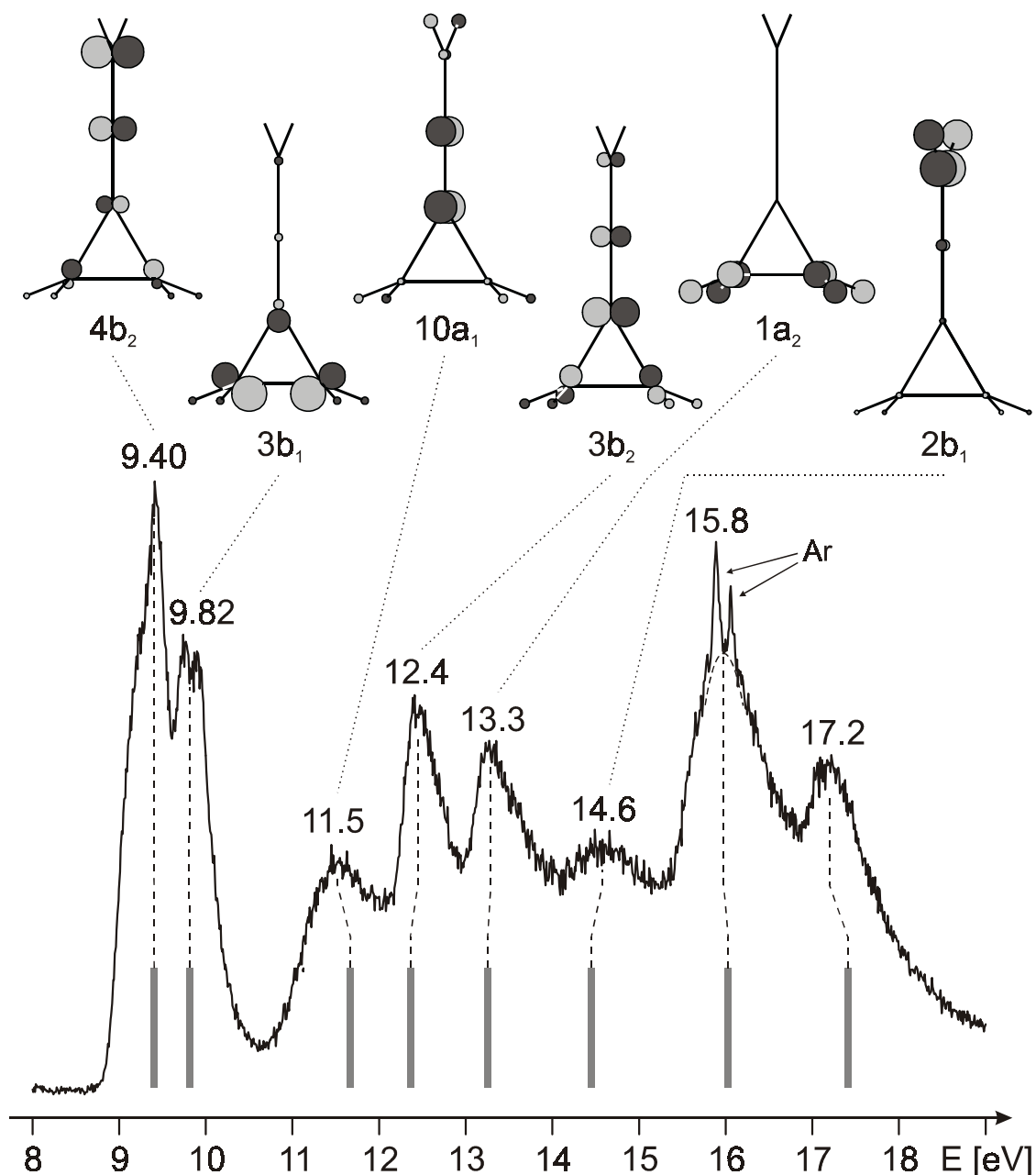
Figure 3-21: PE spectrum of **VCP** [65] together with calculated B3LYP MOs and states calculated with CASPT2, relative to the first vertical IP, at the geometry of neutral **VCP**.

The EA spectrum of ionized **VCP** shows some features that are also found in the spectra of ionized **DMC** and **PRP** (see Figure 3-22). In particular, the three small peaks at 407, 394, and 384 nm are more pronounced than in ionized **DMC**. A weak band at 500 nm indicates the presence of the diene radical cationic species also found on ionization of **DMC** and **PRP**, but it is hardly visible and the corresponding strong one at 310 nm cannot be discerned among other absorptions that rise in this region. Additionally, three sharp peaks are visible between 250 and 300 nm. In the NIR, the weak band of **DIA$^+$** can only be

guessed but a photolysis in the NIR leads to the same changes as found for ionized **DMC** and **PRP**: a weak band at 350 nm increases.

CASSCF/CASPT2 calculations on **VCP**$^{+\cdot}$ predict only transitions with weak oscillator strengths, the strongest of which is in the region of 350 nm, i.e. where a band increases after photolysis in the NIR (see Table 3-8). Presumably, this band is hidden under the strong increase of the absorption at >450 nm.

Table 3-7: Excited states of **VCP**$^{+\cdot}$ at the neutral geometry by CASPT2.

states	PES eV	CASPT2 eV	CASSCF configurations [a]
1^2B_2	-	-	91% $(4b_2)^1$
1^2B_1	0.42	0.41	97% $3b_1 \rightarrow 4b_2$
1^2A_1	2.1	2.27	95% $10a_1 \rightarrow 4b_2$
2^2B_2	3.0	2.96	80% $3b_2 \rightarrow 4b_2$
1^2A_2	3.9	3.89	95% $1a_2 \rightarrow 4b_2$
3^2B_2	5.2	5.05	92% $3b_1 \rightarrow 4b_2$
			$4b_2 \rightarrow 4b_1$
4^2B_2	-	5.64	59% $4b_2 \rightarrow 5b_2$
2^2B_1	-	6.63	87% $4b_2 \rightarrow 4b_1$ (NK)[b]
3^2B_1	6.4	7.20	95% $3b_1 \rightarrow 4b_2$
			$3b_1 \rightarrow 4b_1$
2^2A_2	-	7.85	91% $10a_1 \rightarrow 4b_1$ (NK)[b]
3^2A_2	7.8	8.01	91% $10a_1 \rightarrow 4b_2$
			$4b_2 \rightarrow 4b_1$

[a] Active space: 9 electrons in 1 doubly occupied + 1 virtual a_1, 1 doubly occupied + 1 virtual b_1, in 1 doubly + 1 singly occupied + 1 virtual b_2 and in 1 doubly occupied + 1 virtual a_2 MOs. Occupied MOs depicted in Figure 3-21.

[b] NK = non-Koopmans state, does not show up in PE spectrum.
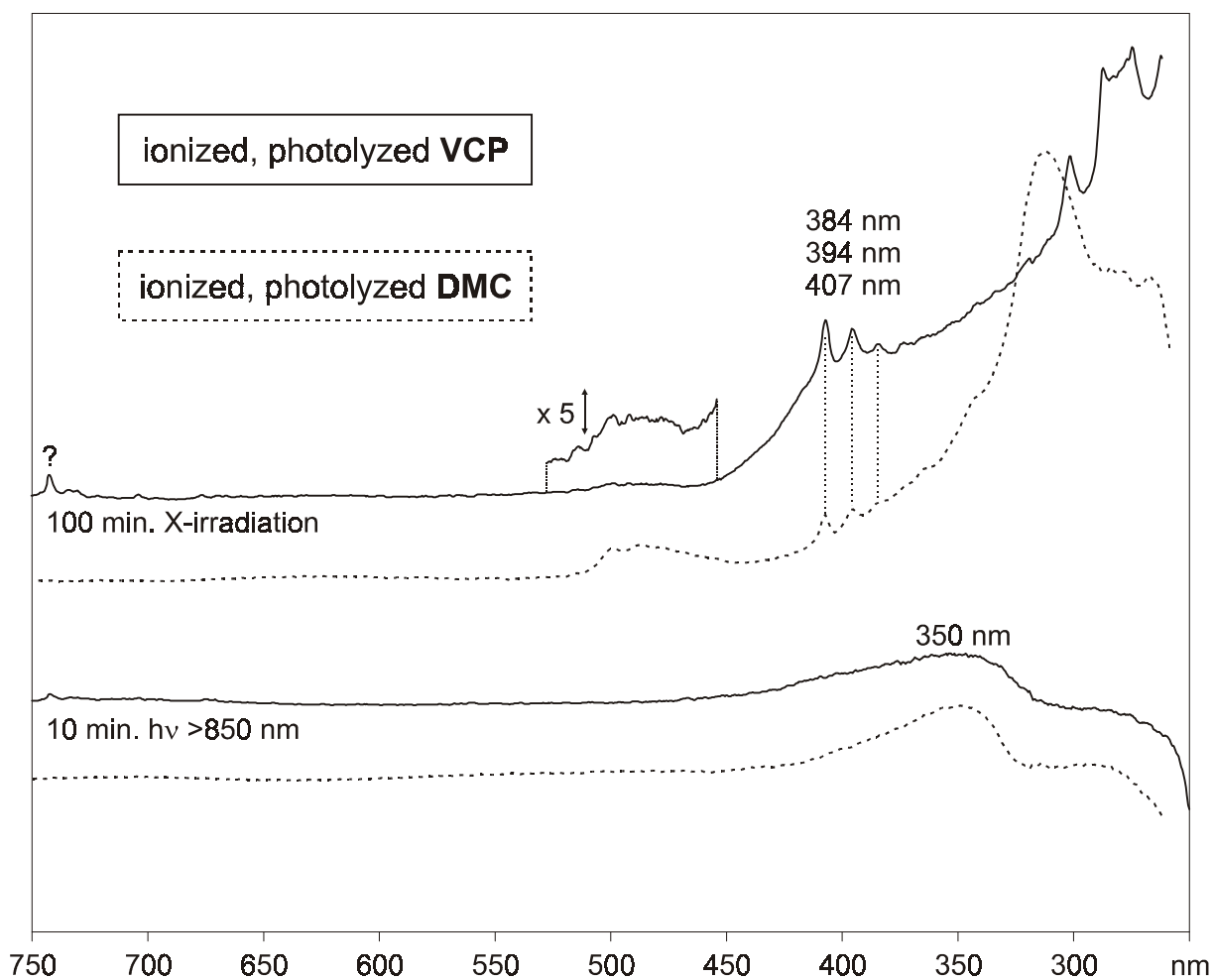
Figure 3-22: EA difference spectra of ionized **VCP** after ionization (top) and subsequent irradiation at >850 nm (bottom) in an Ar matrix. The corresponding EA spectra obtained with **DMC** are shown for reference purposes (dotted lines).

In the IR spectrum we can observe a very small amount of **DIA**$^{+\cdot}$ (only the two strongest bands at 1870 and 2948 cm^{-1} are visible). But on comparing the IR-spectra of ionized and NIR-photolyzed **DMC** and **PRP** (see spectra (b) and (c) in Figure 3-24 and Figure 3-25) with that of ionized **VCP** (b) one can discern the four strongest bands of **VCP**$^{+\cdot}$ at 573, 840, 1025, and 2995 cm^{-1}.

Table 3-8: Excited states of **VCP$^{+\cdot}$** by CASPT2 calculations.

states	UV/Vis		CASPT2			CASSCF configurations [b]
	nm	eV	nm	eV	f^a	
1^{2}B	-	-	-	-	-	91% (7b)^1
2^{2}B			565	2.20	0.001	69% 6b $\rightarrow$ 7b
						16% (7b)^1 (gs)
3^{2}B	350	3.54	376	3.29	0.020	66% 5b $\rightarrow$ 7b
						14% 7b $\rightarrow$ 9b
4^{2}B			365	3.40	0.006	71% 7b $\rightarrow$ 9b
1^{2}A			297	4.17	0.006	90% 11a $\rightarrow$ 7b

[a] Oscillator strength for electronic transition.
[b] Active space: 7 electrons in 2 doubly occupied a and in 2 doubly + 1 singly occupied
+ 2 virtual b MOs, shown in Figure 3-23.
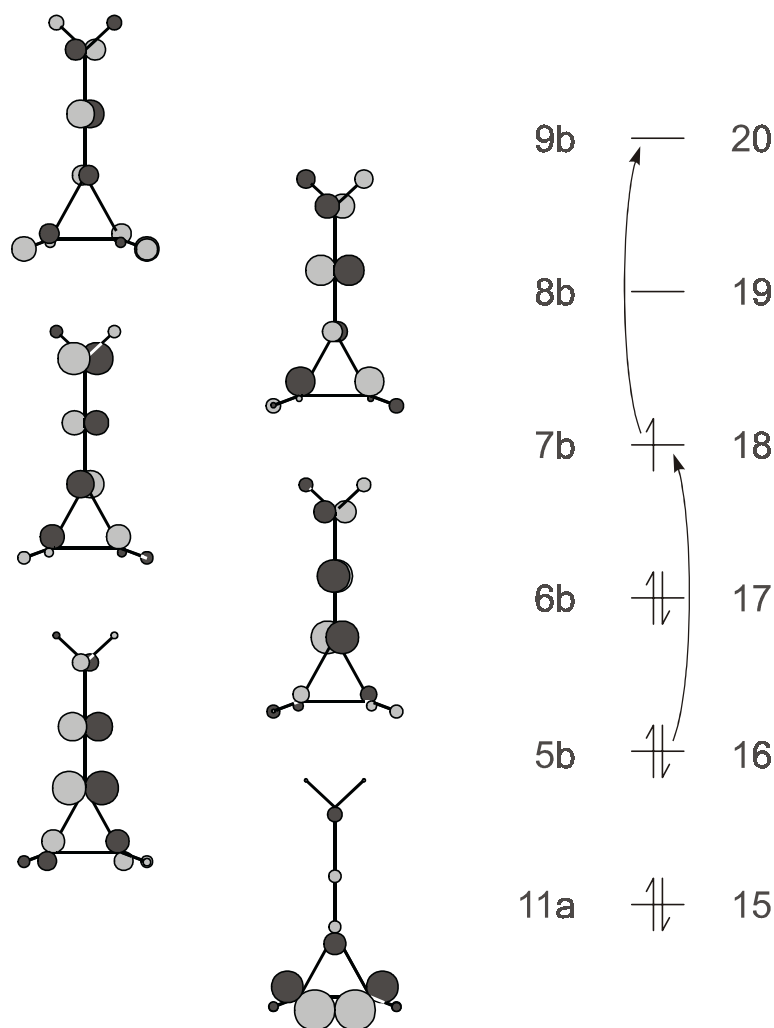
Figure 3-23: HF MOs of **VCP$^+$** at the radical cation geometry (cf. MOs in Figure 3-21).

Figure 3-24: IR spectrum of neutral **VCP** (**a**), difference spectra recorded after ionization (**b**) and subsequent irradiation at >850 nm (**c**) and >515 nm (**d**); (**e**): simulated IR spectrum of **VCP**$^{+\cdot}$ calculated by B3LYP/6-31G* (all frequencies scaled by 0.9575).
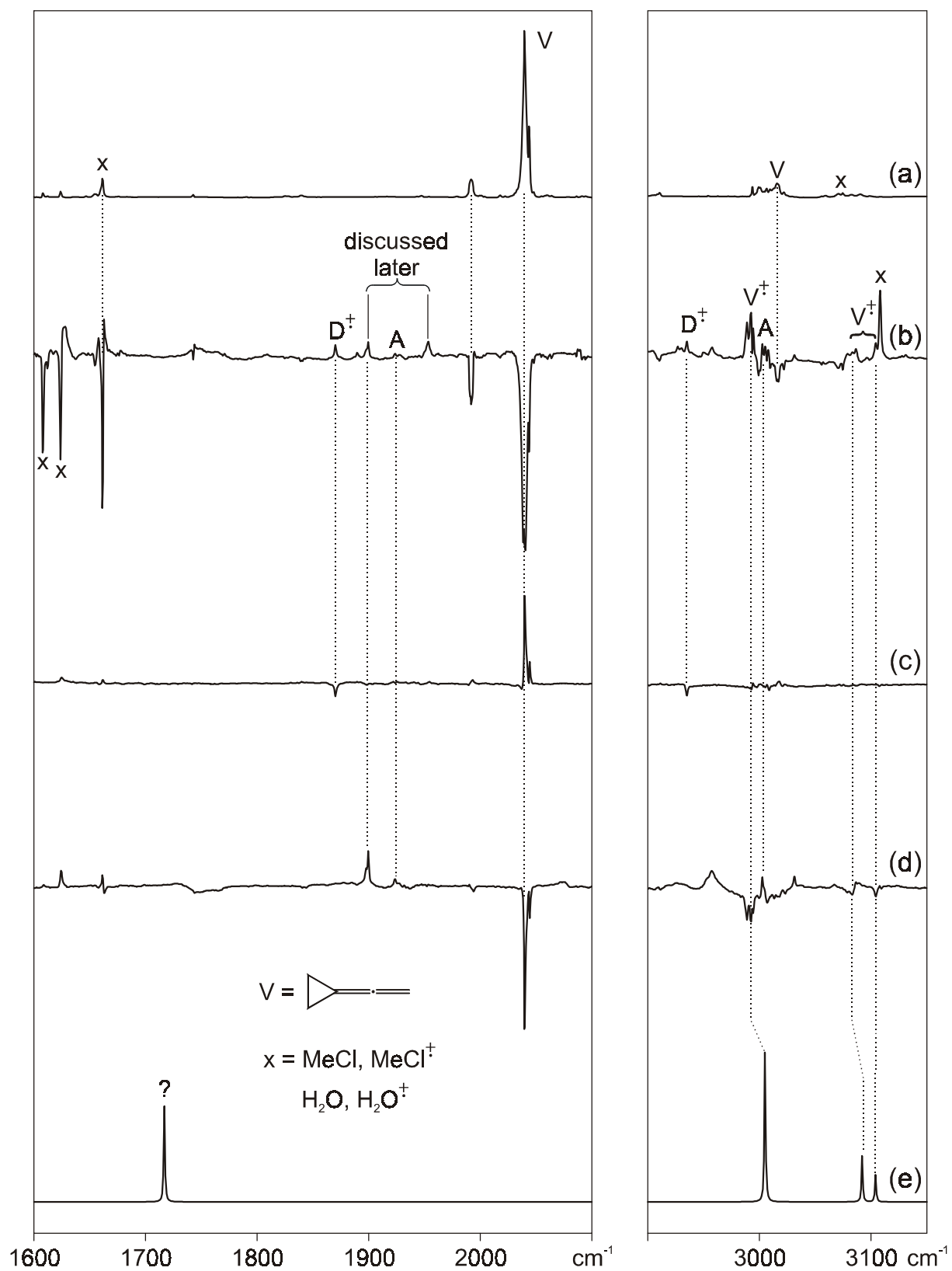
Figure 3-25: legend see Figure 3-24.

Table 3-9: Experimental and calculated vibrational frequencies of **VCP**$^{+\cdot}$.

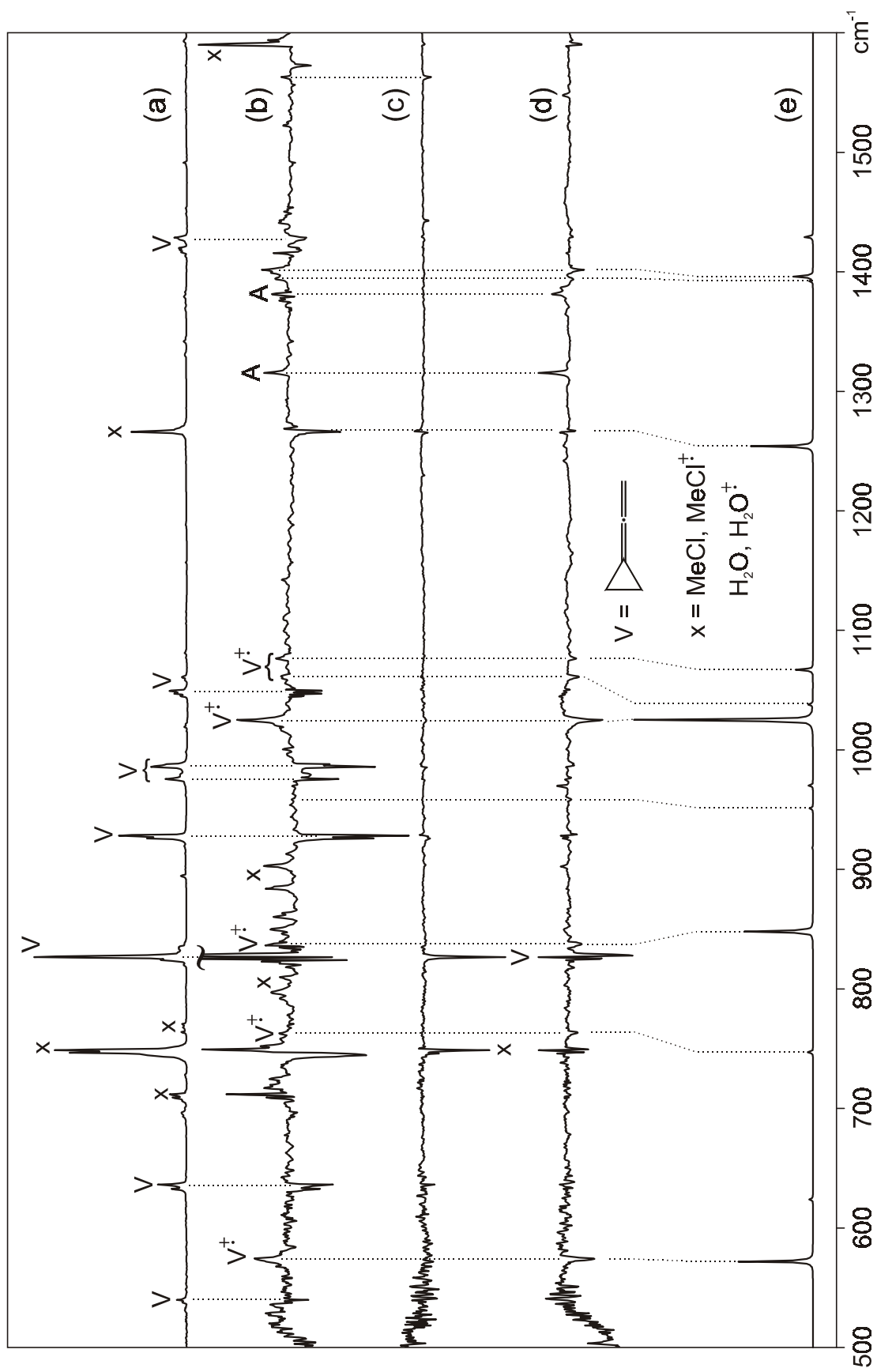|	calc.				exp.		
sym.	freq. [a] [cm^{-1}]	scaled [a] [cm^{-1}]	int. [b] [%]		freq. [cm^{-1}]	int. [b] [%]	Δ [c] [cm^{-1}]
b	128	123	5				
b	182	174	5				
b	361	346	1				
a	473	453	0				
b	479	459	1		468		
a	599	573	42		573	67	0
b	653	625	2				
b	782	748	3		763	11	-15
b	887	849	38		840	33	9
a	956	919	0				
b	995	953	2		959	5	-6
b	1015	972	2				
a	1072	1026	100 [d]		1020	100	6
a	1086	1040	2		1055	20	-15
b	1116	1068	10		1076	11	-8
a	1204	1153	0				
a	1310	1254	35		?		
a	1455	1393	2		1394	7	-1
b	1459	1397	11		1402	18	-5
a	1494	1430	5				
a	1795	1718	57		?		
b	3139	3006	10		2994		12
a	3139	3006	1				
a	3140	3006	78		2994	96	12
b	3230	3093	27		3104	16	-11
a	3232	3095	0				
b	3243	3105	16				

[a] Calculated with B3LYP/6-31G*, scaled by 0.9575.
[b] Intensities in % of the most intense band at 1020 cm^{-1}.
[c] RMS deviation of observed from calculated frequencies is 9.65 cm^{-1}.
[d] Absolute intensity of the most intense peak: 119.5 km/mol.

NIR photolysis of ionized **VCP** leads to a decrease of the **DIA**$^{+\cdot}$ peaks but not to the formation of more **VCP**$^{+\cdot}$. It is unclear what happens in this process: the strongest band of neutral **VCP**, the allenic band at 2040 cm^{-1}, increases, whereas the second strongest one at 827 cm^{-1} decreases! A reneutralization of

VCP is possible but this should concern all IR bands and not only the strongest one.

The vibrational frequencies of **VCP$^{+\cdot}$** were calculated by B3LYP/6-31G* and scaled with a factor of 0.9575 (see Table 3-9). The most intense one is at 1028 cm^{-1} and the allenic vibrational frequency is predicted to have about half of the intensity of the strongest one, and it should be at 1722 cm^{-1}. However we were unable to find any band in the IR spectrum that could possibly be matched with this predicted allenic band of **VCP$^{+\cdot}$**! Another band, predicted at 1258 cm^{-1} with about 35% intensity could not be assigned unambiguously because a peak of CH$_2$Cl$_2$ lies very close to it. On 140 min. irradiation at >515 nm the peaks of **VCP$^{+\cdot}$** disappear again and several bands appear which had already been present after X-irradiation of **VCP** but were so far left unassigned (denoted **A**, **M**, and **N**). We will return later to these peaks and to the changes in the UV/Vis spectra on photolysis.

In contrast to the neutral compound, **VCP$^{+\cdot}$** has C$_2$ symmetry. The allenic methylene group is rotated by 40.1° from the perpendicular conformation[9]. The cumulated double bonds in neutral **VCP** are similar in length (C$_1$-C$_4$ 1.29 Å, C$_4$-C$_5$ 1.31 Å), whereas in the radical cation they differ by 0.06 Å (1.275 Å and 1.335 Å). The two lateral cyclopropane bonds are lengthened by 0.045 Å, while the central cyclopropane bond is shortened by 0.050 Å on ionization of **VCP** (cf. Figure 3-26).

The spin of the radical cation is localized mostly on C$_1$ (51%) and C$_5$ (32%), and the charge is mostly located on the central allenic carbon atom. To bring the twisted methylene group of **VCP$^{+\cdot}$** into a perpendicular position, as in the neutral molecule, requires only 1.77 kcal/mol[10]. To bring it into a position coplanar with the cyclopropane ring requires 5.20 kcal/mol[10] (for comparison, the rotation of the allenic methylene group in neutral **VCP** requires 62.0 kcal/mol[11].

---

[9] This is a general feature of allenes which in the parent compound arises by virtue of a Jahn-Teller distortion of the degenerate ground state. In unsymmetrically substituted allenes vibronic interaction with the lowest excited state is responsible for this distortion.

[10] CCSD(T)/cc-pVTZ//B3LYP/6-31G* level, corrected for ZPVE differences.

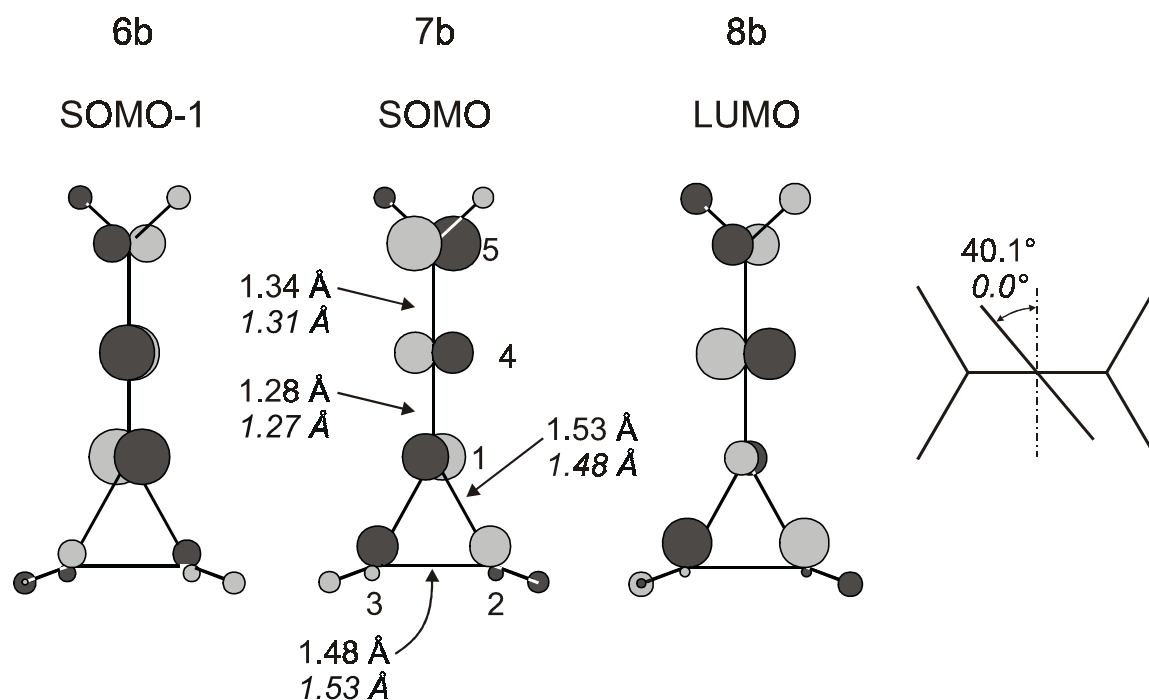[11] B3LYP/6-31G* level, corrected for ZPVE differences.

Figure 3-26: Bondlengths and MOs of **VCP** (normal font) and its radical cation (*italic*) calculated by B3LYP/6-31G* (radical cation geometry depicted).

The **DIA**$^{+\cdot}$ → **VCP**$^{+\cdot}$ ring-closing process, illustrated in Figure 3-27, is slightly endothermic (0.29 kcal/mol)[12]. The barrier for this process is 15.1 kcal/mol (B3LYP/6-31G*, ZPVE corrected), which can readily be surmounted on NIR-irradiation (1400 nm = 20.4 kcal/mol). An IRC calculation starting from this transition state (TS5) points to a disrotatory ring-closing reaction as for the allyl radical [66] and that of the azomethine ylid radical cation (see section 4.2.3.2).

In Figure 3-28 we summarize the cascade of rearrangements that [1.1.1]propellane undergoes on ionization: The loss of an electron leads to a facile distortion of the primary radical cation which eventually results in an opening of one of the three membered rings of **PRP**$^{+\cdot}$, i.e. the formation of the distonic **MBB**$^{+\cdot}$. A second three membered ring is opened by rupture of a lateral bond of **MBB**$^{+\cdot}$ which leads to **DMC**$^{+\cdot}$. However, due to the operation of strong vibronic interactions this cation is still not sufficiently stable to survive, and it opens to **DIA**$^{+\cdot}$ by cleavage of the third lateral cyclopropane bond (note that, in all the inter-

---

[12] CCSD(T)/cc-pVTZ//B3LYP/6-31G* corrected for B3LYP ZPVE differences. At the B3LYP/6-31G* level, the reaction is *exo*thermic by 1.44 kcal/mol (0.26 kcal/mol ZPVE difference corrected).

mediates, the *lateral* cyclopropane bonds are invariably weaker than the *central* ones). Whereas in **PRP**‡ and **MBB**‡ this may be explained by the fact that more strain is relieved on cleavage of a lateral cyclopropane bond, in **DMC**‡ it is owing to strong vibronic interaction that the lateral C-C bond is weakened.
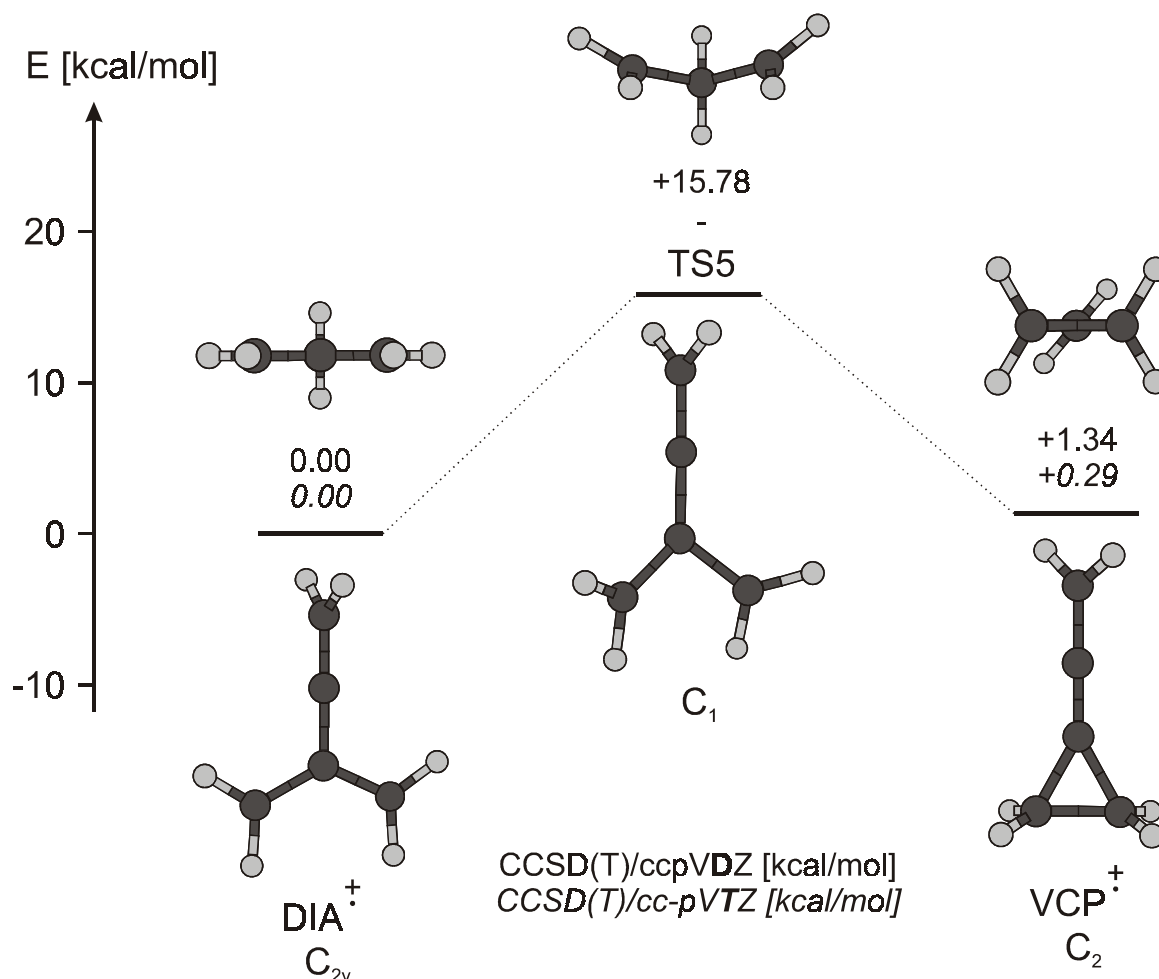
Figure 3-27: Thermochemistry of the ring-closing process of **DIA**‡ to **VCP**‡ calculated on CCSD(T)/cc-pVTZ level, corrected for ZPVE differences at the B3LYP/6-31G* level.

Now that the assignment of **X**, with its electronic absorption band in the NIR and the allenic peak in the IR spectrum, has been secured, we return to the question of the identity of the species giving rise to the diene‡-like electronic absorption features observed on ionization of **PRP**‡ and **DMC**‡ (see Figure 3-15) One possibility is that they stem from **MCB**‡. Although it is difficult to imagine how **MCB**‡ could be formed from **DMC**‡, we decided to explore this possibility in the hope of finding some clue to the identity of the unknown compound(s).
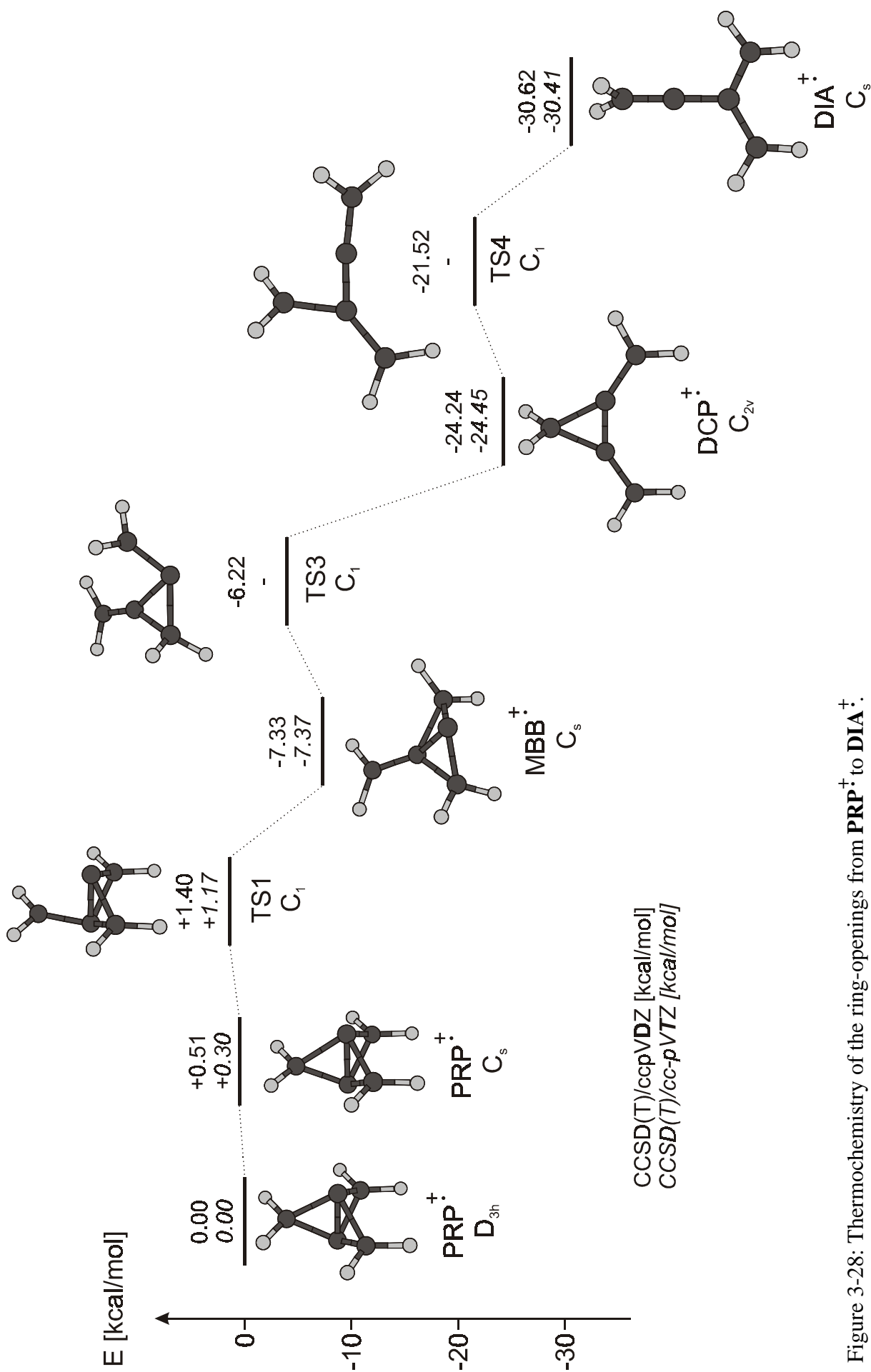
Figure 3-28: Thermochemistry of the ring-openings from **PRP**$^{+\bullet}$ to **DIA**$^{+\bullet}$.

3.7 Ionization of methylenecyclobutene

The photoelectron spectrum of methylenecyclobutene, **MCB**, was measured in our laboratory[13] [65]. It is shown in Figure 3-29. The first PE band which corresponds to ionization from the diene-π-HOMO of **MCB** shows three members of a vibrational progression of 1530 cm^{-1} (0.19 eV). The first excited state of **MCB**‡, 1.85 eV above the ionic ground state at the neutral geometry (1.72 eV by CASPT2, see Table 3-10), corresponds to ionization from the antibonding combination of the lowest π-MO and the pseudo-π CH$_2$ MO of **MCB**. The next three PE bands are due to ionization from σ-MOs. The first such state lies 2.67 eV above the ground state (CASPT: 2.67 eV, the others were not calculated, because only the highest occupied a' MO was included in the active space).
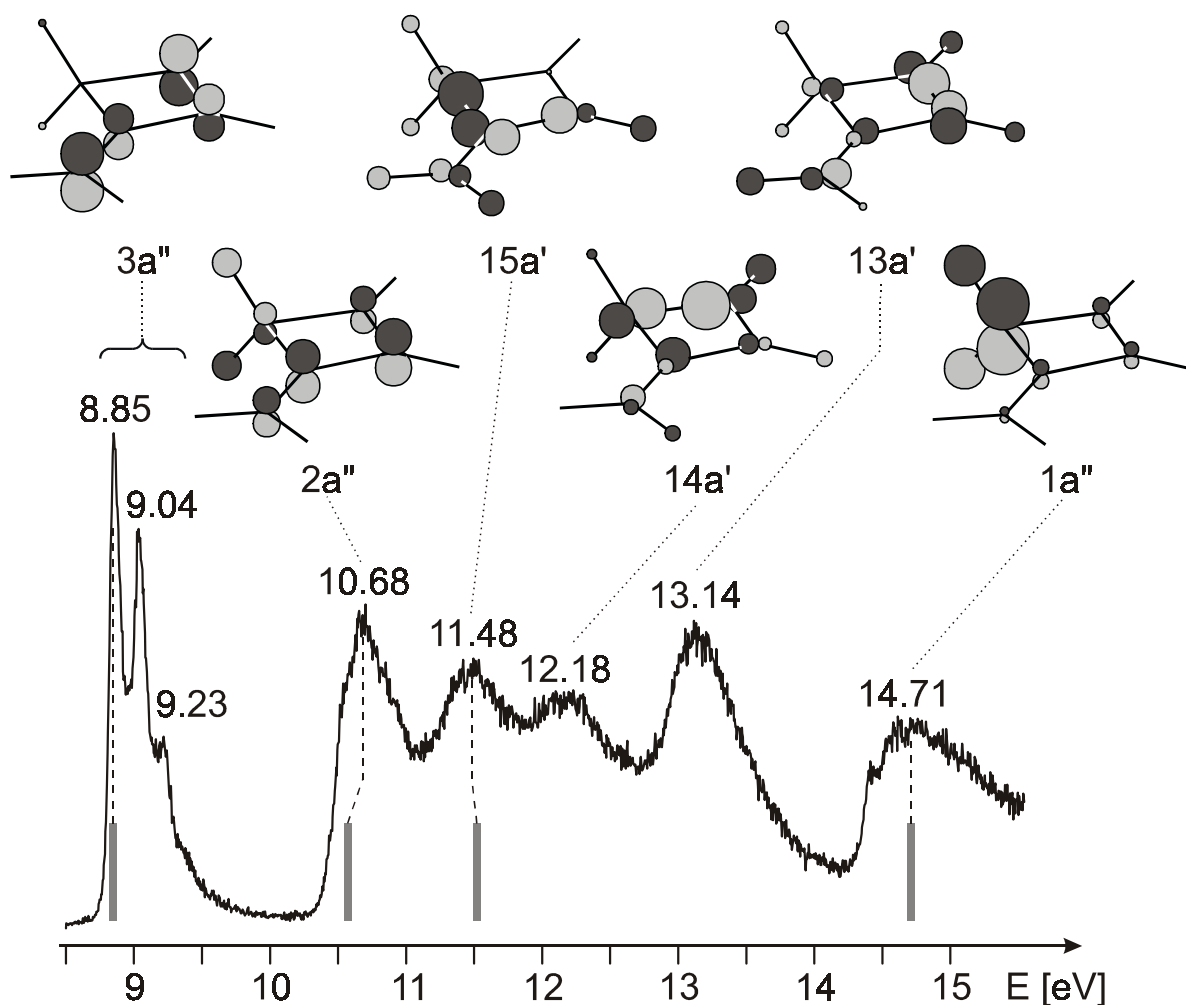

Figure 3-29: PE spectrum of **MCB** together with MOs calculated by the HF method.

The $3^2A''$ state shows 68% contributions of non-Koopmans excitations, and it can therefore not manifest itself in the PE spectrum. However, the predicted $4^2A''$ state is again in very good accord with the 6th band in the PE spectrum.

Table 3-10: Excited states of **MCB**$^{+\cdot}$ at the neutral geometry by CASSCF/CASPT2.

states	PES eV	CASPT2 eV	CASSCF configurations [b]	
$1^2A''$	-	-	92%	$(3a'')^1$
$2^2A''$	1.83	1.72	81%	$2a'' \rightarrow 3a''$
			7%	$3a'' \rightarrow 5a''$
$1^2A'$	2.63	2.67	88%	$15a' \rightarrow 3a''$
$3^2A''$	-	4.29	61%	$3a'' \rightarrow 5a''$
			7%	$2a'' \rightarrow 5a''$
			7%	$1a'' \rightarrow 3a''$
			6%	$2a'' \rightarrow 3a''$
$4^2A''$	5.86	5.86	69%	$1a'' \rightarrow 3a''$

[a] Oscillator strength for electronic transition.

[b] Active space: 7 electrons in 1 doubly occupied + 2 virtual a' and in 2 doubly + 1 singly occupied + 2 virtual a'' MOs. Occupied MOs depicted in Figure 3-29.

On ionization of methylenecyclobutene one obtains the same UV/Vis spectrum as from ionized **PRP**! Only the band in the NIR is missing and the three small peaks around 400 nm are not visible. However, the two diene radical cation bands at 486 and 310 nm are clearly developed as shown in Figure 3-30. However, CASPT2 calculations (Table 3-11) indicate that these bands are not likely to be due to **MCB**$^{+\cdot}$. Although the strong band at 311 nm would match quite well with the predicted absorption of **MCB**$^{+\cdot}$ at 318 nm, the weak band at 486 nm is too far from the band predicted at 615 nm. In addition, the calculated vibrational spectrum of **MCB**$^{+\cdot}$ shows no relation to the new peaks formed on X-irradiation of **MCB** (Figure 3-32).
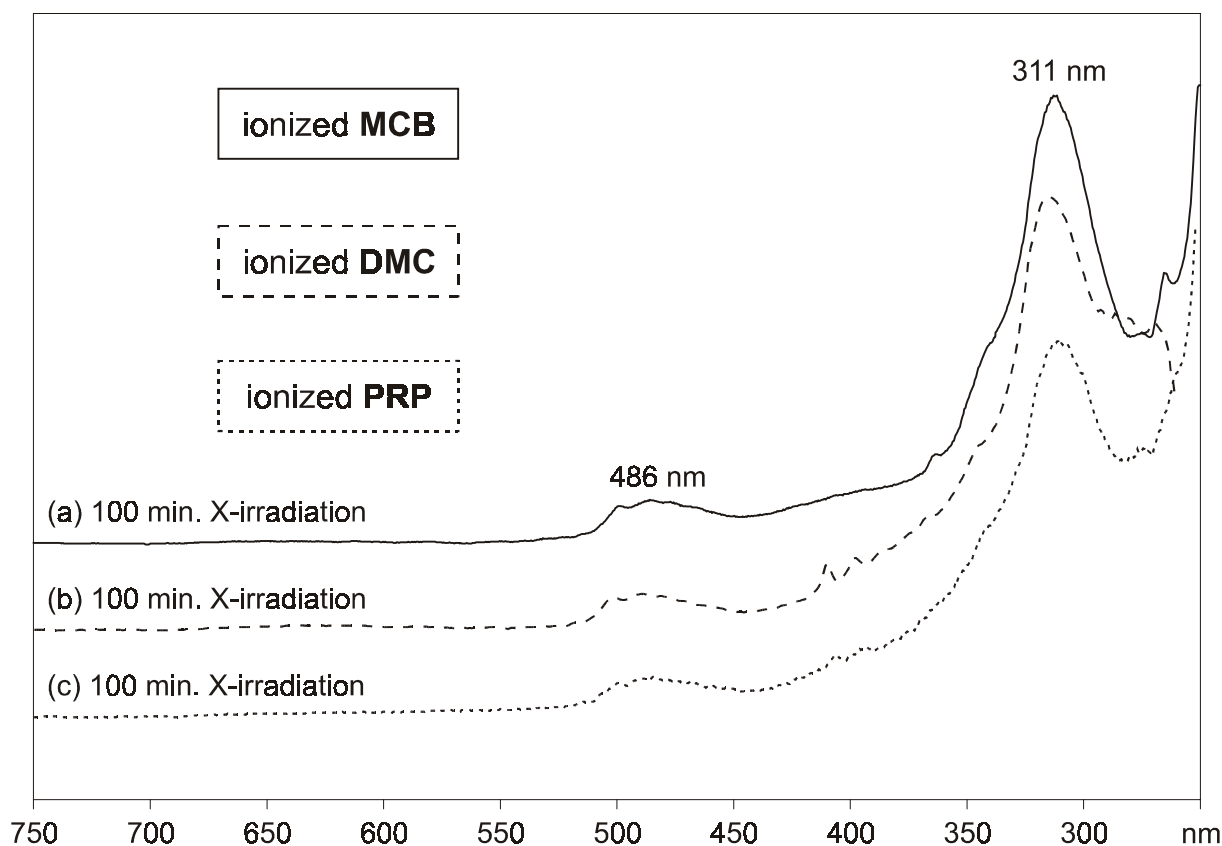
Figure 3-30: EA difference spectrum of **MCB** after ionization (**a**) in Ar matrix with corresponding EA difference spectra of **DMC** (**b**, expanded by a factor 1.8) and **PRP** (**c**, expanded by a factor of 3.5).

Table 3-11: Excited states of **MCB**$^{+\cdot}$ at the radical cation geometry by CASSCF/CASPT2.

states	CASPT2			CASSCF configurations [b]
	nm	eV	f^a	
1^{2}A"	-	-	-	91% (3a")^1
2^{2}A"	615	2.02	0.015	72% 2a" $\rightarrow$ 3a"
				14% 3a" $\rightarrow$ 5a"
1^{2}A'	377	3.29	0.0003	85% 15a' $\rightarrow$ 3a"
3^{2}A"	318	3.90	0.265	61% 3a" $\rightarrow$ 5a"
				13% 2a" $\rightarrow$ 3a"
4^{2}A"	210	5.91	0.011	44% 3a" $\rightarrow$ 4a"
				33% 2a" $\rightarrow$ 5a"

[a] Oscillator strength for electronic transition.

[b] Active space: 7 electrons in 1 doubly occupied + 2 virtual a' and in 2 doubly + 1 singly occupied + 2 virtual a" MOs. Occupied MOs shown in Figure 3-29.

Instead we observe many new bands in the allenic region of the IR spectrum around 1900 cm^{-1} (but almost no **DIA**$^{+}$ at 1870 cm^{-1})! This indicates that **MCB**$^{+}$ undergoes spontaneous ring-opening to the radical cation of vinylallene, **VIA**$^{+}$. The ring-opening can either go to the *E* or to the *Z* conformer of **VIA**$^{+}$, analogous to cyclobutene radical cation which can open by two competitive pathways leading to *cis*- or *trans*-butadiene radical cation, respectively. The activation barriers for the two processes differ by less than 1 kcal/mol at the highest level of theory employed (CCSD(T)/cc-pVTZ//QCISD/6-31G*) [67].

Indeed the CASPT2 prediction for the electronic transitions of **VIA**$^{+}$ (Table 3-12) match quite well with the observed EA spectrum: for *E*-**VIA**$^{+}$ the strongest band is predicted at 307 nm (*f* = 0.638) and a weaker one at 479 nm (*f* = 0.008), and for *Z*-**VIA**$^{+}$ transitions at 326 nm (*f* = 0.448) and at 490 nm (*f* = 0.028) are predicted. In addition, both conformers show a very weak transition at longer wavelengths that corresponds to electron promotion from the π-MO that lies in the molecular plane to the diene-HOMO.
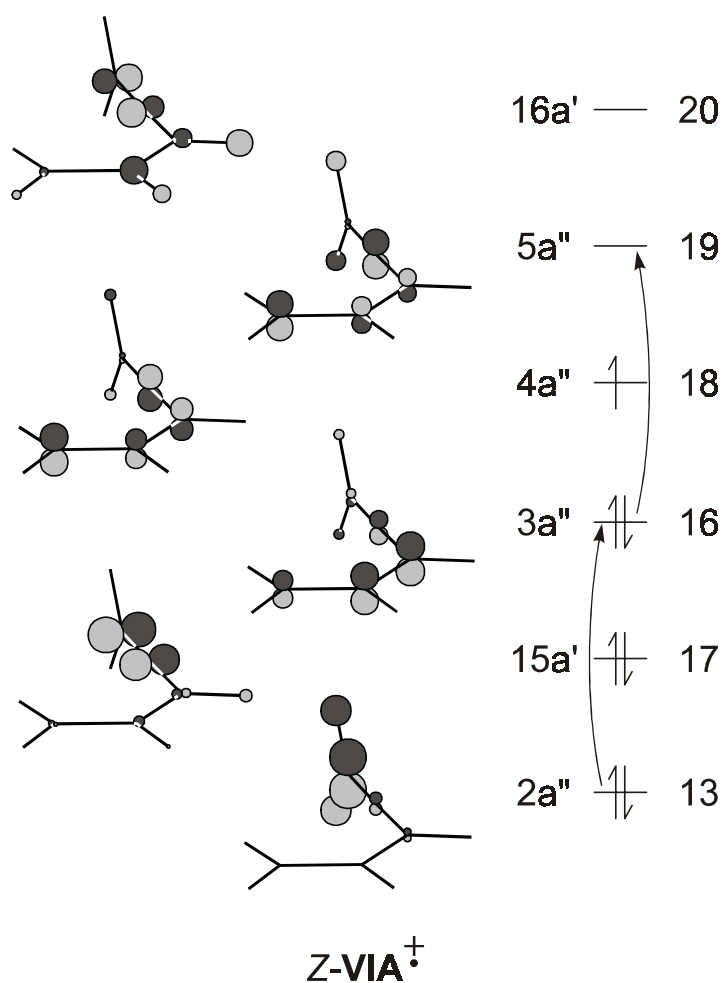

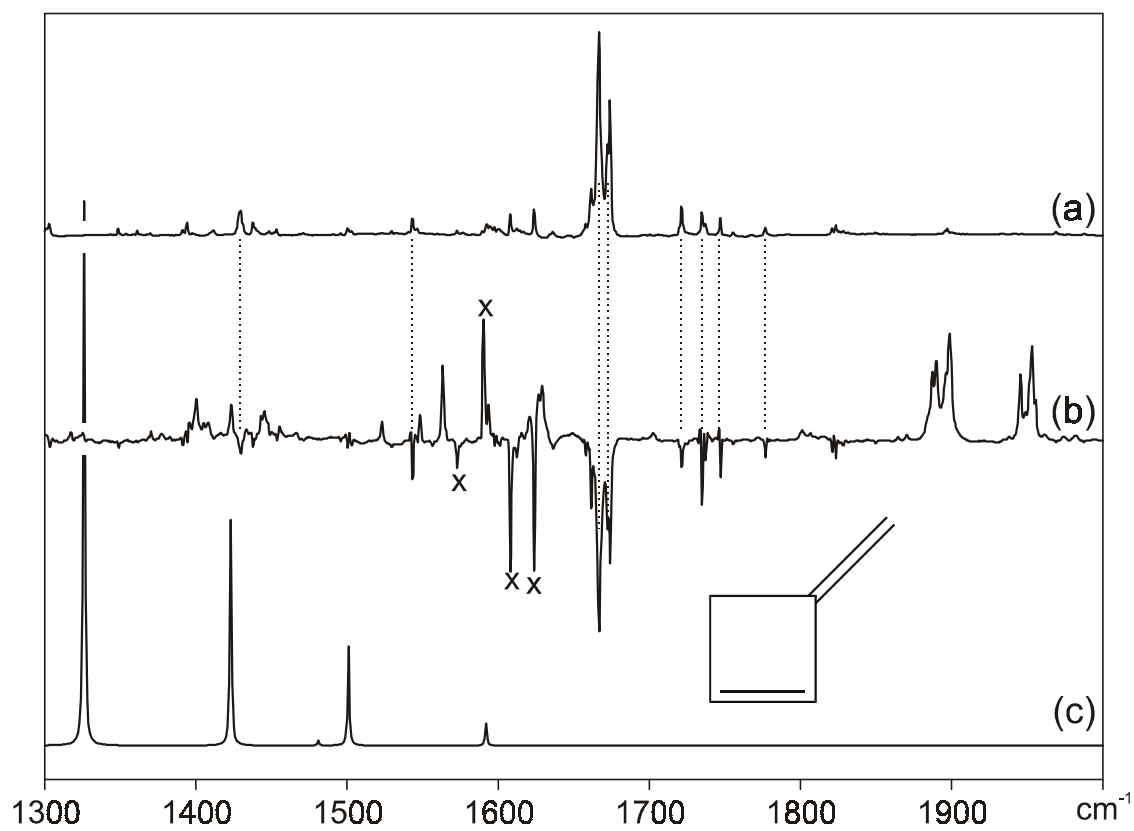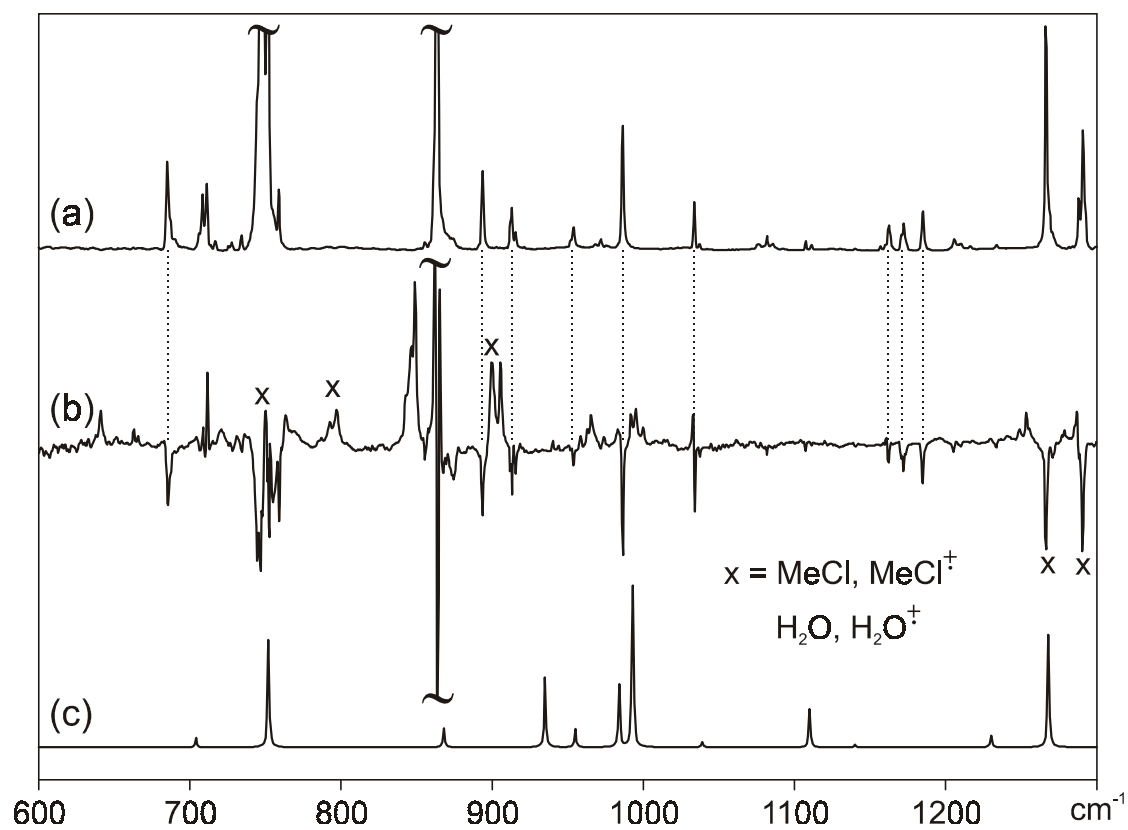Figure 3-31: MOs of *Z*-**VIA**$^{+}$ calculated by the HF method.

Figure 3-32: IR spectrum of neutral **MCB** (**a**) and difference spectrum of **MCB** after X-irradiation (**b**) with calculated spectrum of **MCB$^{+\cdot}$** (**c**, B3LYP/6-31G*, not scaled).

Table 3-12: Excited states of E- and Z-**VIA**$^{+\cdot}$ radical cation by CASPT2 calculations.

radical cation	states	CASPT2			CASSCF
		E [eV]	[nm]	f^a	configurations [b, c]
E-**VIA**$^{+\cdot}$	1^{2}A"	-	-	-	92% (3a")^1
	1^{2}A'	1.63	759	0.0002	89% 15a' → 3a"
	2^{2}A"	2.59	479	0.008	62% 2a" → 3a"
					21% 3a" → 5a"
	3^{2}A"	4.05	307	0.638	39% 3a" → 5a"
					26% 2a" → 3a"
					18% 3a" → 4a"
	2^{2}A'	4.53	274	0.0005	66% 3a" → 5a"
					15a' → 3a"
					21% 15a' → 5a"
Z-**VIA**$^{+\cdot}$	1^{2}A"	-	-	-	93% (3a")^1
	1^{2}A'	1.78	696	0.003	88% 15a' → 3a"
	2^{2}A"	2.53	490	0.028	65% 2a" → 3a"
					25% 3a" → 5a"
	3^{2}A"	3.80	326	0.448	58% 3a" → 5a"
					25% 2a" → 3a"
	2^{2}A'	4.42	281	0.009	66% 3a" → 5a"
					15a' → 3a"
					21% 15a' → 5a"

[a] Oscillator strength for electronic transition.
[b] Active space (E-**VIA**$^{+\cdot}$): 5 electrons in 1 doubly occupied + 1 virtual a' and in 1 doubly + 1 singly occupied + 2 virtual a" MOs.
[c] Active space (Z-**VIA**$^{+\cdot}$): 7 electrons in 1 doubly occupied + 1 virtual a' and in 2 doubly + 1 singly occupied + 2 virtual a" MOs (shown in Figure 3-31).

As expected, the transitions for Z- and E-**VIA**$^{+\cdot}$ lie very close and therefore it is not possible to distinguish whether the bands in the electronic absorption spectrum of X-irradiated **MCB**$^{+\cdot}$ stem from the one or from the other conformer. Perhaps we even have a mixture of both conformers of **VIA**$^{+\cdot}$ after X-irradiation of **MCB**.

3.8 Ionization of vinylallene (VIA)

To confirm the identification of **VIA**$^+$ we synthesized **VIA** and embedded it in an Argon matrix. The spectrum of the neutral compound shows a strong peak at 1945 cm^{-1} which also increases in the spectrum of **MCB** after ionization (cf. Figure 3-30-**b**). This indicates that **MCB** does not only undergo ring-opening on ionization, but that the resulting **VIA**$^+$ is reneutralized to **VIA**.

On ionization of **VIA**$^+$ the peak at 1945 cm^{-1} decreases while another quite broad peak centered at 1890 cm^{-1} increases (Figure 3-33-e). Although the position of this peak matches well with that in the spectrum of ionized **MCB** (Figure 3-33-**a**) its shape is very different, indicating the presence of several conformers after ionization of **MCB**. We optimized the structures of *Z*- and *E*-**VIA** and found an energy difference of 2.34 kcal/mol in favor of *E*-**VIA**[14] presumably due to the repulsion of H atoms in the *Z* conformer. Addition of thermal corrections and T·ΔS to the CCSD(T) energy to give Gibbs free energies at 298 K leads to a difference of 1.92 kcal/mol. The relation

$$\Delta G = -RT \cdot \ln(K)$$

allows to determine the ratio between the two conformers at room temperature, as they are trapped in the matrix. This results in an equilibrium constant of

$$K = \frac{[E - \mathbf{VIA}]}{[Z - \mathbf{VIA}]} = 25.8 .$$

Thus, 96.3% of the **VIA** in the matrix should be present in the *E*-conformation. Therefore we assign the peak at 1945 cm^{-1} to *E*- and the peak(s) at 1953 (1955) cm^{-1} to *Z*-**VIA**. Since we do not expect ionization of **VIA** to be accompanied by complete $E \rightarrow Z$ isomerization, we conclude that the peaks at 1887 and 1890 cm^{-1} belong to *E*- and these at 1896 and 1899 cm^{-1} to *Z*-**VIA**$^+$. The 3 cm^{-1} splittings within these pairs are probably due to site effects.

Unfortunately, B3LYP/6-31G* predicts the shift between the allenic frequencies of *E*- and *Z*-**VIA**$^+$ inversely: for the *E*-rotamer the calculated frequency is 1903 cm^{-1}, whereas for *Z*-**VIA**$^+$ 1897 cm^{-1} are obtained.

---

[14] Relative CCSD(T)/cc-pVTZ energies calculated at B3LYP/6-31G* optimized geometries and corrected for ZPVE differences at the same level.

For the radical cations, the calculated energy difference between the *Z* and *E* conformers - calculated at the same level - is 1.76 kcal/mol.

We could even induce a photochemical *E* - *Z* isomerization of **VIA**$^{+}$ with light of >590 nm. The proof for this is in IR spectrum (**b**) in Figure 3-33 where the peaks we had assigned to *E*-**VIA**$^{+}$ decrease while those of *Z*-**VIA**$^{+}$ increase. Finally, prolonged photolysis at >475 nm led to the complete bleaching of **VIA**$^{+}$ (spectrum **c**).

In Figure 3-34 the full IR spectra are depicted. It can be seen that after ionization of **MCB** (**a**) not only the peaks of **VIA**$^{+}$, but also those of neutral **VIA** (cf. spectrum **e**) increase. Apparently, **MCB**$^{+}$ undergoes ring-opening and reneutralization to **VIA**. The peaks of **VIA**$^{+}$ are not prominent; *E*-**VIA**$^{+}$ can only be detected from three peaks at 849, 1887/1890, and 2950 nm. For *Z*-**VIA**$^{+}$ we observe more peaks but the assignment to the simulated spectrum is difficult. The following peaks could be assigned to *Z*-**VIA**$^{+}$: 865, 965, 1253, (1317), 1548, 1896/1899, 2956, and 3031 nm.

After photolysis of **VIA**$^{+}$ some other IR bands increase, especially in the spectrum of ionized **MCB**$^{+}$, after photolysis at >475 nm. These bands are at 865, 944, 1325, 1423, and 1456 cm^{-1}. The identity of the species which is responsible for these bands is revealed by the UV/Vis spectra (see later).

It is surprising that the EA spectrum of ionized **VIA** is almost congruent with that of ionized **MCB** (see Figure 3-36 spectra **a** and **d**). However, on the basis of the EA spectrum of ionized **VIA**$^{+}$ we cannot distinguish the two conformers, although in this experiment the *E*-conformer should be much more prominent than the *Z*-conformer, as we have concluded on the basis of the IR spectra. But the >590nm photolysis which leads to the *E* - *Z* isomerization results in a slight increase of the absorption at 311 nm and a decrease at 344 nm where we could observe a shoulder in the spectrum obtained after ionization of **MCB**. The broad band at 486 nm does not change much, but it is clearly visible that in does not decrease but rather increase. These arguments indicate that the bands of *Z*-**VIA**$^{+}$ are at 311 and at 486 nm and the strong absorption of *E*-**VIA**$^{+}$ is at lower energy and much less intense than that of *Z*-**VIA**$^{+}$. Unfortunately, both arguments are in contradiction with the CASPT2 prediction for *Z*- and *E*-**VIA**$^{+}$ (Table 3-12).

All our assignments are based on the assumption that neutral **VIA** is deposited in the matrix predominantly in its more stable *E*-conformation. The shape of the allenic peak obtained on ionization of **VIA** indicates that both

conformers of **VIA**$^+$ are formed. However, the peak at 1890 cm^{-1} is clearly dominant and it is also this one which decreases on photolysis at >590 nm of ionized **MCB** where both conformers were apparently formed on ionization.

Irradiation at >475 nm destroys **VIA**$^+$ and leads to an increase of new bands in the IR and EA spectra, not all of which we where able to identify. Two sets of bands can be attributed to the cyclopentadiene radical cation, **CPD**$^+$ [68]: two sharp peaks at 351 and 365 nm and four broader humps at 528, 552, 578, and 608 nm (see Figure 3-36). Calculations show that **CPD**$^+$, which is photostable, is more than 34.3 kcal/mol more stable than **MCB**$^+$ which is isoenergetic with *Z*- and 1.70 kcal/mol above *E*-**VIA**$^+$.[15]

The observation that we obtain much less **CPD**$^+$ in the experiment with **VIA**$^+$ than we obtain from ionized **MCB** seems to indicate that **CPD**$^+$ is formed more easily from *Z*-**VIA**$^+$ than from *E*-**VIA**$^+$.
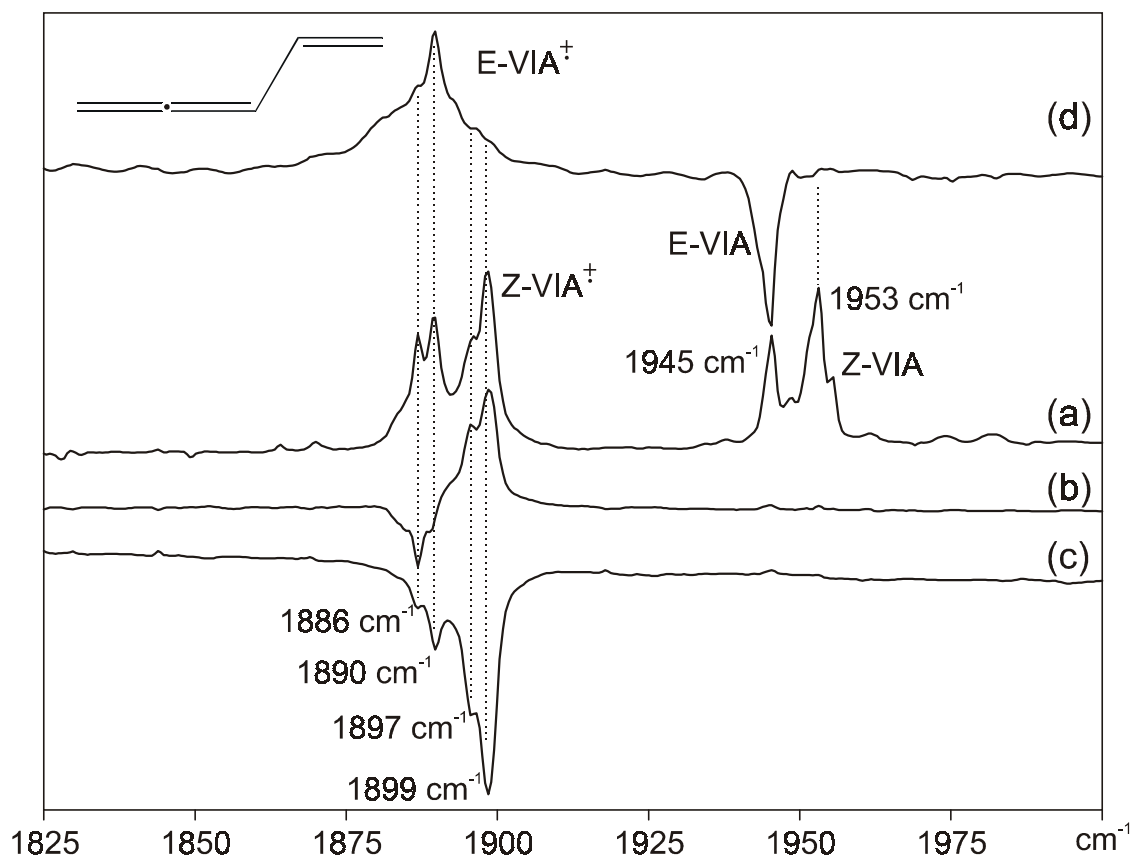
Figure 3-33: Allenic region of IR difference spectra of ionized (**a**) and photolyzed (**b-c**) **MCB** and of ionized **VIA** (**d**).

---

[15] Relative CCSD(T)/cc-pVTZ energies calculated at B3LYP/6-31G* optimized geometries and corrected for ZPVE differences at the same level.
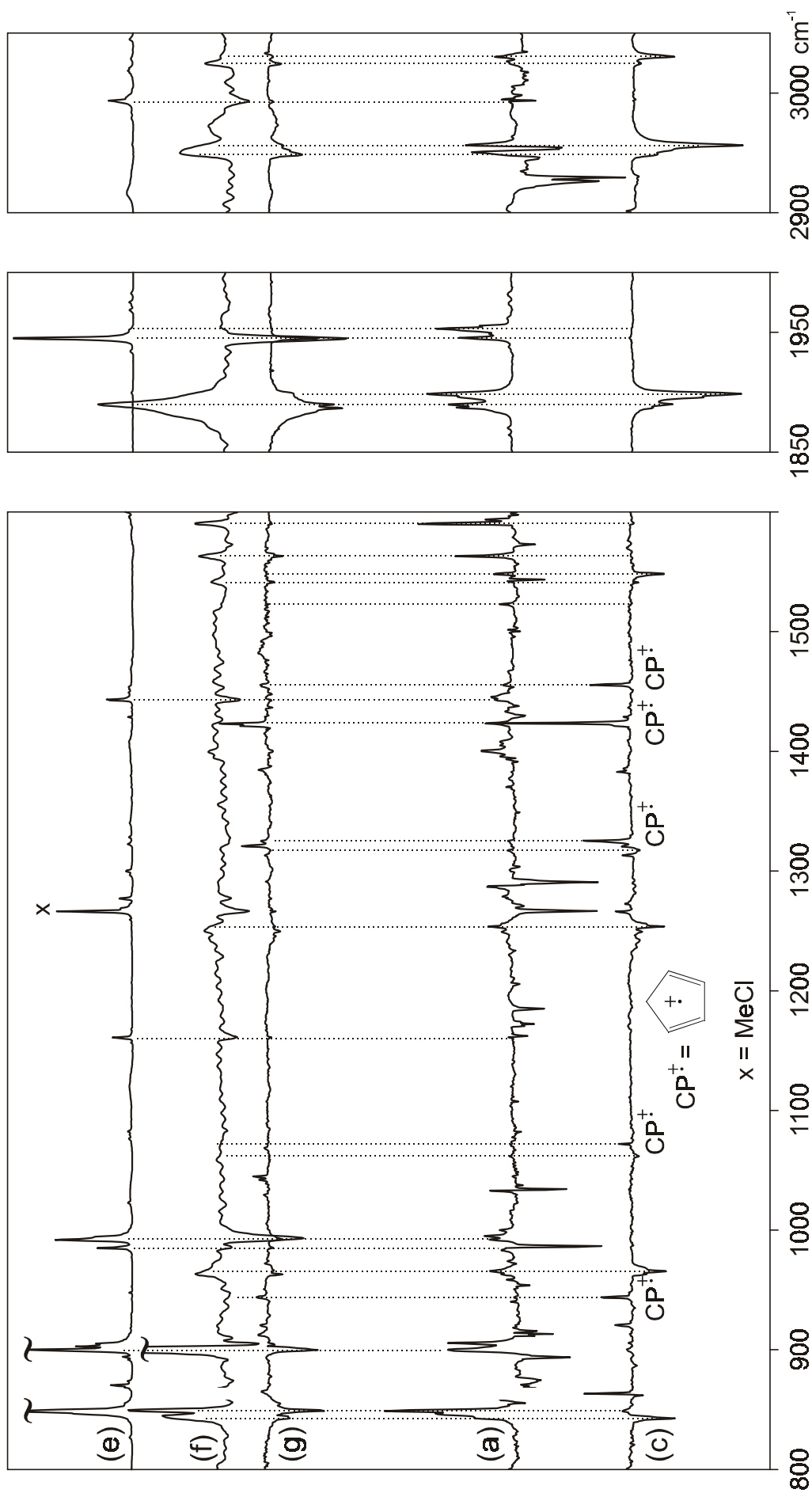
Figure 3-34: IR difference spectra of **MCB** after ionization (**a**) and after irradiation (**c**, 600 min. >475 nm). IR spectrum of neutral **VIA**⁺ (**e**) and difference IR spectra of **VIA**⁺ after ionization (**f**) and after irradiation (**g**, 40 min. >420 nm).
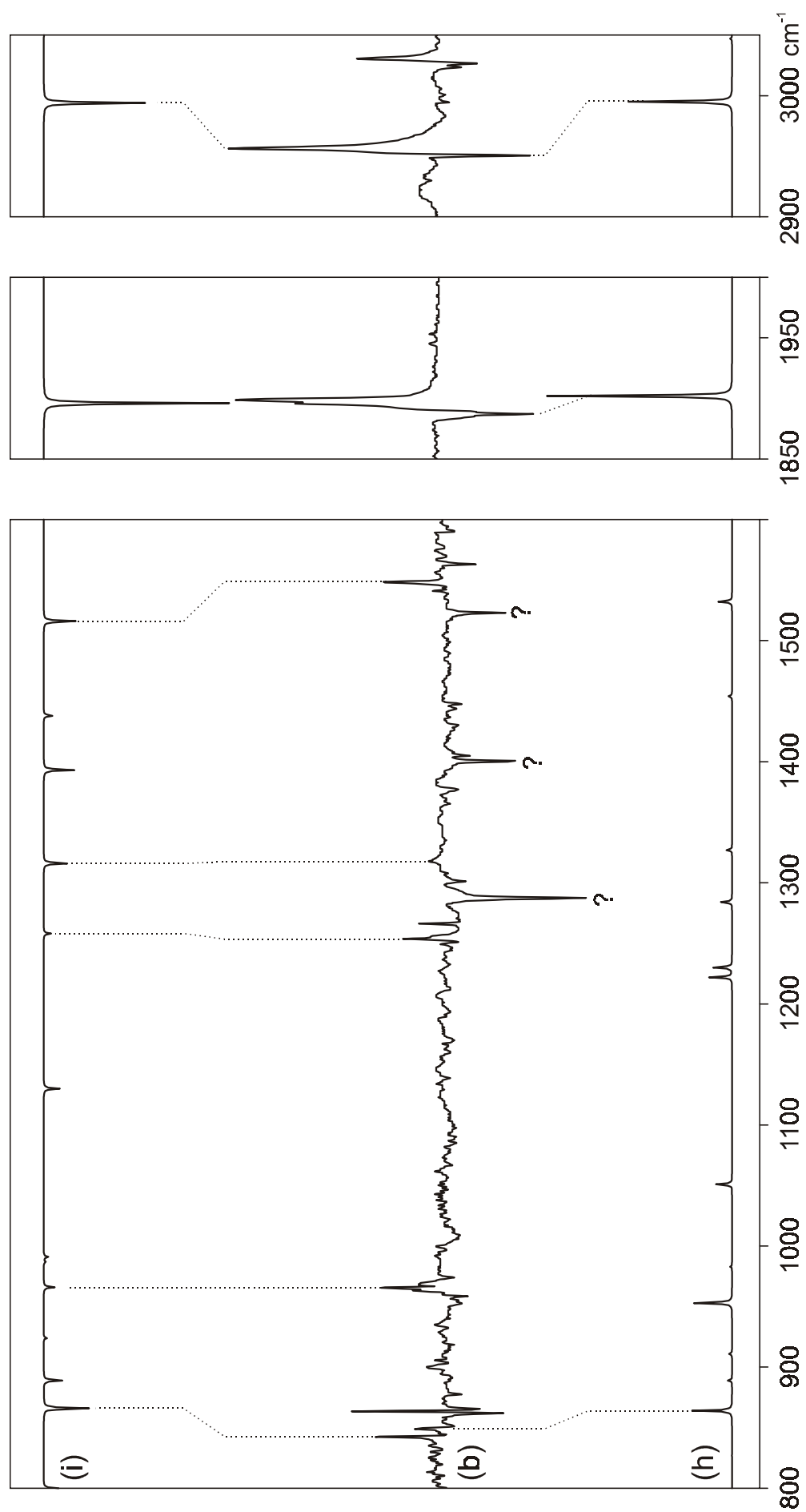
Figure 3-35: IR difference spectrum of photolyzed **VIA**$^{+\cdot}$ (**b**, 160 min. >590 nm) with calculated (B3LYP/6-31G*, scaled with 0.96) IR spectra of *E*- (**h**) and *Z*-**VIA**$^{+\cdot}$ (**i**).
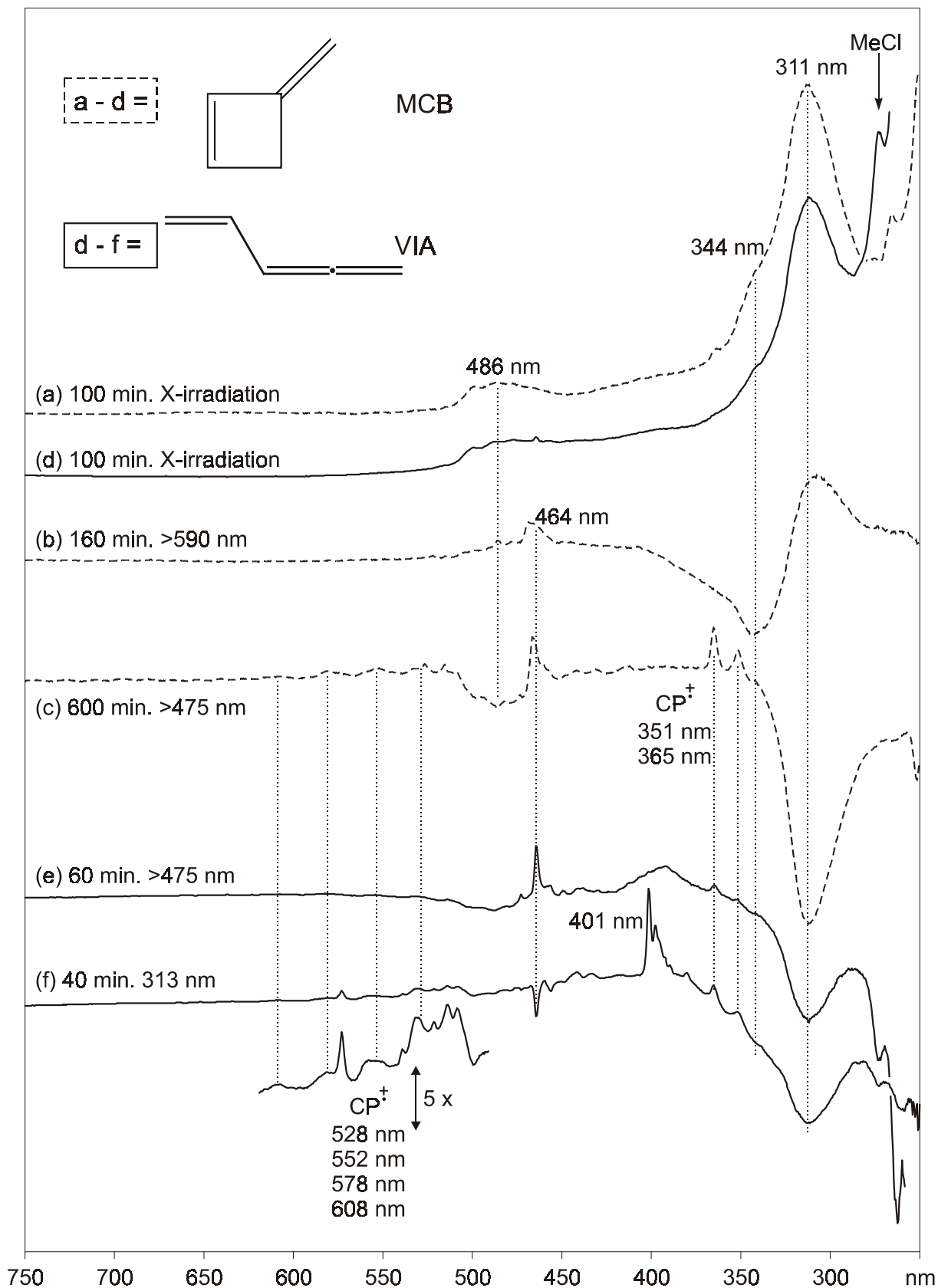
Figure 3-36: EA difference spectrum of ionized and photolyzed **MCB** (**a** - **c**) and **VIA** (**d** - **f**) in Ar matrix.
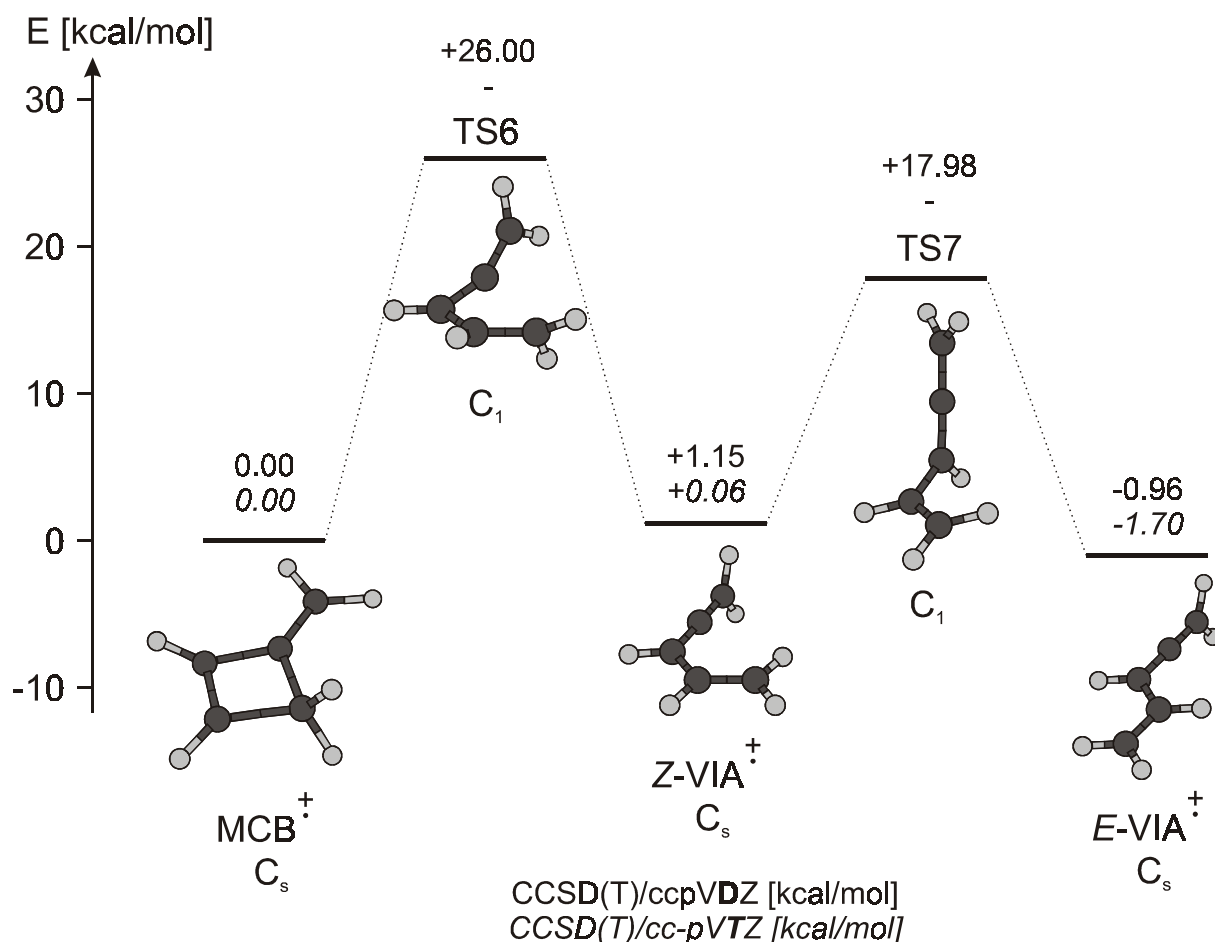
Figure 3-37: Thermochemistry of the ring-opening process of **MCB**$^{+\cdot}$ to *Z*-**VIA**$^{+\cdot}$ and isomerization to *E*-**VIA**$^{+\cdot}$ calculated at CCSD(T) level, corrected for ZPVE differences at the B3LYP/6-31G* level.

The ring-opening of **MCB**$^{+\cdot}$ to *Z*-**VIA**$^{+\cdot}$ has a barrier of 26.0 kcal/mol. The barrier of the rearrangement from **MCB**$^{+\cdot}$ to *E*-**VIA**$^{+\cdot}$ could not be found but the TS for the *E*-*Z* isomerization of **VIA**$^{+\cdot}$ lies 16.8 kcal/mol above *Z*-**VIA**$^{+\cdot}$ which lies itself 1.76 kcal/mol above *E*-**VIA**$^{+\cdot}$.[16] These thermochemical values and the structure of the ring-opening TS are comparable to those for the ring-opening of the cyclobutene to the *cis*-butadiene radical cation (see Figure 3-37 and Reference 67) where the barrier amounts to 18.3 kcal/mol and the process is exothermic by 18.7 kcal/mol[16]. The dihedral angle C_1-C_2-C_3-C_4 at the ring-opening TS of cyclobutene$^{+\cdot}$ is 17.1° at the B3LYP level, whereas in the TS for

---

[16] Relative CCSD(T)/cc-pVTZ energies calculated at B3LYP/6-31G* optimized geometries and corrected for ZPVE differences at the same level (transition states of C_5H_6 isomers are calculated only with the cc-pVDZ basis set due to lack of symmetry).

the **MCB**$^+$ ring-opening it increases to 51.5°. The allenic angle C$_3$-C$_4$-C$_5$ amounts to 162.0° at the TS before it increases to 180° at **VIA**$^+$.

On calculating the thermochemistry of the ring-forming process leading from *Z*-**VIA**$^+$ to **CPD**$^+$ an intermediate minimum on the potential energy surface, called pentadienylidene radical cation, **PDY**$^+$, was found. Its structure is very close to that of **CPD**$^+$ but the energy is 21.6 above *Z*-**VIA**$^+$. The barrier for the hydrogen shift leading from *Z*-**VIA**$^+$ to **PDY**$^+$ is 33.6 kcal/mol but the barrier for the ring-closing of **PDY**$^+$ to **CPD**$^+$ is so small that it disappears on ZPVE correction.
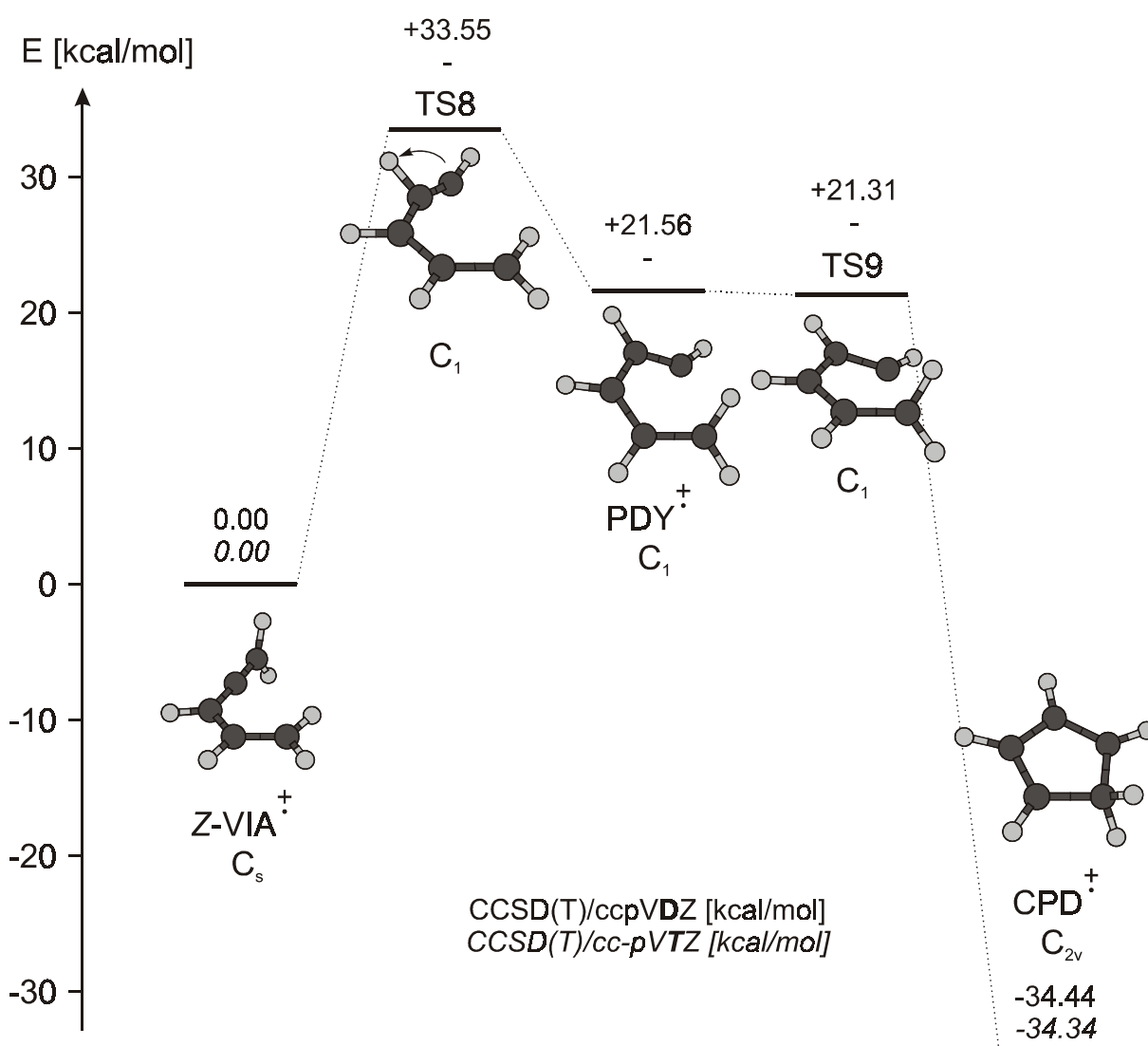

Figure 3-38: Thermochemistry of the ring-closing process of *Z*-**VIA**$^+$ to **CPD**$^+$ via **PDY**$^+$ calculated on CCSD(T)/cc-pVDZ level, corrected for ZPVE differences at the B3LYP/6-31G* level (*Z*-**VIA**$^+$ and **CPD**$^+$ are calculated also with the cc-pVTZ basis set).

3.9 Further photolyses of ionized PRP, DMC, and VCP

As we have shown through experiments with **MCB** and **VIA** the bands at 311 and 486 nm which appear on radiolysis of **PRP**, **DMC** and **VCP** are absorptions of **VIA$^{+\cdot}$**. It is evident that **VIA$^{+\cdot}$** cannot only be bleached if formed from **VIA** or **MCB** and therefore we performed a similar sequence of photolyses also on the other ionized C$_5$H$_6$ isomers.

The strong similarity between the UV/Vis spectra of ionized **VIA, MCB, PRP** and **DMC** leads to the expectation that they should also behave similarly on further photolyses, which is actually the case, as it is documented in Figure 3-39. But interestingly also **VCP$^{+\cdot}$** behaves very similarly. Long photolysis at >515 nm of ionized **DMC** and **VCP** and a shorter one at >475 nm in **PRP** all led to the decrease of a broad band at 350 nm and to an increase of the set of three bands at 407, 394 and 384 nm and of a band at 277 nm. These four increasing bands behave similarly in all the experiments and are therefore assigned to an unidentified species **A**. This species was already quite prominent after ionization of **VPC** and increases more on photolyses at >515 nm or >475 nm, respectively. Also **VIA$^{+\cdot}$** increases, especially in **DMC$^{+\cdot}$** and **VCP$^{+\cdot}$**.

On subsequent irradiation at >475 nm in **DMC$^{+\cdot}$** and **VCP$^{+\cdot}$** the bands of **VIA$^{+\cdot}$** and **A** decrease while the bands of **CPD$^{+\cdot}$** increase. In the experiment with **VCP** we changed the cut-off filter to >420 nm after 5 h, and this accelerated the bleaching of **A** and **VIA$^{+\cdot}$** as well as the formation of **CPD$^{+\cdot}$**. In the experiment with **DMC** we carried out exhaustive irradiation with the >475 nm filter (15 h). In **PRP$^{+\cdot}$** the photolysis was done already from the beginning at >420 nm but lasted only for 100 minutes.

To identify species **A** it would be very important to know whether **CPD$^{+\cdot}$** is formed from **A** or from **VIA$^{+\cdot}$**. Unfortunately, it is not easy to answer this question because **A** and **VIA$^{+\cdot}$** increase and decrease almost simultaneously in the experiments with **DMC**, **PRP**, and **VCP**. It could therefore be that **CPD$^{+\cdot}$** is formed from *both* **A** *and* **VIA$^{+\cdot}$**. The fact that **A** is not formed at all from **MCB$^{+\cdot}$** or from **VIA$^{+\cdot}$**, and the parallel behavior of **A** and **VIA$^{+\cdot}$** on irradiation, leads to the conclusion that the formation of **CPD$^{+\cdot}$** from **A** and from **VIA$^{+\cdot}$** involves two independent processes which are driven by light of similar wavelengths.
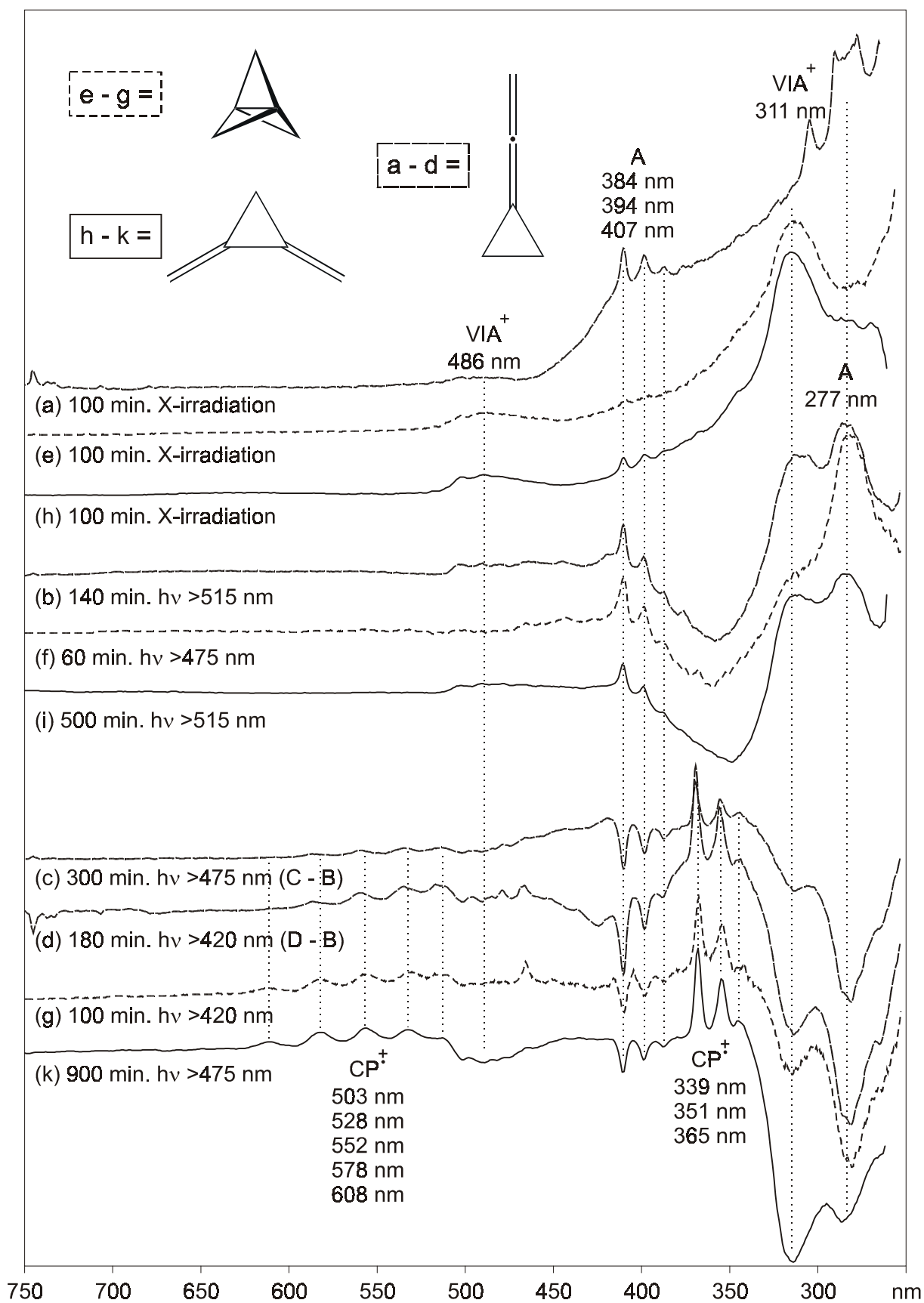
Figure 3-39: EA difference spectra of ionized and photolyzed **VCP** (**a** - **d**), **PRP** (**e** - **g**) and **DMC** (**h** - **k**) in Ar matrix (without spectra after photolysis at >850 nm).
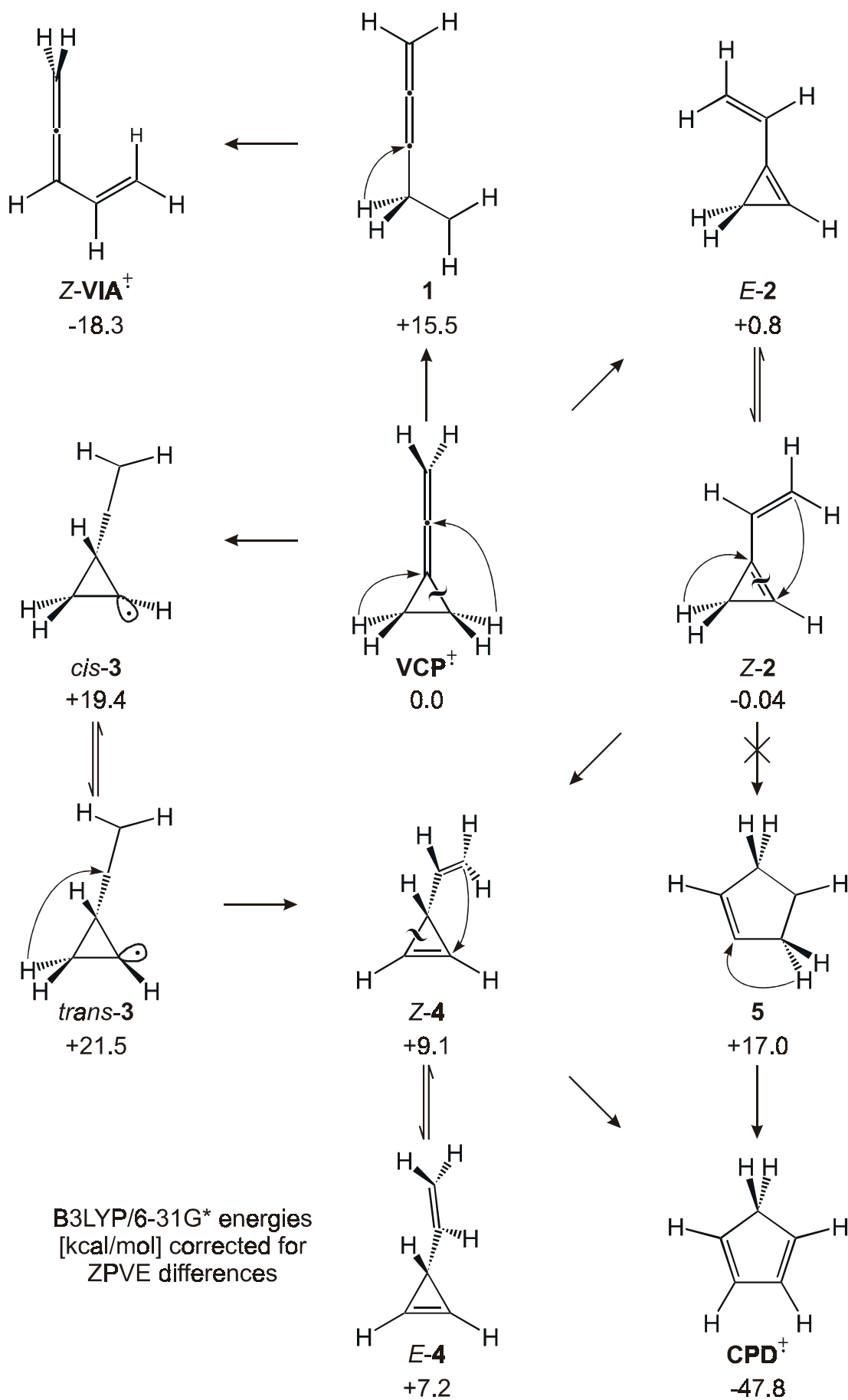
Within the family of C$_5$H$_6$ isomers investigated in this study, two groups of C-H connectivities can be distinguished: **PRP**, **DMC**, and **VCP** (CH$_2$-C-CH$_2$-C-CH$_2$) belong to the first one and **MCB** and **VIA** (CH$_2$-C-CH-CH-CH$_2$) belong to the second one. The first group requires at least two H-shifts to attain the C-H connectivity of **CPD** (CH$_2$-CH-CH-CH-CH) whereas only one single H-shift is needed for members of the second group. **A** could therefore be an intermediate between the first group and **CPD**. Consequently, **A** would have the C-H connectivity of the second group.

Both, **DMC** and **PRP** form **DIA**$^{+\cdot}$ which rearranges to **VCP**$^{+\cdot}$, and ionized **DMC** shows already traces of **VCP**$^{+\cdot}$. Additionally, ionization of **VCP** leads to higher concentrations of **A** than ionization of **PRP** or **DMC**. Therefore, it should be more promising to look for a path from **VCP**$^{+\cdot}$ over a certain radical cation **A** to **CPD**$^{+\cdot}$, including a H-shift during each rearrangement.

The possibilities for rearrangements of **VCP**$^{+\cdot}$ are limited. The rupture of the central bond of the three membered ring leads to **DIA**$^{+\cdot}$ and a lateral bond break leads to a radical cation **1** which on H-shift gives **VIA**$^{+\cdot}$. However, **1** lies 15.5 kcal/mol above **VCP**$^{+\cdot}$ and the H-shift requires an additional 8.8 kcal/mol. Moreover, we end up with **VIA**$^{+\cdot}$, which is not what are we looking for. There must be another rearrangement pathway accessible to **VCP**$^{+\cdot}$.

Since a H-shift from the twisted allenic methylene group of **VCP**$^{+\cdot}$ is not very favorable, a H atom of the cyclopropane ring would have to move to one of the quaternary C atoms. Spin and charge of **VCP**$^{+\cdot}$ are distributed over the three allenic C atoms and it is therefore not apparent which of the two quaternary C atoms is the most "attractive" one for a H atom.

Moving a hydrogen atom from the ring to the central allenic carbon results in 1-vinylcyclopropene radical cation, **2**, which exists in an *E* and a *Z* conformation. They are very close in energy, and also the energy difference to **VCP**$^{+\cdot}$ is less than 1 kcal/mol. One could imagine a ring-closure between the vinyl methylene group and the sp^2 carbon of the cyclopropene. However, to break the cyclopropene double bond is a very unfavorable process and moreover the resulting product **5** lies much too high in energy. But we found two other minima with the same C-H connectivity. One of them, **6**, lies 10.8 kcal/mol and the other, **7**, 13.9 kcal/mol above **VCP**$^{+\cdot}$.

Z-VIA^{+}
-18.3

1
+15.5

E-2
+0.8

cis-**3**
+19.4

VCP^{+}
0.0

Z-2
-0.04

trans-**3**
+21.5

Z-4
+9.1

5
+17.0

B3LYP/6-31G* energies
[kcal/mol] corrected for
ZPVE differences

E-4
+7.2

CPD^{+}
-47.8

Figure 3-40: Possible rearrangements of **VCP^{+}** to **CPD^{+}** on irradiation with light.

Z-2
-0.04

6
+10.8

7
+13.9

CPD‡
-47.8

8
+12.3

9
-7.5

B3LYP/6-31G* energies
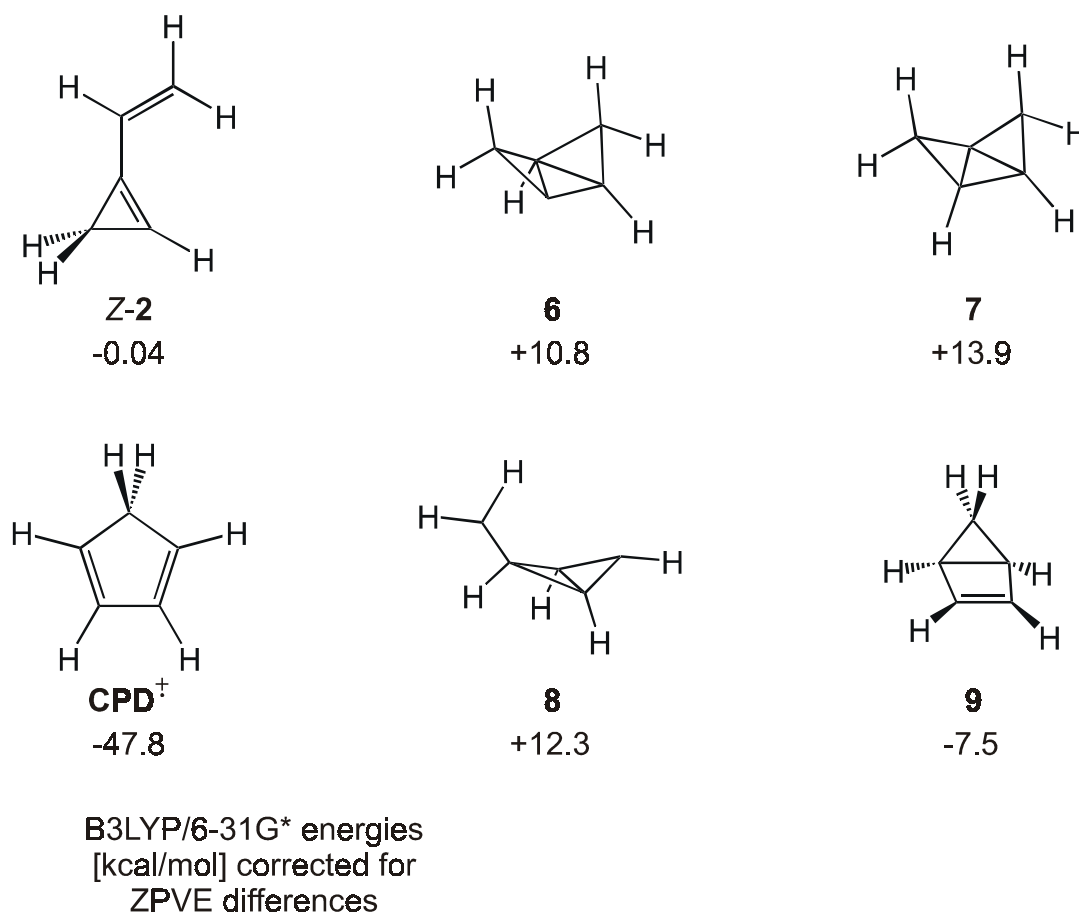[kcal/mol] corrected for
ZPVE differences

Figure 3-41: Further minima of the C-H connectivity of **Z** (**6, 7**) and **CPD**‡ (**8, 9**).

A H-shift of a cyclopropane H of **VCP**‡ to the quaternary cyclopropane C atom results in the strange species **3** where most of the spin is located on the cyclopropane C atom from which the hydrogen has been abstracted. An inversion barrier separates the *cis* from the *trans* conformation which lie 2.1 kcal/mol apart but about 20 kcal/mol above **VCP**‡.

Both, **2** and **3**, can rearrange to vinylcycloprop-2-ene, **4**, which exists also in two conformations *E* and *Z*, 1.9 kcal/mol apart and about 8 kcal/mol above **VCP**‡. **4** has the same C-H connectivity as **CPD** and a ring-closure to **CPD**‡, which is exothermic by 56.9 kcal/mol, should not have a high barrier. However, the search of a transition state between **Z-4** and **CPD**‡ revealed two other minima on the C_5H_6 potential energy surface. One is methylenebicyclobutylidene‡, **8**, which lies 12.3 kcal/mol *above* **VCP**‡ and the other is bicyclopentene, **9**, lying 7.5 kcal/mol *below* **VCP**‡.
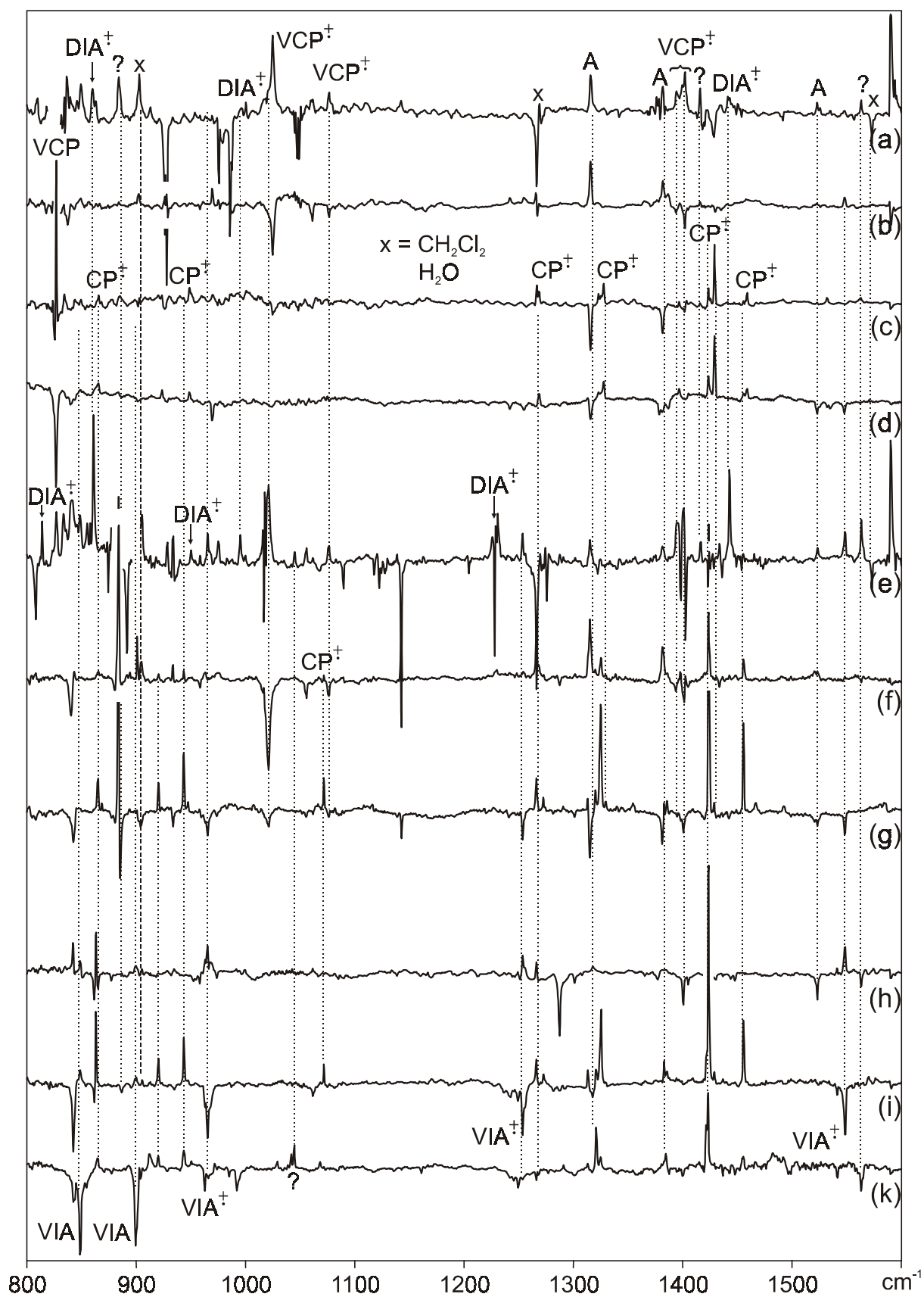
Figure 3-42: IR difference spectra of **VCP** (**a-d**, X-irrad., >515, >475, >420 nm), **DMC** (**e-g**, X-irrad., >475, >420 nm), **MCB** (**h**, **i**, >590, >475 nm) and **VIA** (**k**, >420 nm) in Ar matrix.

The bands of **CPD**$^{+\cdot}$ are also well visible in the IR spectra. Some of them were already seen in the experiment with **MCB**. Some peaks in the IR spectra behave like **A** in the EA spectra and therefore they can be attributed to this species (see Figure 3-42). Additionally to the peaks shown in Figure 3-42, we observed from **CPD**$^{+\cdot}$ also peaks at 612, 2885, and 2901 cm^{-1}, and around 1925 cm^{-1} a peak behaves like one of **A**. There are still many peaks which we cannot attribute. The most intense of them are at 836, 1044, 1415, and at 1563 cm^{-1}.

Table 3-13: Observed IR frequencies of **A**$^{+\cdot}$ and **CPD**$^{+\cdot}$ in Ar matrix.

species	frequency [cm^{-1}]	species	frequency [cm^{-1}]	
A	1315	**CPD**$^{+\cdot}$	612	1325
	1380		866	1423
	1523		944	1456
	1923		1071	2885
	3002		1266	2901

However, we searched also for rearrangements from **DMC**$^{+\cdot}$ to **VIA**$^{+\cdot}$ because we really obtained **VIA**$^{+\cdot}$ on ionization of **DMC** and **PRP**. Actually, we found two transition states leading to Z-**VIA**$^{+\cdot}$ which lie, however, very high in energy (the lower one is 28.9 kcal/mol above **DMC**$^{+\cdot}$). It is therefore possible that there is another way for **DMC**$^{+\cdot}$ to undergo ring-opening and to perform a H-shift to reach the structure of Z-**VIA**$^{+\cdot}$.

Figure 3-44 shows a summarizing scheme of the rearrangements leading from **PRP**$^{+\cdot}$ to **CPD**$^{+\cdot}$ with relative energies of the minima based on CCSD(T)/cc-pVTZ energies which are calculated at the B3LYP/6-31G* optimized geometries and which are corrected for ZPVE differences at the same level. Structures in brackets are transition states and dotted arrows denote that the radical cations take probably a different way than described.
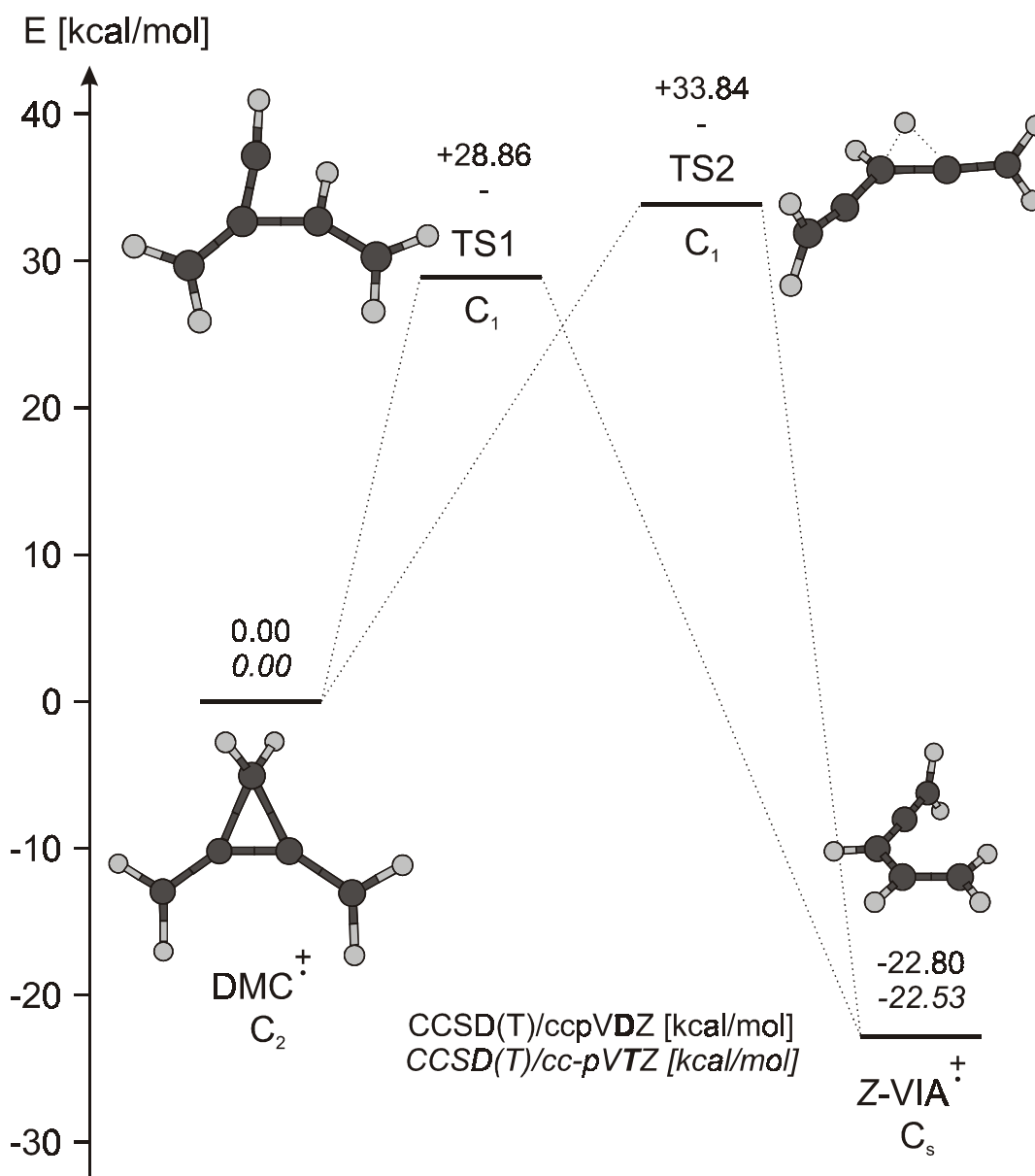
Figure 3-43: Thermochemistry of the ring-opening process of **DMC**$^{+\cdot}$ to *Z*-**VIA**$^{+\cdot}$ over two different transition states calculated on CCSD(T)/cc-pVTZ level, corrected for ZPVE differences at B3LYP/6-31G* level (transition states are calculated with the cc-pVDZ basis set).
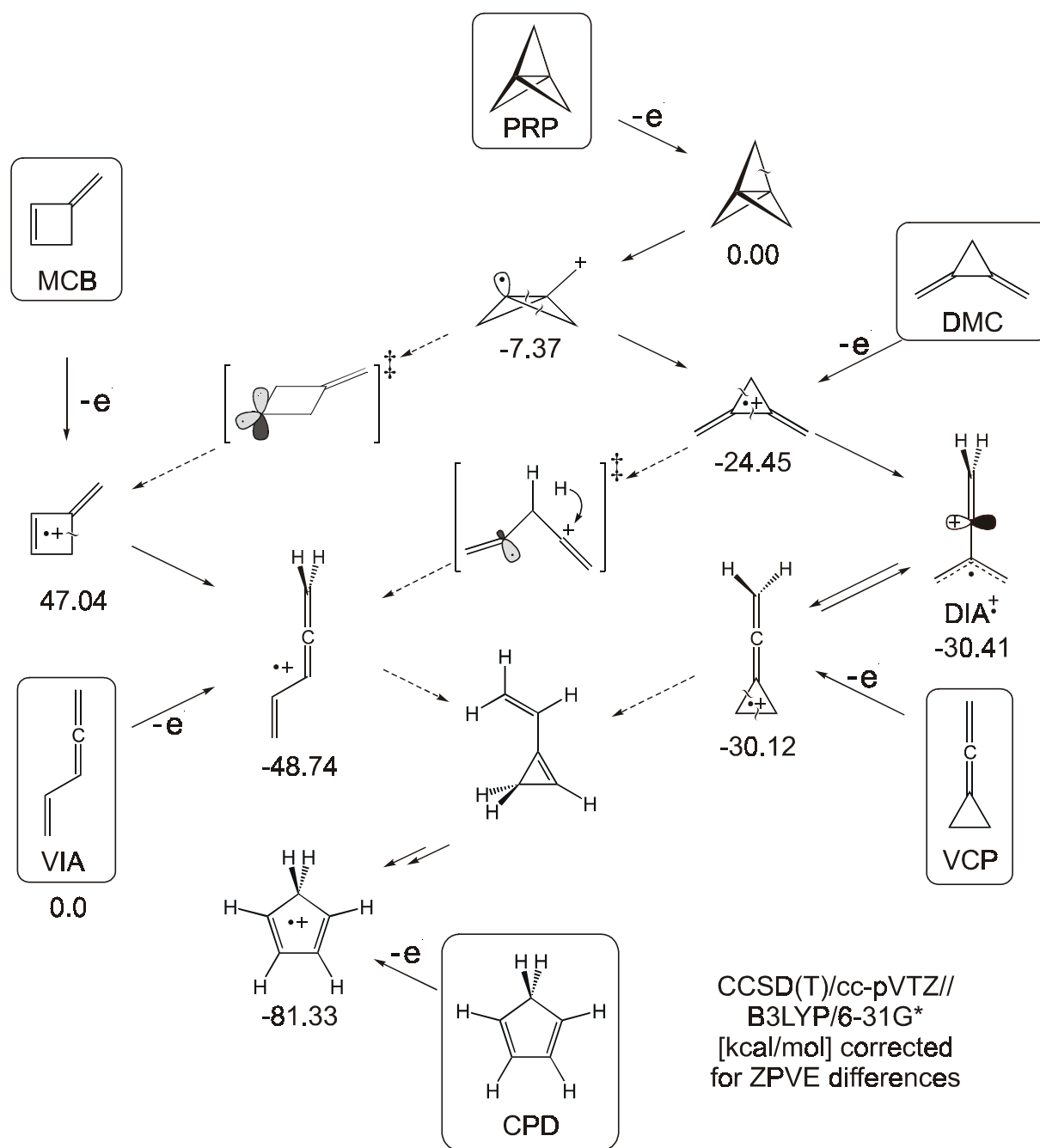
Figure 3-44: Rearrangement paths of ionized **PRP** and other C$_5$H$_6$ isomers.

3.10 Syntheses of C$_5$H$_6$ isomers

3.10.1 Propellane

The first synthesis of [1.1.1]propellane (**PRP**) had been achieved by Wiberg in 1982. They elaborated a way to synthesize this compound in 7 steps. In 1985 Szeimies found a very elegant route to **PRP** in a single step starting from 1,1-di-bromo-2,2-bis-(chloromethyl)-cyclopropane[17] (**2**) and methyllithium (see Figure 3-45). However, this reaction has to be carried out in diethyl ether and it is therefore not possible to extract the product from the solvent. So the two C atoms of the central bond have to be oxidized with iodine to 1,3-diiodobi-cyclo[1.1.1]pentane, **3**, which can easily be crystallized and stored for long time in the refrigerator. The reduction back to **PRP** is effected by slow addition of NaCN in DMSO under vacuum. The product can be trapped by two cooling traps of which the first one is cooled to -10°C to trap DMSO and the second is cooled at 77 K to trap **PRP**. This synthesis has an overall yield of 14%, i.e., 10 g of 1,1-dibromo-2,2-bis-(chloromethyl)-cyclopropane yield 0.3 g of **PRP**.
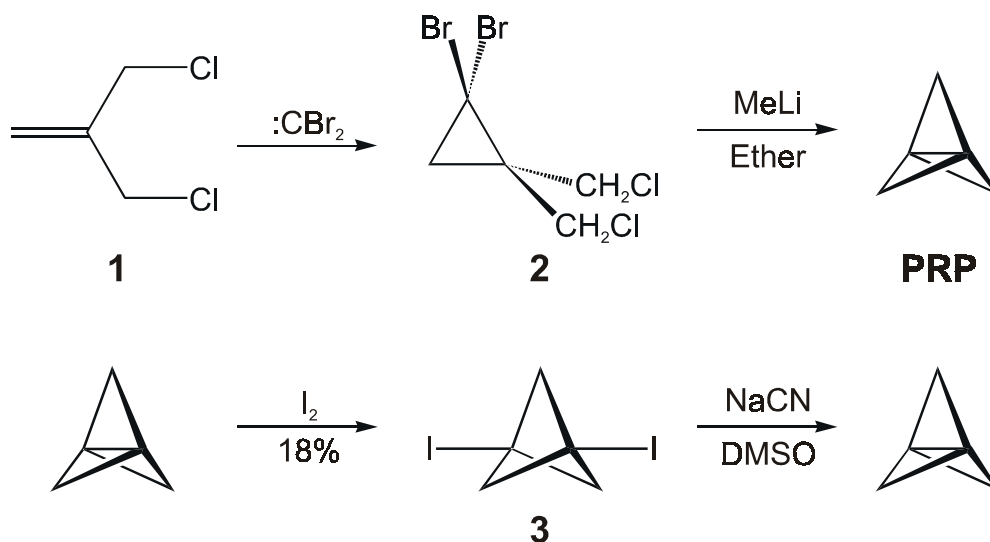

Figure 3-45: Synthesis of **PRP** by Szeimies.

1,3-Diiodobicyclo[1.1.1]pentane (3) [69]. To a septum-capped 250-ml flask containing a magnetic stirring bar 10.0 g of **2** are added. The system is purged

---

with nitrogen and cooled to -78°C with a dry ice/acetone bath. Over a period of 20 - 30 min. 70 ml of 1.4 M methyllithium in ether is injected. The cooling bath is removed and the mixture is stirred for 1 hour. The septum is replaced with a vacuum-line adapter and the ethereal propellane solution is transferred under vacuum to a flask cooled with liquid nitrogen. After warming the flask to -10°C and fitting it with a dropping funnel containing 5.11 g of I$_2$ (based on an estimated propellane yield of 60%) in 210 ml of pentane/ether (5:1) are added dropwise under stirring. After half of the iodine solution has been added, the yellow solution is warmed to room temperature and stirred until it turns clear. The solvent and excess propellane were then distilled under vacuum into a liquid nitrogen cooled trap leaving behind crude **3**. The transferred propellane/ether mixture is warmed to -10°C and the remaining iodine solution is added dropwise until the color change due to excess iodine becomes permanent or until all of the iodine solution is consumed. If the reaction mixture does become permanently discolored, the solution is washed with aqueous sodium thiosulfate to remove the excess iodine and dried with MgSO$_4$. The solvent is removed in vacuum, and the remaining crude **3** is purified by dissolving the crystals in pentane, gravity filtering (if necessary) which eliminates any slight yellowish discoloration, and then the solvent is removed on a rotatory evaporator. The total yield of pure **3** obtained in this way was about 2.5 g. - **^{1}H NMR** (CDCl$_3$): δ = 2.65 (s, **6H**).

The above method for preparation of **3** was found to be superior to Wiberg's method of adding the appropriate amount of I$_2$ crystals directly to the crude propellane solution. When this method was employed, complications arose during the purification process due to solubility problems of the I$_2$ in the relatively small amount of ether.

[1.1.1]Propellane (1) [70, 71]. Propellane can be directly obtained from the crude ether solution of the first reaction by preparative GC. But a better method of preparing solvent free propellane was employed upon learning of the recent communication of by Szeimies et al. [70], and the procedure described therein was modified as follows: A special apparatus was designed and constructed specifically for the execution of this reaction in the most efficient manner. Because of the high propensity of **1** to react with electrophiles, all glassware which would come in contact with propellane was washed first by inserting it for 24 h into a solution of 30 g KOH, 30 ml H$_2$O, and 250 ml EtOH, rinsing it

with distilled water, inserting it for several hours in concentrated ammonia solution, rinsing it with distilled, slightly basic water and drying it carefully.

150 mg **3** are placed in flask **B** along with 2 ml of DMSO. The side-arm at **A** is then charged with 51 mg of NaCN and attached to the ground glass joint of the reaction flask as shown in Figure 3-46.
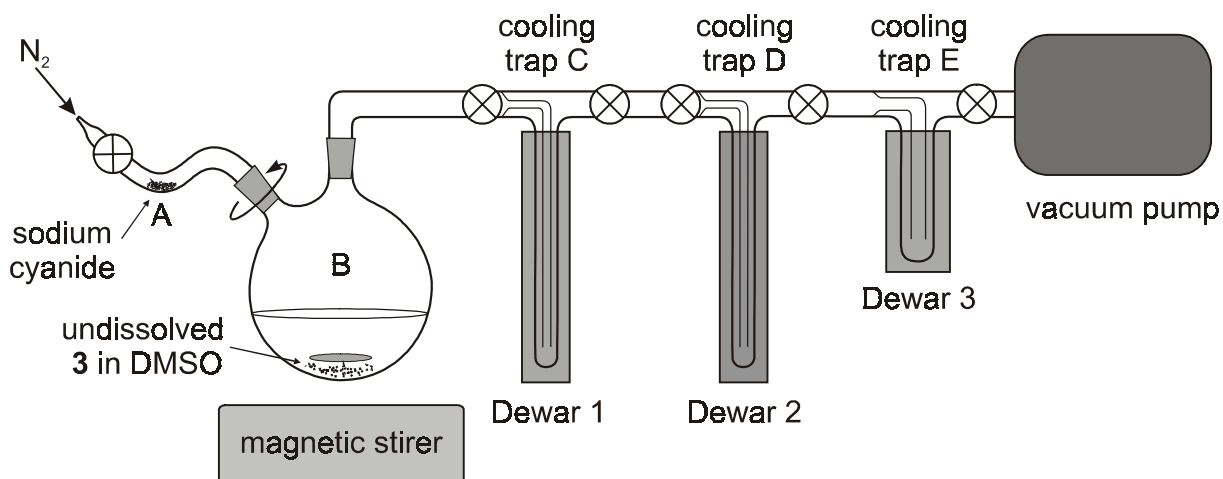
Figure 3-46: Reaction apparatus for preparation of solvent free **PRP**.

A line of traps **C** - **E** linked to a vacuum line are connected to flask **B**, and the system is evacuated after rinsing it with nitrogen through the stopcock at **A**. An ice-salt bath (-20°C) is placed around trap **C** (Dewar 1) and a dry ice acetone bath (-78°C) around trap **D** (Dewar 2). The stopcock is opened and the remainder of the system is evacuated. A liquid nitrogen filled Dewar (3) is then positioned around the final collection trap **E** and the side-arm at **A** is then slowly turned up, admitting the NaCN into the reaction flask **B** over a period of 5 minutes. The magnetic stirrer is activated whereupon propellane begins to collect immediately in the liquid nitrogen trap. The reaction is complete after about 90 minutes, at which time no more propellane can be seen collecting in the trap. Pure propellane condenses at liquid nitrogen temperature as a white, powdery solid, and can be stored for a few days at -78°C without considerable decomposition if the trap is carefully pretreated to remove electrophiles prior to storage. - ^{1}**H NMR** (CDCl$_3$): δ = 2.65 (s, **6H**).

The IR-spectrum of **PRP** obtained by our experiments matches very well with that measured by Wiberg in a 15 K matrix. The frequencies calculated with

B3LYP/6-31G* and scaled by 0.97 also match quite well with the experiment, as it can be seen in Figure 3-47.
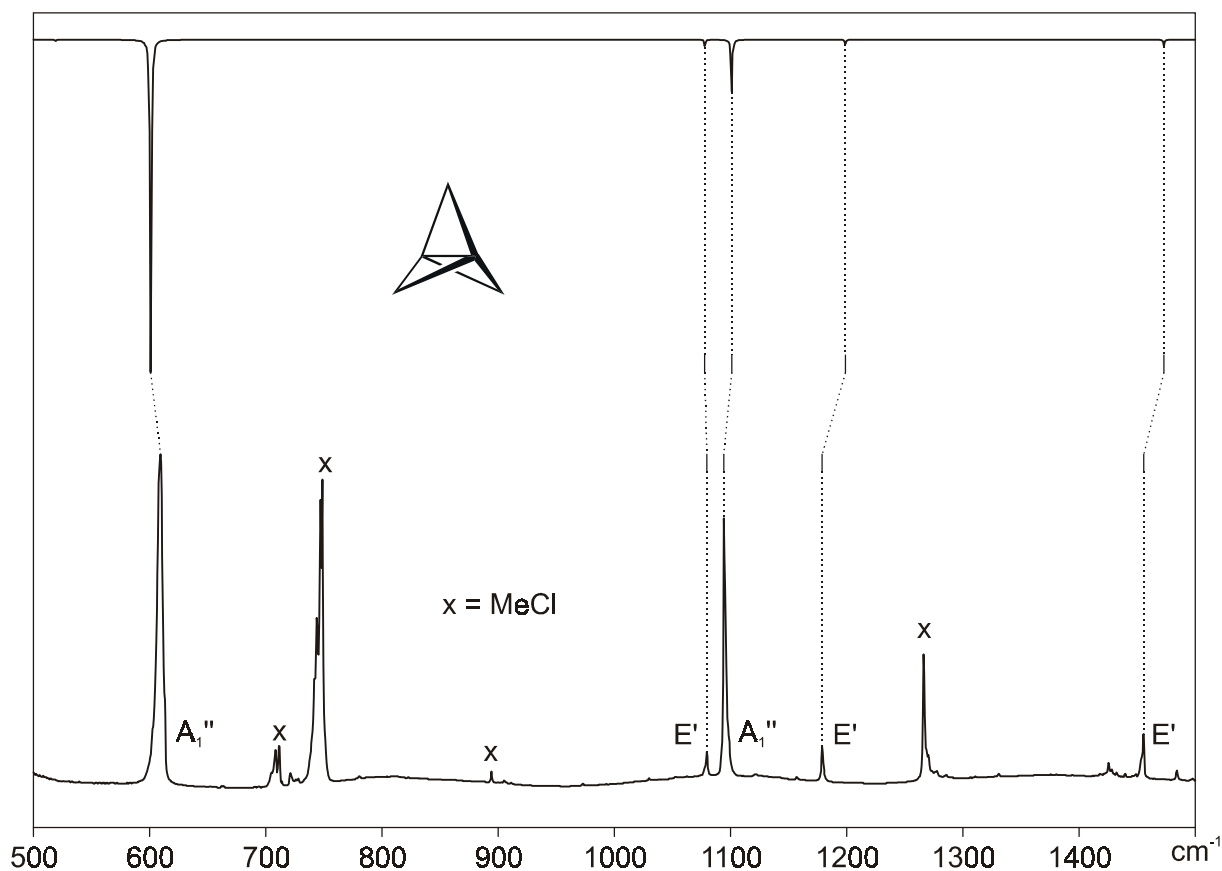
Figure 3-47: IR spectrum of **PRP** in 12 K Ar matrix and simulated spectrum based on a B3LYP/6-31G* force field calculation.

3.10.2 Vinylidenecyclopropane

In 1986 Szeimies reported that, at 430°C, **PRP** isomerizes to **DMC** as the sole product in a flow pyrolysis system [72]. However, much of the experimental detail is omitted from this communication and these results could not be reproduced as reported. In our hands, flow pyrolysis of **PRP** within 400 - 600°C always yielded a combination of **DMC** and **VCP**, in addition to unreacted **PRP**. This product mixture is not surprising in the light of the results reported by Conia in 1970 [73] describing a thermal equilibrium between **VCP** and **DMC** at 320°C. A plausible mechanism for the thermal transformation is depicted in Figure 3-48.
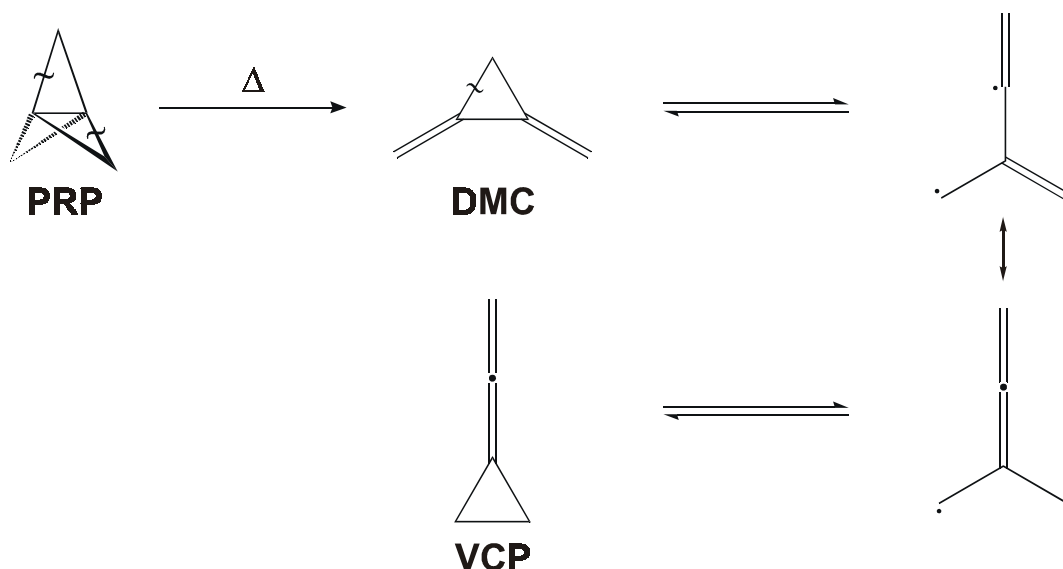
Figure 3-48: Suggested mechanism for the thermolysis of **PRP** and the subsequent thermal equilibrium between **DMC** and **VCP**.

The product ratio of the thermal reaction is apparently dependent both upon the temperature and the flow rate (pressure). Higher temperatures reduce the probability that propellane survives the pyrolysis, but they tend to give rise to increased production of secondary decomposition products. Slower flow rates seem to minimize the formation of **VCP** from **DMC**. According to Conia [73] these two isomers are in a thermodynamical equilibrium. CCSD(T)/cc-pVTZ calculations, corrected at the B3LYP/6-31G* level to give Gibbs free energies result in ΔG^{298K} 2.05 kcal/mol in favor of **DMC**. On the basis of these predictions the ratio of **DMC** to **VCP** should be 9:1 at 450°C. Accordingly, the parameters of the pyrolysis must be adjusted depending the desired product. The experimental setup for the thermolysis is shown in Figure 3-49.

For maximal production of **VCP**, the furnace is heated to about 450°C and the valve on the propellane container is fully opened because the flow rate is controlled by the temperature of Dewar 1 (~ -75°C). Under such conditions the ratio of **VCP** to **DMC** is approximately 1:1. Pure **VCP** and **DMC** were obtained by preparative GC separation on a 35% ODP column of the reaction mixture diluted in n-pentane with the solvent eluting first, followed by **DMC** and finally **VCP**.

^{1}H NMR (**VCP**, CDCl$_3$): δ = 1.52 (t, **4H**), 4.81 (q, **2H**).
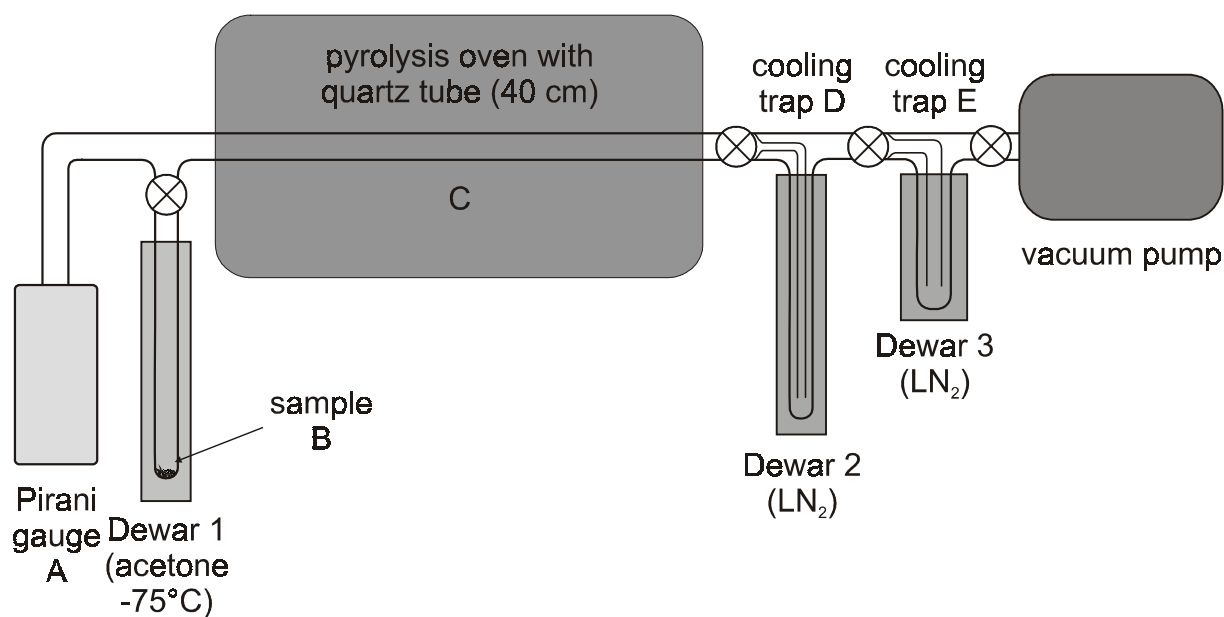
Figure 3-49: Schematics for **PRP** and **VCP** thermolysis.

Since we needed a substantial amount of **VCP** and because the way via **PRP** by pyrolysis is expensive we decided to look for a "wet" method to synthesize **VCP**, and also because we were hoping to obtain more **DMC** by pyrolysis of **VCP**. Actually, Conia [74] had presented in 1970 a synthesis of bicyclopropylidene involving **VCP** as an intermediate. It starts from methylenecyclopropane which itself can be made by dehydrochloration of methallyl chloride, **4**, [75]. The dibromospiropentane, **6**, which is obtained by addition of dibromocarbene to **5** is then reduced by phenyllithium to yield **VCP** [76] (see Figure 3-50).

Potassium amide [77]. A 500-ml three-necked flask equipped with a sealed mechanical stirrer, a dropping funnel, and a gas inlet tube is dipped into a cooling bath of -30°C, and a flux of anhydrous ammonia[18] is introduced through the inlet tube until 250 ml of liquid ammonia are condensed. To the stirred ammonia a small piece of potassium metal is added. After the appearance of a blue color, a few crystals (about 0.12 g) of ferric nitrate hydrate are added, followed by 4.5 g of potassium cut in ~0.5 g pieces, stored under kerosene, and blotted with filter paper before addition.

---

[18] Fluka 09686: 100 ml sFr. 203.20
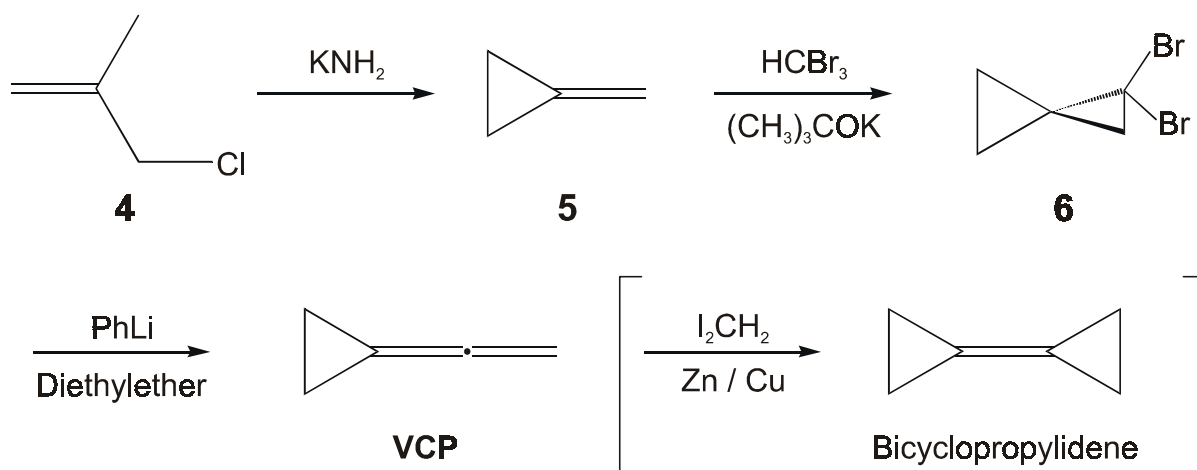
Figure 3-50: Synthesis of **VCP**.

Methlenecyclopropane (5) [75]. After the mechanical stirrer is exchanged by a reflux cooler and the cooling bath is exchanged by an oil bath with a magnetic stirrer, 50 ml of anhydrous tetrahydrofuran is added to the above described KNH_2 solution. The solution is heated to its boiling point and 10 g (0.11 mol) of methallyl chloride[19], **4,** is added dropwise within 10 minutes. Formed **3** and gaseous NH_3 are conducted in an argon flux through 200 ml of a 2.5 M H_2SO_4 solution and collected in a trap cooled to -80°C. Thus, 2 g (34%) of **5** were obtained; GC analysis shows 97% (**3**) and 3% Isobutene.

gem-Dibromospiropentane (6) [76]. A 100-ml three necked flask equipped with a thermometer and a magnetic stirrer is purged with argon. 13.9 g (0.055 mol) of bromoform, 215 mg of benzyltriethylammonium chloride, and 32 ml of methylene chloride are introduced while stirring at room temperature. The mixture is cooled to -10°C at a slight overpressure of argon (balloon). 5 ml (0.067 mol) of **5**, and 13.0 g (0.231 mol) KOH are added sequentially in portions within 5 to 10 min. whereby the solution becomes brown. The cooling bath is removed while stirring under reflux. The mixture starts to react exothermically at about 20°C whereupon the temperature rises to 40°C. After stirring during an additional 25 min, the solution is filtered over celite and washed with pentane. The solvent is evaporated and **6** is purified by fractional distillation at 15 mbar ($bp_{15\ mbar}$: 51-52°C). 8 g (55%) of **6** are obtained as a colorless liquid. n^{20}_D: 1.5413 (Lit.: 1.5430)

---

[19] (3-chloro-2-methyl-1-propene); Fluka 64240: 250 ml sFr. 20.70

Vinylidenecyclopropane (VCP) [76]. 7.8 g (0.035 mol) of **6** and 17 ml of diethyl ether dried over Na/Pb are introduced into a 250-ml three necked flask equipped with a thermometer, a septum, and a dropping funnel, fitted with a bubbler. The solution is cooled to 0°C and 32.3 ml (0.0518 mol) of methyllithium (1.6M in Et$_2$O) are added dropwise within 30 min. whereby the temperature has to be maintained below 15°C. After an additional 20 min. of stirring at 0°C the solution is poured onto 100 ml of ice water and the organic phase is decanted, washed at neutral pH, and dried over MgSO$_4$. The solution which contains ~15% **VCP** is distilled with a 30 cm Vigreux column at atmospheric pressure. 1.0 g (44%) of **VCP** of 90% purity were obtained. Further purification was effected with preparative GC on a 35% ODP column (2m).

^{1}H NMR (CDCl$_3$): δ = 1.52 (t, **4H**), 4.81 (q, **2H**).

The IR spectrum of **VCP** was used to scale a B3LYP/6-31G* force field after transformation into the symmetry adapted combinations of the internal valence coordinates described in Table 3-15 and in Figure 3-51. The resulting frequencies match well with the calculated ones (see Table 3-14). With the scaling constants listed in the rightmost column of Table 3-15, a root mean square deviation between observed and calculated frequencies of 4.92 cm^{-1} was achieved.

Table 3-14: Refined SQM frequencies of **VCP** obtained from a fit over the observed peaks.

nr.	sym.	calc. [cm^{-1}]	obs. [cm^{-1}]	Δ [a] [cm-1]	int. [b] [%]	int.	potential energy distribution [c]
1	a$_1$	3023.0			7.9	7.4	5(99)
2	a$_1$	3005.6	3016.0	-10.0	22.9	21.5	6(99)
3	a$_1$	2038.7	2040.0	-1.3	100.0	93.9	3(56)+4(36)+1(7)
4	a$_1$	1495.4	1493.0	2.9	0.1	0.1	1(25)+4(25)+8(24)+7(15)+3(7)
5	a$_1$	1418.1	1420.0	-1.4	3.5	3.3	7(67)+8(25)
6	a$_1$	1326.0		-4.6	1.3	1.2	8(49)+1(19)+7(15)+4(13)
7	a$_1$	1045.1	1050.0	1.6	11.4	10.7	9(81)+2(17)
8	a$_1$	988.8	987.2	3.0	12.3	11.5	2(64)+3(13)+4(9)+9(8)+1(5)
9	a$_1$	639.1	636.1		9.8	9.2	1(48)+2(21)+3(18)+4(12)
10	a$_2$	3073.2			0.0	0.0	10(99)
11	a$_2$	1141.4			0.0	0.0	13(67)+11(32)
12	a$_2$	897.5			0.0	0.0	11(54)+13(36)+12(10)
13	a$_2$	546.3			0.0	0.0	12(73)+11(18)+13(9)
14	b$_1$	3089.0			8.1	7.6	14(99)
15	b$_1$	3086.0	3075.0	11.3	20.9	19.6	15(99)
16	b$_1$	1052.6			0.6	0.6	20(63)+16(33)
17	b$_1$	986.0			0.1	0.1	17(92)+19(6)
18	b$_1$	742.9			1.0	1.0	16(63)+20(36)
19	b$_1$	366.9			0.0	0.0	19(67)+18(25)+17(6)
20	b$_1$	181.1			3.8	3.6	18(78)+20(11)+19(8)
21	b$_2$	3005.1	3006.0	-1.3	20.7	19.4	22(99)
22	b$_2$	1405.0			0.1	0.1	25(99)
23	b$_2$	1061.0	1061.0	0.0	6.7	6.3	26(96)
24	b$_2$	924.7	928.1	-3.4	13.3	12.5	21(87)+23(9)
25	b$_2$	831.9	827.1	4.8	56.5	53.1	27(97)
26	b$_2$	540.6	539.6	1.0	0.4	0.4	24(57)+23(35)+21(7)
27	b$_2$	183.1			0.8	0.7	23(56)+24(43)

[a]   RMS deviation of observed from calculated frequencies is 4.92 cm^{-1}.

[b]   Intensities in % of the most intense band at 2040 cm^{-1}.

[c]   Contributions in percent (in parentheses) of the symmetry coordinates listed in Table 3-15.

Table 3-15: Definition of internal and symmetry coordinates of **VCP**, together with their optimized scaling factors.

internal coord.[a]	description	composition	symmetry coord. a_1	a_2	b_1	b_2	scaling factors
R_1	ν(C-C)	$r(C_1-C_2)$	S_1			S_{21}	0.9495
R_2	"	$r(C_1-C_3)$					
R_3	"	$r(C_2-C_3)$	S_2				
R_4	ν(C=C)	$r(C_1-C_4)$	S_3				0.9212
R_5	"	$r(C_4-C_5)$	S_4				
R_6	ν(C-H)	$r(C_5-H_6)$	S_5		S_{14}		0.9261
R_7	"	$r(C_5-H_7)$					
R_8	"	$r(C_2-H_8)$					
R_9	"	$r(C_3-H_9)$	S_6	S_{10}	S_{15}	S_{22}	
R_{10}	"	$r(C_2-H_{10})$					
R_{11}	"	$r(C_3-H_{11})$					
R_{12}	ρ(C=C(C_2H_4))	$\beta_1-\gamma_1$				S_{23}	0.8987
R_{13}	δ(C=C=C)$_{ip}$	$\beta_4-\gamma_4$				S_{24}	
R_{14}	σ(CH$_2$)	$2\delta_2-\beta_2-\gamma_2$	S_7			S_{25}	
R_{15}	"	$2\delta_3-\beta_3-\gamma_3$					
R_{16}	"	$2\delta_5-\beta_5-\gamma_5$	S_8				
R_{17}	ω(CH$_2$)	$\varepsilon_{1-2,8,10}$	S_9			S_{26}	0.9648
R_{18}	"	$\varepsilon_{1-3,9,11}$					
R_{19}	"	$\varepsilon_{4-5,6,7}$				S_{27}	
R_{20}	ρ(CH$_2$)	$\beta_2-\gamma_2$		S_{11}	S_{16}		0.8987
R_{21}	"	$\beta_3-\gamma_3$					
R_{22}	"	$\beta_5-\gamma_5$			S_{17}		
R_{23}	ω(C$_2$H$_4$)	$\varepsilon_{4-1,2,3}$			S_{18}		0.9500
R_{24}	δ(C=C=C)$_{oop}$	$\beta_4'-\gamma_4'$			S_{19}		
R_{25}	τ(C=C)	$\tau_1(C_5H_{6,7})$		S_{12}			
R_{26}	τ(ring)	$\tau_2(C_2H_{8,10})$		S_{13}	S_{20}		
R_{27}	"	$\tau_1(C_3H_{9,11})$					

[a] see Figure 1-51, except for wagging coordinate $e_{i-j,k,l}$ which are defined as atom i moving out of the plane defined by atoms j,k, and l.

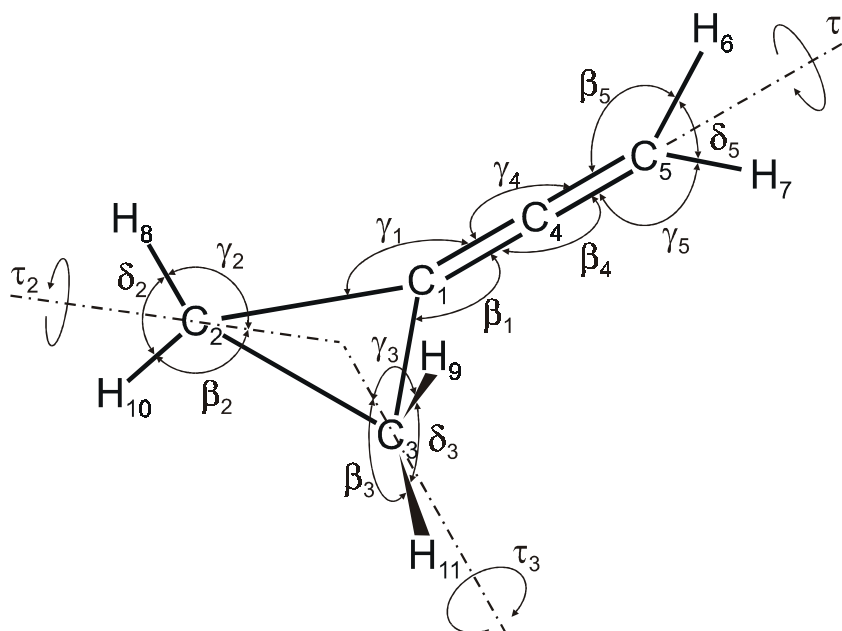[b] $\beta_4'-\gamma_4'$ is perpendicular to $\beta_4-\gamma_4$.

Figure 3-51: Internal coordinates of **VCP** (the wagging coordinates ε are not shown).

3.10.3 Dimethylenecyclopropane

As described in the previous section, **VCP** and **DMC** are in thermal equilibrium at 320°C [73]. To obtain **DMC**, **VCP** was pyrolyzed at 500°C using the apparatus shown in Figure 3-49. The pressure of **VCP** was controlled by the temperature of the acetone cooling bath and was kept at 0.1 mbar. (Initially, the acetone bath has about -80°C, then the temperature is raised to -75°C by stirring the bath, which leads to a pressure of 0.1 mbar. Then the bath is covered and the magnetic stirrer is switched off. After about 90 min. the bath has to be cooled down again.) The 40 cm quartz tube in the pyrolysis oven is empty. To obtain about 0.2 ml of product one has to conduct the pyrolysis during 6 h. The mixture is separated by preparative GC on a 2 m column of 35% ODP on chromosorb. The temperature of the column is 35°C and that of the injector is 100°C. Not more than 50 μl are injected each time to obtain a good separation. The first peak in the chromatogram is **DMC** and the second is unreacted **VCP** which can be recovered to perform another pyrolysis.

[1]**H NMR** (**DMC**, CDCl$_3$): δ = 1.58 (m, **2H**), 5.31 (m, **2H**), 5.54 (m, **2H**).

3.10.4 Methylenecyclobutene

The synthesis of methylenecyclobutene, **MCB**, requires 6 steps (see Figure 3-52). It starts with 100 g (0.901 mol) of 2,3-dichloro-1-propene[20], **7**, which is dehalogenated with zinc in ethanol at 78°C within 90 min. to yield allene [78, 79] (20.0 g, 55.4%). In the second step 5.3 g (0.132 mol) **8** are condensed with 28 g (0.528 mol) acrylonitrile in an inox steel reactor and heated during 20 h to 190°C [80] to yield 3-methylenecyclobutanecarbonitrile, **9** (6.15 g, 50.0%) which can be purified by fractional vacuum distillation at 41 mbar.
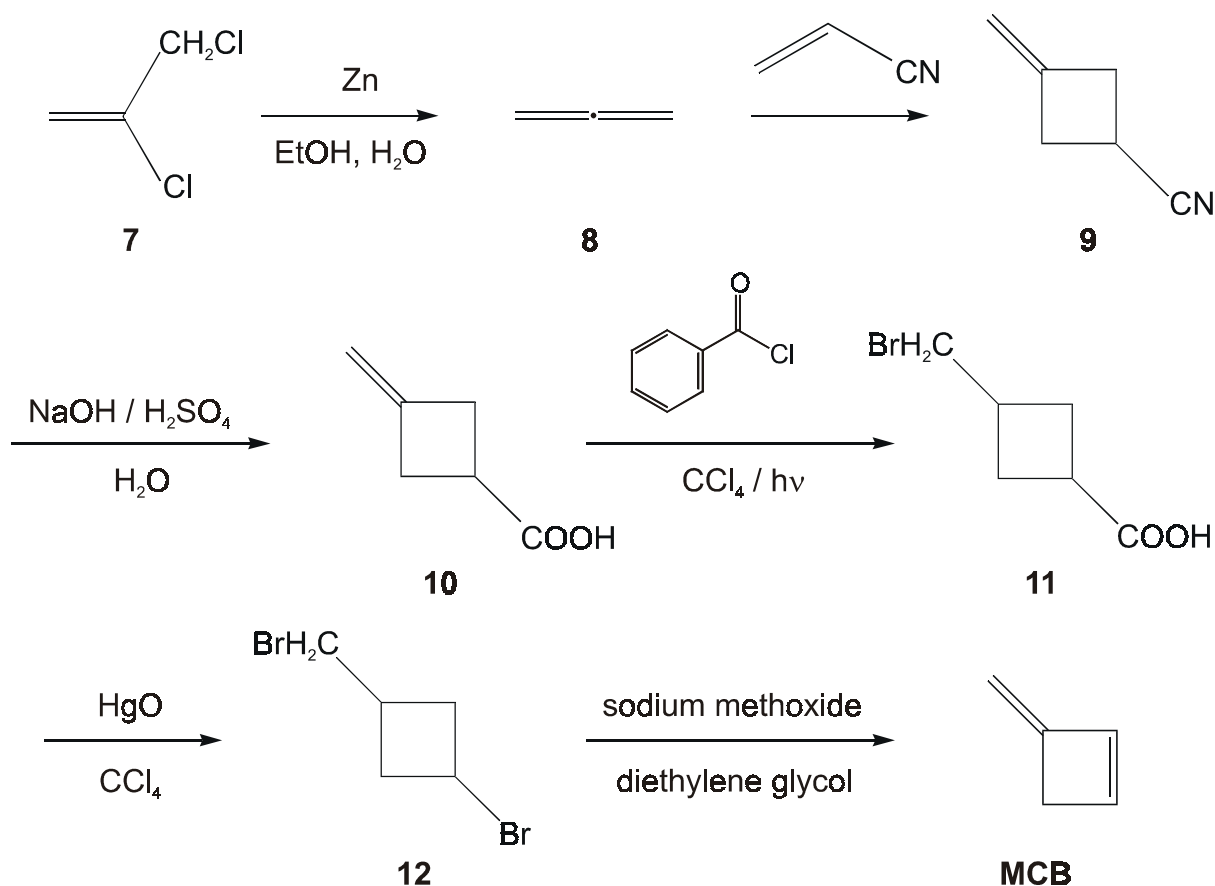

Figure 3-52: Synthesis of **MCB**.
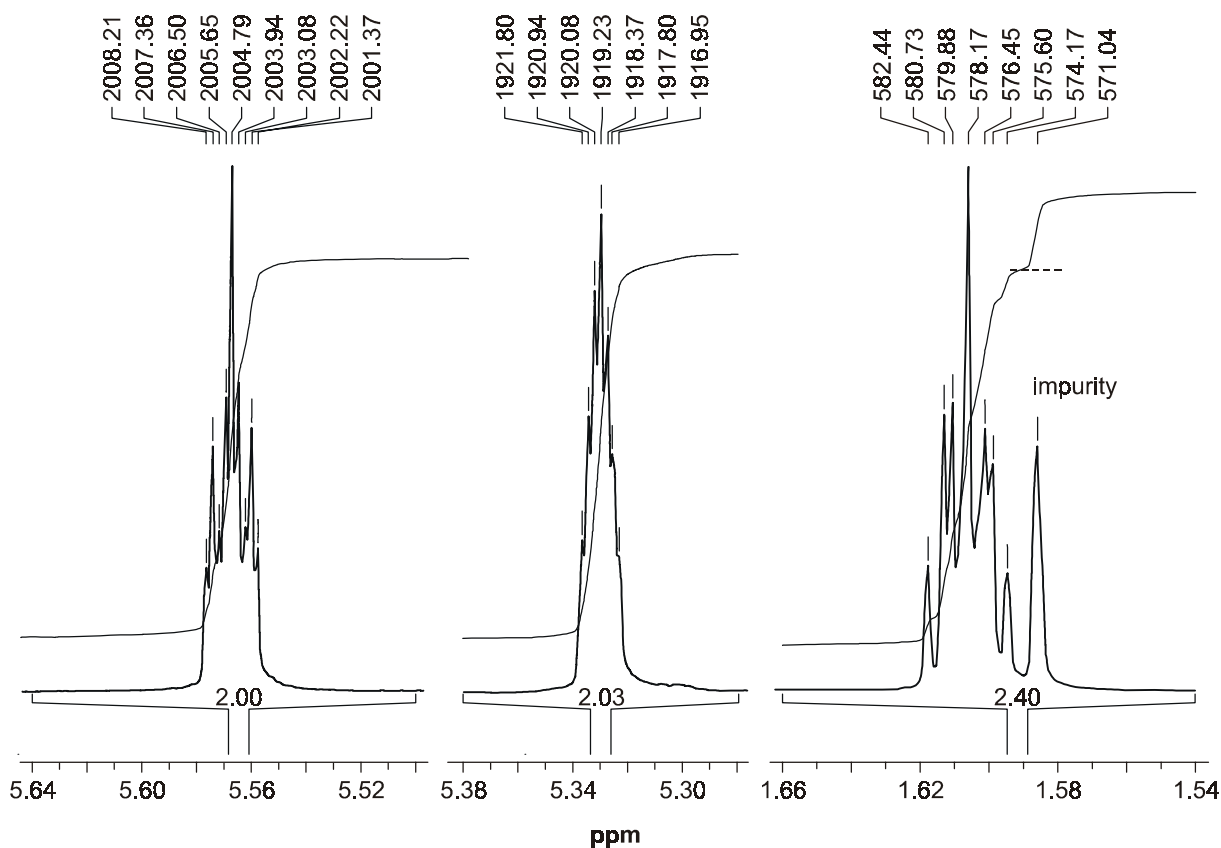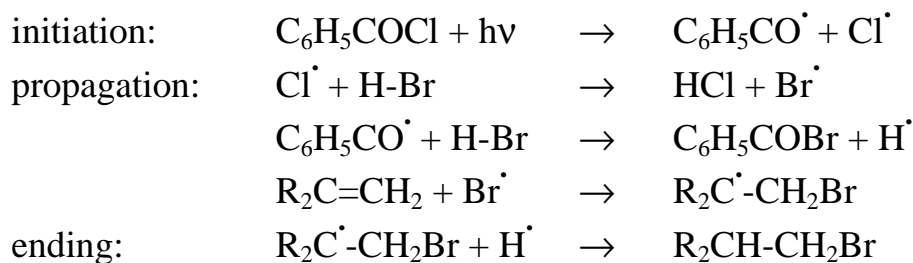
In the third step 6.1 g (0.066 mol) of **9** are hydrolyzed with NaOH to the amide in water at 100°C within 24 h. Then the amide is hydrolyzed with H_2SO_4 in Et_2O under reflux within 50 h to the carboxylic acid which is enriched in the organic phase [81]. We obtain 6.86 g (0.061 mol → 93.5%) of 3-methylene-cyclobutane carboxylic acid, **10**.

---

[20] Fluka 36319: 100 ml sFr. 114.60

Figure 3-53: 360 MHz NMR of **DMC**.

The fourth step is a radical addition of hydrobromic acid (HBr) to the methylene group which is initiated photochemically [82]. Gaseous HBr is slowly injected into a well stirred mixture of 4.8 g (0.043 mol) of the carboxylic acid, **10**, 154 mg benzoyl chloride [83], and 40 ml tetrachloromethane. During 60 min. the solution is exposed to light from a halogen lamp. The absorption of HBr is controlled with two bubblers.

initiation:	C$_6$H$_5$COCl + hν	→	C$_6$H$_5$CO$^\bullet$ + Cl$^\bullet$
propagation:	Cl$^\bullet$ + H-Br	→	HCl + Br$^\bullet$
	C$_6$H$_5$CO$^\bullet$ + H-Br	→	C$_6$H$_5$COBr + H$^\bullet$
	R$_2$C=CH$_2$ + Br$^\bullet$	→	R$_2$C$^\bullet$-CH$_2$Br
ending:	R$_2$C$^\bullet$-CH$_2$Br + H$^\bullet$	→	R$_2$CH-CH$_2$Br

5.4 g (0.028 mol, 65.6%) liquid 3-(bromomethyl)cyclobutane carboxylic acid, **5**, were obtained from this reaction.

In the fifth step of the sequence the carboxylic acid group is exchanged by a bromine atom by reductive decarboxylation with red mercury oxide in tetrachloromethane [82]. A solution of 5.4 g (0.028 mol) of **11** and 5.6 g (0.035 mol) of dimercury bromide in 20 ml CCl$_4$ is added dropwise within 50 min. to a light protected solution of 6.06 g (0.028 mol) of red mercury oxide in 60 ml tetrachloromethane boiling under reflux. The product is stirred for 30 min., filtered on celite, washed with saturated sodium carbonate and with saturated sodium chloride and purified by vacuum distillation at 1 mbar. 2.4 g (0.011 mol, 37.5%) of 3-(bromomethyl)cyclobutylbromide, **12**, were obtained.

The last step is a double dehydrobromination with sodium methoxide in diethylene glycol [84]. 2.54 g (0.047 mol) of sodium methoxide are dissolved in 35 ml diethylene glycol and heated to 170°C at 300 mbar. 2.4 g (0.011 mol) of **12** are introduced in portions with a syringe. The solution is heated and stirred for 40 min. while the product is collected in a cooling trap which is connected between the reaction flask and the vacuum pump. About 300 mg of **MCB** are obtained which are very volatile and show a strong tendency to polymerization.

^{1}H NMR (CDCl$_3$): δ = 2.94 (s, **2H**), 4.43 (s, **1H**), 4.65 (s, **1H**), 6.28 (s, **1H**), 6.62 (d, **1H**).

3.10.5 Vinylallene

The synthesis of vinylallene, **VIA**, can be effected in 4 steps. It starts with a pyrolysis of 11.8 g (0.10 mol) 3-sulfolene [85], **13**, to butadiene, **14**, at 130°C. 5.1 g (94%) of butadiene are obtained (b.p.: -4.5°C).

The next step is an addition of dibromocarbene [86, 87] to **14**, forming 1,1-dibromovinylcyclopropane, **15**. To a stirred solution of 19.5 g (0.36 mol) **14** in 25 ml pentane at -20°C 16.5 g (0.147 mol) potassium tert.-butoxide are added in portions. Then 27.2 ml (0.11 mol) bromoform are added dropwise within 60 min. by keeping the temperature below -10°C. The solution is stirred during 2 h at -10 °C and then warmed to room temperature. Then **15** is extracted with water and pentane and purified by distillation at 20 mbar. 13.3 g (54%) of liquid **15** are obtained.

The third step is a dehalogenation of **15** with methyllithium [88]. 4.52 g (0.02 mol) of **15** are dissolved in 5 ml Et$_2$O and cooled down to -78°C. 15ml (0.024 mol) 1.6 M solution of methyllithium in Et$_2$O is added with a syringe

within 10 minutes. The temperature has to be kept below -30°C. After 30 min. the solution is warmed to room temperature and distilled at 40°C. A mixture of 85% Et$_2$O, 10% bromomethane, 3% cyclopentadiene, **CP**, and 1.5% **VIA** is obtained. Because of the very similar boiling points of the two hydrocarbons, and the very similar retention time in the preparative GC, **CP** has to be removed by Diels-Alder reaction with maleic anhydride which forms 5-norbornene-2,3-carboxylic anhydride (bicyclo[2.2.1]-hept-5-en-2,3-carboxylic anhydride), **16**. For this, 0.98 g (0.010 mol) maleic anhydride are added to the solution. The solution is stirred during 2 h and then purified by fractional distillation between 35° and 43°C. A mixture of 92% Et$_2$O, 7% CH$_3$Br and 1% **VIA** is obtained. The solution can now be separated by preparative GC which leads to 55 mg of pure **VIA**.

^{1}H NMR (CDCl$_3$): δ = 4.88 (m, **2H**), 4.95 (m, **1H**), 4.15 (m, **1H**), 5.80 (m, **1H**), 6.16 (m, **1H**).
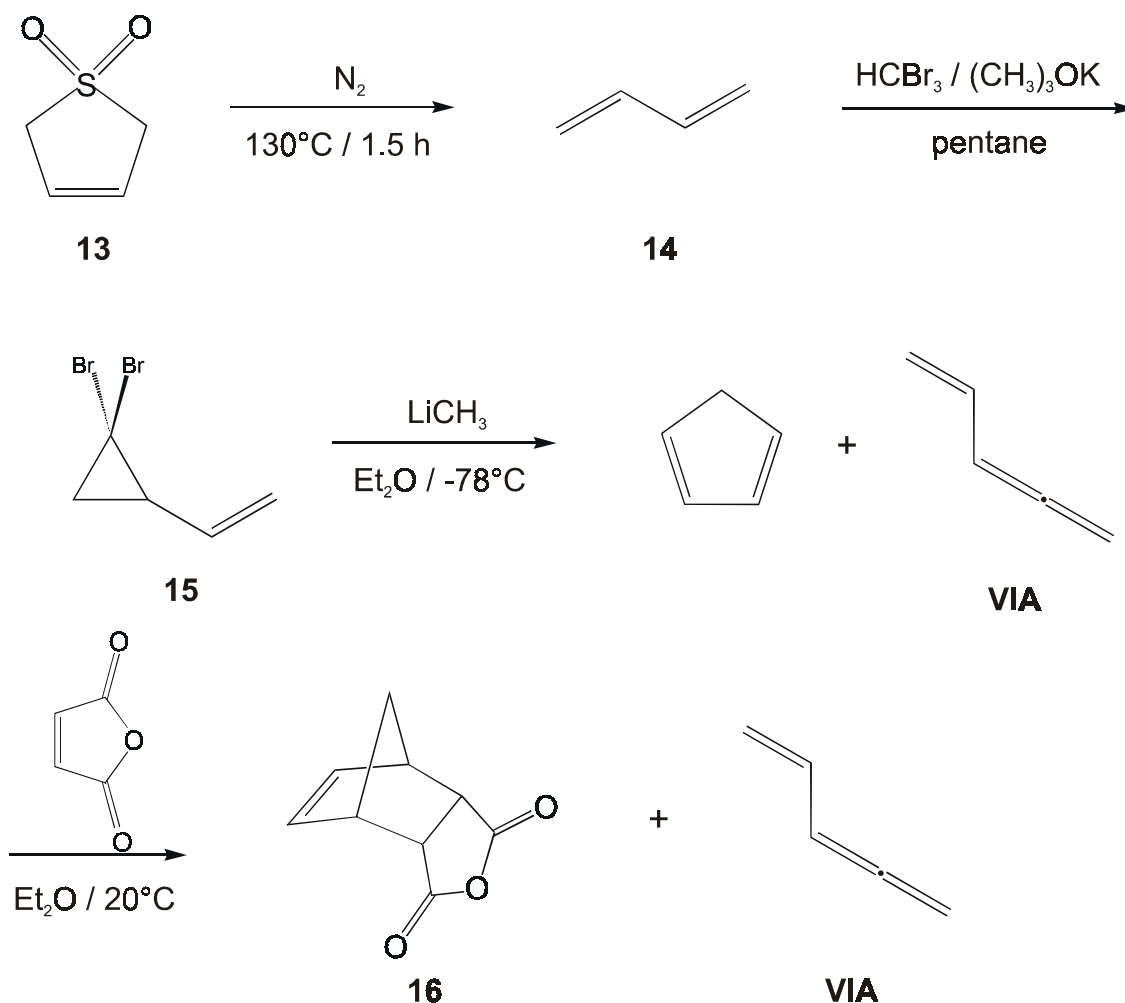

Figure 3-54: Synthesis of **VIA**.

3.11 Conclusion

On ionization of [1.1.1]propellane (**PRP$^{+\cdot}$**) in cryogenic matrices, a photo-labile species with a broad, weak NIR band (λ_{max} = 1440 nm) and an ESR spectrum consisting of a 14.8 G quintet of 5.4 G triplets is formed. On NIR irradiation this species is converted into the radical cation of vinylidenecyclo-propane (**VCP$^{+\cdot}$**), which was generated independently by ionization of **VCP**. The features of the photolabile intermediate are compatible with its assignment to the radical cation of dimethylene allene (**DIA$^{+\cdot}$**) Quantum chemical calculations were carried out to confirm this hypothesis. **DIA$^{+\cdot}$** is also formed on ionization of dimethylenecyclopropane (**DMC**) which suggests that **DMC$^{+\cdot}$** is an intermediate in the formation of **DIA$^{+\cdot}$** from **PRP$^{+\cdot}$**.
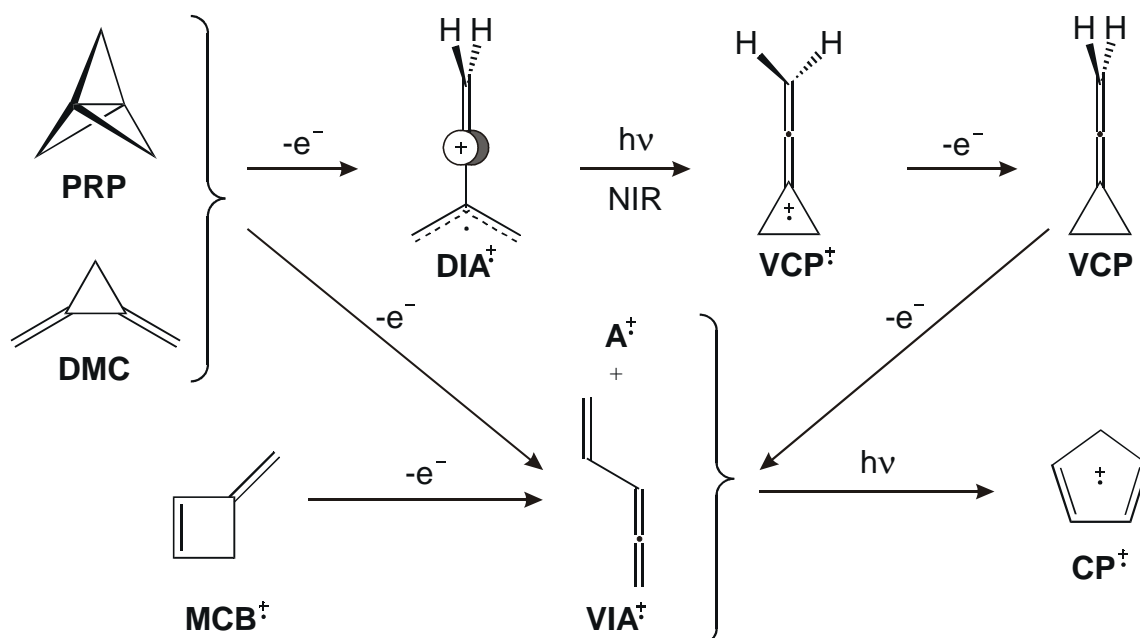
Optical spectra indicate the formation of additional products on ionization of **PRP**, **DMC**, or **VCP** in Freon and Argon matrices, notably the radical cation of vinylallene (**VIA$^{+\cdot}$**), which was also generated independently by ionization of **VIA**. In addition, Argon matrix experiments reveal the presence of another intermediate, **A$^{+\cdot}$**, which can be transformed photochemically into the radical cation of cyclopentadiene (**CP$^{+\cdot}$**). The mechanisms of the above transformations are discussed on the basis of quantum chemical calculations. Intermediate **A** could not be identified but several species which could be responsible for the corresponding spectroscopic manifestations are proposed. Further work will also be needed to elucidate the identification of some other species which were observed during the above transformations.

4. Ionization of Aziridines

4.1 Introduction

Aziridines and their reactions are of great interest due to their synthetic and pharmacological importance [89, 90]. On irradiation or on thermal activation the aziridine ring opens to yield the corresponding azomethine ylid **Y** which can be trapped in [3+2] cycloadditions with various dipolarophiles **A=B**, such as, e. g., dimethylacetylenedicarboxylate, to form nitrogen containing five membered heterocycles [91, 92]. Under photoinduced electron transfer (PET) conditions, aziridines may be oxidized to the corresponding radical cations, which can react in a similar manner [93, 94, 95, 96, 97].
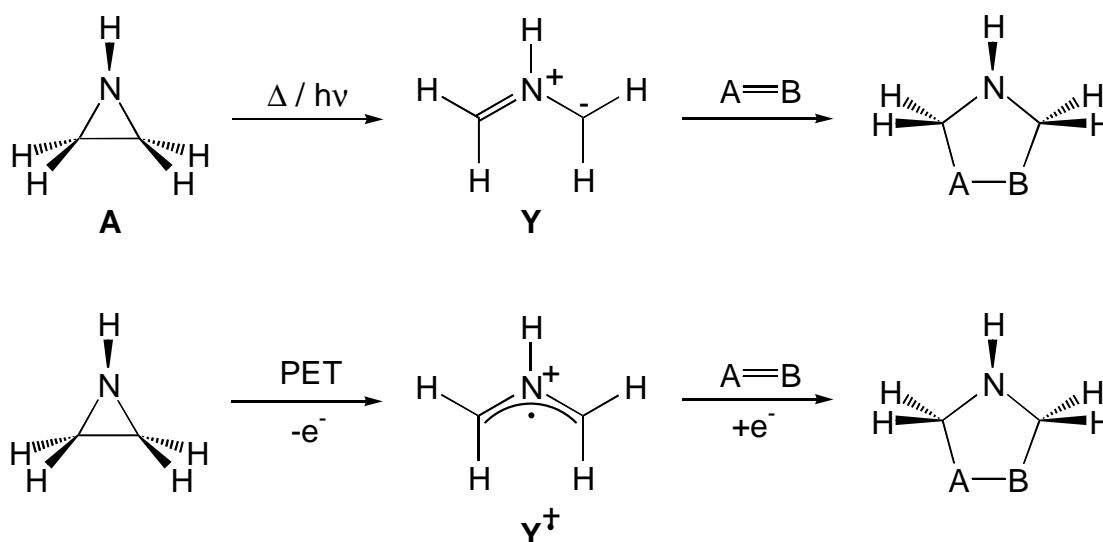
Figure 4-1: [3+2] Cycloaddition; "classical" and under PET conditions.

In the course of investigations by the group of Mattay aimed at applications of aziridines in organic synthesis [95, 98] we became interested in the reactive intermediates of [3+2] cycloadditions, i.e. azomethine ylids and their radical cations. In this study we investigate the aziridine radical cations and their follow-up products using X- and γ-irradiation to produce these intermediates from their neutral aziridine precursors which are embedded in Argon matrices or in Freon glasses.

4.2 Parent aziridine radical cation

4.2.1 Previous work

The photoelectron (PE) spectrum of **A** was measured in 1969 by Basch et al. [99] and again in 1988 by Rademacher et al. [100]. It is shown in Figure 4-2 together with calculated energies of the electronic states of A^{+} at the neutral geometry relative to the ionic ground state. The results of the CASPT2 calculations and the differences of vertical experimental ionization potentials are listed in Table 4-1.
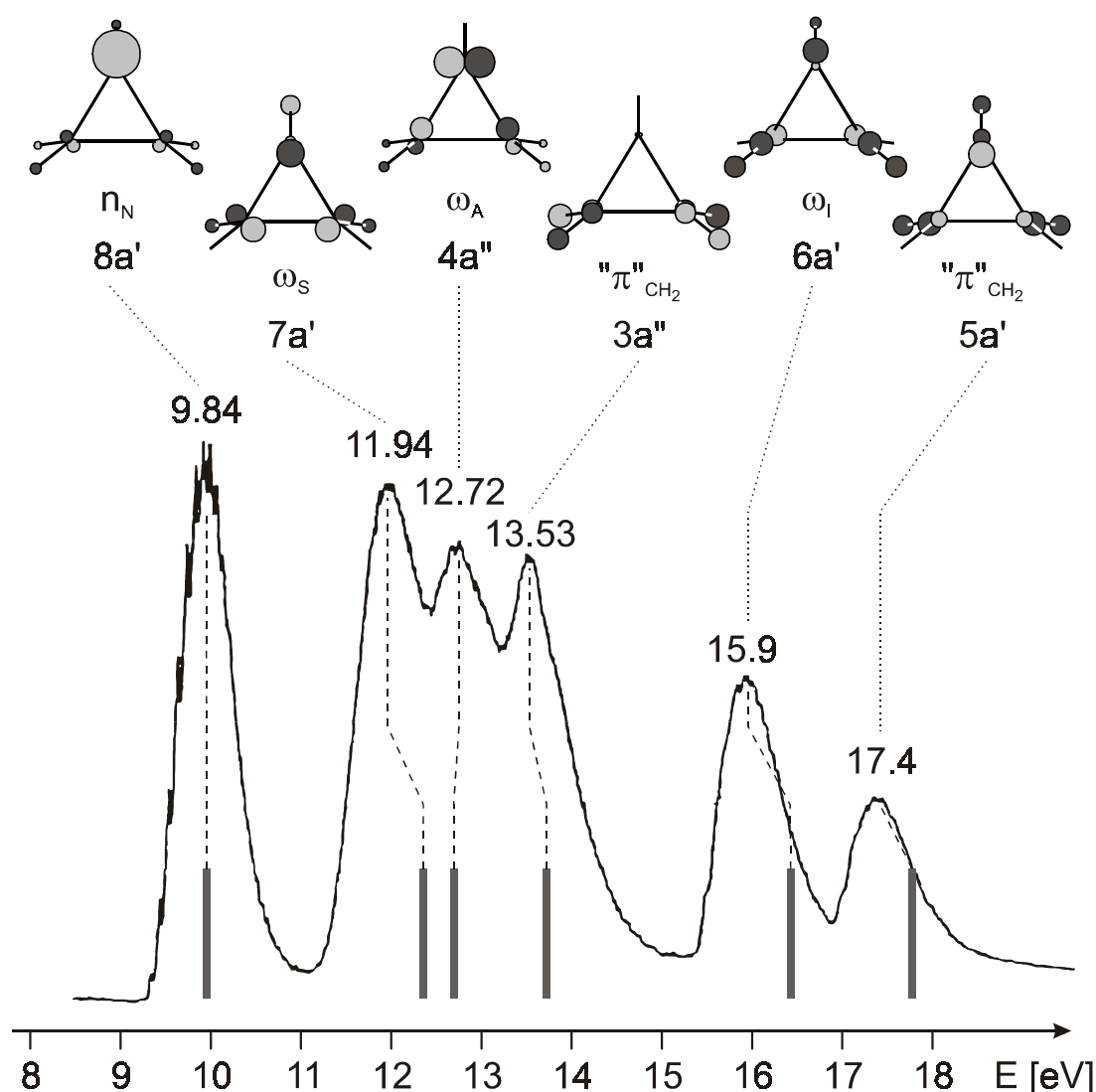

Figure 4-2: PE spectrum of **A** and results of CASPT2 calculations (gray bars). Molecular Orbitals are from a HF calculation on neutral **A**.

The assignment of the PE spectrum had not always been unambiguous: Basch et al. assigned the second band (11.94 eV) to ionization from the anti-symmetric Walsh-type MO (ω_A), based on minimal basis set SCF calculations, whereas Rademacher et al. assigned this band to ionization from the symmetric Walsh MO (ω_S) and the band at 12.72 eV to ionization from the ω_A orbital, based on MNDO calculations.

Table 4-1: Excited states of $\mathbf{A}^{+\cdot}$ at the neutral geometry, as measured by PE spectroscopy and calculated by CASPT2, and at radical cation geometry as calculated by CASPT2.

experimental		CASPT2				
		neutral geometry		radical cation geometry		
states	PES, eV	eV	CASSCF conf. [a]	eV	nm	CASSCF conf. [b]
$1^2A'$	$(9.84)^c$	(0)	62% $(8a')^1$ (gc) [d]	(0)	-	57% $(8a')^1$ (gc) [d]
			24% $(7a')^1$			19% $(7a')^1$
			6% $(6a')^1$			17% $(6a')^1$
$2^2A'$	+2.10	2.40	34% $(6a')^1$	3.46	358	38% $(8a')^1$ (gc) [d]
			31% $(7a')^1$		$(0.02)^e$	30% $(7a')^1$
			29% $(8a')^1$ (gc) [d]			26% $(6a')^1$
$1^2A''$	+2.88	2.74	95% $(4a'')^1$	4.72	263	91% $(4a'')^1$
$2^2A''$	+3.69	3.77	91% $(3a'')^1$	5.29	235	86% $(3a'')^1$
$3^2A'$	+6.06	6.49	32% $(7a')^1$	7.87	158	61% $(5a')^1$
			30% $(6a')^1$			21% $(6a')^1$
			30% $(5a')^1$			8% $(7a')^1$
$4^2A'$	+7.51	7.84	57% $(5a')^1$	9.08	137	35% $(7a')^1$
			23% $(6a')^1$			31% $(6a')^1$
			8% $(7a')^1$			26% $(5a')^1$

[a] Active space: 11 electrons in 3 occupied + 2 virtual a' and in 2 occupied + 3 virtual a" MOs. (MOs see Figure 4-2).

[b] Active space: 11 electrons in 8 occupied + 1 virtual a' and in 2 occupied + 3 virtual a" MOs. (MOs see Figure 4-2).

[c] First vertical ionization potential.

[d] Ground configuration.

[e] Oscillator strength f for electronic transition from the ground state.

The results of our CASSCF calculations show for $A^{+\cdot}$, at the neutral as well as at the radical cation geometry, a highly mixed ground state which is very unusual for radical cations.

According to the CASSCF calculations the second PE band cannot be assigned to the ionization out of the ω_S (or, for that matter, and other single) MO because the $2^2A'$ state is composed of three configurations with very similar weights. This is in contrast to the two following $^2A''$ states (Figure 4-3) which are dominated by single configurations.

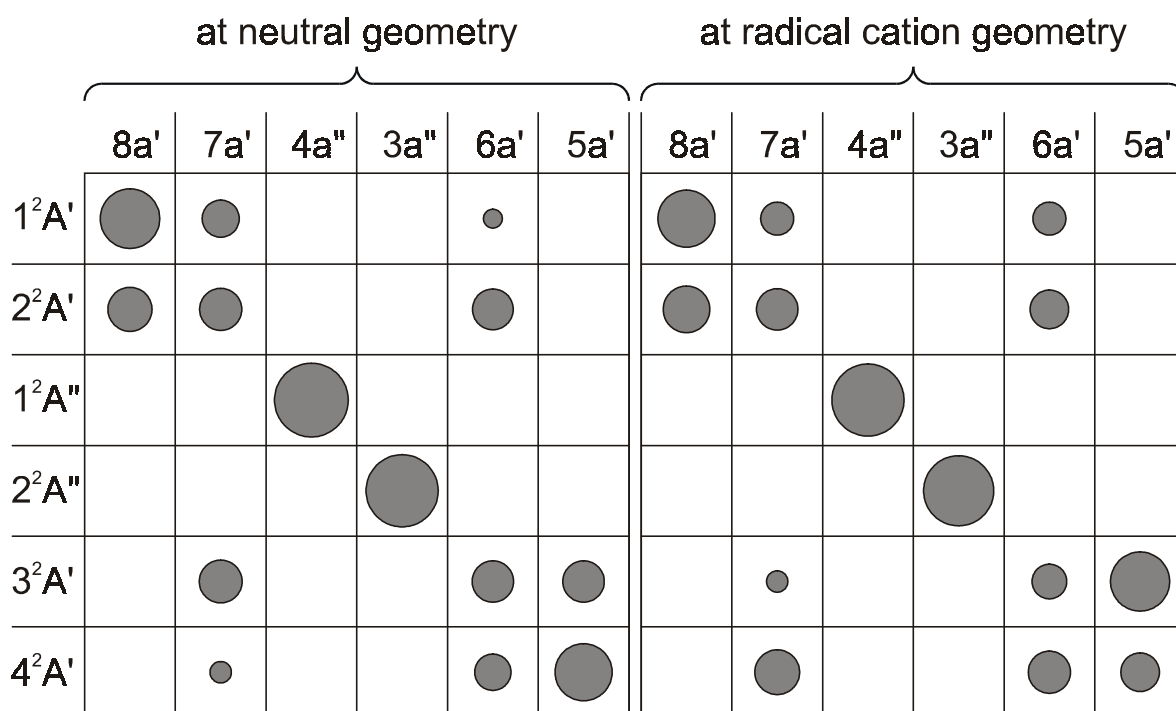|	at neutral geometry						at radical cation geometry					
	8a'	7a'	4a"	3a"	6a'	5a'	8a'	7a'	4a"	3a"	6a'	5a'
$1^2A'$	●	●			•		●	●			●	
$2^2A'$	●	●			●		●	●			●	
$1^2A''$			●						●			
$2^2A''$				●						●		
$3^2A'$		●			●	●		•			●	●
$4^2A'$		•			●	●	●				●	●

Figure 4-3: Graphic representation of the CASSCF configurations of $A^{+\cdot}$. The areas of the circles are proportional to the percentage of the weight of the configurations (columns) in the different states (rows).

Interestingly, all the $^2A'$ states are predicted too high by CASPT2. Perhaps this is due to an overestimation of the stability of the ionic ground state by this method.

In 1972, Holmes and Terlouw [101] found that the ion generated from **A** was indistinguishable from the open chain isomer $Y^{+\cdot}$ produced from dimethyl-amine, the same energy release, peak shape, and shift upon exchange deuteration

being found in each case. Consequently, they suggested that the radical cation from aziridine may possess a ring-opened structure in the gas phase.

This proposal recieved support from ab initio calculations by Lien and Hopkinson [102] at the 6-31G*// 4-31G level which predicted a planar C_{2v} azomethine ylid radical cation 26.5 kcal/mol below the ring-closed aziridine radical cation, both species corresponding to minima on the $C_2H_5N^{\ddagger}$ potential energy hypersurface. However, the height of the barrier to ring-opening was not investigated in that work.

In 1986 Williams and Qin [103] provided the first experimental proof for the ring-opening of the aziridine radical cation. The cationic species detected by ESR spectroscopy following γ-irradiation of a solid solution of **A** in a CFCl$_3$ matrix at 77 K was assigned to the C-C ring-opened isomer.

4.2.2 Experimental part

4.2.2.1 Electronic spectra

On stepwise X-irradiation of **A** embedded in an argon matrix, two bands appear at 308 and 380 nm (see Figure 4-4). The latter band shows vibrational structure with maxima at 414, 395, 381, and 368 nm. Whereas the intensity of that band asymptotically reaches a final value after about 90 min. of X-irradiation, the sharper one at 308 nm continues to grow on longer X-irradiation which means that it cannot belong to an ionic species (see previous chapter), but must be due to a rearranged neutral compound. An evident candidate is the ring-opened aziridine, i.e. the azomethine ylid **Y**. Consequently the band at 380 nm could be assigned to **Y**‡.

Indeed the excitation energies predicted by CASPT2 calculations support this assignment, although the predicted wavelength of 286 nm (4.33 eV) for **Y** does not match very well with the experimental value of 308 nm (4.03 eV) (see Table 4-2). The same method predicts an EA band for **A**‡ at 358 nm (3.46 eV) (see Table 4-1) which lies in between the two observed bands.

Additionally, we can observe another set of two very sharp bands at 257 and 264 nm which behave also like a secondary neutral species: After 45 min. of X-irradiation they are hardly visible, but after 90 minutes they continue to increase.
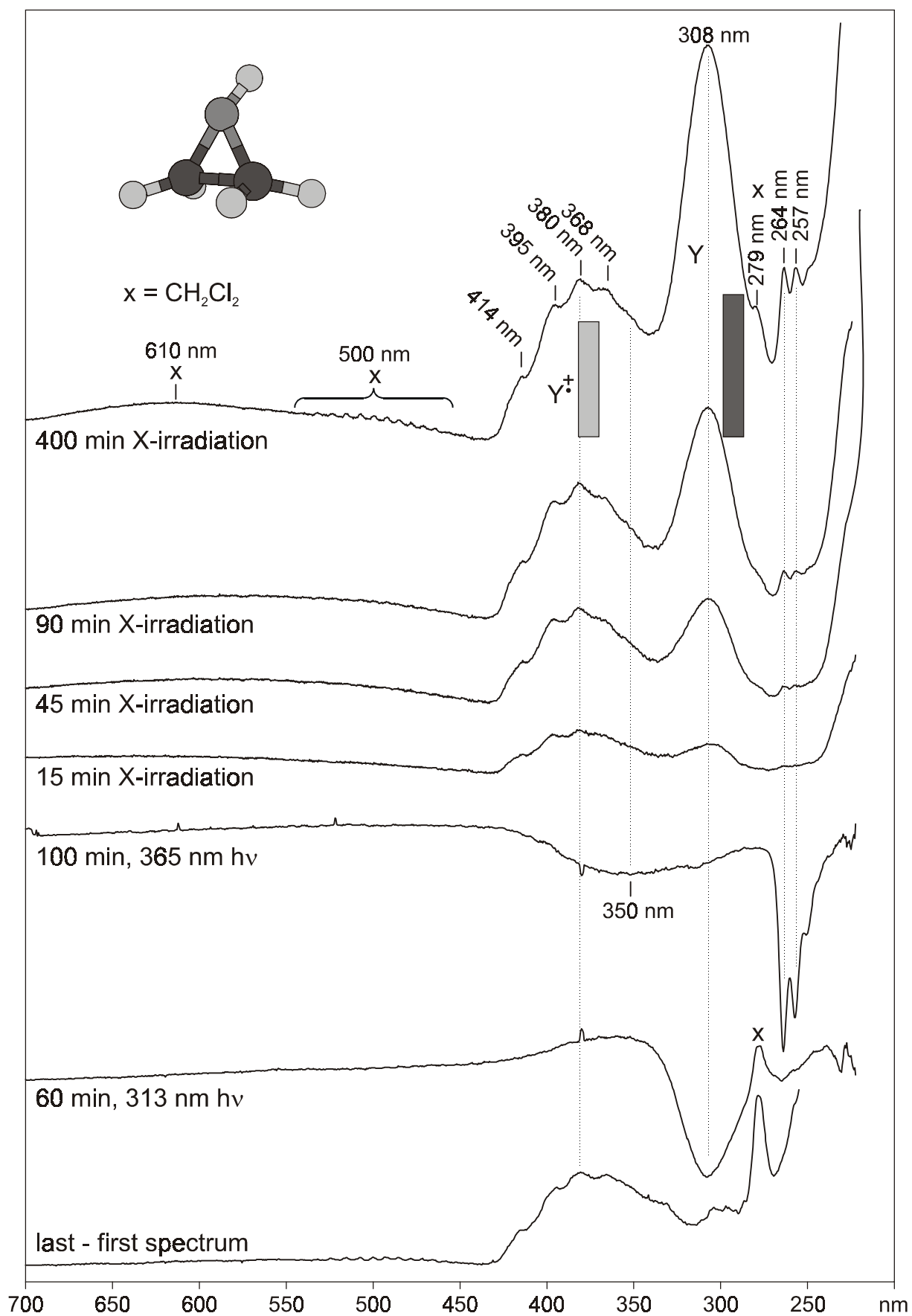
Figure 4-4: EA difference spectra of **A** in Ar matrix at 12 K after several time increments of X-irradiation and after irradiation at 365 and 313 nm.

One cannot readily think of another C_2H_5N isomer which could be formed on ionization of **A** to which these bands could be assigned. Maybe the IR-spectra will help to solve this problem.

On 100 min. photolysis at 365 nm these two sharp peaks disappear, along with a broad band peaking at 350 nm. On a 60 min. irradiation at 313 nm the band we assigned to **Y** disappears completely. In contrast, the structured band at 380 nm we assigned to $\mathbf{Y}^{\ddot{+}}$ is not affected by any of these photolyses.

Table 4-2: Excited states of the azomethine ylid radical cation ($\mathbf{Y}^{\ddot{+}}$) and of the neutral azomethine ylid (**Y**) calculated by CASPT2.

| | states | EAS | | CASPT2 | | | CASSCF |
		nm	eV	nm	eV	f^a	configurations [b, c]
$\mathbf{Y}^{\ddot{+}}$	1^2A_2	-	-	-	-	-	93% $(1b_1)^2 (1a_2)^1$
	1^2B_1	381	3.25	372	3.33	0.072	69% $1a_2 \rightarrow 2b_1^*$
							-22% $1b_1 \rightarrow 1a_2$
	2^2B_1	-	-	169	7.33	0.380	57% $1b_1 \rightarrow 1a_2$
							+28% $1a_2 \rightarrow 2b_1^*$
Y	1^1A_1	-	-	-	-	-	90% $(1b_1)^2 (1a_2)^2$
	1^2B_2	308	4.03	286	4.33	0.470	79% $1a_2 \rightarrow 2b_1^*$
							10% $1a_2 \rightarrow 4 b_1^*$
	2^1A_1	-	-	182	6.81	0.021	67% $(1a_2)^2 \rightarrow (2 b_1^*)^2$
							21% $1b_1 \rightarrow 2 b_1^*$

[a] Oscillator strength for electronic transition.

[b] Active space for the radical cation: 3 electrons in 1 singly occupied + 3 virtual a_2 and 1 doubly occupied + 3 virtual b_1 MOs.

[c] Active space for the neutral molecule: 4 electrons in 1 doubly occupied + 3 virtual b_1 and 1 doubly occupied + 1 virtual a_2 MOs.

The electronic excitations in $\mathbf{Y}^{\ddot{+}}$ are comparable to those of the allyl radical to which it is iso-π-electronic (Figure 4-5). The higher electronegativity of the N atom in $\mathbf{Y}^{\ddot{+}}$ causes a lowering of the b_1 and the b_1^* orbitals (the SOMO (a_2) remains unaffected because it has a node at the N atom). Therefore, the two $^2B_1$ configurations ($a_2 \rightarrow b_1^*$ and $b_1 \rightarrow a_2$) which were degenerate in allyl are separated in energy.
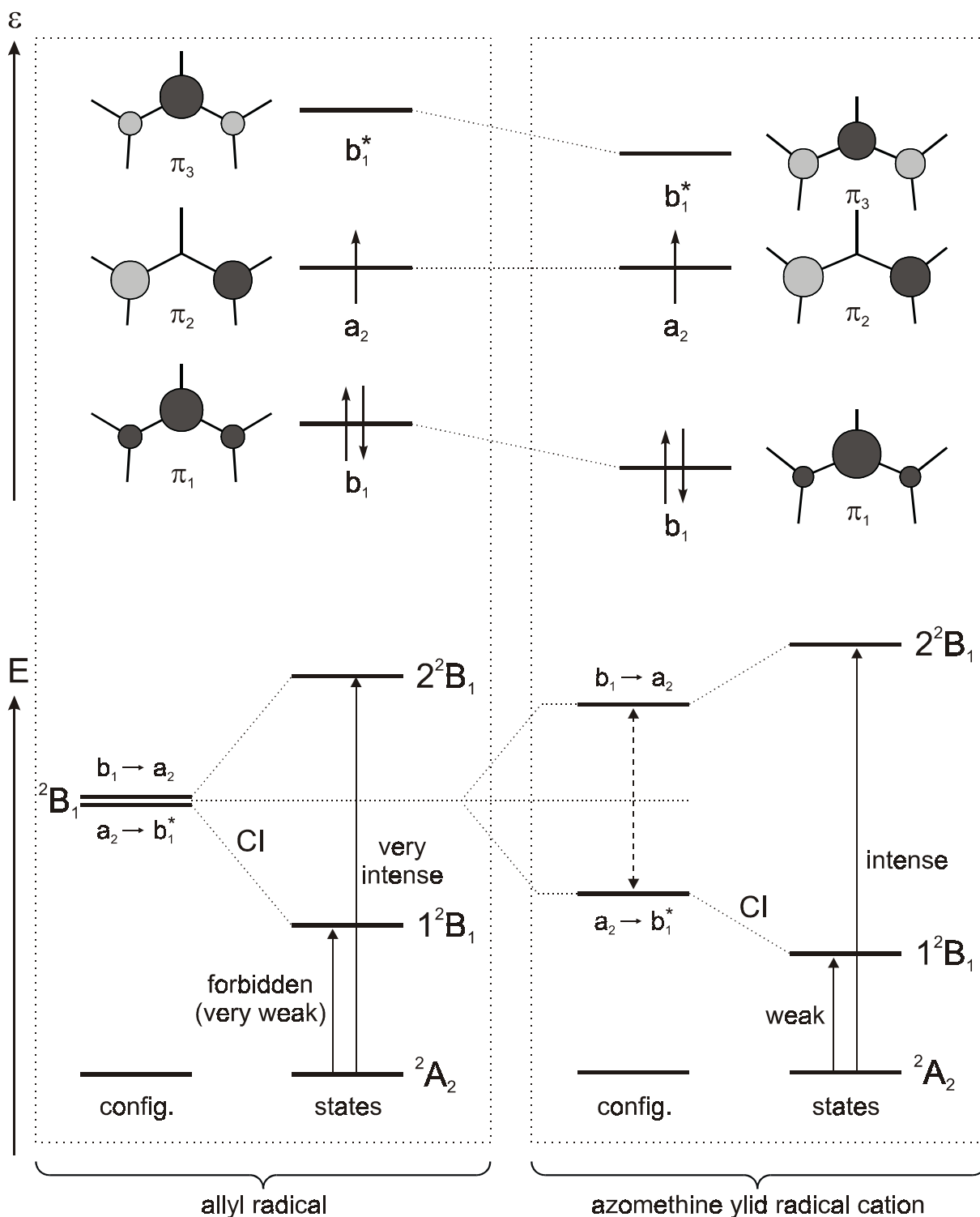
Figure 4-5: Comparison between orbitals, configurations, and states of the allyl radical and azomethine ylid radical cation ($\mathbf{Y}^{\cdot+}$).

Because the electric dipole transition moments for $b_1 \rightarrow a_2$ and for the $a_2 \rightarrow b_1^*$ electron promotion are identical in magnitude and orientation, they cancel exactly in allyl, where these two excitations carry equal weights in the 1^2B_1 and

$2\,^2B_1$ states. However, in $\mathbf{Y}^{+\cdot}$ the mixing of the $a_2 \rightarrow b_1^*$ and the $b_1 \rightarrow a_2$ excitations is no longer equal, hence the transition moments no longer cancel as efficiently as in allyl. Therefore the $^2A_2 \rightarrow 1\,^2B_1$ electronic transition in $\mathbf{Y}^{+\cdot}$ carries a small, but nonzero oscillator strength. These qualitative consideration are borne out by the CASSCF/CASPT2 calculations listed in Table 4-2 which predict a 3:1 mixing of the two excited $^2B_1$ configurations in the $1\,^2B_1$ state.

In contrast, $\mathbf{Y}$, which is iso-π-electronic to the allyl *anion*, but has a lower SOMO - LUMO gap, has comparatively intense first electronic transition which carries the full transition moment of the $a_2 \rightarrow b_1^*$ excitation.

In a next step the IR spectra were consulted to see whether any bands behave like the EA bands and how they match with the calculated ones.

4.2.2.2 IR spectra

Figure 4-7 shows the IR spectra after 90 (b-a) and 400 (c-b) minutes of X-irradiation and the difference spectrum after 60 min. of photolysis at 313 nm (d-c). Above and below the experimental spectra we show the calculated IR-spectra of $\mathbf{Y}^{+\cdot}$ and $\mathbf{Y}$, respectively.

It can be seen that after 90 min. of X-irradiation several new peaks are already very conspicuous and they do not change on further irradiation. These peaks are assigned to $\mathbf{Y}^{+\cdot}$ (cf. Table 4-3). Most of them show site splitting (the two peaks at 1155 and 1166 nm show such a strong splitting that it is hard to believe that they belong to the same vibration but in fact they behave completely parallel over the whole X-irradiation process so that they cannot be assigned to different species).

During the photolyses the bands assigned to $\mathbf{Y}^{+\cdot}$ do not change at all, whereas another set of bands decreases on photolysis at 313 nm. This set of bands shows a slow but continuous increase during the ionization process. The four most intense bands of this set match quite well with the simulated spectrum of $\mathbf{Y}$ drawn at the bottom of Figure 4-7.

Unsurprisingly, the photolysis which bleaches $\mathbf{Y}$ leads to an increase of the bands of neutral $\mathbf{A}$, i. e. the ring-opening process appears to be photoreversible. The increase of $\mathbf{A}$ cannot be observed in the EA spectrum because the transitions of neutral $\mathbf{A}$ are too far in the UV (around 175 nm [99]).

On the other hand, the agreement of the IR peaks assigned to $\mathbf{Y}^{+}$ with those calculated for this species leave more to be desired. Perhaps future scaled force field calculations will help to resolve that problem.

So far, only $\mathbf{Y}$ and $\mathbf{Y}^{+}$ were assigned, but the UV/Vis spectra Figure 4-4 show at least one more neutral compound which is formed on ionization ($\lambda_{max} =$ 264, 257 nm). If we focus on the range between 1900 and 2200 cm^{-1} in the IR spectra (see Figure 4-8), we observe three groups of intense peaks that increase on long X-irradiation (spectrum a$_3$) of which the one around 1915 cm^{-1} is completely bleached on photolysis at 365 nm (spectrum b). The position of these bands points towards a (hetero)allenic moiety as the carrier of the signals. Formation of cumulated double bonds from C_2H_5N requires the net loss of molecular hydrogen, H_2. There are only two possibilities for an allenic molecule with the formula C_2H_3N: either the nitrogen atom is positioned between the two carbon atoms ($\mathbf{B}$) or it is located at the end ($\mathbf{C}$). The IR spectra of both species are known. That of $\mathbf{B}$ has been measured by Maier et al. [104] ($\nu_{C=N=C} = 1915$ cm^{-1}) and that of $\mathbf{C}$ by Jacox and Milligan [105, 106] ($\nu_{C=N=C} = 2040$ cm^{-1}). A third set of bands was found at 2061 cm^{-1}, i.e. at the frequency of the $N \equiv C$ stretching vibration of isocyanomethane ($\mathbf{D}$) [107]. Also, peaks of other neutral C_2H_5N isomers were detected: N-methylmethanimine $H_2C=N-CH_3$ ($\mathbf{E}$) [108, 109], cis- ($\mathbf{F}$) and trans-ethanimine, $H_3C-CH=NH$ ($\mathbf{G}$) [108].
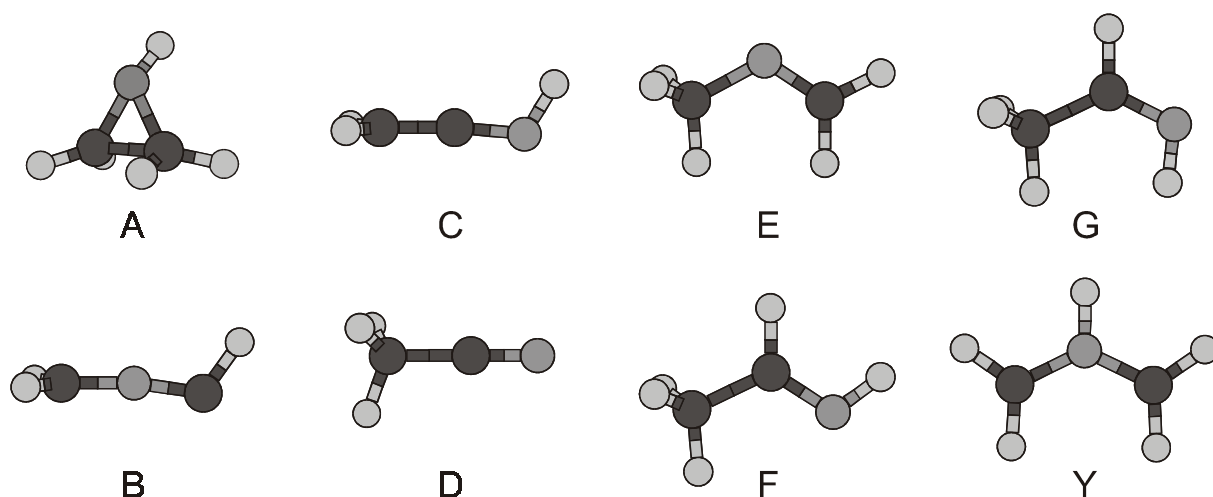
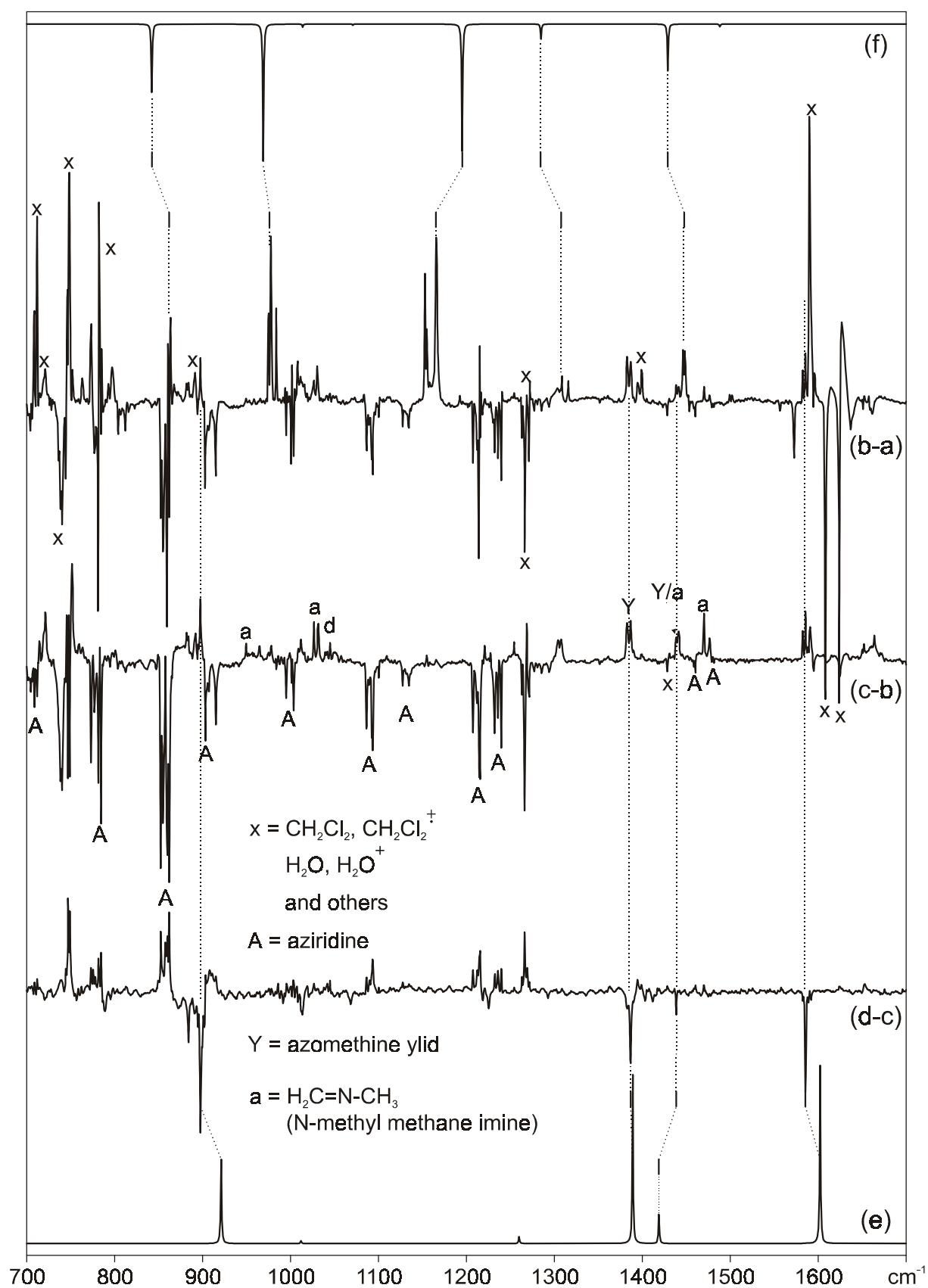Figure 4-6: C_2H_5N and C_2H_3N isomers observed in an aziridine Argon matrix after long X-irradiation.

Figure 4-7: IR difference spectra of X-irradiated (**b-a**: 90 min., **c-b**: 400 min.) and photolyzed (**d-c**: 60 min. 313 nm) **A**. Calculated IR spectra of **Y** (**e**) and $\mathbf{Y}^{+}$ (**f**) (B3LYP/6-31G* frequencies scaled by 0.97).

Table 4-3: Vibrational structure of $\mathbf{Y}$ and $\mathbf{Y}^{+\cdot}$ calculated by B3LYP/6-31G* (frequencies scaled by a factor of 0.97) compared to the frequencies of the IR bands assigned to $\mathbf{Y}$ and $\mathbf{Y}^{+\cdot}$, respectively, from Ar matrix experiments.

	sym.	mode	calc. [cm^{-1}]	exp. [cm^{-1}]	Δ [cm^{-1}]	rel. int. [%]
$\mathbf{Y}$	a_1		457			1
	a_1		1063			0
	a_1		1258			3
	a_1		1470			0
	a_1		3089			1
	a_1		3199			6
	a_1	NH str	3391	3403	12	6
	b_1		403			100 [a]
	b_1	N-H wag + tors	919	898	-21	39
	a_2		245			0
	a_2		517			0
	b_2		647			0
	b_2		1010			1
	b_2	NH wag (+ as CH$_2$ scis)	1386	1386	0	79
	b_2	as CH$_2$ scis (+ NH wag)	1417	1438	21	13
	b_2	as C-C str + NH wag	1599	1585	-14	83
	b_2		3083			2
	b_2		3199			1
$\mathbf{Y}^{+\cdot}$	a_1		470			0
	a_1		1083			1
	a_1		1299	1315	16	11
	a_1		1504	1502	-2	2
	a_1		3113			1
	a_1		3238			14
	a_1	NH str	3386	3315	-71	98
	b_1		539	531		20
	b_1	N-H wag + tors.	852	863	11	50
	a_2		980	978	-2	100 [a]
	a_2		507			0
	b_2		837			0
	b_2		1026			2
	b_2	NH wag (+ as CH$_2$ scis)	1208	1155 (1166)	-42	93
	b_2	as CH$_2$ scis (+NH wag)	1444	1446	2	34
	b_2	as C-C str + NH wag	1542			0
	b_2		3102	3050 (?)	-52	67
	b_2		3238			8

[a] Absolute intensities of the most intense peaks: 217.0 ($\mathbf{Y}$) and 119.9 km/mol ($\mathbf{Y}^{+\cdot}$).

Presumably the radical cations of C - F are also present in the matrix, but their concentrations must be very low and with so many IR-peaks it is impossible to assign them only based on the calculated spectra, especially because most of them do not show any photosensitivity.
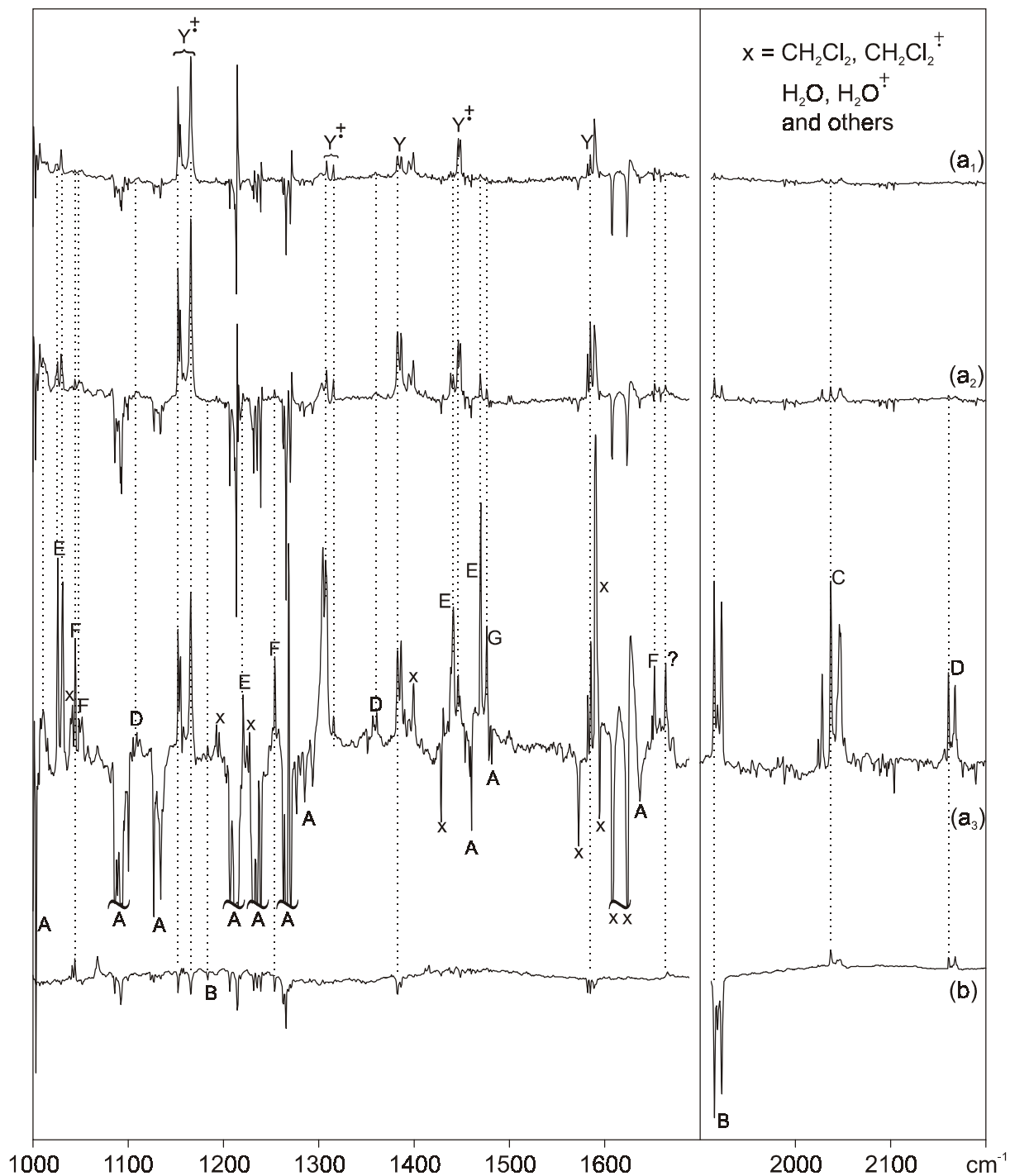

Figure 4-8: IR spectra of X-irradiated (a_1: 45 min., a_2: 90 min., a_3: 1000 min.) and photolyzed (**b**: 100 min. 365 nm) Aziridine. **A**: neutral aziridine, **Y**: H_2C-NH-CH_2, **B**: HC=N=CH_2, **C**: H_2C=C=NH, **D**: H_3C-N≡C, **E**: H_2C=N-CH_3, **F**: cis-H_3C-CH=NH, **G**: trans-H_3C-CH=NH.

4.2.3 Theoretical part

4.2.3.1 Neutral aziridine (A)

Neutral **A** has C_s symmetry due to pyramidalization at the N atom. The inversion reaction has an experimental activation barrier of 19.1 kcal/mol [110] which is reproduced very well by our calculations ($\Delta E^{\ddagger} = 18.7$ kcal/mol)[1] or those of Nielsen ($\Delta E^{\ddagger} = 19.0$ kcal/mol)[2] [111].

In the C_{2v} point group the HOMO of **A** has b_1 and the HOMO-1 has a_1 symmetry. On pyramidalization of the N atom the molecule loses the twofold rotation axis and a mirror plane. The two orbitals HOMO and HOMO-1 can therefore mix, because they belong to the same irreducible representation (Figure 4-9). Usually a mixing of two orbitals causes an increase of the energy gap but here this effect is offset by the stabilization gained by the n_N lone pair through rehybridization (the energy of the HOMO-1 is not much affected by pyramidalization at the N atom).
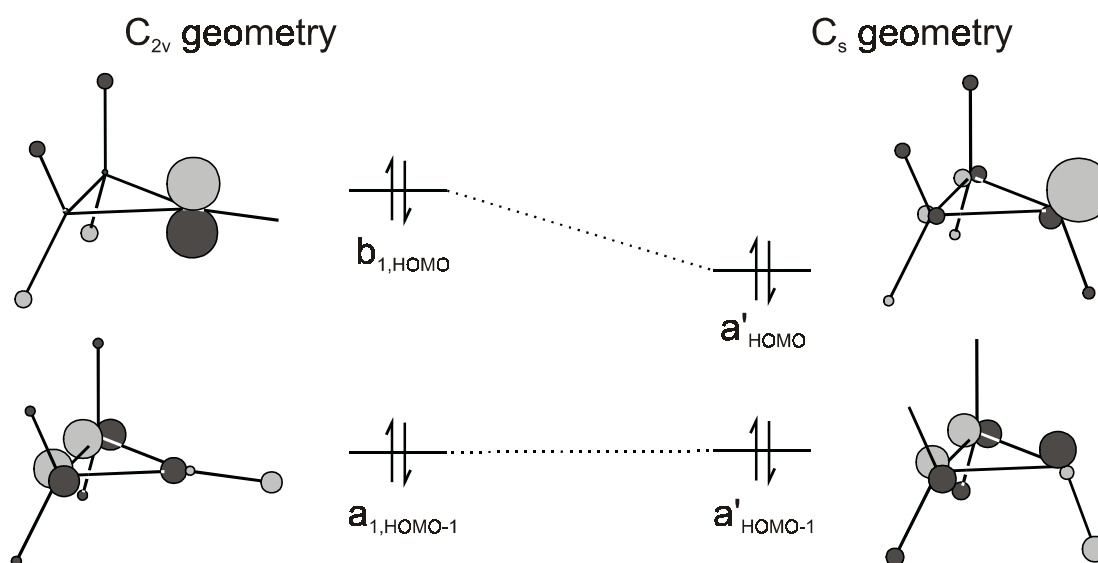

Figure 4-9: HOMO and HOMO-1 of **A** in C_{2v} and in C_s symmetry.

---

[1] Relative CCSD(T)/cc-pVTZ energies calculated at B3LYP/6-31G* optimized geometries and corrected for zero-point vibrational energy, ZPVE, differences at the same level.

[2] Relative cc-VQZ/MP2 energies calculated at MP2/6-31G* optimized geometries and corrected for ZPVE differences at the same level.

For the ring-opening of neutral **A** the Woodward-Hoffmann rules predict a conrotatory movement of the two methylene groups. Indeed, calculations at the B3LYP/6-31G* level predict a transition state (TS) for the concerted ring-opening which lies 46.2 kcal/mol above **A**. The endothermicity of the **A** → **Y** reaction is calculated to be 19.5 kcal/mol. Single point calculations at the CCSD(T)/cc-pVTZ level raise the endothermicity to 20.4 kcal/mol, whereas the barrier remains at 46.2 kcal/mol. (Nielsen [111] has calculated a barrier of 46.5 kcal/mol and an endothermicity of 19.4 kcal/mol[2].)

Inspection of the TS geometry shows that it has nearly C_2 symmetry (not fully, due to a residual slight pyramidalization of the N atom, but imposing C_2 symmetry raises the energy of the TS by only a few cal/mol). Hence, planarization at the N atom must occur early in the ring-opening reaction.

The intrinsic reaction coordinate (IRC) shown in Figure 4-10 demonstrates that the first step of the reaction is indeed a complete "depyramidalization" of the N-atom of **A** while almost no rotation of the methylene groups has occurred[3]. In the region of this (near) C_{2v} structure the energy curve shows a shoulder which lies about 5 kcal/mol above the transition state for the N inversion.

Between the IRC points 90 and 91, at a twisting angle of 108°, the HOMO and the HOMO-1 cross (because both are doubly occupied, this leads to no discontinuity in the potential energy surface). At the TS the future allylic HOMO of **Y** has still small coefficients at the N-H bond which must disappear on the way to the product.

The MOs of azomethine ylid (**Y**) show the expected allylic pattern: the HOMO consists of two p-AOs of opposite sign on the C atoms and it has a node on the N atom. According to B3LYP and MP2 calculations [111], the equilibrium structure of neutral **Y** has C_2 symmetry; but it is nearly planar and very close to a C_{2v} structure, 3 cal/mol above C_2, which represents a transition state for the "inversion" of the ylid.

---

[3] The inset plot in Figure 4-10 shows the dihedral angles α and β between the CH$_2$ planes and the CNC plane and the pyramidalization angle Θ as a function of the reaction coordinate. Initially Θ decreases from 67° to 0° (respectively increases from 113° to 180°) and the dihedral angles grow from 86.6° to 90°, at which point when the molecule reaches C_{2v} symmetry. Only then do the dihedral angles start to decrease/increase synchronously.
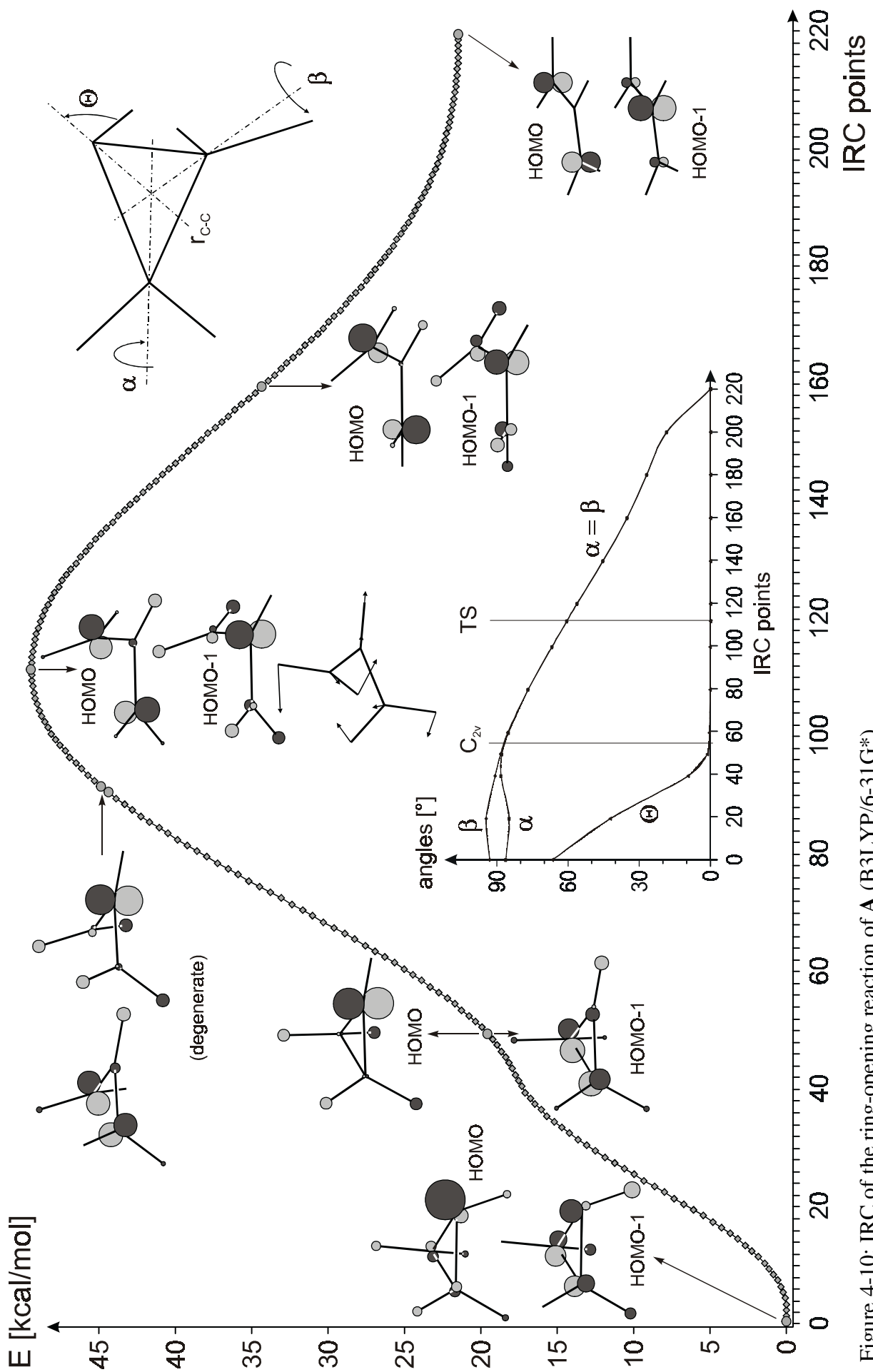
Figure 4-10: IRC of the ring-opening reaction of **A** (B3LYP/6-31G*)

4.2.3.2 Aziridine radical cation

On ionization of amines the pyramidalization at the N atom usually decreases, and amine radical cations are often planar. This fact can be explained with the VSEPR (valence shell electron pair repulsion) model which is based on the premise that the arrangement of electron pairs around a central atom is determined by their mutual repulsion. In a neutral amine the highest distance of the electron pairs is reached in a tetrahedral arrangement of the three N-R bonds and the lone pair. On ionization amines loose an electron from the lone pair. Now the repulsion between the electrons in the N-H bonds is minimized if the hybridization of the N-atom is changed to $sp^2 + p$.

Another way to look at this is by taking into account the effect of rehybridization as shown in Figure 4-11 and Figure 4-12. For neutral amines (8 e^-) the energy is invariant to rehybridization because the stabilizing energy of the six higher lying 2p-electrons is the same as the destabilizing energy of the two lower lying 2s-electrons for all three situations of hybridization. However, in the case of ionized amines going from an sp^3 to an sp^2+p situation results in an advantage, because the $sp^3 \rightarrow p$ destabilization energy $(1 \cdot \Delta sp/4)$ is offset by the $sp^3 \rightarrow sp^2$ stabilization energy $(6 \cdot \Delta sp/12)$.
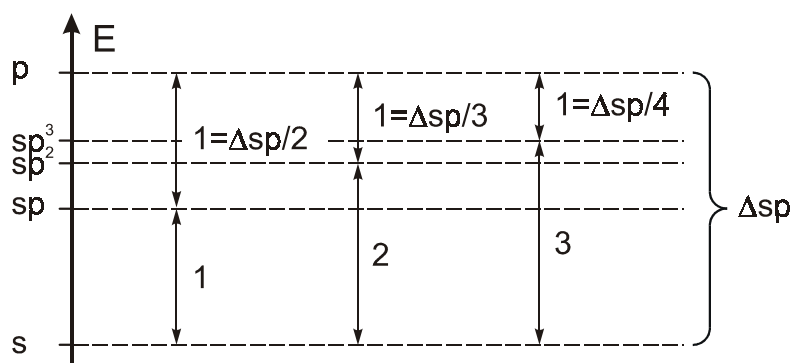

Figure 4-11: relative energies of three sp-hybrid orbitals compared to those of pure s and p orbitals. Δsp denotes the energy difference between a pure s and a pure p-AO.

For $\mathbf{A}^{+\cdot}$ this reasoning does not apply because the bond between two of the three substituents keeps the angle between them small and constrains the orbitals close to an sp^3 configuration. Therefore also the lone pair has to keep a certain s character and the N atom cannot fully planarize.

pyramidalized N-atom
= sp^3 hybridization
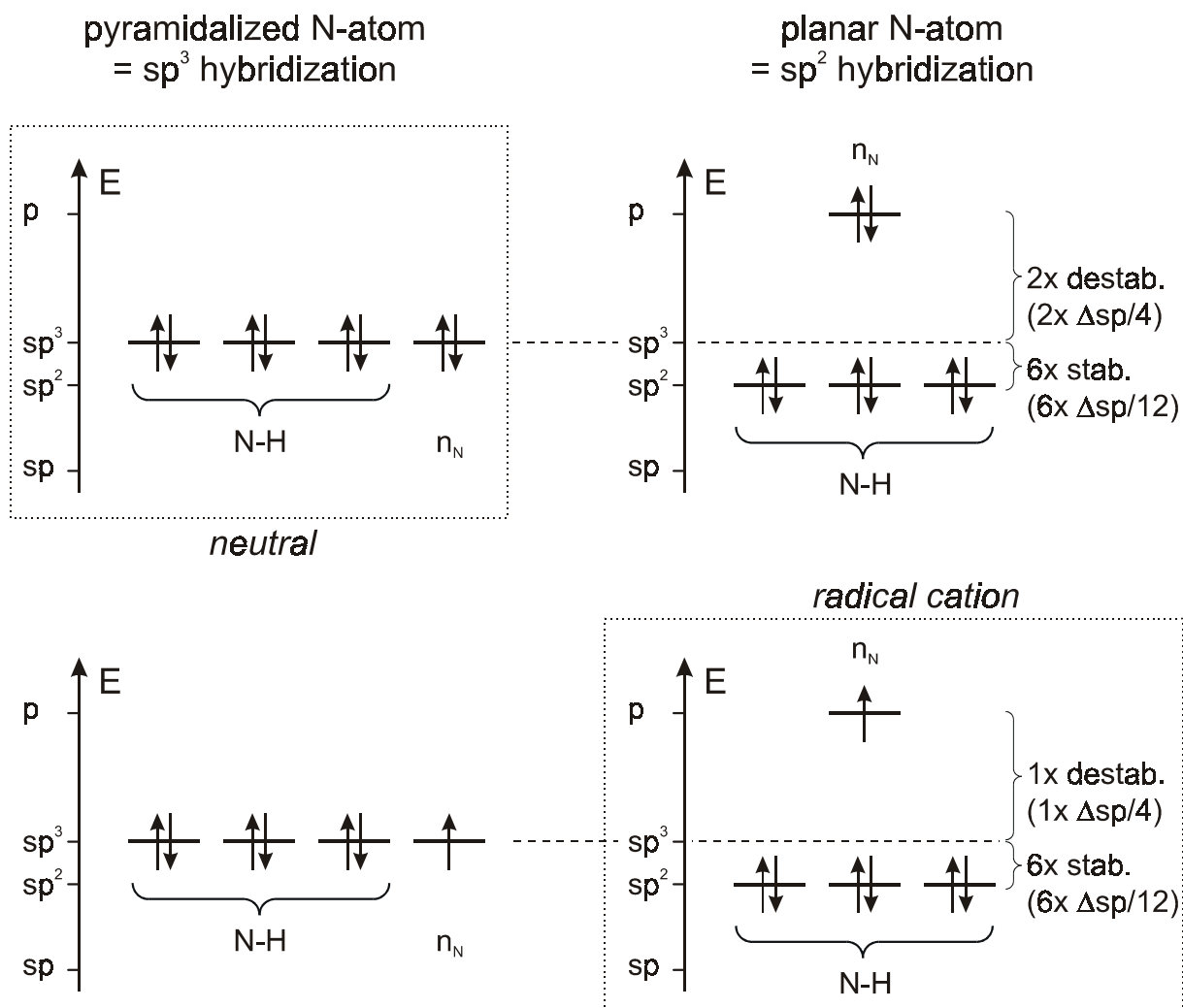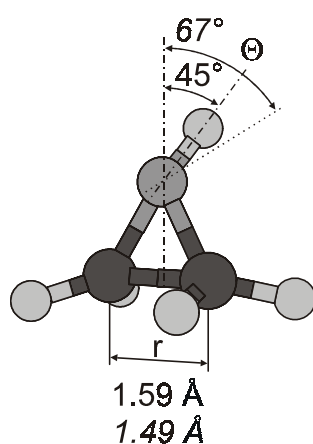
planar N-atom
= sp^2 hybridization

Figure 4-12: Hybridization of amines in the neutral and in the ionized configuration

Figure 4-13: Geometry of ionized and *neutral* **A** according to B3LYP/6-31G* calculations

As it can be seen from the HOMO of **A** (cf. Figure 4-9), ionization occurs mainly from the N-lone pair and only to a small part - due to the mixing of the HOMO with the HOMO-1 which have the same symmetry in C$_s$ - from the C-C

σ-bond. According to B3LYP/6-31G* the C-C bond lengthens by only 0.1 Å on ionization of **A** but this could still facilitate the ring-opening by C-C bond cleavage. Although the N lone pair looses almost one e⁻, **A**$^{+\cdot}$ retains a remarkable pyramidalization angle Θ of 45° (compared to 67° in neutral **A**). However, the calculated inversion barrier has decreased to a mere 0.56 kcal/mol[4] (0.84 kcal/mol[5]) compared to 19 kcal/mol for the neutral molecule!

One may try to predict the reaction pathway of the ring-opening of **A**$^{+\cdot}$, from a state correlation diagram (see Figure 4-14). The $^2B_1$ ground state of **A**$^{+\cdot}$ correlates with an excited state of **Y**$^{+\cdot}$. In both states the SOMOs have very small coefficients at the C atoms and therefore the correlation is valid both for con- or disrotatory reaction.[6]

Conversely, the ground state of **Y**$^{+\cdot}$ has $^2A_2$ symmetry and, along a *disrotatory* pathway (C_s symmetry retained), it correlates with a higher $^2B_2$ excited state of **A**$^{+\cdot}$ which decays to the lowest $^2B_2$ state, 73 kcal/mol above the ground state[5] (this $^2B_2$ state correlates in turn with a very high lying excited state of **Y**$^{+\cdot}$). Along a *conrotatory* pathway (C_2 symmetry retained) the $^2A_2$ ground state of **Y**$^{+\cdot}$ correlates with the first excited state of **A**$^{+\cdot}$ ($^2A_1$, 39 kcal/mol above $^2B_1$ ground state[5]). From this, one is inclined to conclude that the conrotatory pathway looks more probable because the correlation lines cross at lower energy.

However, in order to cross from the ground state surface of **A**$^{+\cdot}$ to that of **Y**$^{+\cdot}$, the system must lose all symmetry, i.e. no assumptions of symmetry can be made in the search for the transition state.

To find the TS for the ring-opening reaction of **A**$^{+\cdot}$ we performed first a linear synchronous transit (LST) calculation whereby the starting product is geometrically transformed into the final product in constant intervals at each of which one calculates a single point energy. The highest energy point is then used as the starting geometry for a search of the TS, i.e. a first order saddle point.

---

[4] Relative CCSD(T)/cc-pVTZ energies calculated at B3LYP/6-31G* optimized geometries and corrected for ZPVE differences at the same level.

[5] B3LYP/6-31G* level.

[6] The next lower lying state has $^2B_2$ symmetry, but it is almost degenerate with the $^2B_1$ state of **Y**$^{+\cdot}$ (2 kcal/mol difference). The lowest $^2A_1$ state lies 94 kcal/mol above the ground state.
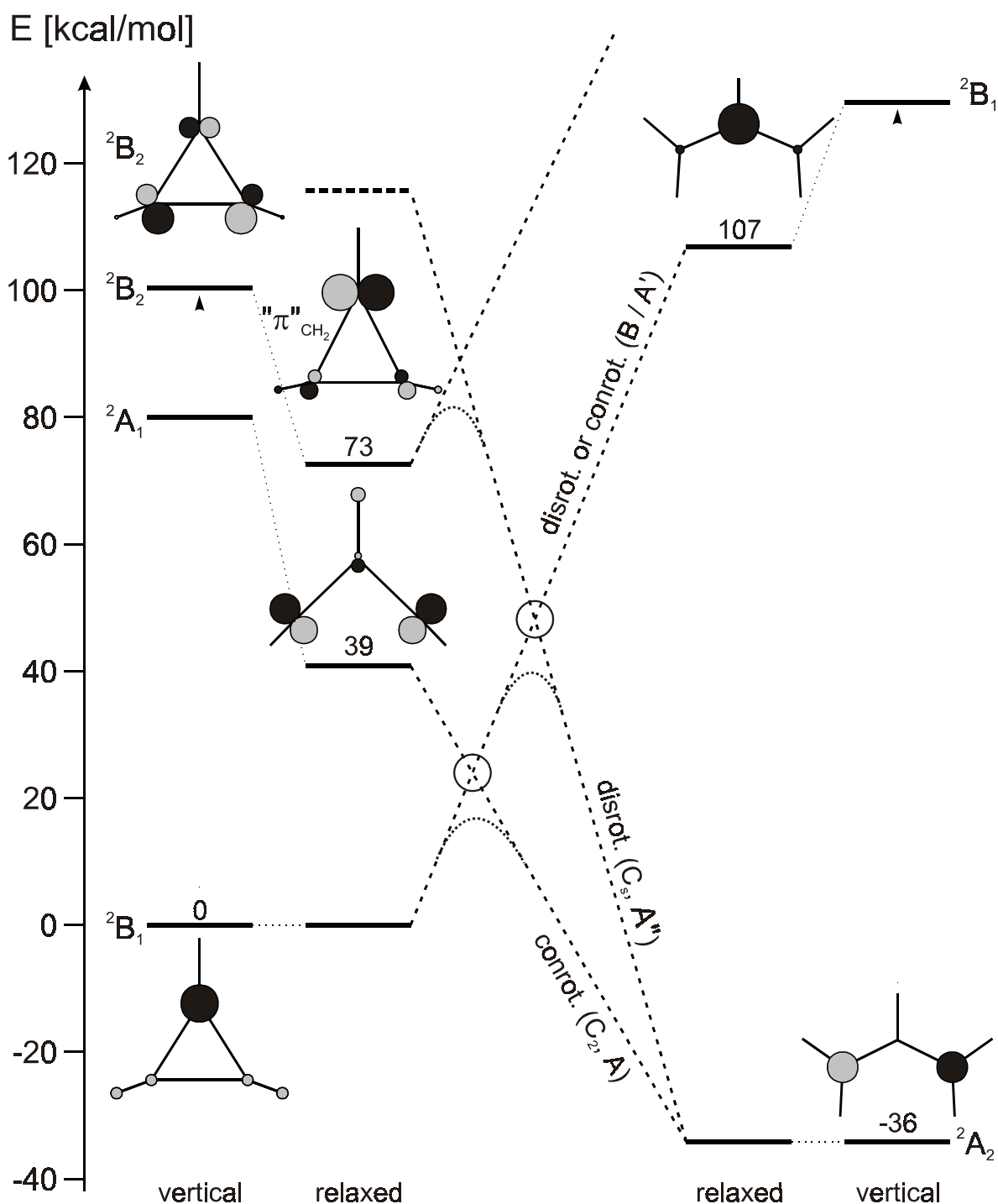
Figure 4-14: MO correlation diagram (ZPEV corrected) of closed and opened $\mathbf{A}^{+}$ according to calculations at B3LYP/6-31G* level.

Note that the conrotatory (C_s) and the disrotatory (C_2) transformations of $\mathbf{A}$ to $\mathbf{Y}$ lead to different LST paths as it is depicted in Figure 4-15.

Thereby one finds that for neutral $\mathbf{A}$ the conrotatory transformation goes over a much lower barrier than the disrotatory transformation. However, for the $\mathbf{A}^{+}$ two paths starting from $\mathbf{A}^{+}$ and from $\mathbf{Y}^{+}$ respectively, cross at a point which

lies *lower* than the transition over the conrotatory path. A following TS optimization of the point close to the crossing point leads indeed to a TS which shows that the reaction must involve a highly non-concerted movement of the two methylene groups. Also if one starts a TS optimization of the radical cation ring-opening at the geometry of the neutral conrotatory ring-opening TS of **A** the disrotatory TS is found immediately.
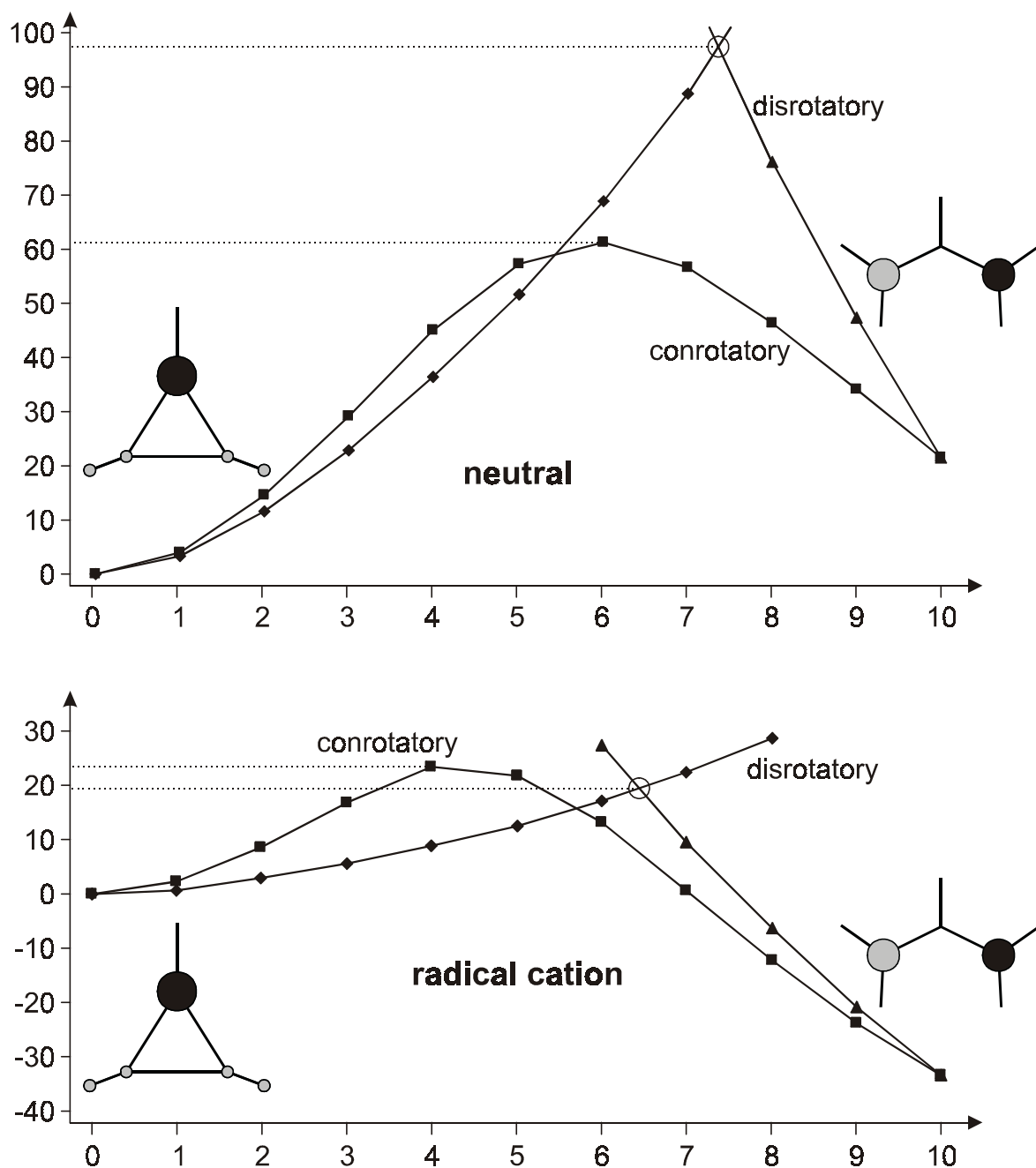

Figure 4-15: Single point energies for the con- and the disrotatory ring-opening of **A** and **A**$^{+\cdot}$, respectively, in 10 steps. Geometries generated by the linear synchronous transit method (LST) from **A** and **Y** by Spartan. Level of calculation: B3LYP/6-31G*.

At the highest level of theory employed in this study the TS for the $\mathbf{A}^{+\cdot} \rightarrow \mathbf{Y}^{+\cdot}$ reaction lies 10.5 kcal/mol above $\mathbf{A}^{+\cdot}$ and the exothermicity of the reaction is 33.0 kcal/mol[7].

Given a TS, the reaction pathway can again be investigated by an IRC calculation. The orbitals of the starting radical cation $\mathbf{A}^{+\cdot}$ have a similar shape to those of neutral $\mathbf{A}$ (cf. Figure 4-17, leftmost MO), except that the mixing between the "π"$_{CH_2}$ orbitals at the C atoms and the now almost completely p-type lone pair orbital of the N atom is more pronounced. The inset to Figure 4-17 shows in detail what happens to the critical geometry parameters during the reaction. The pyramidalization angle Θ first grows slightly (to 50.3° at the 25th point of the IRC) before it starts to decrease.

The dihedral angles α and β which describe the rotations of the CH_2 groups do not have starting values of 90° but of 81.2° / 98.8° because of the rather strong C_s distortion of the radical cation. Initially, both angles change concertedly in a disrotatory manner but around point 30 on the IRC, β begins to decrease until it reaches 96.3° at point 79 on the IRC, while α continues to decrease smoothly. One could deduce a conrotatory ring-opening from this behavior but after point 79 on the IRC, when α has already reached a value of 41.8°, β changes again its rotation direction and continues to increase rapidly to 180°. Thus the overall stereochemistry of the reaction ends up being disrotatory.

The coefficient of the p orbital at the N atom decreases continually in the course of the reaction. The p-AO on one of the C-atoms shrinks and becomes more and more polarized before it reaches 100% s character at IRC point 82nd. Then it re-emerges on the opposite side of the CH_2 plane by gaining again some p character, thus achieving a change of phase. The p character increases and the s character decreases until the orbital becomes again a 100% p AO on $\mathbf{Y}^{+\cdot}$. During the phase-change the p orbital on the opposite C atom increases in size to compensate the electron density. One can even observe a weak shoulder in the energy curve of the IRC which arises because the radical cation "thinks" that it could keep one CH_2 group perpendicular to the CNC plane before it "realizes" that the planar structure is energetically more stable.

---

[7] Relative CCSD(T)/cc-pVTZ energies calculated at B3LYP/6-31G* optimized geometries and corrected for ZPVE differences at the same level.

In contrast to the ring-opening of neutral **A**, no crossing of MO's is observed in the $\mathbf{A}^{+} \rightarrow \mathbf{Y}^{+}$ process and the overall stereochemistry of $\mathbf{A}^{+}$ is disrotatory.

E [kcal/mol]

+10.5

0.0

-33.0

+46.2

IP Aziridine
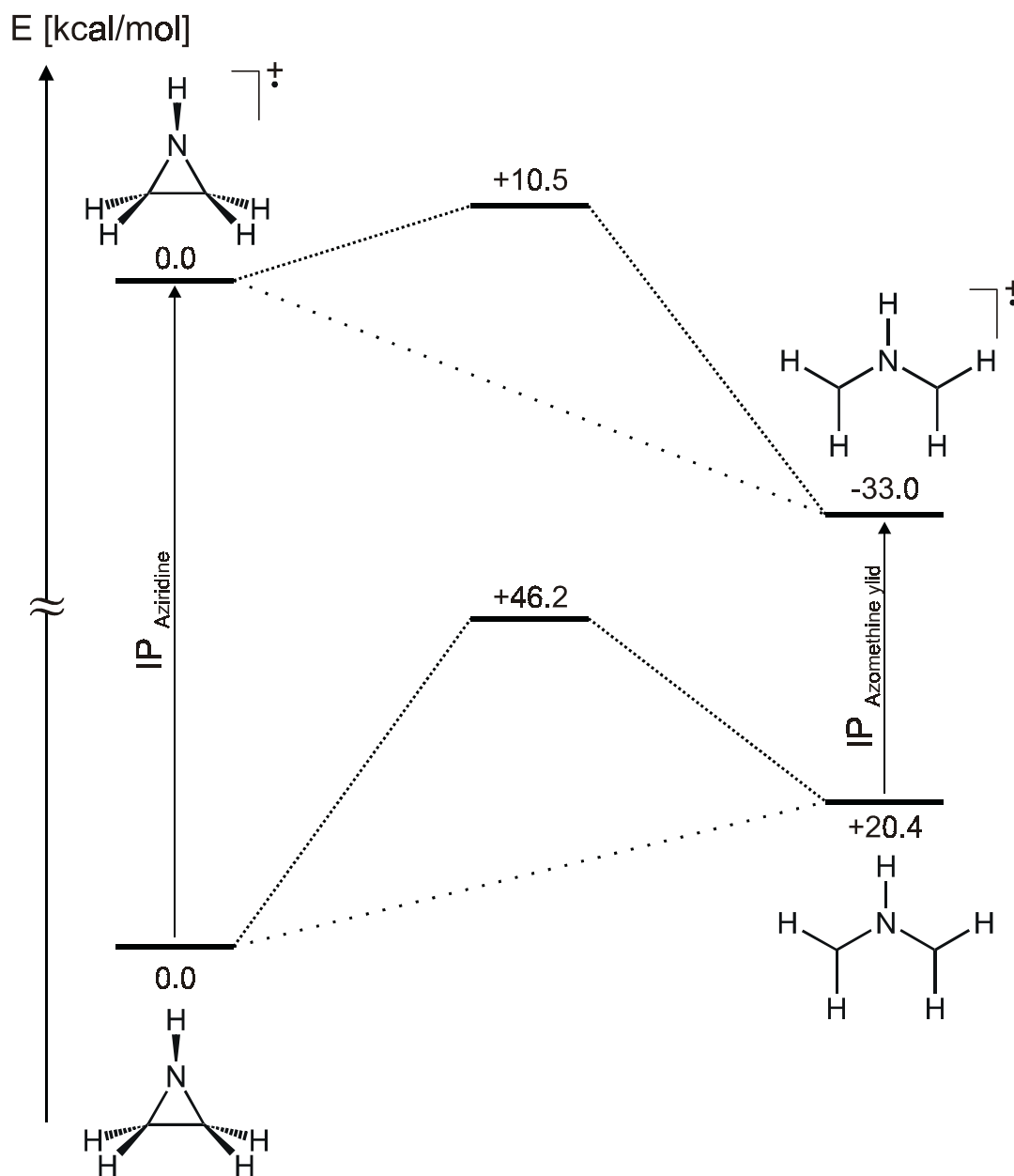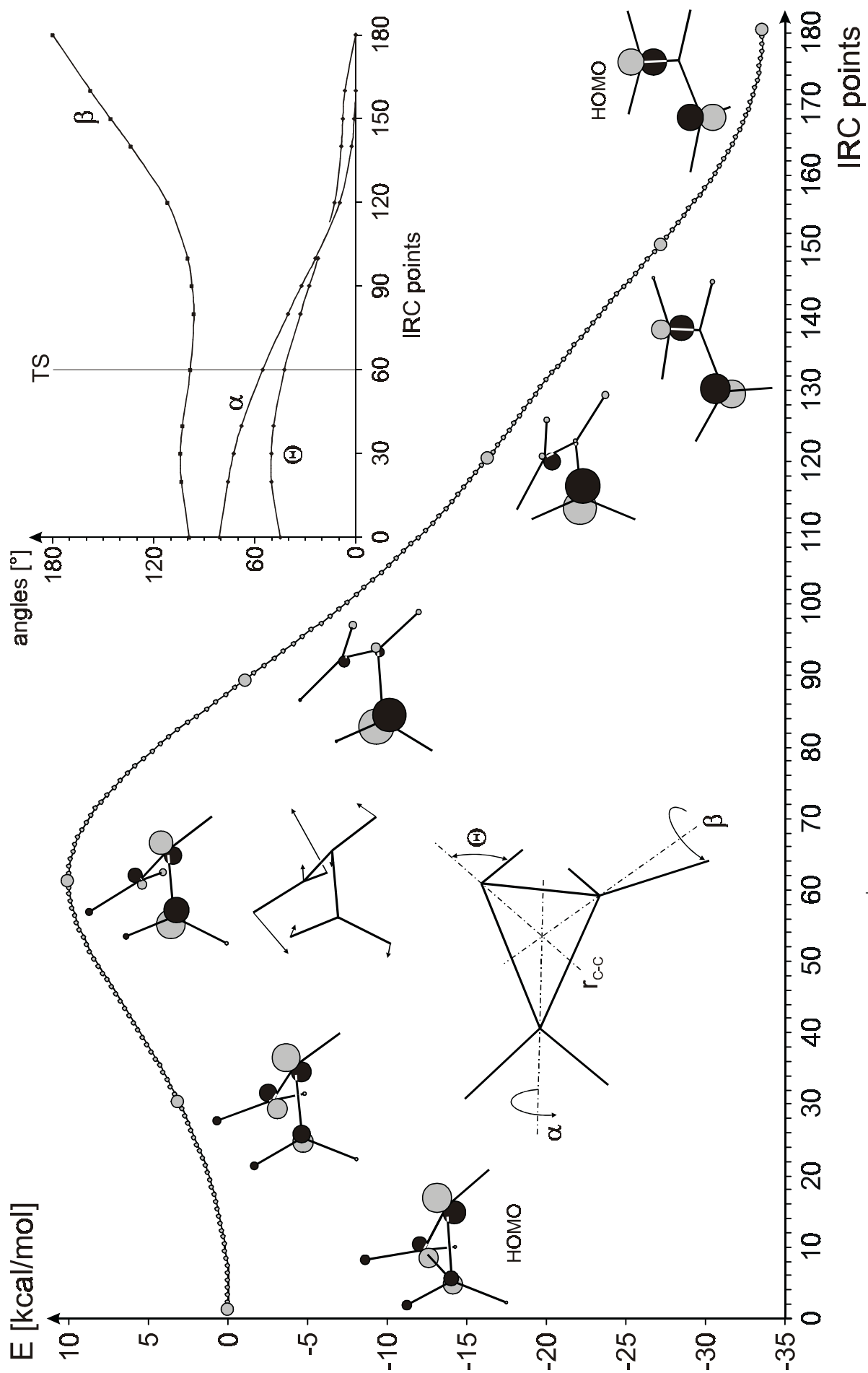
IP Azomethine ylid

+20.4

0.0

Figure 4-16: Summarizing illustration of the ring-opening thermochemistry for neutral and ionized **A** (relative CCSD(T)/cc-pVTZ energies calculated at B3LYP/6-31G* optimized geometries and corrected for zero-point vibrational energies at the same level).

Figure 4-17: IRC of the ring-opening reaction of **A**$^{\cdot+}$ (B3LYP/6-31G*).

4.3 N-methylaziridine

4.3.1 Photoelectron spectrum

The photoelectron spectrum of N-methylaziridine (**NMA**) was measured 1988 by Rademacher et al. [100]. It is depicted in Figure 4-18 together with calculated SCF-MOs of neutral **NMA**. The PE spectra of **A** and of **NMA** look similar, but the HOMO which contains mainly the N lone pair lies 0.61 eV higher in **NMA**. Within the framework of the Koopmans theorem the sequence of the next two Walsh type orbitals is inverted. The C-C-bonding one (ω_S) remains almost unshifted at ≈ 12 eV, whereas the C-C-antibonding orbital (ω_A) is destabilized by 1.43 eV through interaction with a pseudo-π orbital of the CH_3 group. A shift of only 0.15 eV is observed for the $"\pi"_{CH_2}$ orbital which is followed immediately by the $"\pi"_{CH_3}$ MO.
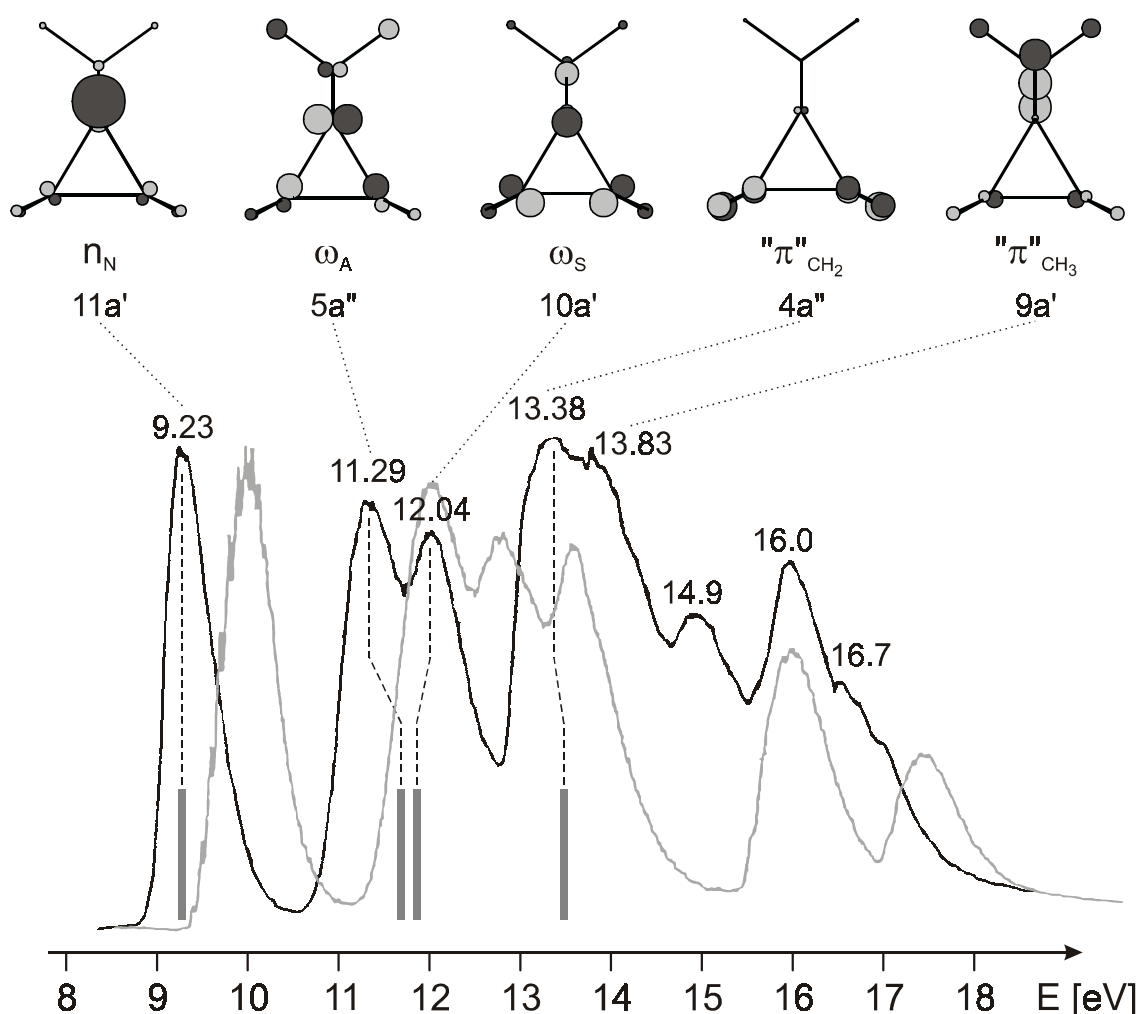

Figure 4-18: PE spectrum of **NMA** and SCF MOs. In gray the spectrum of parent aziridine is reproduced for reference purposes (see Figure 4-2 for assignment).

The bars are the energies of excited electronic states of **NMA**$^{+\cdot}$ relative to its ground state, calculated with CASPT2 at the neutral geometry (cf. Table 4-4) (the ground state is set to the first vertical IP at 9.23 eV).

Table 4-4: Excited states of N-methylaziridine radical cation (**NMA**$^{+\cdot}$) measured by PE spectroscopy and calculated by CASPT2 at the neutral geometry.

states	PES eV	CASPT2 eV	CASSCF configurations [a]
1^2A'	(9.23)	(0)	93% $(11a')^1$
1^2A"	+2.06	2.46	97% 5a" $\rightarrow$ 11a'
2^2A'	+2.81	2.63	92% 10a' $\rightarrow$ 11a'
2^2A"	+4.15	4.20	96% 4a" $\rightarrow$ 11a'

[a] Active space: 15 electrons in 5 occupied + 0 virtual a' and in 3 occupied + 1 virtual a" MOs. Occupied MOs depicted in Figure 4-18.

4.3.2 Potential energy surfaces

4.3.2.1 Neutral N-methylaziridine

Neutral **NMA** has C$_s$ symmetry and a calculated pyramidalization angle of 59.3° (compared to 66.8° for **A**). Its barrier for nitrogen inversion is 19.9 kcal/mol[8] (15.8 kcal/mol[9]) which is about 1 kcal/mol higher than for **A**.[10]

As in the parent compound, nitrogen pyramidalization leads to a mixing of the N lone pair with the symmetric Walsh type σ orbital located mostly in the C-C bond.

---

[8] CCSD(T)/cc-pVTZ single point calculation, geometry and zero-point vibrational energy (ZPVE) difference correction of a B3LYP/6-31G* calculation.

[9] B3LYP/6-31G* calculation, ZPVE difference corrected.

[10] The reaction includes a rotation of the methyl group by 60°. The TS has also C$_s$ symmetry but the plane of symmetry lies in the aziridine ring whereas in the reactant the plane of symmetry is perpendicular to the aziridine ring. Therefore at the TS one methyl H atom lies in the plane of symmetry and the two other hydrogens of the methyl group are out of plane.

The ring-opening of **NMA** takes place by a highly concerted conrotatory movement following the Woodward-Hoffmann rules, like in the case of **A**. The calculated barrier is 44.2 kcal/mol[8] (43.8 kcal/mol[9]) and the endothermicity is 19.8 kcal/mol[8] (20.8 kcal/mol[9]). The corresponding values for the parent compound, **A**, were 46.2 kcal/mol and 19.5 kcal/mol respectively, i.e. the thermochemistry and the kinetics of the ring-opening process are hardly affected by N-methylation in the neutral aziridine. As we will see below, this is not the case for the radical cation.

4.3.2.2 N-Methylaziridine radical cation

Following the theoretical considerations outlined in section 3.2.3.2, ionization leads to a "depyramidalization" at the N-atom of aziridine. The pyramidalization angle of **NMA**$^{+\cdot}$ decreases by 33.9° to 25.4° (by 22.1° to 44.7° for **A**). Consequently the nitrogen inversion barrier drops strongly to 0.45 kcal/mol[8] which is slightly less than for the parent radical cation **A**$^{+\cdot}$ where the inversion barrier is 0.56 kcal/mol[8].

The ring-opening reaction also shows strong similarities to that of **A**$^{+\cdot}$. The TS is far from having any symmetry. It lies 16.0 kcal/mol[8] (16.9 kcal/mol[9]) above **NMA**$^{+\cdot}$ which is a significantly higher activation barrier for ring-opening than that found for **A**$^{+\cdot}$ (10.5 kcal/mol). This can be explained in part by the Bell-Evans-Polanyi principle because the exothermicity (24.2 kcal/mol[8]/ 22.1 kcal/mol[9]) is 8.8 kcal/mol smaller than for the parent radical cation. Obviously, **NMA**$^{+\cdot}$ is better stabilized by the methyl group than **NMY**$^{+\cdot}$ which is due to the node at the N atom in the SOMO of **NMY**$^{+\cdot}$.

It has to be mentioned that the geometry of neutral **NMY** is slightly different from that of **NMY**$^{+\cdot}$. Both have C$_s$ symmetry, but in the neutral molecule the plane of symmetry is *perpendicular* to the allylic moiety, whereas in the radical cation the plane of symmetry is *coplanar* to the allylic plane at the potential energy minimum (see Figure 4-19).
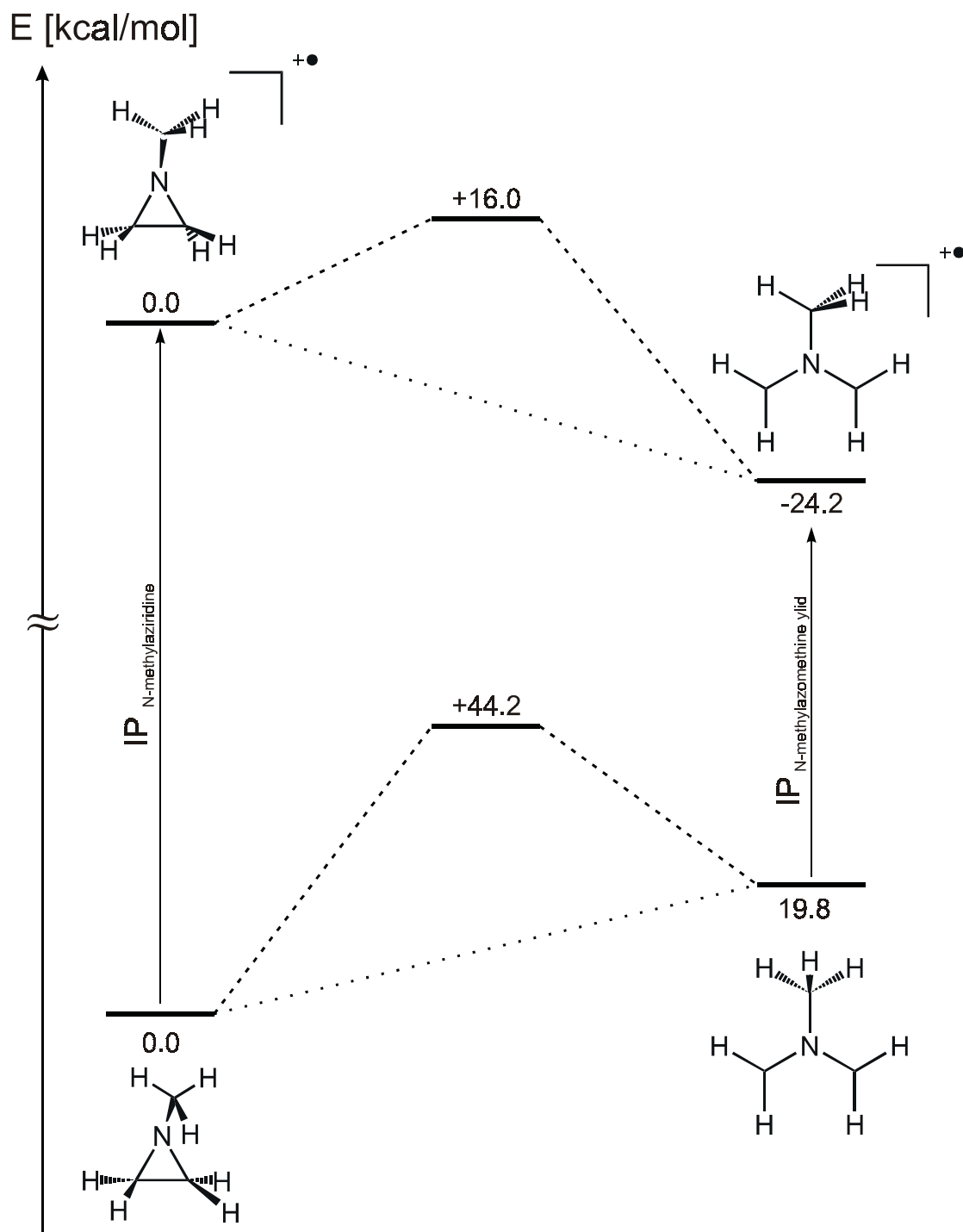
Figure 4-19: Summarizing illustration of the ring-opening thermochemistry for neutral and ionized **NMA** (relative CCSD(T)/cc-pVTZ energies calculated at B3LYP/6-31G* optimized geometries corrected for ZPVE differences at the same level).

4.3.3 Experimental part

The experimental IR spectrum of **NMA** matches quite well with the spectrum calculated by B3LYP/6-31G* (see Figure 4-20).
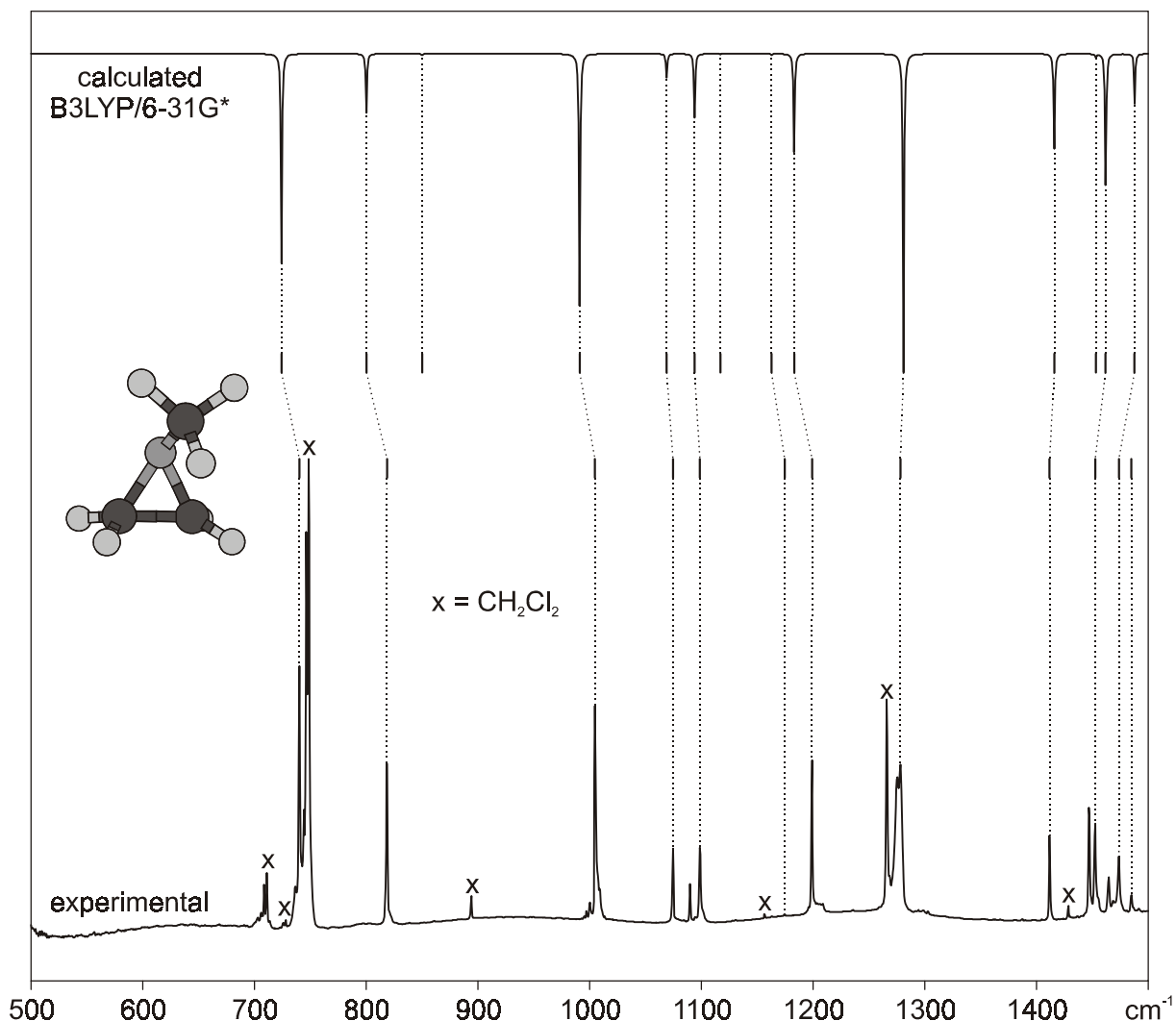

Figure 4-20: IR spectra of **NMA** measured in Ar matrix at 12 K and calculated at B3LYP/6-31G* level.

4.3.3.1 EA spectra

NMA embedded in an Ar matrix and subjected to stepwise X-irradiation leads to similar EA spectra as were found in the case of **A**: a structured pattern peaking at 409 nm (vibrational components at 392 and 433 nm) and a peak at 330 nm (Figure 4-21). It can be seen that the pattern at 409 nm does not increase anymore after 90 minutes of X-irradiation which is a strong indication that it is

due to a radical cation. Therefore, the structured pattern could be the absorption of **NMY**$^{+\cdot}$ but, unlike **Y**$^{+\cdot}$, it turns out to be a photolabile species: It can be bleached at >420 nm within 20 minutes. CASPT2 calculations predict a rather weak band at 389 nm (cf. Table 4-5).

The band at 330 nm continues to increase slightly on longer X-irradiation. It could therefore be the neutral ring-opened **NMY**. The strongest electronic transition for this species is predicted at 313 nm (cf. Table 4-5). The band can be bleached by 15 minutes of irradiation at this wavelength. However, this band does not increase as strongly as the band of **Y** in the experiment with **A** (cf. Figure 4-4). Obviously, the formation of **Y** competes with that of another species, **B**, which shows a set of three peaks at 264, 257, and 250 nm. This set increases more strongly than the band of **Y** on long X-irradiation, and in the end it is much more pronounced than in the experiment with **A** where we had observed the very same bands. There we had assigned species **B** to the azoallenic molecule $HC=N=CH_2$ which arises by loss of H_2 from **A** or **Y** [104]. However, in the case of the methyl derivative, **B** can only be formed by net loss of methane and it seems even that X-irradiated **NMA** tends more to loss of methane than X-irradiated **A** tends to loss of H_2. **B** is a neutral molecule and therefore the peaks increase steadily on long X-irradiation. On 4 h irradiation at 313 nm **B** can be bleached completely. In another experiment presented in (Figure 4-23) we bleached **NMY**$^{+\cdot}$ at >420 nm within 30 minutes whereby only a weak decrease of **B** was observed. On continued irradiation at >420 nm of 15 h a large part of **B** was bleached, without touching, however, the absorption of neutral **NMY** at 330 nm which can be photolyzed subsequently - together with the rest of **B** - by irradiation at >375 nm within 120 minutes.

On X-irradiation of **NMA** a small band at 302 nm also increases which behaves like that of a radical cation. It is not bleached by any of the previous irradiations performed in this set of experiments. An interesting observation is, that on photolysis at >475 nm the structured band of **NMY**$^{+\cdot}$ *increases* slightly while a band at 357 nm (**D**) decreases, which could have been hidden between the increasing bands of **NMY**$^{+\cdot}$ and **NMY** in the difference spectra after X-irradiation. Unfortunately it is too far from the predicted transition of **NMA**$^{+\cdot}$ at 315 nm (see Table 4-6) to permit an assignment of the 357 nm band to this

species.[11] Thus the photochemical precursor of **NMY**$^{+\cdot}$ in the >475 nm irradiation experiment remains unidentified.

Table 4-5: Excited states of **NMY**$^{+\cdot}$ and **NMY** calculated by CASPT2.

	states	UV/Vis		CASPT2			CASSCF
		nm	eV	nm	eV	f^a	configurations ^{b}
NMY$^{+\cdot}$	1^2A"	-	-	-	-	-	89% (3a")^1
	2^2A"	409	3.03	389	3.18	0.054	64% 3a" $\rightarrow$ 4a"
							21% 2a" $\rightarrow$ 3a"
	3^2A"			190	6.52	0.277	57% 2a" $\rightarrow$ 3a"
							29% 3a" $\rightarrow$ 4a"
	4^2A"			139	8.93	0.194	67% 2a" $\rightarrow$ 3a"
							3a" $\rightarrow$ 4a"
							16% 2a" $\rightarrow$ 4a"
NMY	1^1A'	-	-	-	-	-	89% (10a')^2 (6a")^2
	1^1A"	330	3.76	313	3.97	0.397	88% 6a" $\rightarrow$ 11a'
	2^1A"			273	4.54	0.0003	49% 6a" $\rightarrow$ 15a'
							42% 6a" $\rightarrow$ 14a'
	3^1A"			205	6.06	0.0005	50% 6a" $\rightarrow$ 14a'
							-41% 6a" $\rightarrow$ 15a'
	2^1A'			203	6.10	0.093	85% 6a" $\rightarrow$ 7a"

^{a} Oscillator strength for electronic transition.
^{b} Active space for **NMY**: 4 electrons in 1 occupied and 6 virtual a' + 1 occupied and 3 virtual a" MOs. Active space for **NMY**$^{+\cdot}$: 5 electrons in 2 doubly + 1 singly occupied + 8 virtual a" MOs (depicted in Figure 4-22).

---

[11] Note, that the CASSCF configurations of **NMA**$^{+\cdot}$ showed in this table are quite different from those of **NMA**$^{+\cdot}$ at the neutral geometry listed in Table 4-4. The ^{2}A' states are not as pure as they are in **NMA**$^{+\cdot}$ at the neutral geometry. Interestingly, this is only the case for the CASSCF configurations; CASPT2 shows quite pure configurations.
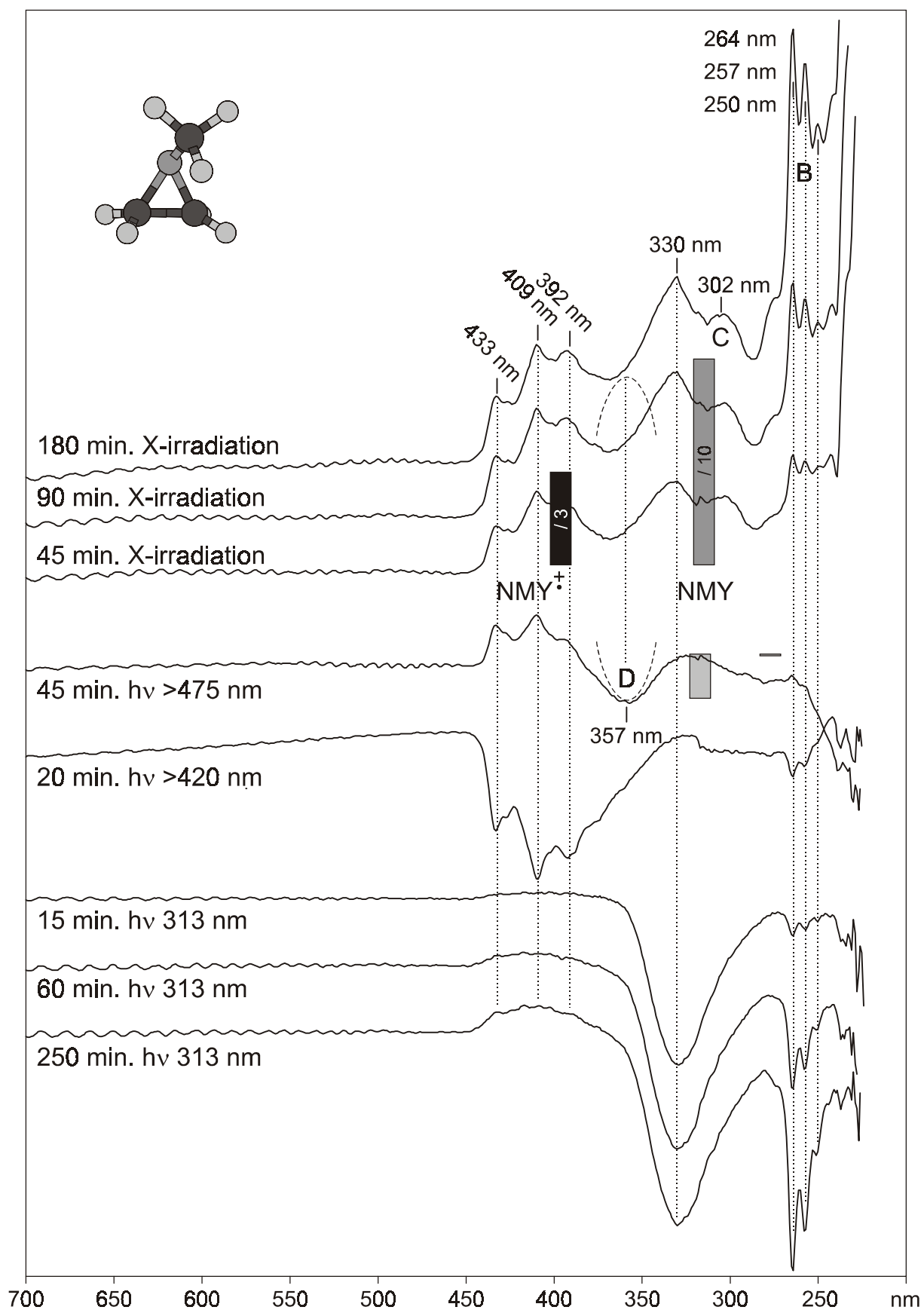
Figure 4-21: EA difference spectra of **NMA** after X-irradiation (45, 90, and 180 minutes) and after irradiation (45 min. at >475 nm; 20 min. at >420 nm; 15, 60, and 250 min. at 313 nm).
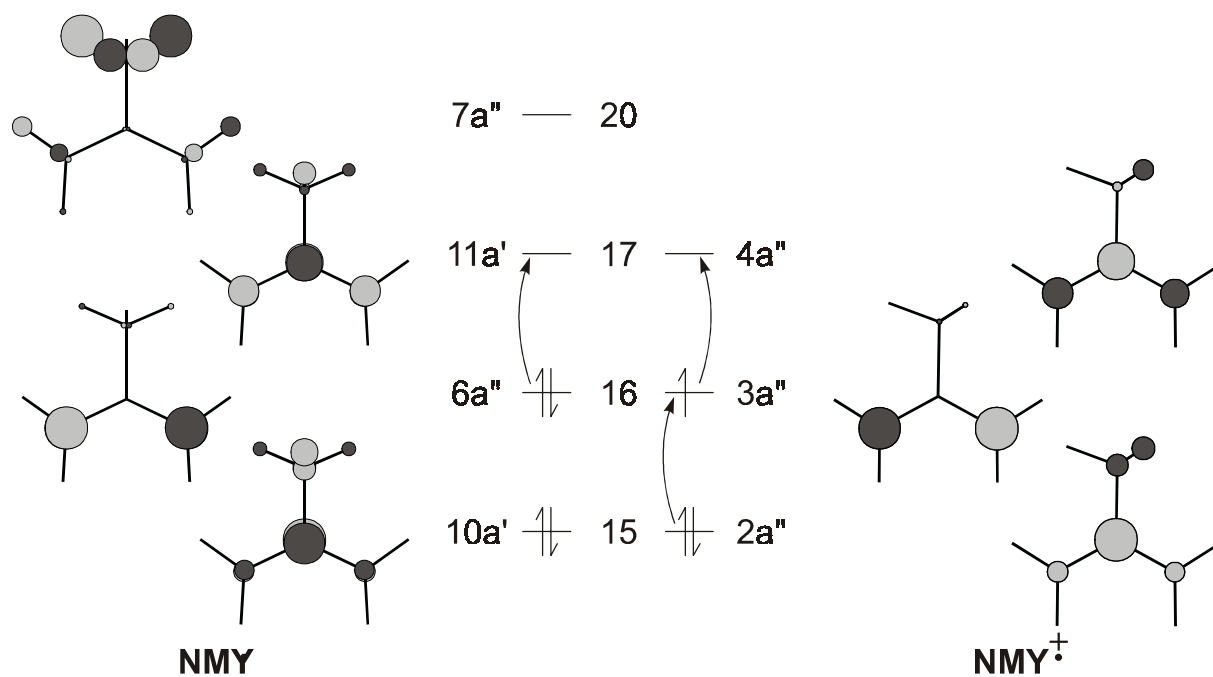
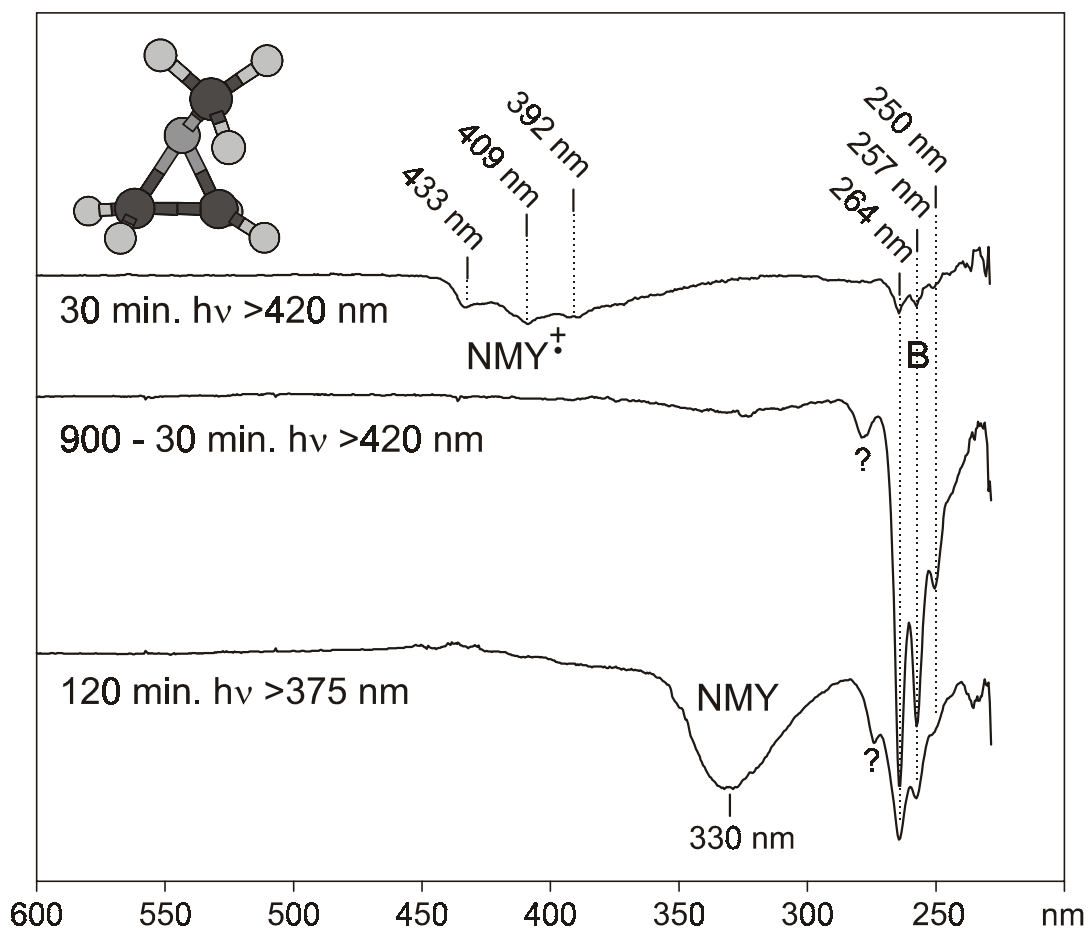Figure 4-22: SCF MOs of **NMY$^{+\cdot}$** and **NMY** with CASSCF predicted main electronic transitions.

Figure 4-23: EA difference spectra of **NMA** after irradiation at >420 nm and at >375 nm.

4.3.3.2 IR-spectra

In the IR spectra the peaks that behave like the structured band system peaking at 400 nm in the EA spectra are most prominent. However, they do not match very well with the frequencies of $\mathbf{NMY}^{\ddagger}$ calculated by B3LYP/6-31G* (see Figure 4-24). Surprisingly, no peaks of neutral **NMY** could be observed. in particular, in the IR difference spectrum after 15 min. of irradiation at 313 nm, no band is decreasing around 1580 cm^{-1} where the strongest absorption of **NMY** is predicted.

The reason for the lack of any manifestation of **NMY** in the IR could be that only very little of it is formed (note that the oscillator strength for the electronic transition of **NMY** at 330 nm is more than seven times higher than that of the 409 nm transition of $\mathbf{NMY}^{\ddagger}$. Hence about seven times less **NMY** is formed, presumably due to efficient decomposition of this molecule by loss of methane, see below.

At 870 cm^{-1} a peak increases after 45 min. of ionization and continues to grow on longer X-irradiation. It behaves like the electronic transitions at 264, 257, and 250 nm and also like an IR peak at 1915 cm^{-1}. This 870 cm^{-1} peak is the strongest band of the azoallenic species $HC=N=CH_2$ which was also observed after prolonged X-irradiation of **A**. However, we were not able to locate this peak in those experiments because it was too close to bands of neutral **A** which decreased strongly on ionization.

Table 4-6: Excited states of $\mathbf{NMA}^{\ddagger}$ calculated by CASPT2.

states	CASPT2			CASSCF configurations [b]
	eV	nm	f^{a}	
1^{2}A'	-	-	-	81% (11a')^1
				17% (10a')^1
1^{2}A"	3.93	316	0.0001	97% 5a" $\rightarrow$ 11a'
2^{2}A'	3.94	315	0.009	81% (10a')^1
				17% (11a')^1
2^{2}A"	5.53	224	0.033	96% 4a" $\rightarrow$ 11a'

[a] Oscillator strength for electronic transition.
[b] Active space: 15 electrons in 4 doubly and 1 singly occupied a' and in 3 occupied + 1 virtual a" MOs. Occupied MOs depicted in Figure 4-18.

Furthermore, two peaks at 1028 and at 1216 cm^{-1} increase also on longer X-irradiation and therefore they must be absorptions of neutral molecules. They could not be bleached and we were also not able to assign them to any species.

Further work will be required to elucidate all details of the chemistry of **NMA** on X-irradiation and to improve the agreement between measured and calculated IR bands of **NMY**$^{+\cdot}$.

Figure 4-24: IR difference spectra of **NMA** (**a**) after (45 min.) and (**b**) (180 - 45 min.) X-irrad.; (**c**) after 45 min. irrad. at >475 nm and (**d**) after 40 min. >420 nm. (**e**) spectrum of **NMY**$^{+\cdot}$ calculated on B3LYP/6-31G* level, all frequencies scaled by a factor of 0.96.

4.4 N-Phenylaziridines

4.4.1 Experimental part

A PE spectrum of N-phenylaziridine, **NPA**, was measured in 1982 by two groups [112, 113]. It is shown in Figure 4-25 together with the PE spectrum of N,N-dimethylaniline, **DMA**, measured in 1968 by Baker, May and Turner and remeasured in our laboratory[12] [114]. Additionally, the calculated[13] MOs of these molecules are plotted in this figure.

The similarity of the two PE spectra is obvious: the three first peaks show the same shape, and they can be assigned to the same sequence of MOs. Compared to **NPA** the first and the third bands in **DMA** are slightly shifted towards lower energy, whereas the second one has almost the same energy. This is due to the fact that the HOMO-1 is located exclusively in the phenyl ring because it has a node at the point of substitution. The first and the third MO are the antibonding and the bonding combinations, respectively, of the "bis-allylic" component of the benzene HOMO and the N lone pair.

The main transition in the EA spectrum of **DMA**‡ is known to be at 473 nm [115] which corresponds to 2.62 eV, whereas $I_{v,1}$ - $I_{v,2}$ in the PE spectrum of **DMA** amounts to 2.41 eV. This difference is explained in Figure 4-26. In the PE spectrum we see electronic state energies of the radical cation at the *neutral* geometry, whereas in the UV/Vis spectrum of radical cation we see transitions between the same electronic states at the *radical cation* geometry. The N-C$_{Ph}$ bond in **DMA** is *antibonding* in the HOMO and therefore ionization causes a *shortening* of this bond compared to the neutral molecule. On the other hand in the HOMO-2 this interaction is *bonding* and therefore ionization from this MO causes a *lengthening* of the N-C$_{Ph}$ bond. These opposite effects result in an increase of the vertical distance between the potential curves of these two states on ionization and therefore to a higher excitation energy in the UV/Vis spectrum.

In **NPA** (see Figure 4-26) the MO coefficients at the N-C$_{Ph}$ bond are even larger, which amplifies this effect.

---

[12] Acknowledgement to Ms. A.-C. Sergenton.

[13] B3LYP/6-31G* MOs.
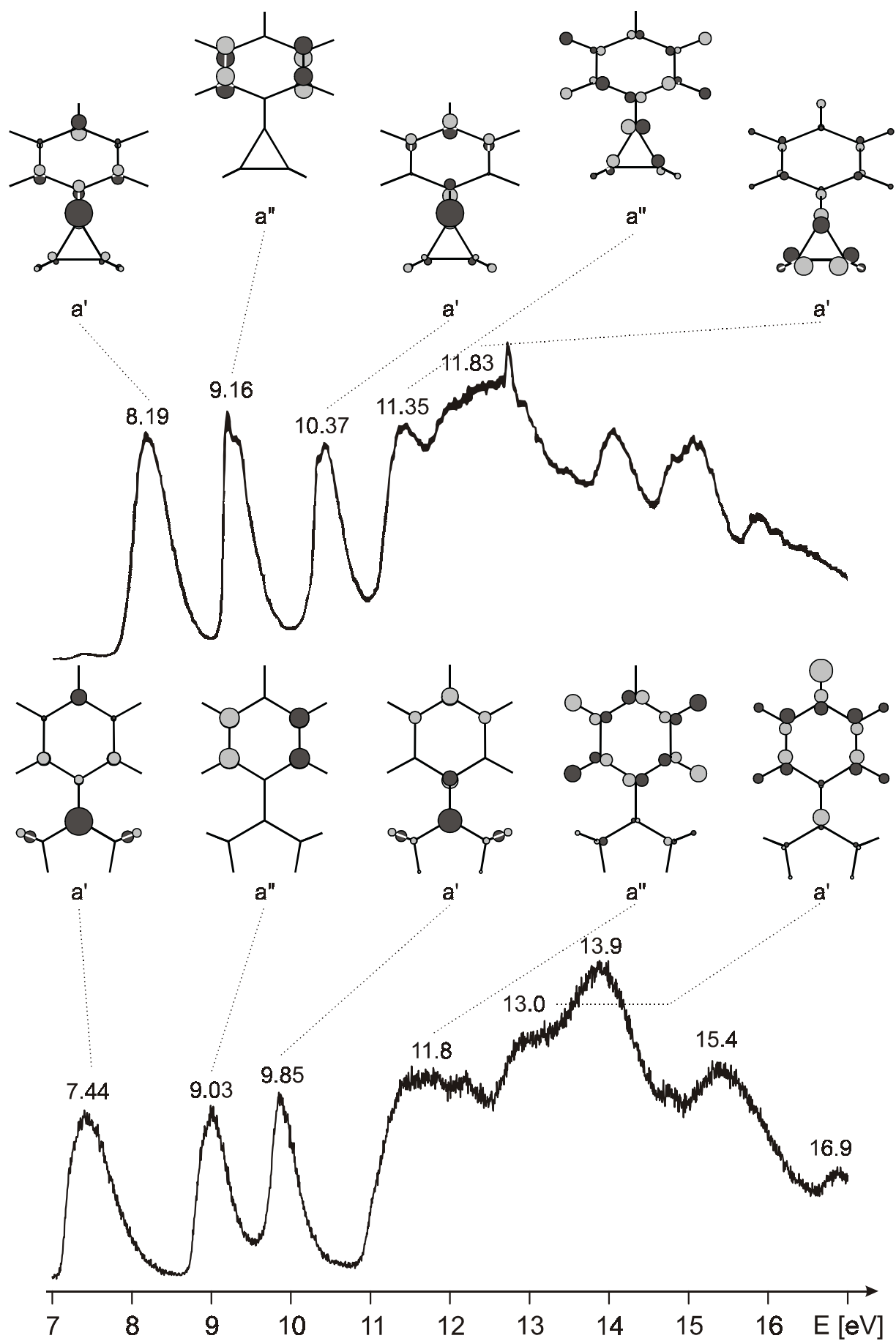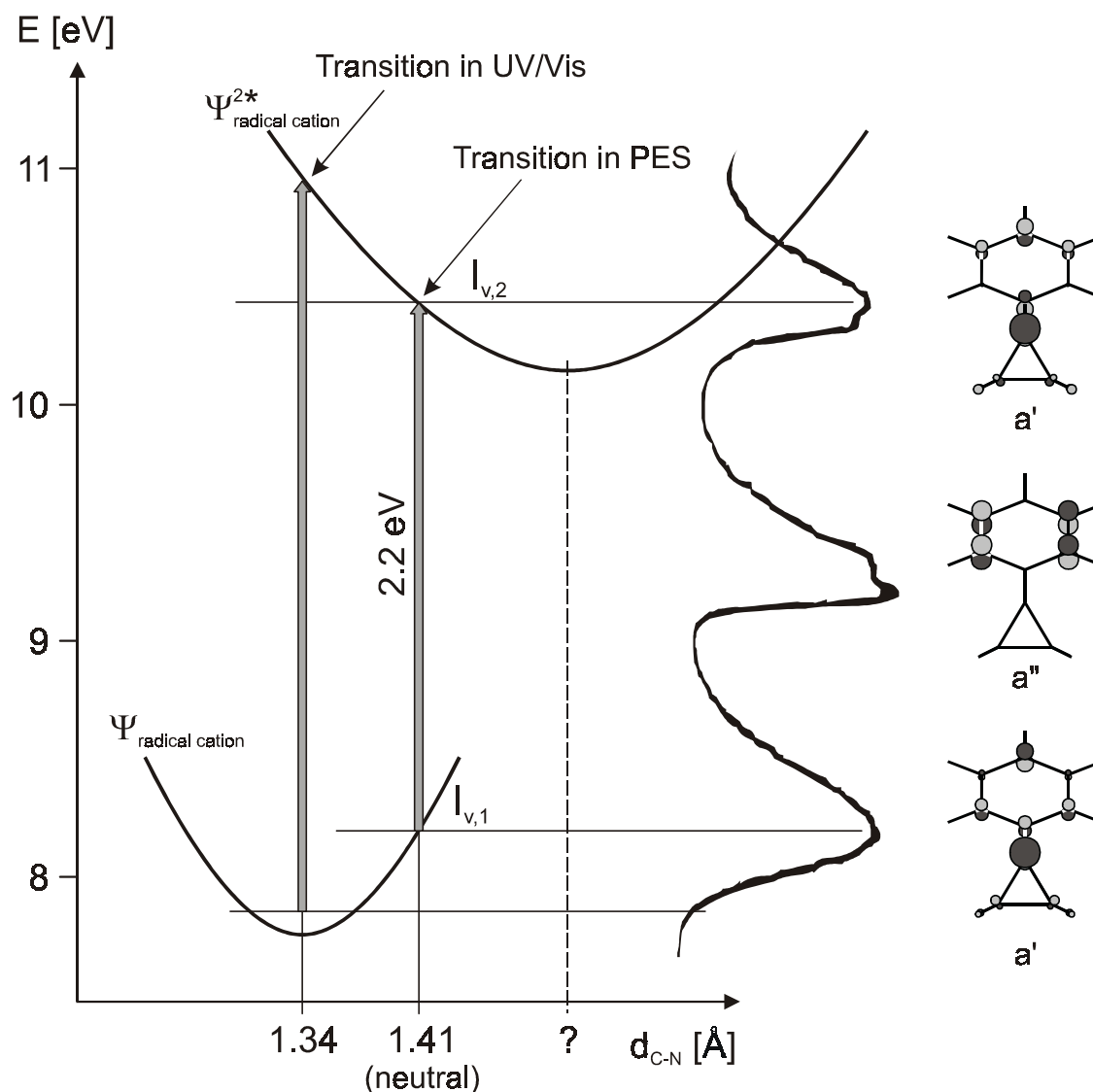
Figure 4-25: PE spectrum of **NPA** and of **DMA**.

Figure 4-26: Potential energy curves along the C-N bond length of **NPA**$^{+\cdot}$ (ground state and 2nd exited state) together with PE spectrum.

After ionization of **NPA** a band at 446 nm with a shoulder at 428 nm appears in the EA-spectrum. This spectrum looks very similar to that of N,N-dimethylaniline radical cation (**DMA**$^{+\cdot}$) which has a very nice intense yellow color, although the absorption of **NPA**$^{+\cdot}$ is slightly blue-shifted compared to **DMA**$^{+\cdot}$ (see Figure 4-1).

Ionized C-methyl-N-phenylaziridine (**PMA**) and C,C'-dimethyl-N-phenyl-aziridine (**PDMA**) have very similar EA-spectra where the main band is only red-shifted by 6 nm for ionized **PMA** and by 7 nm for **PDMA**. The shoulder on the high energy side gets weaker in the C-substituted species.
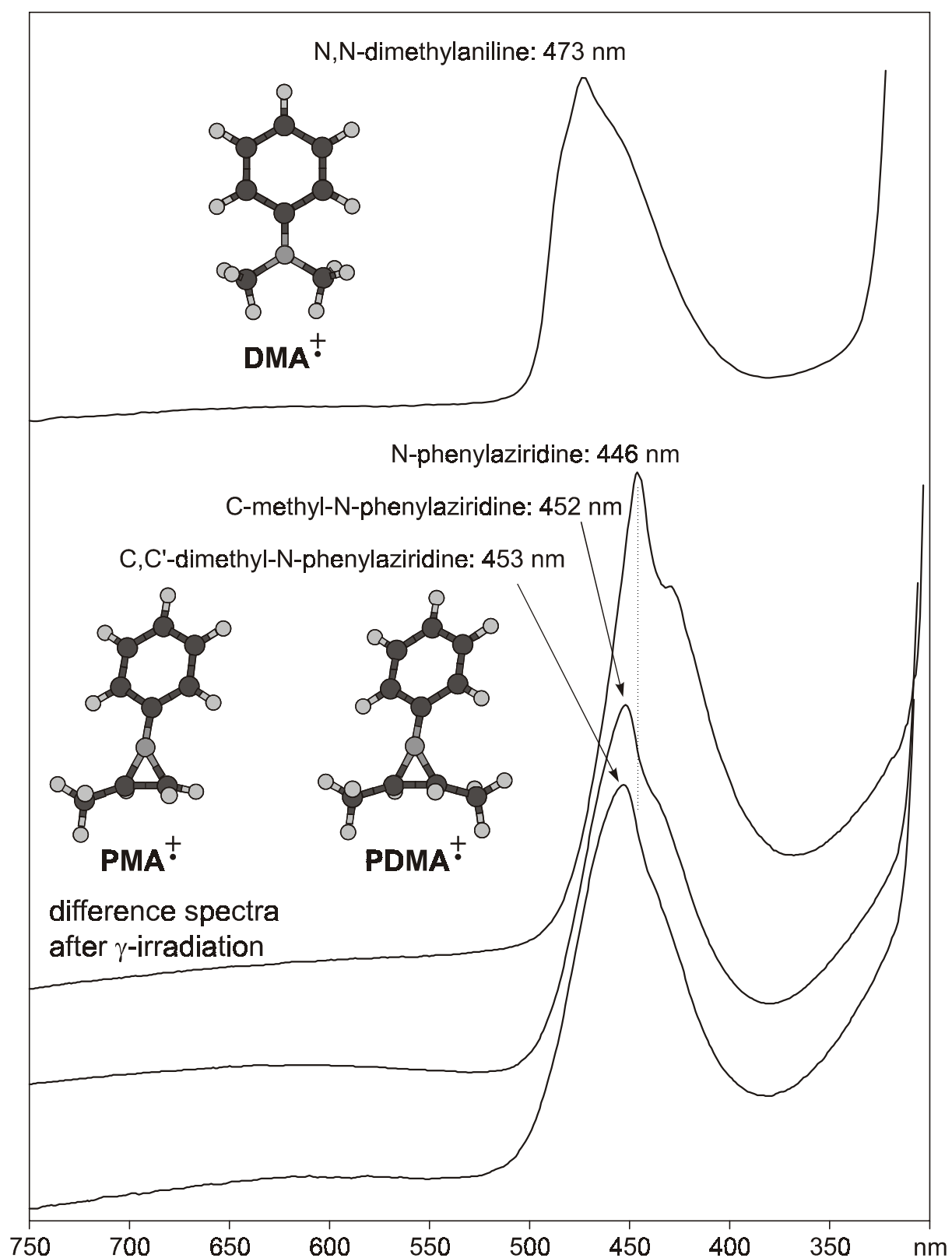
Figure 4-27: Spectra of γ-irradiated C-methyl substituted **NPA** and **DMA** in Freon glasses.

The parallel behavior of these three species shows that C-methyl substitution does not entail notable changes in the electronic structure of **NPA$^{+\cdot}$**.
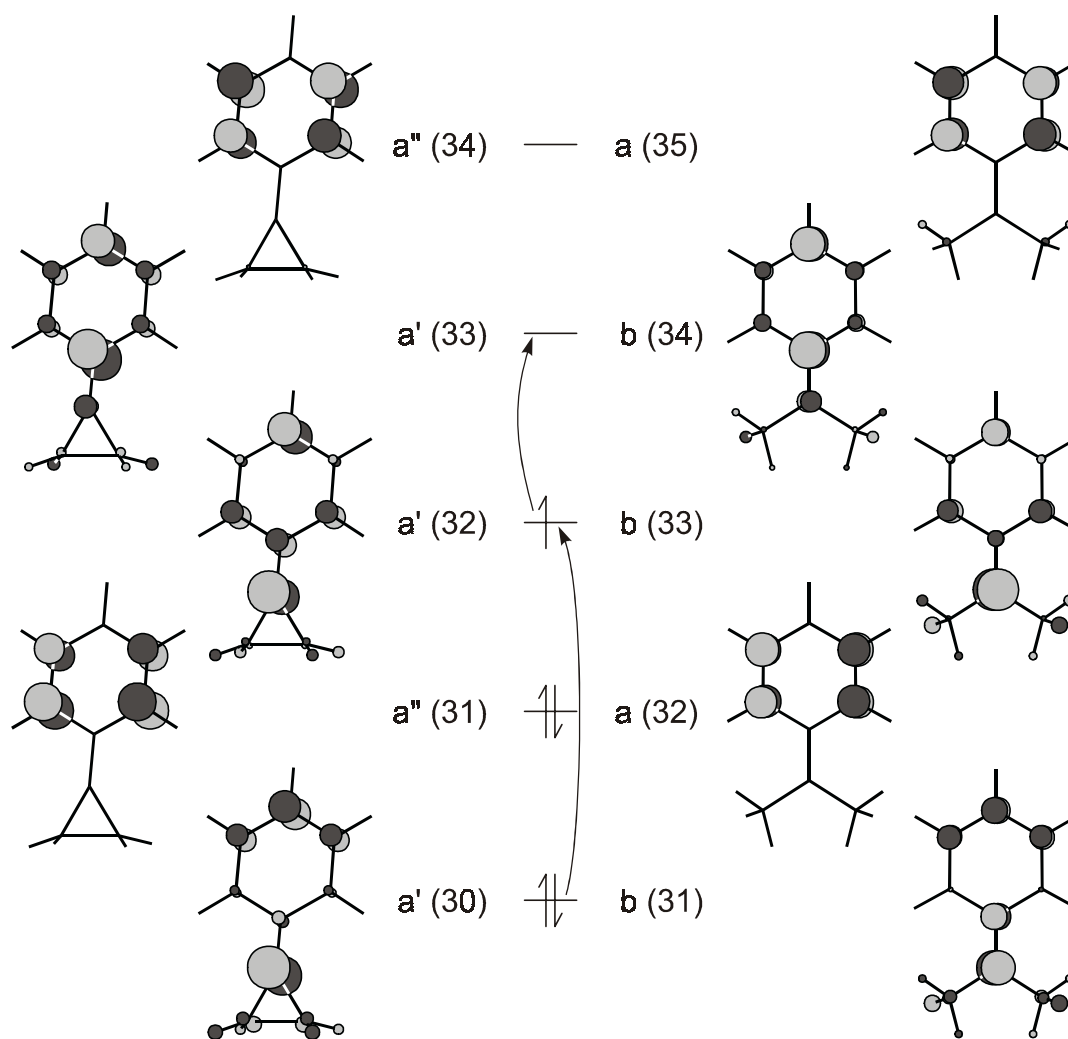
Figure 4-28: HF MOs of **NPA** and **DMA**. Main excitations in radical cations indicated by arrows.

The similarity of the EA-spectra of ionized **NPA** and **DMA** is a strong indication that **NPA** remains ring-closed on ionization. Also, subsequent irradiations at different wavelengths do not lead to any changes in the spectrum, hence ring-opening cannot be induced by light.

The nature of the electronic transition responsible for the intense bands in **NPA**[+] and its C-methyl derivatives may be explained by a td-B3LYP calculation which predicts a strong transition (oscillator strength $f = 0.0123$) at 397 nm which is mainly composed of SOMO-2 $\rightarrow$ SOMO ($\pi \rightarrow \pi$) and of SOMO $\rightarrow$ LUMO excitation ($\pi \rightarrow \pi^*$) (see Table 4-7 and Figure 4-28, left side). The SOMO-1 $\rightarrow$ SOMO transition, predicted at 690 nm is not visible in the EA-spectrum because of it's small oscillator strength ($f = 0.0001$). Although quantitative agreement between experiment and theory leaves to be desired, the

nature of the electronic transition is probably correctly described by td-B3LYP (see Figure 4-28).

For **DMA**$^{+}$, td-B3LYP predicts a strong transition at 420 nm and a weak one at 682 nm ($f = 0.0017$). Thus, the shift of the electronic excitations going from **DMA**$^{+}$ to **NPA**$^{+}$ (calc.: 23 nm, obs.: 27 nm) is reproduced correctly by this method. For **PMA**$^{+}$ and **PDMA**$^{+}$ td-B3LYP shows red-shifts of the strongest band of only 2 nm and 5 nm respectively, which represents a slight underestimation (exp.: 8 nm and 9 nm respectively).

Table 4-7: Results of td-B3LYP calculations on the radical cations of **NPA** and **DMA**.

radical cation	state	f ^{b}	λ [nm]	excitations ^{a}	weighting factor
NPA^{+}	1^2A"	0.0001	690	31a" $\rightarrow$ 32a'	1.04
	1^2A'	0.0123	397	32a' $\rightarrow$ 33a'	0.45
				30a' $\rightarrow$ 32a'	0.95
	2^2A'	0.0046	287	31a" $\rightarrow$ 34a"	0.90
				32a' $\rightarrow$ 33a'	0.41
				26a' $\rightarrow$ 32a'	0.35
				31a" $\rightarrow$ 33a'	0.71
DMA^{+}	1^2B	0.0017	682	32a $\rightarrow$ 33b	1.01
	1^2A	0.1088	420	33b $\rightarrow$ 34b	0.39
				31b $\rightarrow$ 33b	0.94
	2^2A	0.0121	289	32a $\rightarrow$ 35a	0.79
				33b $\rightarrow$ 34b	0.28
				28b $\rightarrow$ 33b	0.38
				32a $\rightarrow$ 34b	0.63

^{a} Oscillator strength for electronic transition.

^{b} MOs see in Figure 4-28.

4.4.2 Mechanistic considerations

The above observation raises the question why parent aziridine radical cation, $\mathbf{A}^{+\cdot}$, spontaneously undergoes ring-opening on ionization, whereas the N-phenyl derivative $\mathbf{NPA}^{+\cdot}$ does not. One reason may be the differences of the SOMOs of these two species from which the ionization occurs. In the case of the parent compound the non-bonding MO (NBMO) mixes with the bonding σ-orbital of the C-C bond. On ionization this mixing gets stronger and therefore the C-C σ-bond looses electron density (see Figure 4-9).

In **NPA** we can also observe this mixing of the NBMO with a C-C σ-orbital, however on ionization it disappears almost completely and hence the C-C bond is barely weakened by the ionization. This can be seen at the geometry of calculated **NPA** and its radical cation (see Figure 4-29). The N-Ph bond of the neutral molecule is bent from the plane by an angle of $\Theta = 53.2°$ and the C-C bond length in the aziridine ring is 1.50 Å. After ionization the pyramidalization angle Θ decreases to 17.4°, but the C-C bond remains almost unaffected with an increase of only 0.02 Å. In spite of the high formal charge on the N-atom, $\mathbf{NPA}^{+\cdot}$ remains slightly pyramidal (however, planarization of $\mathbf{NPA}^{+\cdot}$ to C_{2v} symmetry requires only 0.09 kcal/mol *before* and -0.09 kcal/mol (!) *after* correction for ZPVE differences).
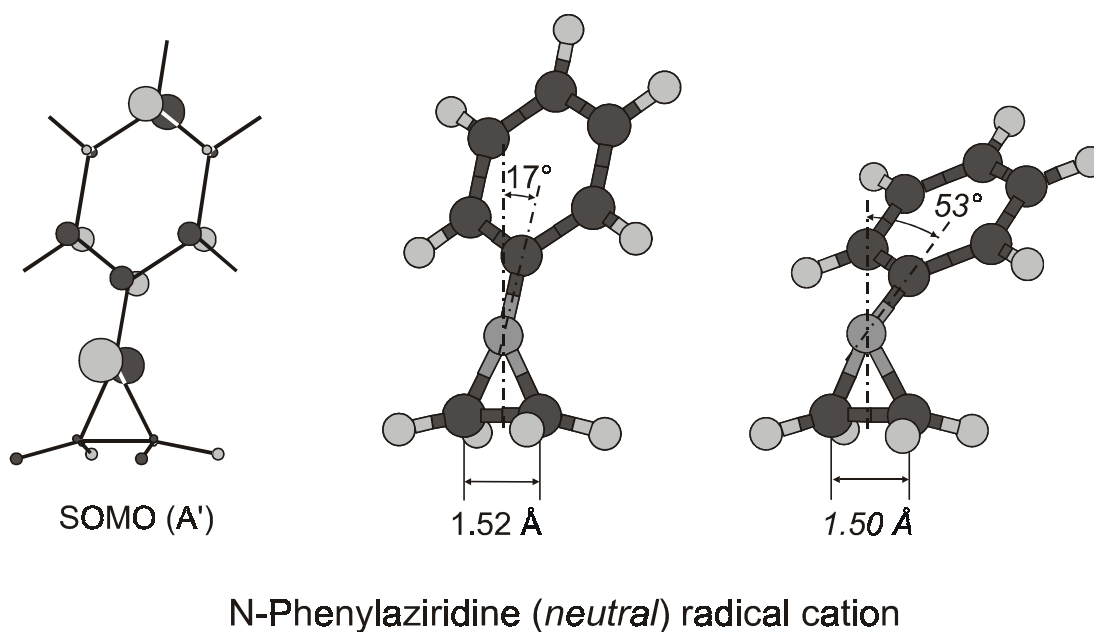

SOMO (A')   1.52 Å   1.50 Å

N-Phenylaziridine (*neutral*) radical cation

Figure 4-29: SOMO and geometry of $\mathbf{NPA}^{+\cdot}$ and geometry of neutral **NPA**.

Another, perhaps more important reason for the stability of $\mathbf{NPA}^{+\cdot}$ is the benzylic resonance that stabilizes the N-Ph moiety. It is lost on ring-opening, because in the N-phenylazomethine ylid, $\mathbf{NPY}^{+\cdot}$, the phenyl ring is attached at a nodal site of the allylic SOMO. A measure for the resonance stabilization of $\mathbf{NPA}^{+\cdot}$ is given by the barrier for rotation of the phenyl ring which is calculated to be 26.3 kcal/mol[14]. On the other hand, rotating the phenyl ring in $\mathbf{NPY}^{+\cdot}$ into a position perpendicular to the allylic CNC plane requires only 0.6 kcal/mol (to rotate the phenyl ring into plane requires 4.7 kcal/mol because of the steric repulsion between the H atoms). As a consequence, this loss of resonance energy of the ring-opening which was exothermic by 24.2 kcal/mol in N-methylaziridine, $\mathbf{NMA}^{+\cdot}$, becomes endothermic by 1.2 kcal/mol in $\mathbf{NPA}^{+\cdot}$ - a difference of 25.4 kcal/mol which is almost identical to the difference of benzylic resonance stabilization energies between $\mathbf{NPA}^{+\cdot}$ and $\mathbf{NPY}^{+\cdot}$ (26.3 - 0.6 = 25.7 kcal/mol). This drastic change in the overall thermochemistry affects of course also the barrier for the ring-opening which increases from 10.5 kcal/mol in $\mathbf{A}^{+\cdot}$ (16.0 kcal/mol in $\mathbf{NMA}^{+\cdot}$) to 33 kcal/mol in $\mathbf{NPA}^{+\cdot}$.

This strong increase in the ring-opening barrier can also be explained with benzylic resonance: twisting the phenyl ring in the ring-opening transition state by 90° (at the TS the phenyl ring has not effected any rotation relative to the aziridine ring) leads to a second order saddle point[15] and requires only 9.6 kcal/mol. Therefore we have lost 26.3 - 9.6 = 16.7 kcal/mol of the benzylic resonance at the TS. It remains 33 - 16.7 = 16.3 kcal/mol of the total ring-opening barrier which is very close to that of $\mathbf{NMA}^{+\cdot}$ (16.0 kcal/mol). (cf. Figure 4-30)

The phenyl ring and the heteroallylic plane of $\mathbf{NPY}^{+\cdot}$ are twisted by 53° and the SOMO is the same as for the parent radical cation, with a node at the N-atom.

---

[14] If this twisted conformation of $\mathbf{NPA}^{+\cdot}$ is constrained into C_{2v} symmetry where the N atom is not pyramidalized we obtain a second order saddle point which is 26.7 kcal/mol above $\mathbf{NPA}^{+\cdot}$. All the energies in this paragraph are calculated by B3LYP/6-31G*, corrected for ZPVE differences at the same level.

[15] This point was calculated by optimizing a Z-matrix of the TS where all the parameters were previously converged and only the dihedral angle between the phenyl ring and the aziridine moiety was frozen in a 90° twisted position.
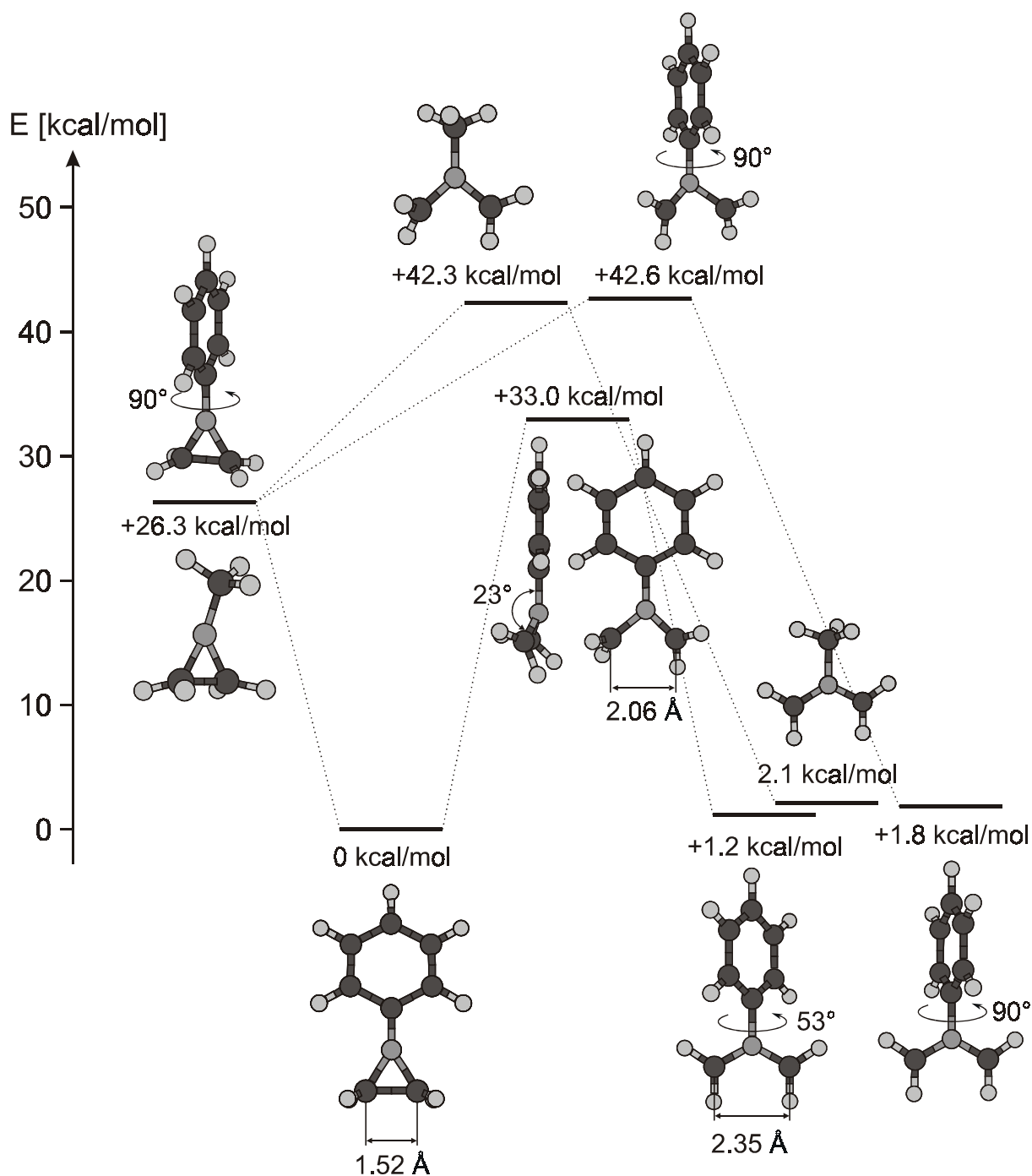
Figure 4-30: Comparison between the ring-opening thermochemistry of **NMA**[+.], and of normal and phenyl-ring twisted **NPA**[+.].

Rotation of one of the allylic methylene groups in **NPY**[+] requires 16.7 kcal/mol, a typical number for such allylic systems (Sustmann [116] has measured the rotational barrier to be 15.7 ± 1.0 kcal/mol in the allyl radical). This low lying transition state indicates the possibility of a pathway for ring-opening of **NPA**[+] that does not lead through the high-lying TS in Figure 4-32.
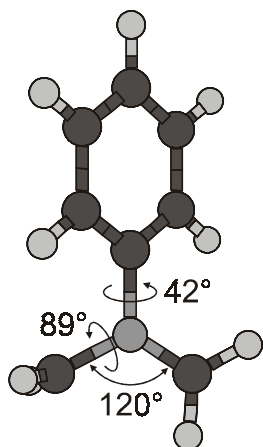
Figure 4-31: TS for the rotation of one methylene group of ring-opened $\mathbf{NPA}^{+\cdot}$ which is lying 16.7 kcal/mol higher than closed $\mathbf{NPA}^{+\cdot}$.

In order to find out whether there is a lower lying TS for the ring-opening of $\mathbf{NPA}^{+\cdot}$ we scanned the potential energy surface by stepping the parameters which change most during the ring-opening process, i.e. the CNC angle α of the ring which grows from 62° to 122°, and the dihedral angle β between the phenyl ring and the aziridine ring which increases from 0° to 53°. For this calculation the geometry of $\mathbf{NPA}^{+\cdot}$ was defined by a Z-matrix whereby the geometry of the phenyl ring was frozen and the angle between the two rings was defined by way of a dummy atom standing perpendicularly to the aziridine ring above the nitrogen atom (see Figure 4-32).

First the dihedral angle β was fixed and the angle α was opened from 62° to 122° in increments of 8°. At the angle of $\alpha = 92°$ the first methylene group suddenly rotates by 90° into the plane of symmetry and at $\alpha = 98°$ the other methylene group follows and the molecule stays in C_s symmetry for further increases of α (the rotation of the methylene groups cannot occur at the same time because the steric interaction between the two endo-allylic hydrogens would be too strong at this small angle α).

Secondly the dihedral angle β was decreased from 90.0° to 84.7° in steps of 5.3° and the angle α scanned back from 122° to 62°. Again, a sudden rotation of the methylene groups takes place between $\alpha = 86°$ and 98°. While the angle α decreases, the open form reaches a geometry which looks very similar to the TS for the rotation of one methylene group. However, the ground state surface of the ring-closed $\mathbf{NPA}^{+\cdot}$ can never be reached without a further uphill step towards a geometry similar to that of the TS for the ring-opening found previously.
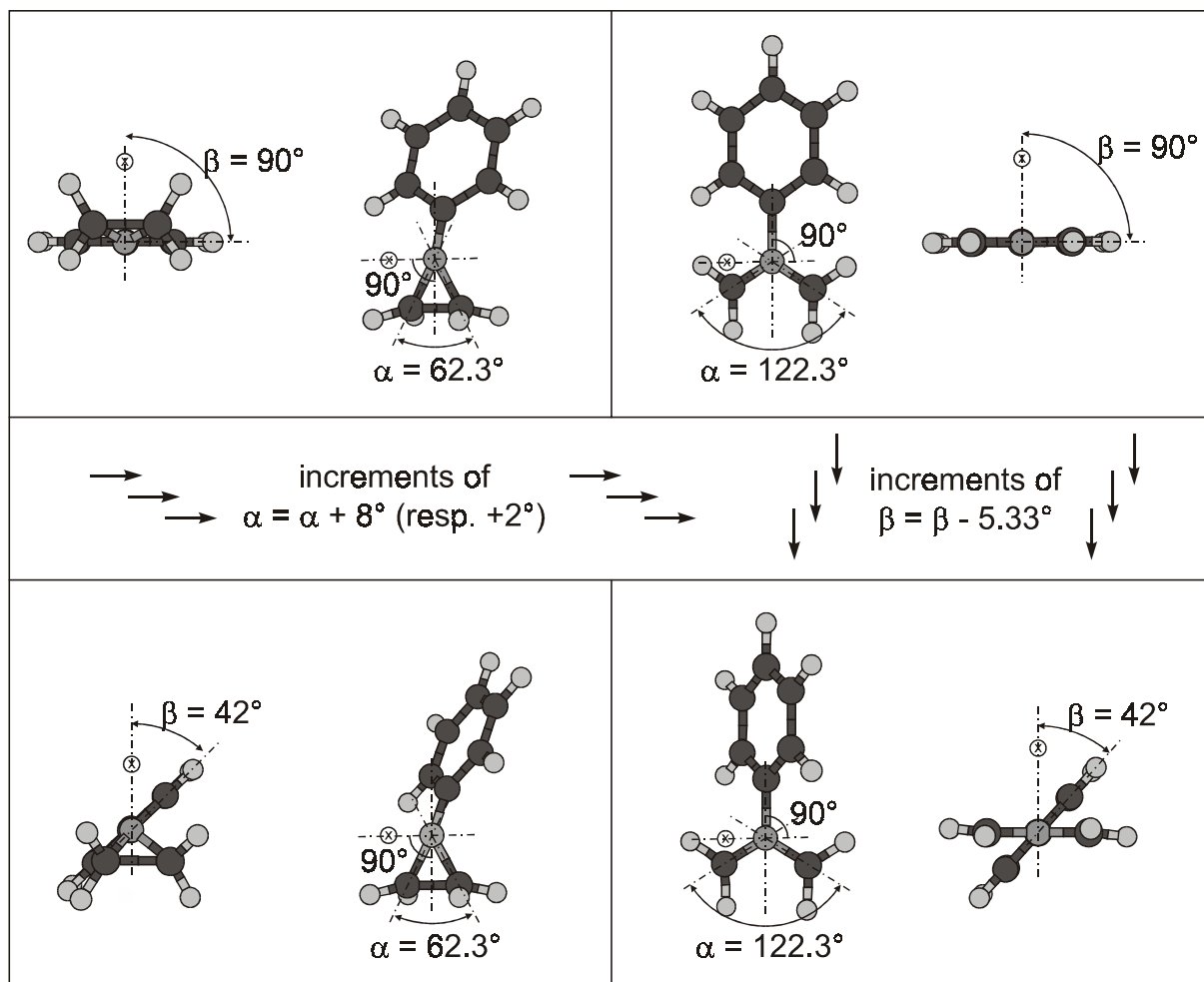
Figure 4-32: Geometries of the starting and the ending structures for the **NPA**$^{+\cdot}$ hypersurface scan.

With this procedure the geometries corresponding to all possible combinations of the angles α and β were optimized. In a second calculation the part between the angles $\alpha = 86°$ and $98°$ where the sudden rotations of the methylene groups take place was scanned again in increments of $1°$ to follow the way uphill until the radical cation "falls down" on the other hypersurface. Especially on the way from the allylic form to the closed aziridine ring the energies increase steadily (until 46 kcal/mol higher than ring-closed **NPA**$^{+\cdot}$). On the other hand the ring-closed radical cation "realizes" quite early that it can escape the constraint of the increase of the angle α by taking an allylic conformation (see Figure 4-33). However, no transition state was found at lower-lying energy than that found previously and shown in Figure 4-30. The lowest transition was found 34.4 kcal/mol above **NPA**$^{+\cdot}$ at $\alpha = 95.3°$ and $\beta = 84.7°$, which is very close to the true TS ($\alpha = 95.9°$ and $\beta = 85.4°$).
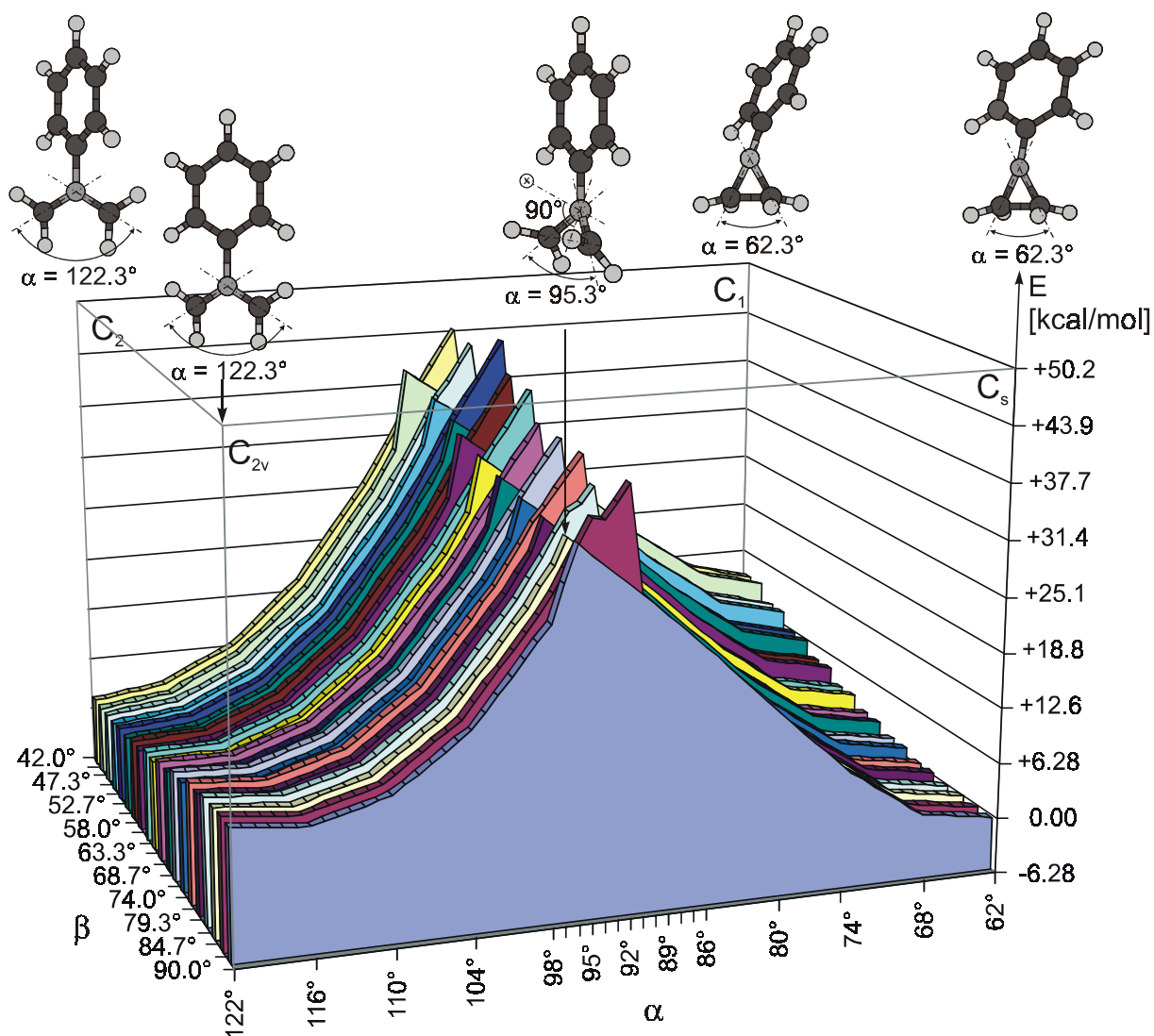
Figure 4-33: Scan of the hypersurfaces of **NPA**$^{+\cdot}$, closed and open.

Thus, we exclude an alternative pathway for ring-opening of **NPA**$^{+\cdot}$ and note that the high barrier precludes this process.

4.4.3 C-Methyl substituted N-phenylaziridines

At the B3LYP/6-31G* level the potential energy surface of the radical cation of ring-closed N-phenyl-C-methyl aziridine (**PMA**$^{+\cdot}$) shows two minima. The phenyl ring can stand *syn* or *anti* to the methyl group (Figure 4-34). The energy difference of these two minima is only 0.014 kcal/mol and the pyramidalization angle Θ is 17.8° for the *syn* conformation and 19.2° for the *anti* conformation of **PMA**$^{+\cdot}$. These values are very close to that in **NPA**$^{+\cdot}$ ($\Theta = 17.4°$). The N inversion barrier is also very small (0.13 kcal/mol), and disappears after

correction for the ZPVE difference (-0.06 kcal/mol), similar to $\mathbf{NPA^+}$ (see section 4.4.2). The radical cation of the *dimethyl* derivative, $\mathbf{PDMA^{+\cdot}}$, is also pyramidalized ($\Theta = 20.3°$, $\Delta E^{\ddagger}$(inversion) = 0.18 kcal/mol, -0.04 kcal/mol after correction for ZPVE differences).
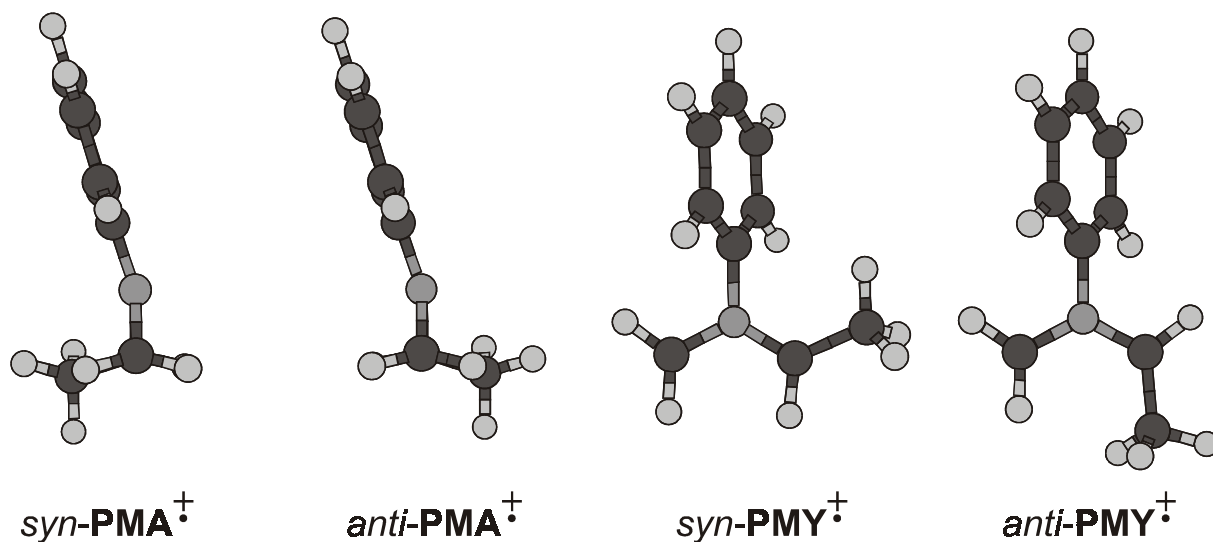

$syn\text{-}\mathbf{PMA^{+\cdot}}$ $\qquad$ $anti\text{-}\mathbf{PMA^{+\cdot}}$ $\qquad$ $syn\text{-}\mathbf{PMY^{+\cdot}}$ $\qquad$ $anti\text{-}\mathbf{PMY^{+\cdot}}$

Figure 4-34: Structures of *syn*- and *anti*-$\mathbf{PMA^{+\cdot}}$ and $\mathbf{PMY^{+\cdot}}$.

The ring-opened $\mathbf{PMA^{+\cdot}}$, called $\mathbf{PMY^{+\cdot}}$, show also two minima which correspond to a *syn* or an *anti* position of the methyl group relative to the phenyl ring. As in $\mathbf{NPY^+}$ the phenyl ring is twisted from the allylic plane, but in *syn*-$\mathbf{PMY^+}$ the dihedral angle is higher (74°) than in the *anti*-conformation (57°) because of steric interactions witch lead to a slightly greater stability of the *anti*-conformation of 0.77 kcal/mol.

In ring-opened $\mathbf{PDMA^{+\cdot}}$, called $\mathbf{PDMY^+}$, three different conformers exist: *syn-syn*, *syn-anti*, and *anti-anti*. The most stable one is the *syn-anti* conformation because of the lowest steric interactions. In that conformation the phenyl ring is twisted by 78° from the allylic plane. It requires only 0.023 kcal/mol to bring it into a perpendicular conformation.

In the *syn-syn* conformation, which is 0.63 kcal/mol less stable than the *syn-anti* conformation, the phenyl ring is perpendicular to the allylic plane. Therefore this radical cation has C_{2v} symmetry ($^2A_2$ ground state). The highest energy conformation is *anti-anti*-$\mathbf{PDMY^+}$ where the phenyl ring is rotated 57° from the allylic plane. Because of the rather strong steric interactions of the two

methyl groups this conformation of the radical cation lies 3.6 kcal/mol higher in energy than the *syn-anti* one. It has C_2 symmetry with a ^2A ground state.

The ring-opening reaction of **PMA**$^{+\cdot}$ proceeds by way of a TS which lies 28.6 kcal/mol above the reactant and has a very similar structure as that for the **NPA**$^{+\cdot}$ ring-opening reaction. The methyl group is positioned *anti* to the phenyl ring. An IRC calculation shows that the reaction ends at the slightly higher lying *syn*-**PMY**$^{+\cdot}$. Therefore the stereochemistry of the ring-opening is conrotatory and it shows an exothermicity of 2.9 kcal/mol.

Also the ring-opening reaction of **PDMA**$^{+\cdot}$ ends in the second lowest lying conformer *syn-syn*-**PDMY**$^{+\cdot}$. The TS looks again very similar to that for the **NPA**$^{+\cdot}$ ring-opening. The reaction barrier is 24.1 kcal/mol and the exothermicity is 6.1 kcal/mol. The ring-opening is again conrotatory. The results are summarized in Table 4-8.

Table 4-8: Thermochemistry of the ring-opening reaction of **NPA**$^{+\cdot}$ and C-methylated **NPA**$^{+\cdot}$.

compound	ΔE_0 [a] [kcal/mol]	barrier $\Delta E_0^{\ddagger}$ [a] [kcal/mol]
NPA$^{+\cdot}$	+1.2	33.0
PMA$^{+\cdot}$	-2.9	28.6
PDMA$^{+\cdot}$	-6.1	24.2

[a] B3LYP/6-31G* energies, corrected ZPVE differences.

Obviously the exothermicity increases and the barrier decreases going to C-substituted compounds. This may be explained by the fact that the methyl groups extend the heteroallylic system and can therefore stabilize the ring-opened product and the transition state by hyperconjugation.

4.4.4 N-(p-Cyanophenyl)aziridine

As explained above, aziridine radical cations must cross from the (unreactive) n_N ionized state to the (reactive) σ_{C-C} ionized state to undergo efficient ring-opening. Hence, a possible strategy to accelerate this reaction is to narrow the gap between these two states, for example by attaching electron-withdrawing substituents to the N-phenyl ring. In this perspective we investigated N-(p-cyanophenyl)aziridine (**NPA-CN**).

However, on ionization of **NPA-CN** a strong band at 488 nm with a shoulder at higher energy appears in the EA-spectrum. This spectrum looks very similar to that of **NPA**$^+$, but it red-shifted by 42 nm (see Figure 4-35). This is no indication for a ring-opening of **NPA-CN**$^+$, and even subsequent photolyses do not change the spectrum (the matrix keeps its weak orange color).
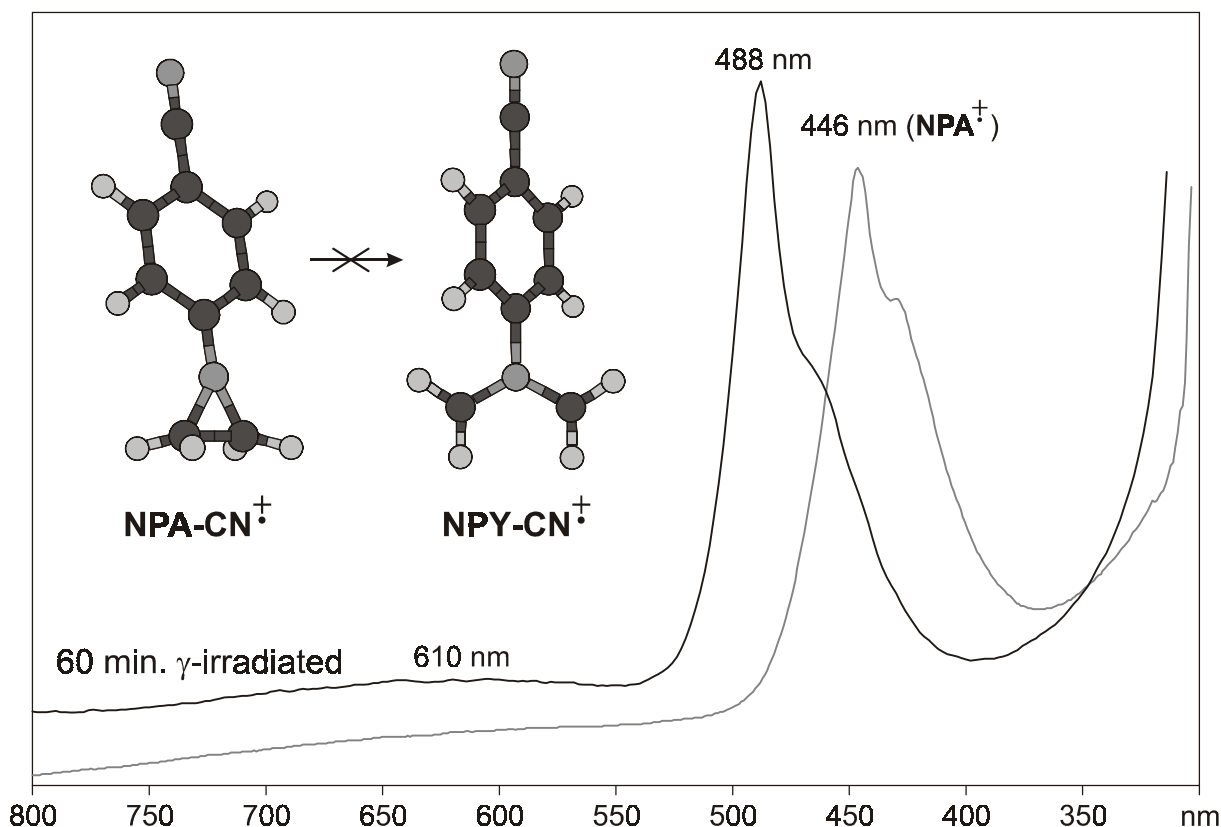

Figure 4-35: EA difference spectrum of ionized **NPA-CN** (black) in Freon glass at 77 K with the analogous spectrum of **NPA** (gray).

Calculations confirm this behavior. The thermochemistry does not change much compared to **NPA**$^+$ - the endothermicity has increased to 1.56 kcal/mol

and the activation barrier for the reaction to 33.1 kcal/mol ($\mathbf{NPA}^{+\cdot}$: 1.2 kcal/mol and 33.0 kcal/mol).

The "pyramidalization" angle for $\mathbf{NPA\text{-}CN}^{+\cdot}$ drops from 51.5° for the neutral to 13.2° for the radical cation and the C-C bond length rises from 1.50 Å to 1.52 Å. Inversion of $\mathbf{NPA\text{-}CN}^{+\cdot}$ requires only 0.094 kcal/mol, but to rotate the phenyl ring into a perpendicular conformation requires 26.8 kcal/mol - 0.5 kcal/mol more than in $\mathbf{NPA}^{+\cdot}$. In the open form the ring is twisted by 53.8° from the plane of the allylic system. Thus the benzylic resonance is the decisive factor responsible for the high activation barrier for ring-opening in $\mathbf{NPA}^{+\cdot}$.

Obviously the cyano group at the phenyl ring did not help to provoke ring-opening of $\mathbf{NPA}^{+\cdot}$, whereas it was possible to decrease the reaction barrier by adding methyl groups at the carbons of the aziridine ring.

4.5 C-Phenylaziridines

4.5.1 Experimental EA spectra

Two C-phenylaziridines were investigated: the N-methyl substituted (**MPA**) and the N-t-butyl substituted derivative (**BPA**). On ionization both compounds show very similar spectra (a weak band at 580 nm and a strong band at 398 nm) which can both be bleached with light of λ >590 nm, as shown in Figure 4-36. (The strong band at 296 nm is not affected by photolysis.) The spectra obtained from **BPA** and **MPA** are not distinguishable but they are completely different from that of **NPA**$^{+}$, i.e. the electronic structures of the two ionized compounds are obviously not comparable.
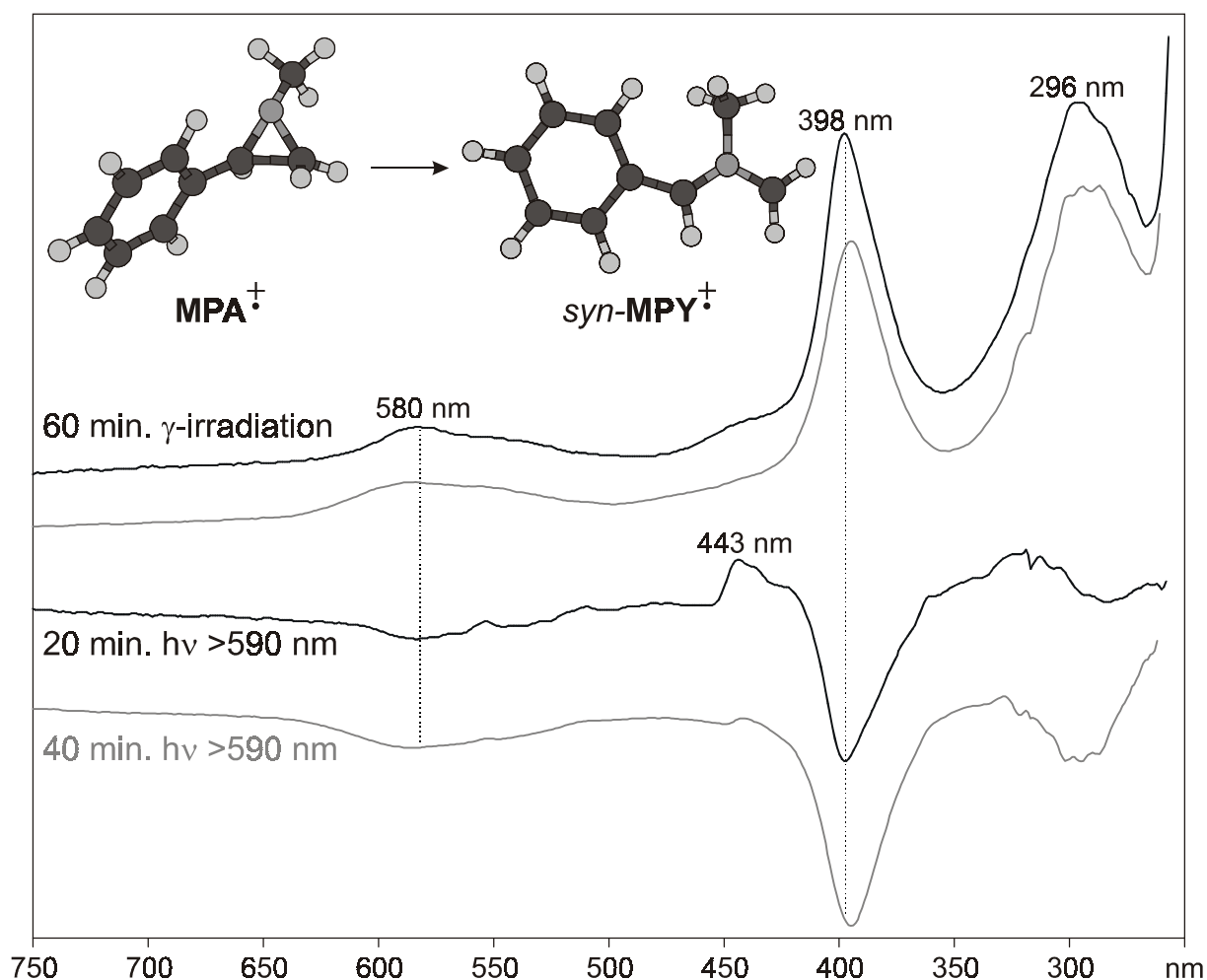

Figure 4-36: EA difference spectra of ionized and photolyzed **MPA** (black) and **BPA** (gray) in Freon glass at 77 K.

4.5.2 Thermochemistry of ring-opening

B3LYP/6-31G* calculations show that ionization in C-phenylaziridines occurs from a phenyl MO which extends strongly into the C-C σ bond of the aziridine, hence that bond is weakened and elongated by 0.12 Å in the process (see Figure 4-37). This weakening of the C-C bond facilitates the ring-opening process remarkably and it is conceivable that this reaction occurs already on ionization.

SOMO

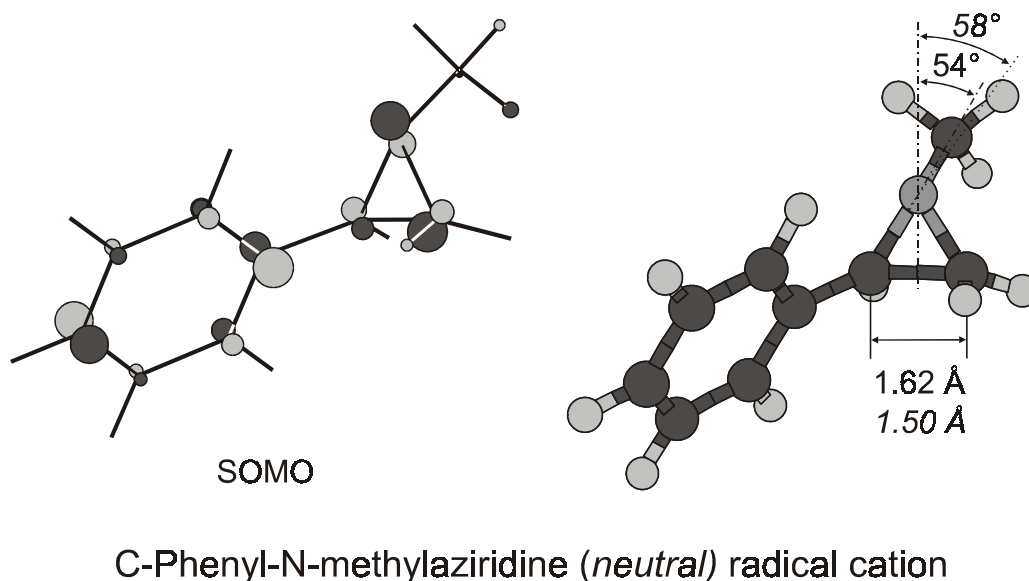C-Phenyl-N-methylaziridine (*neutral)* radical cation

Figure 4-37: Geometry and HOMO of neutral and ionized **MPA**.

After ring-opening, the phenyl ring is attached to a terminal position of the allylic moiety, with which it can therefore enter into resonance. Consequently, the ring-opening process of **MPA**‡ becomes exothermic by 25.0 kcal/mol and the barrier drops to 4.0 kcal/mol[16] (see Figure 4-38) compared to **NMA**‡ where the exothermicity of the ring-opening reaction is 24.2 kcal/mol and the barrier is 16.0 kcal/mol. Interestingly, the effect of the phenyl group on the overall thermochemistry appears to be small. This must be due to the fact that the phenyl ring stabilizes the reactant aziridine radical cation by a similar amount as the product allylic radical cation.

To prove this conjecture we twisted the phenyl ring in the reactant and the product by 90° to suppress the benzylic resonance. We found that this process

---

[16] B3LYP/6-31G*, ZPVE difference corrected energies

requires 7.2 kcal/mol[17] in $\mathbf{MPA}^{+\bullet}$ and 8.0 kcal/mol[18] in *syn*-$\mathbf{MPY}^{+\bullet}$. This confirms that the phenyl rings exert about the same stabilizing effect in both species. Incidentally, the preferential stabilization of $\mathbf{MPY}^{+}$ by 0.8 kcal/mol amounts exactly to the difference in exothermicity of the ring-opening between $\mathbf{MPA}^{+}$ and $\mathbf{NMA}^{+\bullet}$!

The same procedure allowed us to determine the stabilizing influence of the C-phenyl ring on the *transition state* (TS) where a rotational barrier of 18.7 kcal/mol[19] was found. This demonstrates that the stabilizing effect of the phenyl ring is much stronger at the TS than it is at the reactant (7.2 kcal/mol) or the product (8.0 kcal/mol). Moreover, the lowering of the ring-opening activation barrier by 12.0 kcal/mol on going from $\mathbf{NMA}^{+\bullet}$ to $\mathbf{MPA}^{+\bullet}$ is very close to the difference in stabilization by the phenyl ring between $\mathbf{MPA}^{+}$ and its ring-opening TS: 18.7 - 7.2 = 11.5 kcal/mol!

The two conformers of $\mathbf{MPY}^{+}$ have an energy difference of only 0.6 kcal/mol in favor of the *anti* conformation. In both cases steric interactions with an ortho H atom of the phenyl ring are involved (in the *anti*-geometry with an allylic H atom and in the *syn* conformation with the methyl H atoms).

The thermochemical values for the ring-opening process are similar for the differently N-substituted species. However, the exothermicity decreases notably on going to larger N-alkyl substituents: by 7.5 kcal/mol from N-H to N-Me and by another 1.9 kcal/mol from N-Me to N-t-Bu. Obviously, the aziridine radical cation, $\mathbf{A}^{+\bullet}$, profits more from stabilization by an N-alkyl substituent than the

---

[17] B3LYP/6-31G*, ZPVE difference corrected.; the point on the potential energy surface was found by performing a scan where the phenyl group was rotated in increments of 10°; at the energetically highest point we performed a TS search. (By accident we found also the rotation barrier for the methyl group: 1.6 kcal/mol.

[18] B3LYP/6-31G*, ZPVE difference corrected; Because of the C_s symmetry of this structure the radical cation could be optimized in this conformation. The methyl group keeps its position relative to the phenyl ring; the rotation of the group by 60° results in a second order transition state which is 0.02 kcal/mol above the first order TS.

[19] B3LYP/6-31G*, ZPVE difference corrected. Note, that the geometry at a 90° twist angle of the phenyl ring was optimized, as it was done previously in the case of $\mathbf{NPA}^{+\bullet}$.

azomethine ylid radical cation, $\mathbf{Y}^{+\cdot}$, because the latter has a node at the N atom in the SOMO, whereas $\mathbf{A}^{+\cdot}$ has a large coefficient there.
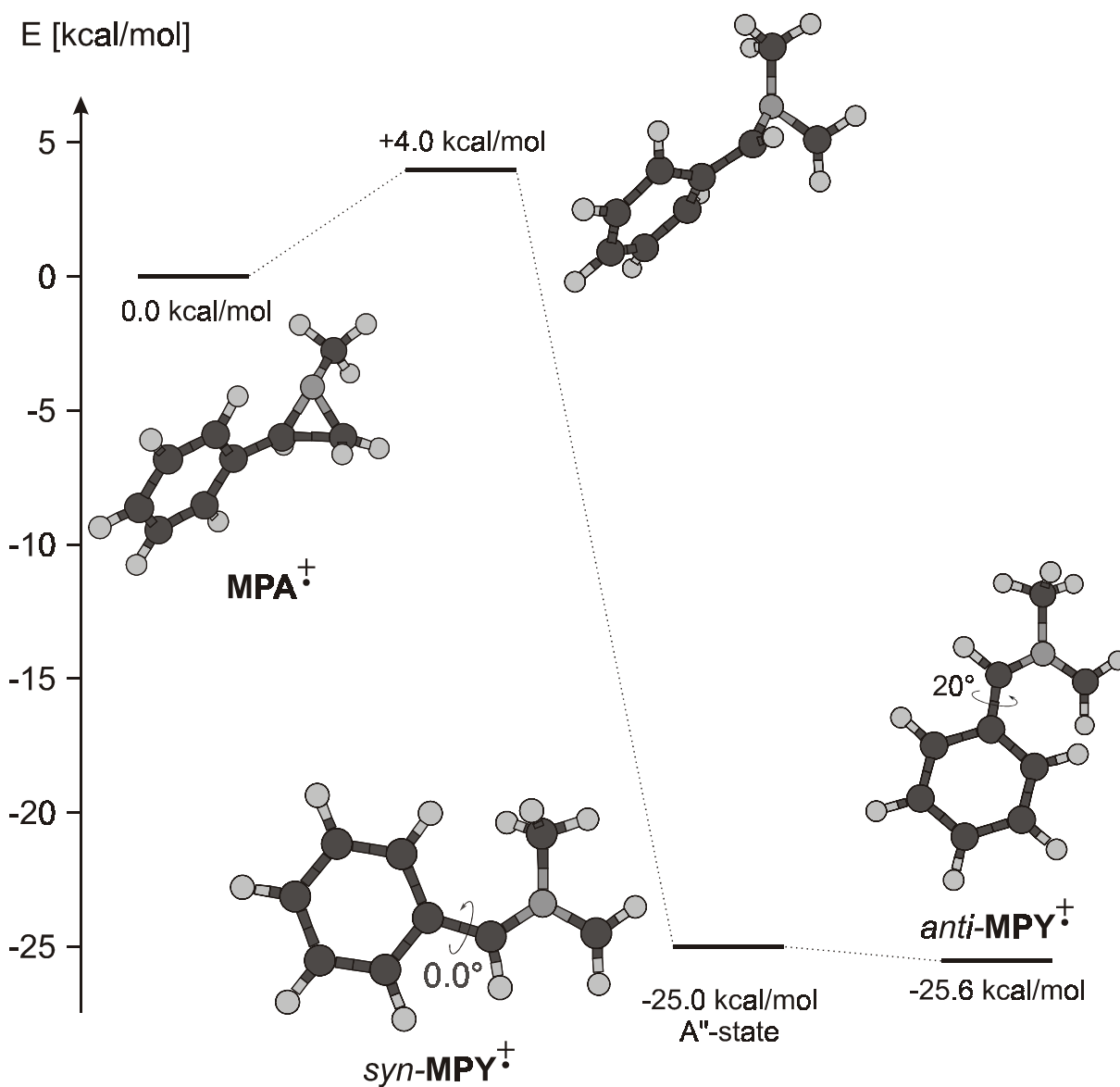
E [kcal/mol]

Figure 4-38: Thermochemistry of the ring-opening of $\mathbf{MPA}^{+\cdot}$. (B3LYP/6-31G* geometries; energies corrected ZPVE differences).

According to the Bell-Evans-Polanyi principle the activation barrier should decrease on increasing the exothermicity of the reaction. However, this is not what is found computationally (see Table 4-9).

Table 4-9: Thermo- and stereochemistry of the ring-opening of studied N-substituted **CPA**$^{+\cdot}$.

radical cation	ΔE_0^{a} [kcal/mol]	barrier $\Delta E_0^{\ddagger}$^{a} [kcal/mol]	stereochemistry of ring-opening	symmetry of the ylid$^{+\cdot}$
CPA$^{+\cdot b}$	-32.5	3.8	conrotatory	C_s
MPA$^{+\cdot}$	-25.0	4.0	conrotatory	C_s
BPA$^{+\cdot}$	-23.1	3.6	disrotatory	C_1

^{a} B3LYP/6-31G* energies corrected for ZPVE differences.

^{b} **CPA** = C-phenylaziridine.

The activation barriers for H- and for methyl-substituted **CPA**$^{+\cdot}$ are slightly higher than that of t-Bu substituted one. There are two related reasons for this behavior: first, the disrotatory ring-opening reaction of **BPA**$^{+\cdot}$ leads (for steric reasons) to the *anti*-conformer whereas in the other two cases the *syn*-conformer is formed; secondly, in contrast to **A**$^{+\cdot}$ and **BPA**$^{+\cdot}$, the ring-opening reactions of **CPA**$^{+\cdot}$ (C-phenylaziridine$^{+\cdot}$) and **MPA**$^{+\cdot}$ are conrotatory (this has been proven by IRC calculations on B3LYP/6-31G* level) therefore the Bell-Evans-Polanyi principle cannot be applied to **BPA**$^{+\cdot}$, because it is not part of a homologous series.

Table 4-10: Geometrical values of ring-opening transition states of **A**$^{+\cdot}$ and N-substituted **CPA**$^{+\cdot}$.

radical cation	α [°]^a	β [°]^a	Θ [°]^a	Λ [°]^b	$r_{c\text{-}c}$ [Å]
A$^{+\cdot}$	55.3	81.7	42.4	-	2.04
CPA$^{+\cdot}$	67.6	95.0	53.4	5.84	2.01
MPA$^{+\cdot}$	64.0	93.5	44.4	4.77	2.00
BPA$^{+\cdot}$	63.0	92.6	39.1	4.45	1.98

^{a} Definition of the angles see Figure 4-10.

^{b} Dihedral angle between the C-N bond and the connected phenyl ring.

In the transition states no differences can be discerned in the three cases, as shown in Table 4-10. The "decision" whether the C-phenyl group turns to a *syn* or an *anti* conformation is taken after having passed the TS because the phenyl

substituent is always connected to the methylene group which starts to rotate conrotatory only after passing the point of highest energy (see description of the ring-opening process of parent aziridine radical cation, $\mathbf{A}^{+\cdot}$, in the previous chapter).

4.5.3 Modeling of EA spectra

For ring-opened $\mathbf{MPA}^{+\cdot}$, called $\mathbf{MPY}^{+\cdot}$, both td-B3LYP and CASPT2 calculations were carried out. Once again, quantitative accord between td-B3LYP prediction and experimental band positions is poor, but these calculations nevertheless permit a qualitative understanding of the electronic structure of $\mathbf{MPY}^{+\cdot}$. In Table 4-11 td-B3LYP results for the *syn* and the *anti* conformation of $\mathbf{MPY}^{+\cdot}$ are listed. The strong band at 398 nm in the experiment can be assigned to the strongest predicted excitation at 358 nm in the *syn* or 381 nm in the *anti* conformer. The two main contributions to this excitation are SOMO-2 $\rightarrow$ SOMO and SOMO $\rightarrow$ LUMO excitations (see Figure 4-39).
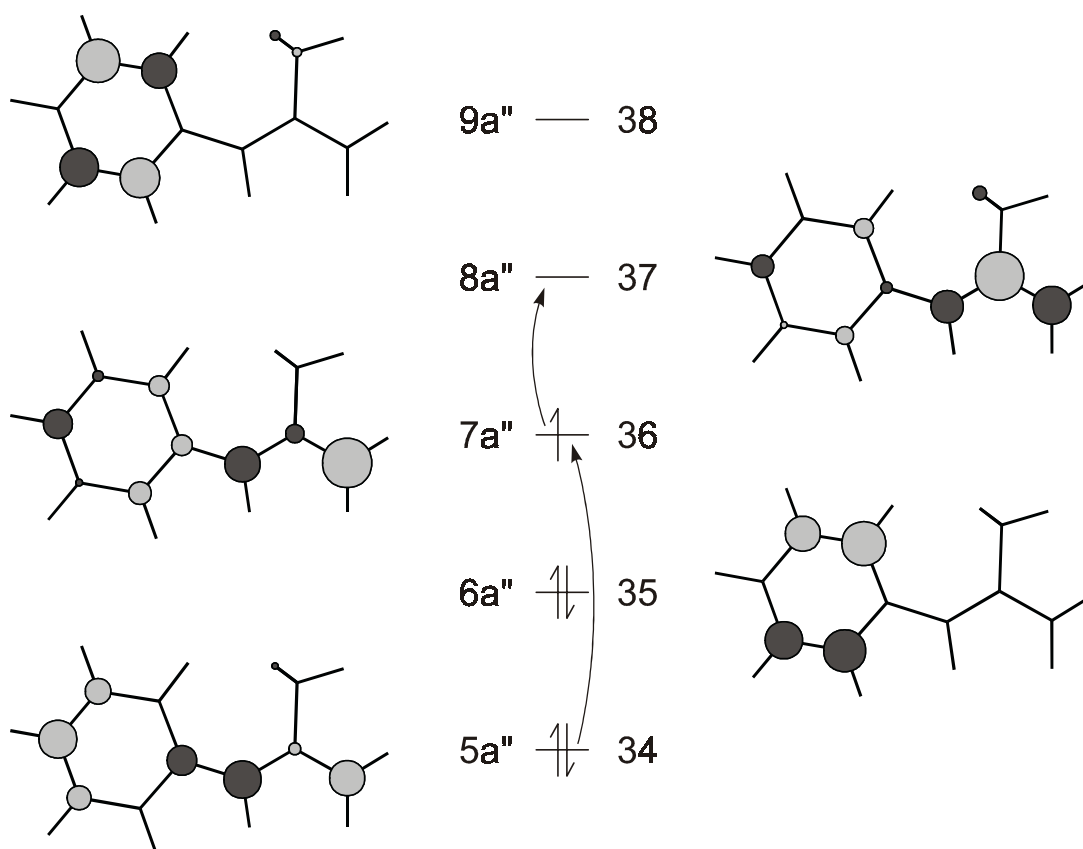

Figure 4-39: HF MOs of **MPY**; main contributions to the electronic excitation of the radical cation at 400 nm are indicated by arrows (cf. Table 4-11).

Note that in the *anti* conformation of **MPY**$^+$ the phenyl ring is twisted out of the CNC plane by 20°. As a result the excitations of the *anti* conformer are shifted to lower energies. Based on the td-B3LYP results we cannot, however, decide which conformer is formed in the experiment.

Table 4-11: Results of td-B3LYP calculations on *syn*- and *anti*-**MPY**$^+$.

State	nm		f^a		Excitations	Weighting factor [b]
	syn	*anti*	*syn*	*anti*		
1	500	*526*	0.0002	*0.0001*	6a" → 8a"	-0.24
					6a" → 7a"	0.99
2	492	*497*	0.0041	*0.0016*	7a" → 8a"	0.86
					5a" → 7a"	0.60
3	358	*381*	0.0490	*0.0328*	7a" → 8a"	-0.39
					5a" → 7a"	0.70
4	316	*322*	0.0011	*0.0009*	6a" → 8a"	0.93
					6a" → 8a"	-0.26

^{a} Oscillator strength for electronic transition.

^{b} These factors are from the calculation of the *syn*-conformer; they are similar to that of the *anti* conformer within 20%.

In contrast, CASPT2 calculations on the two conformations of **MPY**$^+$ are in much better accord with the experimental values, in particular for the *syn* conformer, as shown in Table 4-12 (compare also Table 4-13).

We therefore conclude that the observed species is the *syn*-conformer of **MPY**$^+$., in agreement with the finding that the TS found for the ring-opening process leads also to the *syn*-conformer. Therefore, we can say that the td-B3LYP method overestimates the first excitation at 583 nm by 0.36 eV and the third excitation at 398 nm by 0.33 eV whereas the excitations predicted by CASPT2 are in good accord with the experiment.

Table 4-12: Calculated electronic transitions of *syn*-**MPY**[+] using the CASPT2 method

states	UV/Vis		CASPT2			CASSCF
	[nm]	[eV]	[nm]	[eV]	f^a	configurations [b]
1^2A"	-	-	-	-	-	75% (6a")^1
2^2A"	583	2.12	584	2.12	0.028	44% 6a" $\rightarrow$ 8a"
						20% 4a" $\rightarrow$ 6a"
3^2A"	(440 sh)	(2.82)	484	2.56	0.002	55% 5a" $\rightarrow$ 6a"
						10% 4a" $\rightarrow$ 6a"
4^2A"	398	3.12	396	3.13	0.252	28% 4a" $\rightarrow$ 6a"
						19% 6a" $\rightarrow$ 8a"
						10% 6a" $\rightarrow$ 7a"

[a] Oscillator strength for electronic transition.
[b] Active space: 9 electrons in 5 occupied + 4 virtual a" MOs. Below the a" orbitals there are 30 a' orbitals; therefore the 6a" orbital in this table corresponds to orbital 36 in Figure 4-39.

Table 4-13: Calculated electronic transitions of *anti*-**MPY**[+] using the CASPT2 method.

states	UV/Vis		CASPT2			CASSCF
	[nm]	[eV]	[nm]	[eV]	f^a	configurations [b]
1^2A	-	-	-	-	-	77% (36a)^1
2^2A	583	2.12	566	2.19	0.010	31% 34a $\rightarrow$ 36a
						27% 36a $\rightarrow$ 37a
						10% 36a $\rightarrow$ 39a
3^2A	(440 sh)	2.82	485	2.56	0.002	62% 35a $\rightarrow$ 36a
4^2A	398	3.12	407	3.05	0.129	23% 34a $\rightarrow$ 36a
						17% 36a $\rightarrow$ 37a
						16% 36a $\rightarrow$ 40a
						12% 32a $\rightarrow$ 36a
5^2A	-	-	286	4.33	0.005	27% 35a $\rightarrow$ 36a
						36a $\rightarrow$ 39a
						14% 35a $\rightarrow$ 36a
						36a $\rightarrow$ 37a
						11% 35a $\rightarrow$ 39a

[a] Oscillator strength for electronic transition.
[b] Active space: 9 electrons in 5 occupied + 4 virtual MOs.

4.6 C,C-Diphenylaziridine

4.6.1 EA spectra

Apparently aziridines with a phenyl ring on a carbon atom open sponta-
neously on ionization. There is no reason why C,C'-diphenyl substituted aziri-
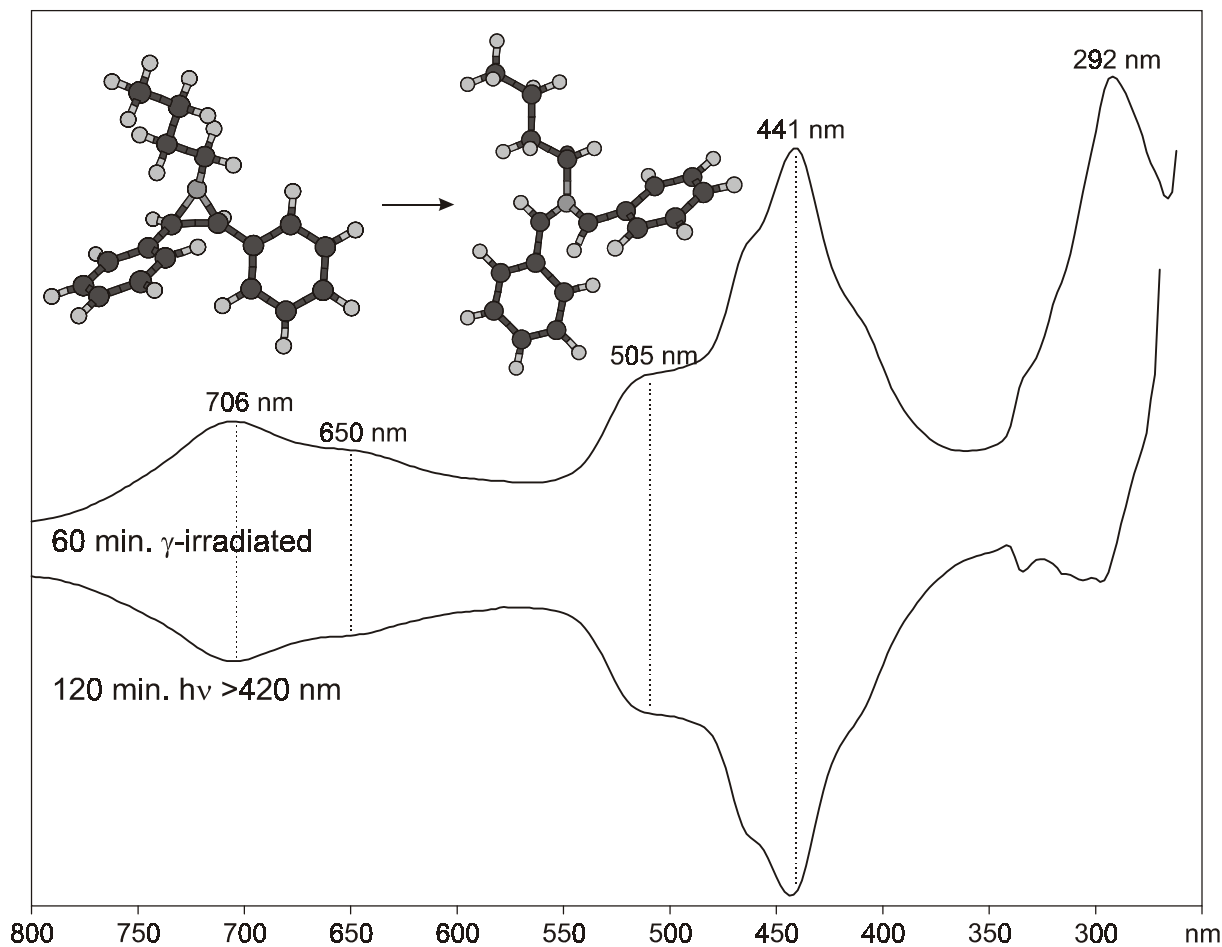dines should not to do likewise.

Figure 4-40: EA difference spectra of **BDPA** in Freon glass at 77 K after ionization and after
subsequent photolysis.

Experiments were only done with the N-n-butyl substituted cis-C,C'-
diphenylaziridine (**BDPA**). The EA-spectrum after ionization shows a strong
band at 441 nm, a weaker band at 706 nm, and several shoulders between these
two bands (see Figure 4-40), which results in a deep yellow color of the matrix.
On 2 h >420 nm irradiation all bands are completely bleached, apart from one at
292 nm, and no new bands appear. The fact that the spectrum after ionization is

qualitatively similar to that of **MPY**[+]· suggests the conclusion that **BDPA** is also not stable as a radical cation and opens spontaneously on ionization forming **BDPY**[+]·.

A td-B3YLP-calculation on **BDPY**[+]· predicts two strong excitations at 413 nm (oscillator strength f = 0.509) and at 616 nm (f = 0.134) (Table 4-14). They are mainly the positive and the negative combination of the two allylic transitions where the coefficients on the terminal allylic carbons are extended into the phenyl rings because of the benzylic resonance (see Figure 4-41).

This calculation is not in sufficiently good accord with the observed spectrum to permit an unambiguous assignment. However, for a system of that size ($C_{15}NH_{13}$), a CASSCF/CASPT2 calculation is out of question.

Table 4-14: Result of a td-B3LYP calculation on **MDPY**[+]·.

State	Oscillator strength f^a	Wavelength [nm]	Excitations	Weighting factor
1	0.134	616	56a → 57a	0.91
			53a → 56a	-0.38
2	0.003	474	55a → 57a	0.23
			55a → 56a	0.96
3	0.002	470	54a → 57a	-0.23
			54a → 56a	0.96
4	0.509	413	56a → 57a	0.25
			53a → 56a	0.87
5	0.013	396	53a → 57a	0.55
			52a → 56a	0.74
6	0.006	332	55a → 57a	0.88
			55a → 57a	-0.36

^{a} Oscillator strength for electronic transition.

4.6.2 Potential energy surface

Calculations were done on N-H (**DPA**[+]·), on N-methyl- (**MDPA**[+]·) and on N-n-butyl-cis-C,C'-diphenyl substituted aziridine radical cations as well as on the ring-opened ylid radical cations. However, the influence of the N-alkyl substituent on the ring-opening of diphenyl substituted aziridines is weak and therefore, only results on **MDPA**[+]· will be discussed.
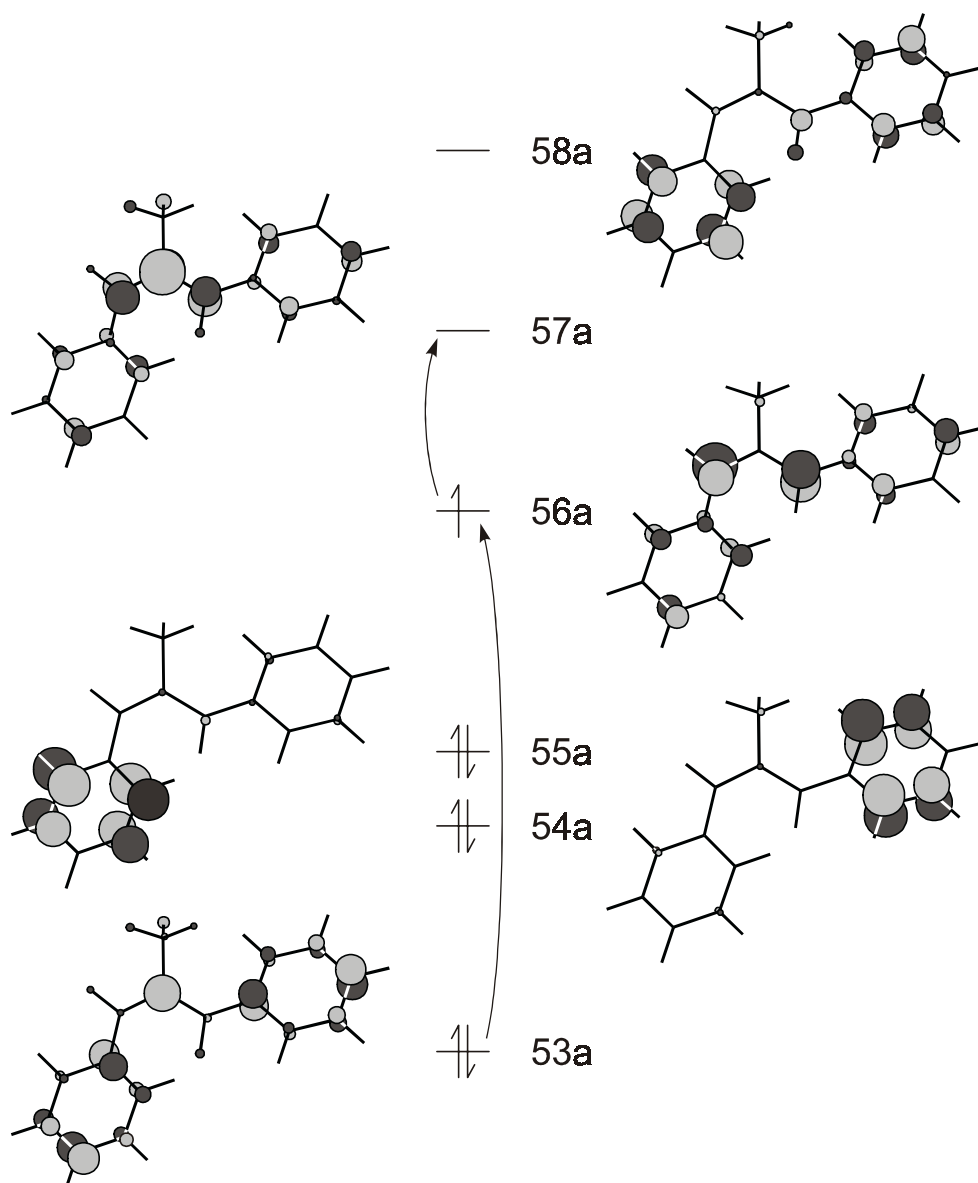
Figure 4-41: HF MOs of *syn-anti*-**MDPY**; main contributions to the electronic excitations at 413 and 616 nm are indicated by arrows.

Like in C-phenylaziridines, ionization in C,C'-diphenylaziridines occurs from a combination of phenyl MOs that extend into the C-C σ bond of the aziridine ring. In the present case, the weakening of the bond is very pronounced, as measured by the change of the C-C bondlength on ionization ($\Delta r_{CC} = 0.33$ Å, as opposed to 0.12 Å in C-phenylaziridine and 0.02 Å in parent aziridine radical cation). The N-pyramidalization angle is, however, again not strongly affected by the ionization (see Figure 4-42).

No strong differences in geometry changes on ionization were found between the three derivatives. They show almost the same C-C bond lengthening

of 0.33 Å. The change of the N-pyramidalization angle is small and it increases on going to larger substituents.

SOMO

C,C'-Diphenyl-N-methylaziridine (*neutral*) radical cation
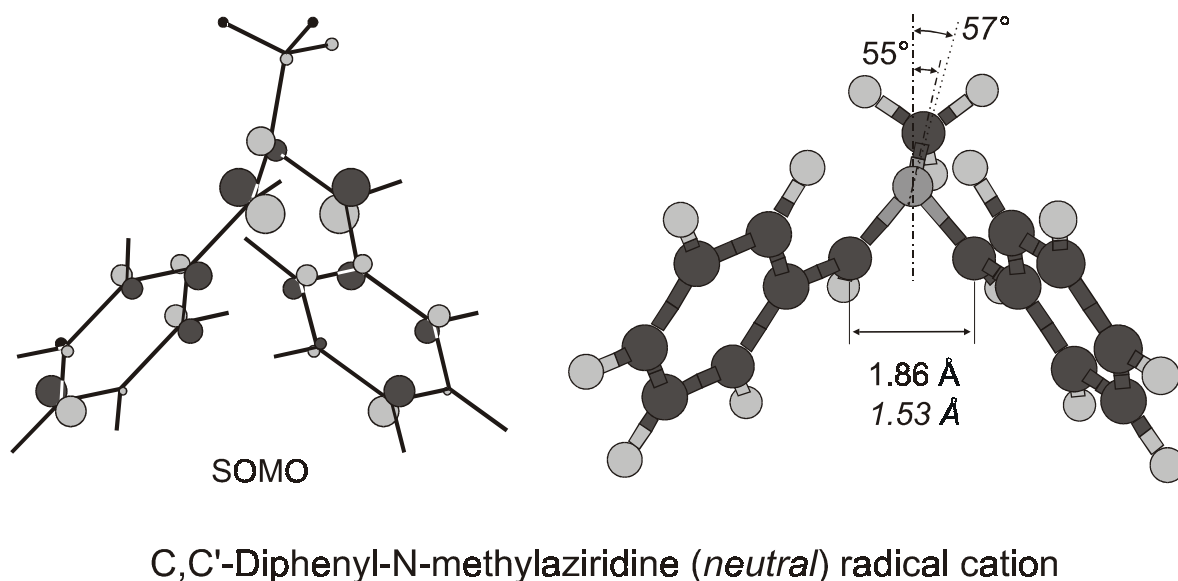
Figure 4-42: Geometry and SOMO of neutral and ionized **MDPA**.

For steric reasons the ring-opened form, **MDPY**$^{+}$, must be the *syn/anti* conformation. This implies that the ring-opening is a conrotatory process.

B3LYP/6-31G* calculations predict an exothermicity of 25.5 kcal/mol (cf. Figure 4-43) which is very close to the value obtained for the singly phenyl substituted compound (25.0 kcal/mol). Obviously the stabilizing contribution of the benzylic resonance by the second phenyl ring is again very similar in the reactant and in the product. In **MDPY**$^{+}$ we have, in principle, a more extended π-system than in **MDPA**$^{+}$. However, due to steric interactions with the *o*-hydrogen atoms, both phenyl rings are slightly twisted from the plane of the allylic system (the dihedral angles between the plane of the allylic moiety and the phenyl rings are between 15 and 20°, depending how they are measured). This foils part of the additional stabilization of **MDPY**$^{+}$ by the second phenyl ring.

Again we can twist the phenyl rings by 90° to get a measure of the benzylic resonance stabilization. In **MDPA**$^{+}$ the energy increases by 10.1 kcal/mol if one ring is twisted, whereas in **MDPY**$^{+}$ the twist of the *anti* standing phenyl ring requires 6.9 kcal/mol. These energies are real phenyl ring rotation barriers because the geometries were optimized as transition states (during the optimiza-

tions the energies dropped by 10 kcal/mol and by 5 kcal/mol for **MDPA**$^{+\cdot}$ and **MDPY**$^{+\cdot}$ respectively!).
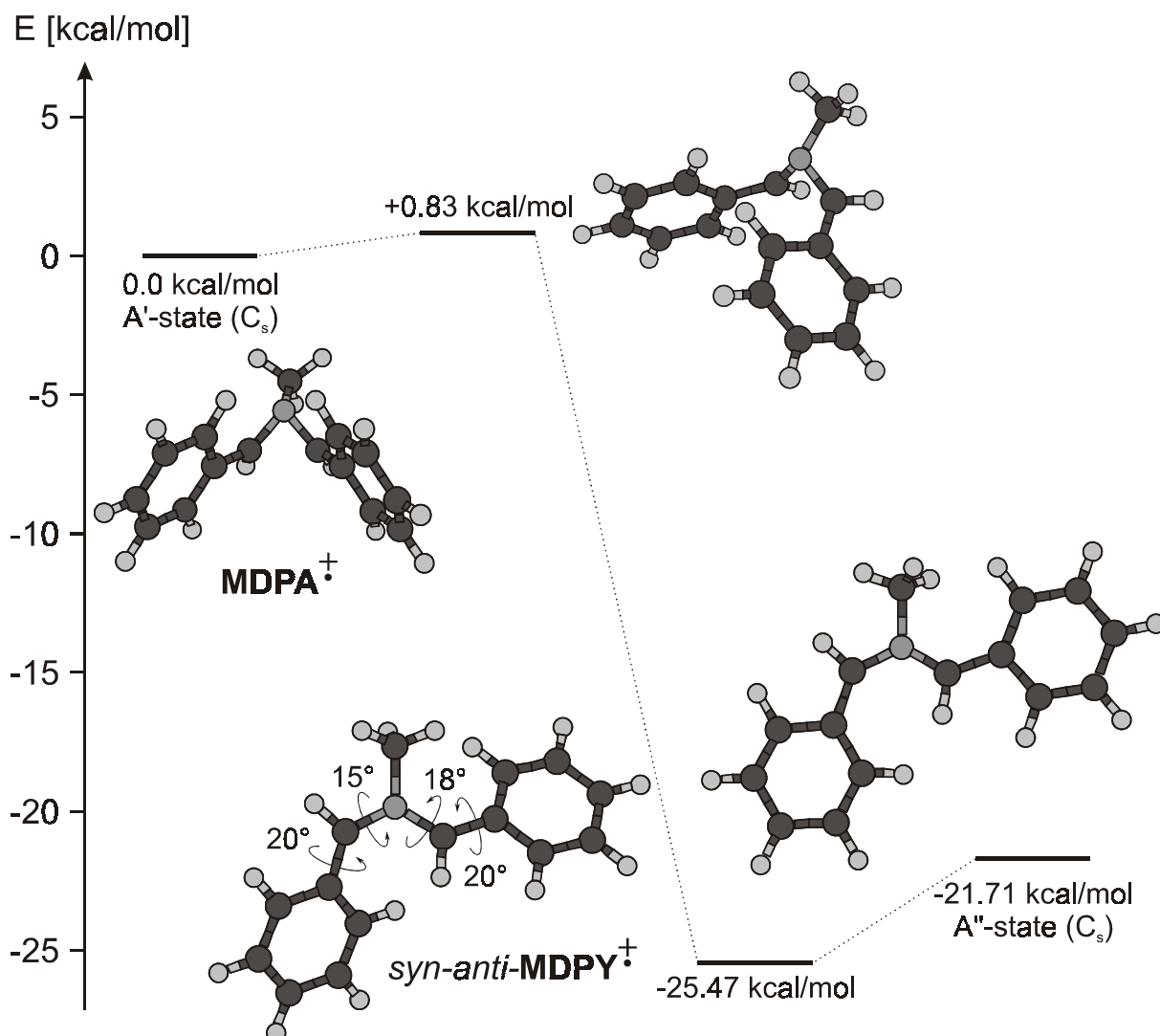

Figure 4-43: Thermochemistry of the ring-opening of **MDPA**$^{+}$ (B3LYP/6-31G* geometries; energies corrected for ZPVE differences at the same level).

A TS search for the ring-opening process led to a species which lies only 0.8 kcal/mol above **MDPY**$^{+\cdot}$. Because of the steric interactions the dihedral angles between the planes of the allylic moiety and the phenyl rings are between 15° and 20° which still allows some allylic-benzylic resonance. To force the molecule into a planar conformation requires 3.8 kcal/mol.

4.7 N,C-Diphenylaziridine

4.7.1 Experimental part

After finding that an N-phenyl substituent effectively prevents aziridines from undergoing ring-opening on ionization (or on subsequent photolyses), whereas C-phenyl substituted aziridines open spontaneously on ionization, one may ask which effect prevails in N,C-diphenylaziridine (**NCPA**).

In a Freon matrix a very broad band with a maximum at ca. 630 nm and a sharper band at 444 nm with a shoulder on the high energy side arise on ionization (Figure 4-44). The sharp band looks very similar to that of **NPA**$^{+\cdot}$ at 446 nm. A td-B3LYP calculation for **NCPA**$^{+\cdot}$ predicts very weak bands in the NIR (see theoretical part) and a stronger band at 402 nm (oscillator strength f = 0.0113; the main band of **NPA**$^{+\cdot}$ had also been predicted 50 nm too high with a similar oscillator strength). The similar shape of the bands and the small difference in energy between the main bands in **NCPA**$^{+\cdot}$ and in **NPA**$^{+\cdot}$ is strong evidence that **NCPA** remains also ring-closed on ionization. Both species show the same benzylic resonance of the N-phenyl moiety, whereas the C-phenyl ring does not enter into resonance with the aziridine ring. Therefore the EA-spectrum of **NCPA**$^{+\cdot}$ must be similar to that of **NPA**$^{+\cdot}$. Lower-lying charge transfer excitations between the two phenyl rings show only weak oscillator strengths in td-B3LYP calculations.

Irradiation at >590 nm causes a bleaching of the broad visible band and the formation of three new bands at 522 nm, 489 nm and 467 nm, together with a very weak set of bands at 760 nm, 690 nm and 630 nm (note, however, that the intensity of the 444 nm band does not seem to be affected by this process!). These two sets of bands increase some more on irradiation at >515 nm, which leads also to a marked decrease of the 444 nm peak, but they are bleached at >475 nm. It can be excluded on the basis of td-B3LYP/6-31G* predictions that the set of bands is due to absorptions of ring-opened **NCPA**$^{+\cdot}$ (**NCPY**$^{+\cdot}$).

According to these calculations **NCPY**$^{+\cdot}$ should not have any electronic excitations above 600 nm. The first transition for the *syn* conformer of **NCPY**$^{+\cdot}$ is a weak one (oscillator strength f = 0.0018), predicted at 520 nm. The next stronger one should be at 429 nm (f = 0.0029 nm) and the strongest one with an oscillator strength of f = 0.0419 should be at 368 nm.
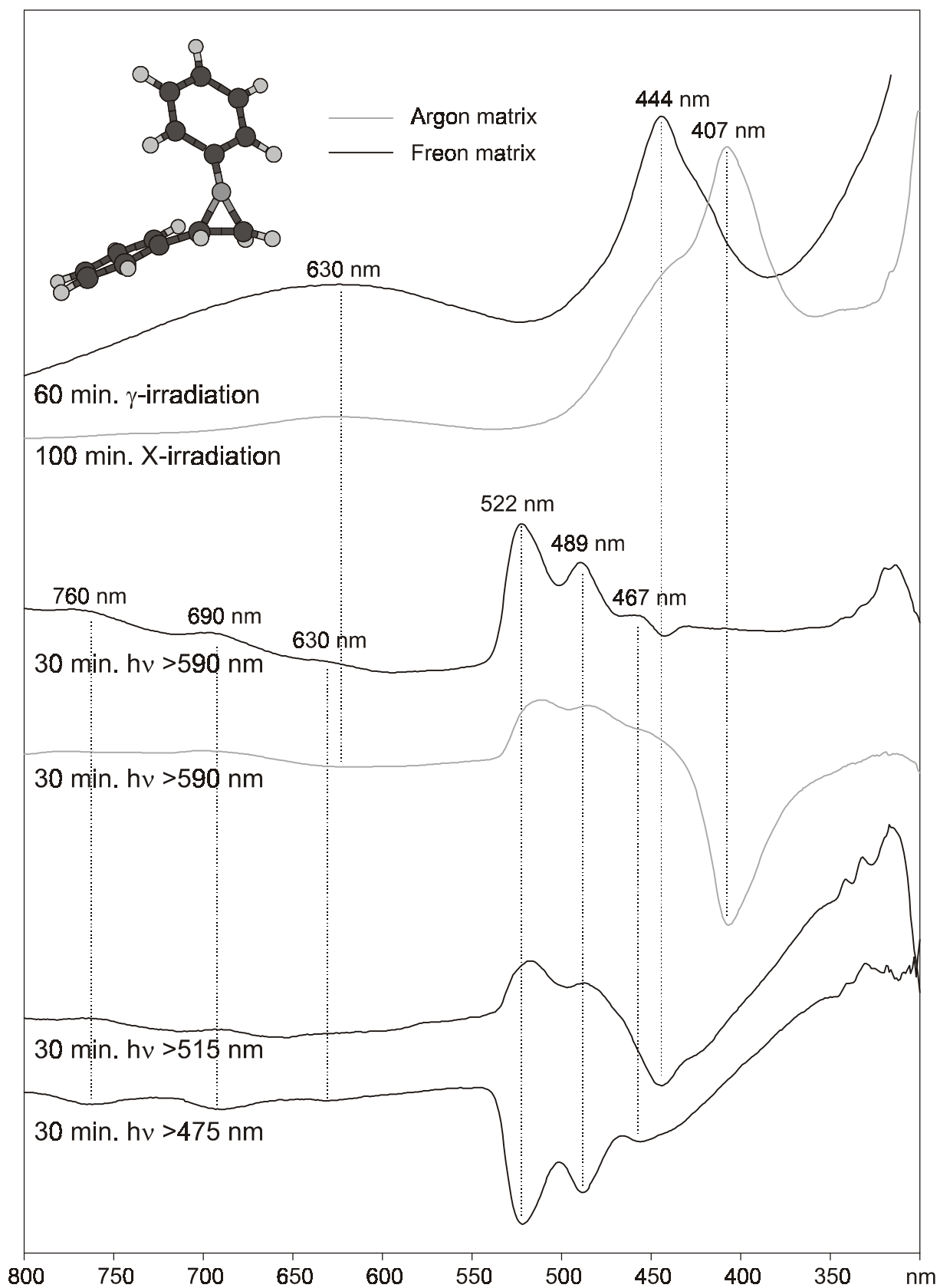
Figure 4-44: EA difference spectra of ionized and irradiated **NCPA** in Freon glass at 77 K (black) and in Ar matrix at 12 K (gray).

These predictions match better with the EA-spectrum of ionized **NCPA** in an Argon matrix which is very different from that observed in the Freon mixture (see Figure 4-44). There we find a sharp band at 407 nm with a shoulder at the low energy side, and a very weak and broad band at 630 nm. The shoulder could be due to some ring-closed **NCPA**$^{+.}$ which remains after ionization. Irradiation at >590 nm leads to a decrease of the band at 407 nm and also to an increase the set of bands at 522 nm mentioned in the Freon matrix experiment. This behavior can be compared with that of **MPY**$^{+.}$.

In **NCPA**$^{+.}$ the N-phenyl moiety was decisive for the EA spectrum because of the benzylic resonance. This allows us to compare the spectrum with that of **NPA**$^{+.}$. For **NCPY**$^{+.}$ the situation is different: the N-phenyl ring is now at a node of the heteroallylic system, twists out of the allylic plane, and no benzylic resonance occurs. On the other hand the C-phenyl substituent is coplanar with the heteroallylic moiety and can therefore enter into resonance with it. This leads to a spectrum which we can compare with that of **MPY**$^{+.}$. (Weak, broad band at ca. 580 nm, intense sharper band at ca. 400 nm, cf. Figure 4-36)

4.7.2 Potential energy surfaces

The HOMO of the neutral compound has a large coefficient at the N-lone pair. This leads to a big change of the "pyramidalization" angle after ionization. On the other hand the C-C bond length changes very little (see Figure 4-45) because of the very small coefficients at the C atoms. The HOMO of the neutral molecule and the SOMO of the radical cation look very similar.

According to B3LYP geometry optimizations only the *syn* conformation is a minimum on the **NCPA**$^{+.}$ hypersurface. An optimization of the *anti* conformation of **NCPA**$^{+.}$ leads to an energy plateau 1.12 kcal/mol above the *syn* minimum, but on this plateau no minimum for the *anti* conformation can be found and the geometry converges by N inversion.

The thermochemistry of the ring-opening reaction of **NCPA**$^{+.}$ ($\Delta E_0 =$ -9.5 kcal/mol, see Figure 4-46) is much closer to that of **NPA**$^{+.}$ ($\Delta E_0 =$ +1.2 kcal/mol) than to that of **CPA**$^{+.}$ ($\Delta E_0 = $ -32.5 kcal/mol) which indicates that the effect of the N-phenyl substituent predominates.

SOMO

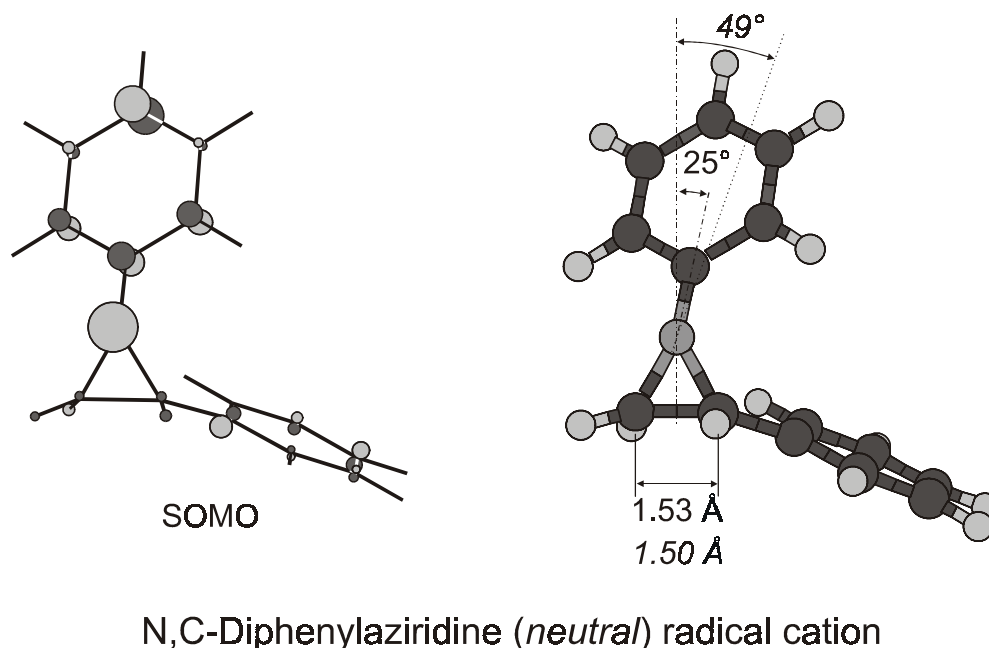N,C-Diphenylaziridine (*neutral*) radical cation

Figure 4-45: Geometry and HOMO of neutral and ionized **NCPA**.

In contrast, the *activation barrier* for the ring-opening of **NCPA**[+] ($\Delta E_0^{\ddagger}$ = 19.4 kcal/mol) lies almost midway between that of **NPA**[+] ($\Delta E_0^{\ddagger}$ = 33.0 kcal/mol) and that of **CPA**[+] ($\Delta E_0^{\ddagger}$ = 3.8 kcal/mol), i.e. at the TS the effects of the N-phenyl and the C-phenyl substituent tend to cancel.

Suppressing the benzylic stabilization through the N-phenyl ring in **NCPA**[+] by rotating this substituent to a perpendicular conformation raises the energy by 16.7 kcal/mol, whereas the stabilization by the C-phenyl substituent evaluated in the same fashion is only 2.8 kcal/mol. In **NCPY**[+] twisting the C-phenyl ring to 90° requires 10.5 kcal/mol.[20]

4.7.3 Substituted N,C-diphenylaziridines

Electron withdrawing substituents on the N-phenyl ring should narrow the gap between the state formed by ionization from the benzylic PhN-moiety relative to that formed by ionization from the Ph-C-C group. This had already been tried with **NPA** where the experiment did, however, not provide any hint for a ring-opening of **NPA-CN** on ionization. The same test was tried with C-phenyl-N-p-cyanophenylaziridine (**NCPA-CN**) embedded in Freon matrix.

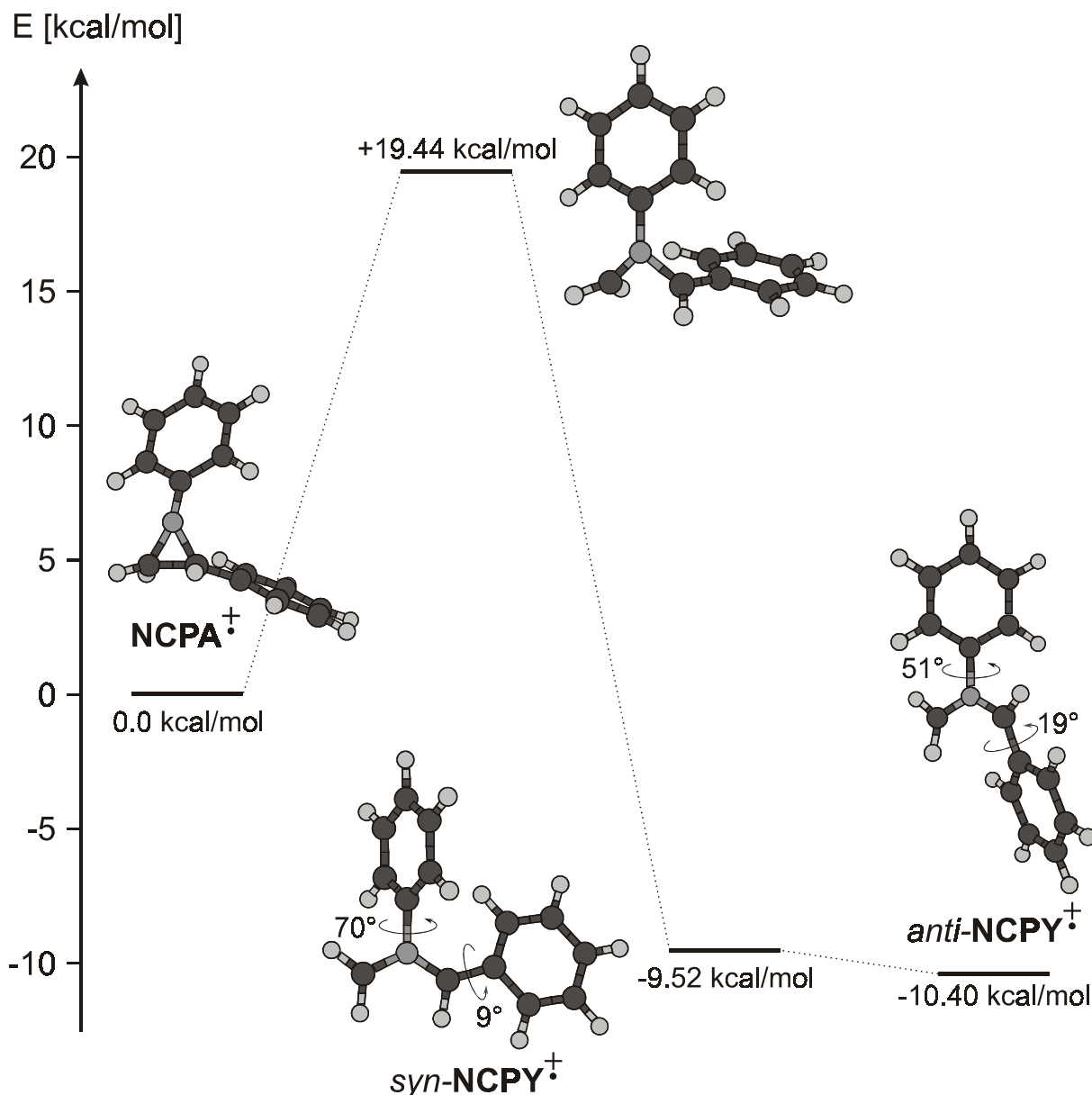[20] Calculations by B3LYP/6-31G*, corrected for ZPVE differences at the same level.

E [kcal/mol]

Figure 4-46: Thermochemistry of the ring-opening of **NCPA**$^{+\bullet}$ (B3LYP/6-31G* geometries; energies corrected for ZPVE differences at the same level).

The EA-spectrum after γ-irradiation of **NCPA-CN** has exactly the same shape as those of the other ring-closed N-phenyl substituted aziridine radical cations. The position of the strong band at 484 nm with the shoulder at the high energy side is only blue-shifted by 4 nm relative to that of **NPA-CN**$^{+\bullet}$ (cf. section 4.4.4. and Figure 4-47). This indicates that **NCPA-CN** remains also closed on ionization.

However, in contrast to **NPA-CN**$^{+\bullet}$, photolysis of this cation at >760 nm leads to a bleaching of the 484 nm band while two new bands appear: a sharp one at 414 nm and a broad, weak one at around 630 nm. A comparison with the spectrum of ionized **MPA** (section 4.5.1) indicates that the two new bands may

be attributed to the ring-opened aza-allylic cation. Thus, the ring-opening of **NCPA-CN**[+] can be induced by photolysis. Compared to **NCPY**[+] the band at 415 nm is only 8 nm red shifted because the CN substituent has no strong influence on this transition. In the ring-opened radical cation it is the C-phenyl ring which establishes a chromophore with the heteroallylic group. If a CN group would be attached to the C-phenyl ring, also this band would be shifted.

On subsequent irradiation at >590 nm the strong band at 414 nm and the broad band at 630 nm decrease while two new bands at 493 nm and at 530 nm, together with two weak bands at 703 nm and at 760 nm, grow in. These bands must belong to the same unknown product which also appears on >590 nm photolysis of **NCPA**[+]. In both cases this intermediate product can be bleached at shorter wavelengths.

The thermochemistry of this reaction confirms that the ring-opening should occur more easily than for **NCPA**[+]. The electron withdrawing substituent on the N-phenyl ring seems to decrease the stabilizing effect of the benzylic system at the transition state and the barrier drops from 19.4 to 14.3 kcal/mol, whereas the exothermicity remains almost constant at 11.0 kcal/mol.

Table 4-15: Thermochemistry of the ring-opening of substituted **NCPA**[+].

radical cation	ΔE_0 [a] [kcal/mol]	barrier $\Delta E_0^{\ddagger}$ [a] [kcal/mol]
NCPA[+]	-9.5	19.4
NCPA-CN[+]	-11.0	14.3
NCPA-OMe[+]	-3.8	24.4

[a] B3LYP/6-31G* energies corrected for ZPVE differences at the same level.

A different behavior is observed for C-phenyl-N-p-methoxyphenylaziridine (**NCPA-OMe**[+]): a strong broad band with a maximum at 478 nm appears. It shows a shoulder at the low energy side and no photolysis is able to bleach this band. The matrix has a faint pink color. The position of the band and its insensibility towards photolyses leads to the conclusion that it must be the ring-closed aziridine radical cation.
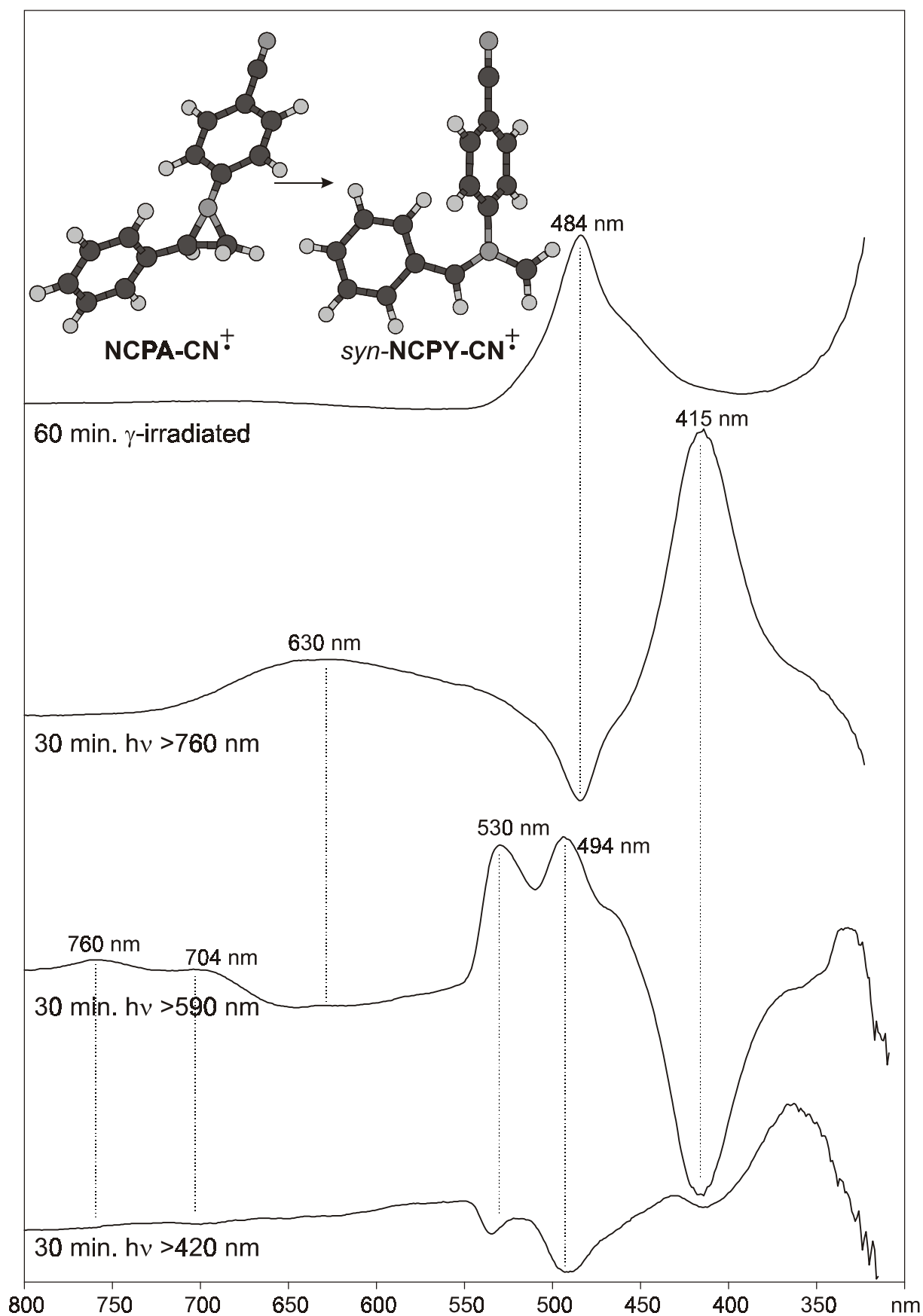
Figure 4-47: EA difference spectra of **NCPA-CN** in Freon glass at 77 K after γ-irradiation and after subsequent photolyses.

A td-B3LYP calculation of this radical cation predicts a strong absorption at 447 nm ($f = 0.0160$) and a weak one at 836 nm ($f = 0.0022$) together with two very weak ones in between. The prediction for the open allylic form (**NCPY-OMe$^{+\cdot}$**) shows its strongest absorption at 385 nm and another strong one at 344 nm which does not match at all with the experiment.

The calculated thermochemistry of the ring-opening reaction of **NCPA-OMe$^{+\cdot}$** shows an exothermicity of 3.8 kcal/mol and a reaction barrier of 24.4 kcal/mol. This confirms the electron-donating effect of the methoxy group because this barrier is 3.2 kcal/mol higher than that of the **NCPA$^{+\cdot}$** ring-opening reaction. The lowered exothermicity can be explained with a stronger stabilization of the reactant compared to the product: whereas the raised electron density in the N-phenyl moiety can develop its stabilizing effect, it has no more influence on the ring-opened radical cation because the ring is twisted out of the allylic plane which inhibits the formation of a phenyl-allylic resonance stabilization.

4.8 N,C,C-Triphenylaziridine

4.8.1 Experimental part

After having studied various mono- and di-phenyl substituted aziridines, and after having seen that a C-phenyl substituent may counteract the stabilizing effect of the N-phenyl group, it is of interest to investigate also the C,C',N-triphenylaziridine radical cation, **TPA**$^{+\cdot}$. Does it open spontaneously on ionization like C-phenyl or C,C'-diphenylaziridines or does it need further energy input by light like N,C-diphenylaziridines?

Ionized **TPA** embedded in a Freon matrix shows only a weak band at 450 nm and a very broad and weak band around 600 nm. The color of the matrix is grass green. The band at 450 nm we know already from N-phenyl substituted aziridines (**NPA**$^{+\cdot}$: 446 nm, **NCPA**$^{+\cdot}$: 444 nm) and the broad band we have also seen at **NCPA**$^{+\cdot}$. According to td-B3LYP the C-phenyl substituents of **TPA**$^{+\cdot}$ and **NCPA**$^{+\cdot}$ are not involved in the transitions which cause the bands at 450 and at 600 nm (see Figure 4-48).

However, a very short photolysis (3 min.!) at >715 nm leads to a huge increase of a band at 450 nm and to the formation of a set of new bands at 755 nm, 682 nm and 622 nm. The matrix color changes to a very intense yellowish green. These bands can be completely bleached by a longer irradiation at >475 nm.

A td-B3LYP calculation predicts weak bands at 1400 nm and at 887 nm and a stronger one at 417 nm with an oscillator strength of $f = 0.0121$ for **TPA**$^{+\cdot}$. However for the ring-opened *syn/anti* radical cation, **TPY**$^{+\cdot}$, strong bands at 656 nm, 487 nm and especially at 443 nm ($f = 0.1018$, 0.0177, 0.3205 respectively) are predicted. Although the excited state energies are overestimated by 0.23 eV, 0.72 eV and 0.04 eV, respectively by the td-B3LYP method, it reflects quite well what happens in this experiment: on ionization **TPA** stays ring-closed and it ring-opens to **TPY**$^{+\cdot}$ extremely photosensitively by shining light of >715 nm on it.
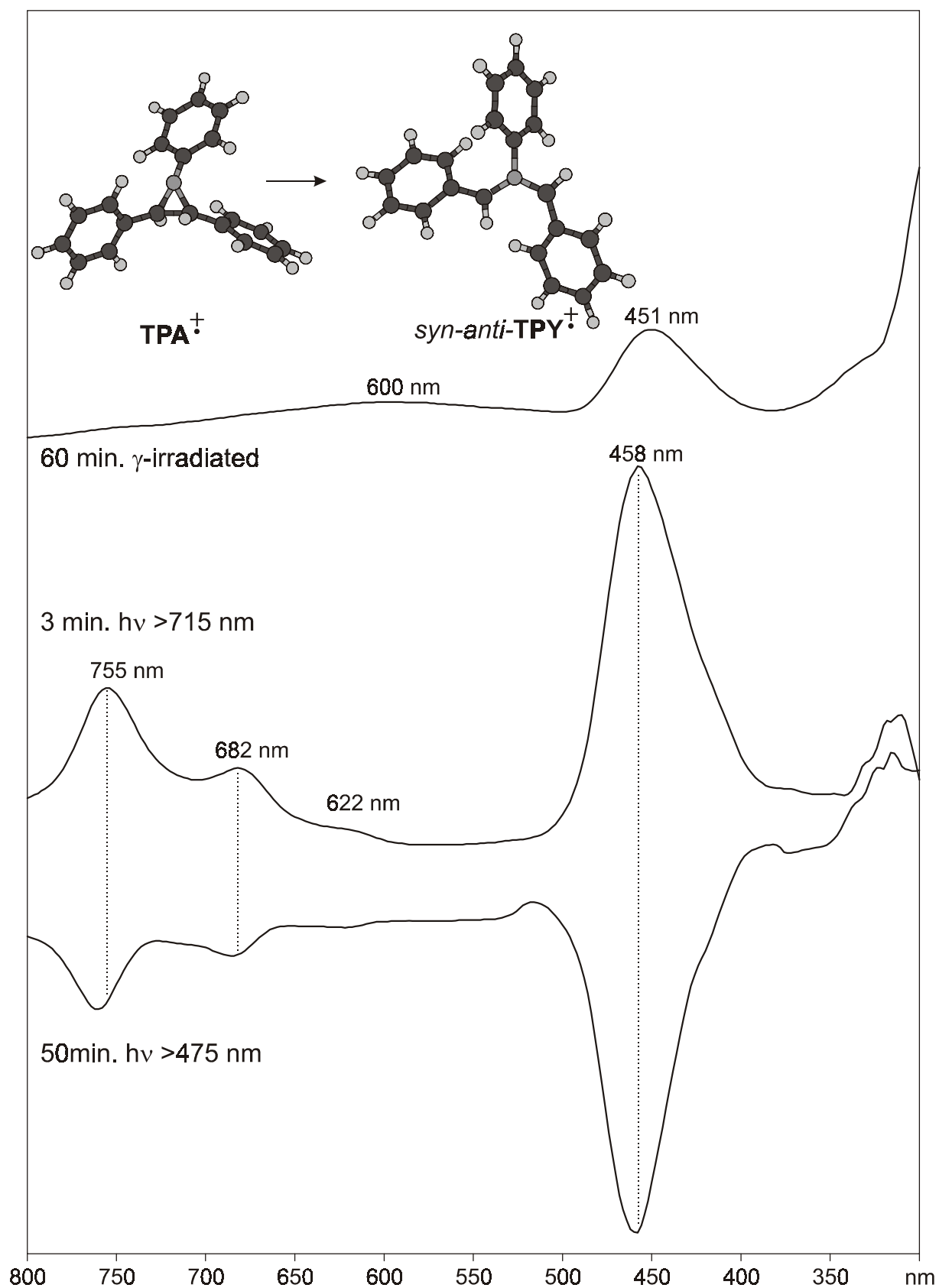
Figure 4-48: EA difference spectra of ionized and irradiated **TPA** in Freon glass at 77 K.

4.8.2 Potential energy surface

Computational investigations show a weaker change of the "pyramidalization" angle ($-15°$) and a stronger change of the C-C bondlength ($+0.05$ Å) than in the case of **NCPA** ($-24°$ and $+0.03$ Å). This is consistent with the notion that an additional phenyl group on a C atom weakens the C-C bond of the aziridine ring in the radical cation (see Figure 4-49).

Thermochemical calculations predict an activation barrier for the ring-opening of 5.3 kcal/mol and an exothermicity of 17.9 kcal/mol (see Figure 4-50). This is a much lower barrier and a much higher exothermicity than we found for **NCPA**$^{+}$ and it is similar to the thermochemistry of **MPA**$^{+}$ where the barrier is 4.0 kcal/mol and the exothermicity is 25.0 kcal/mol. These informations lead to the conclusion that ionized **TPA** should undergo spontaneous ring-opening on ionization, like C-phenyl or C,C'-phenyl substituted aziridines.

SOMO

N,C,C'-Triphenylaziridine (*neutral*) radical cation
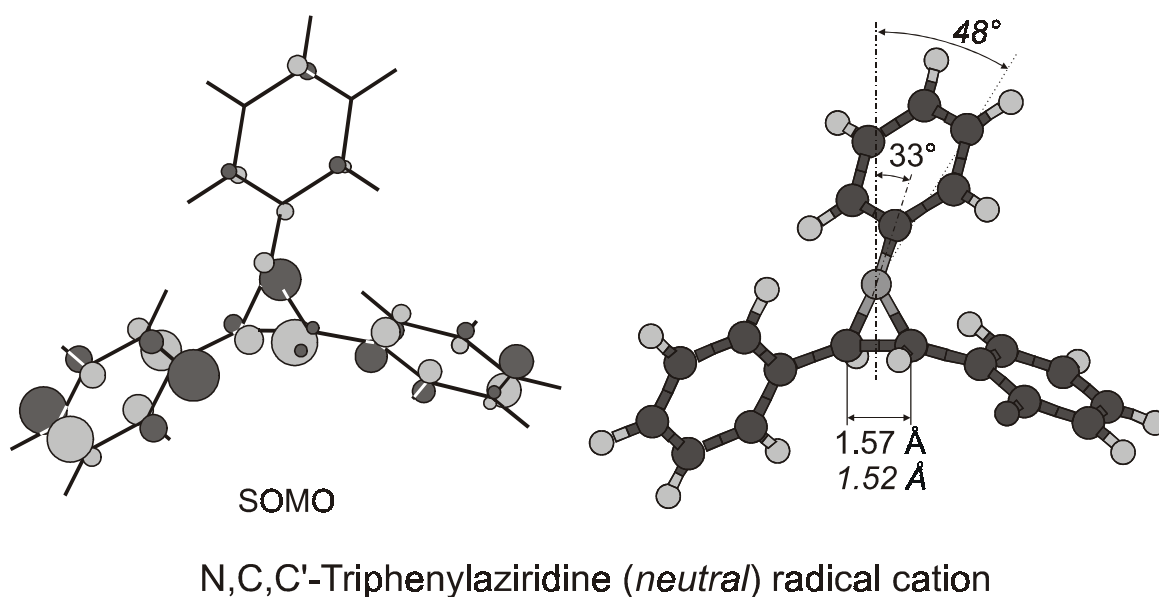
Figure 4-49: Geometry and SOMO of neutral and ionized **TPA**.

An IRC calculation shows that the TS for the ring-opening reaction of **TPA**$^{+}$ leads to the *syn-syn* conformation of **TPY**$^{+}$. This conformation has C_2 symmetry and its ^2A ground state lies 1.7 kcal/mol lower than the *anti-anti* conformation which has also C_2 symmetry and a ^2A ground state. The *syn-anti* conformation has no symmetry and it lies 1.8 kcal/mol higher than the *syn-anti* conformation.
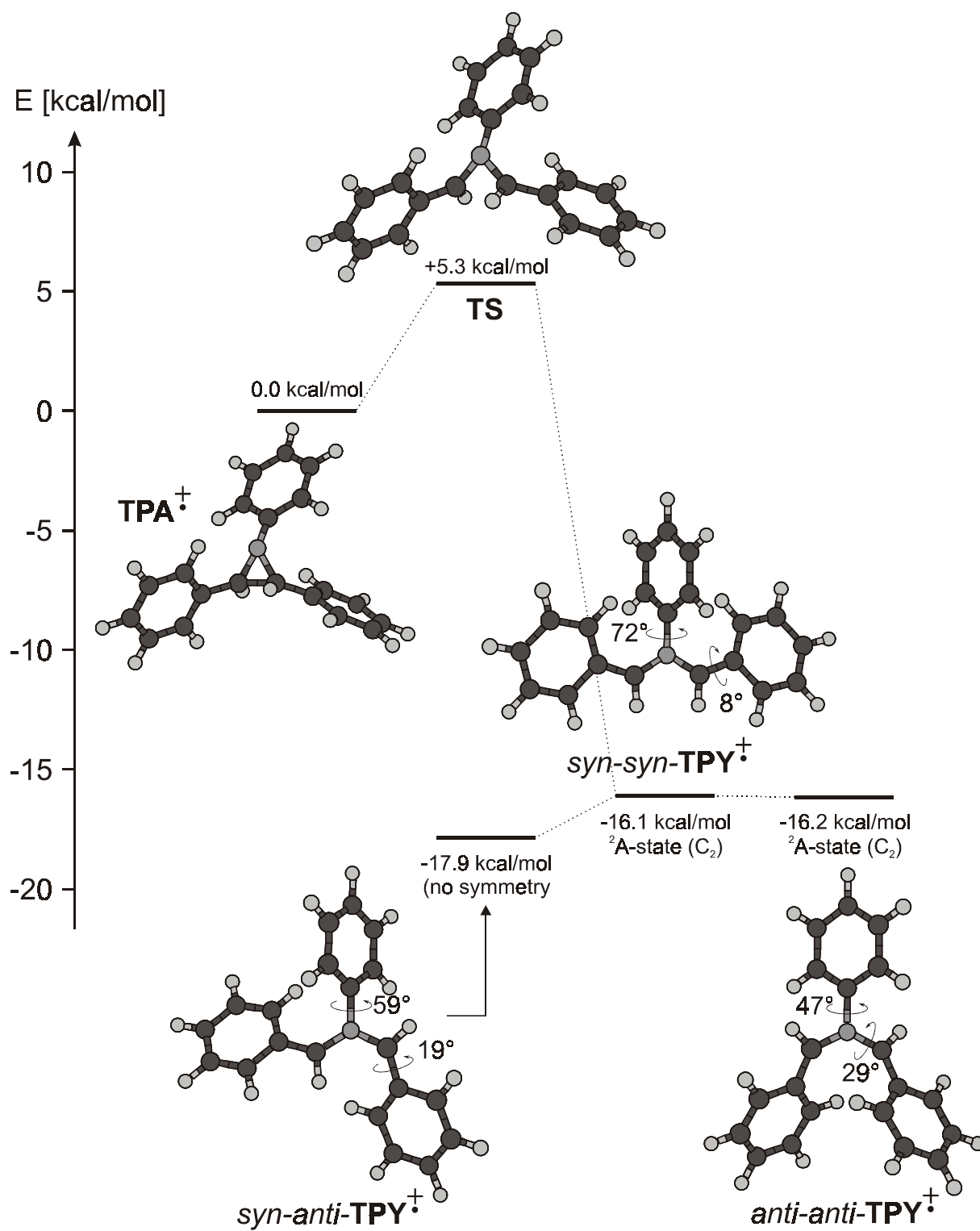
E [kcal/mol]

Figure 4-50: Thermochemistry of the ring-opening of **TPA**$^{+\bullet}$ (ZPVE difference corrected B3LYP/6-31G* energies).

4.9 Conclusions

In the course of this work we were able to generate azomethine ylid, **Y**, which is iso-π-electronic to the allyl radical. It is of theoretical interest to investigate experimentally the force constants for the symmetric and asymmetric stretching deformation of the C-N bonds of **Y** and to compare them with those of the allyl radical. By investigating also the **Y**-d1 and the **Y**-d4 it should be possible to determine these force constants by fitting the force field of this three isotopomers.

Furthermore, we showed that substituents - particularly phenyl substituents - play a very important role in determining the behavior of aziridines under photoinduced electron transfer (PET) conditions. N-phenyl rings stabilize preferentially the aziridine, whereas C-phenyl rings stabilize preferentially the ring-opened azomethine ylid by benzylic resonance. The amount of this stabilization can be assessed by calculating the energy increase on going to structures where the phenyl ring is 90 degrees twisted, i.e. where resonance between the phenyl moiety and the aziridine or the azomethine ylid is suppressed. Experiments and calculations showed that N-phenylaziridine, **NPA**, is too strongly stabilized to undergo ring-opening on ionization (or with light on subsequent excitation of the radical cation in the visible or in the UV). Methyl groups on the C atoms of **NPA** cause some lowering of the ring-opening transition state but the effect is too weak to allow a thermal crossing of the barrier.

In contrast, C-phenyl substitution leads to a pronounced stabilization of the ring-opening TS, whereas the stabilization of the reactant and of the product are quite similar. Therefore N-H and N-alkyl-C-phenylaziridines undergo immediate ring-opening on ionization.

The question which effect "wins" in ionized *C,N*-diphenyl aziridine could not be answered satisfactorily. However for Triphenylaziridine, **TPA**, a quite short photolysis on low intensity is enough to induce ring-opening.

Thus, the use of aziridines, opened by ionization to perform [3+2]cycloadditions with dipolarophiles **A=B**, is limited to derivatives where substituents do not stabilize the ring-closed form too much.

5. References

[1]   L. Andrews, G. C. Pimentel, *J. Chem. Phys.* **44**, 2361 (1966).

[2]   P. H. Kasai, *Phys. Rev. Lett.* **21**, 67 (1968).

[3]   D. E. Milligan, M. E. Jacox, *J. Chem. Phys.* **51**, 1952 (1969).

[4]   M. E. Jacox, D. E. Milligan *J. Chem. Phys.* **54**, 3935 (1971).

[5]   R. O. Allen, J. M. Grzybowski, L. Andrews, *J. Phys. Chem.* **79**, 898 (1975).

[6]   L. Andrews, R. O. Allen, J. M. Grzybowski, *J. Phys. Chem.* **79**, 904 (1975).

[7]   F. T. Prochaska, L. Andrews, *J. Chem. Phys.* **67**, 1091 (1977).

[8]   R. Rosetti, L. E. Brus, *Chem. Phys. Lett.* **69**, 447 (1980).

[9]   T. A. Miller, V. Bondybey, in: *Molecular Ions: Spectroscopy, Structure and Chemistry*, T. A. Miller, V. Bondybey eds.: North Holland, Amsterdam (1983).

[10]   K. Roth, *Ph. D. Dissertation Nr. 958*, Universität Freiburg, Schweiz (1989).

[11]   T. Bally, in: *Radical Ionic Systems*, Ed: A. Lund, M. Shiotani, Kluwer Academic: Doordrecht (1991).

[12]   T. Bally, *Habilitation*, Universität Freiburg, Schweiz (1988).

[13]   D. F. Evans, *Nature* **176**, 777 (1955).

[14]   M. Kasha, *J. Opt. Soc. Am.* **38**, 1068 (1948).

[15]   P. Bennema, G. H. Hoijtink, J. H. Lupinski, L. J. Oosterhoff, P. Selier, J. d. W. Van Voorst, *Mol. Phys.* **2**, 431 (1959).

[16]   T. Shida, W. H. Hamill, *J. Chem. Phys.* **44**, 2369 (1966).

[17]   T. Shida, W. H. Hamill, *J. Chem. Phys.* **44**, 2375 (1968).

[18]   T. Shida, T. Kato, *Chem. Phys. Lett.* **68**, 106 (1979).

[19]   M. C. R. Symons, *Chem. Soc. Rev.* **13**, 393 (1984).

[20]   A. Grimison G. A. Simpson, *J. Phys. Chem.* **72**, 1776 (1968).

[21]   W. H. Hamill, in: *Radical Ions*, Ed: E. T. Kaiser and L. Kevan, Wiley-Interscience: New York (1968).

[22]   A. Szabo, N. S. Ostlund, *Modern Quantum-Chemistry, Introduction to Advanced Electronic-Structure Theory*, McGraw-Hill: New York (1989).

[23]   *Modern Electronic Structure Theory*, Part I & II, Ed: D. R. Yarkony, World Scientific: Singapore (1995).

[24] R. G. Parr, W. Yang, *Density Functional Theory of Atoms and Molecules*, Oxford University Press: New York (1989).

[25] *Gaussian 98*, Rev. A.7, M. J. Frisch, G. W. Trucks, H. B. Schlegel, G. E. Scuseria, M. A. Robb, J. R. Cheeseman, V. G. Zakrzewski, J. A. Montgomery, Jr., R. E. Stratmann, J. C. Burant, S. Dapprich, J. M. Millam, A. D. Daniels, K. N. Kudin, M. C. Strain, O. Farkas, J. Tomasi, V. Barone, M. Cossi, R. Cammi, B. Mennucci, C. Pomelli, C. Adamo, S. Clifford, J. Ochterski, G. A. Petersson, P. Y. Ayala, Q. Cui, K. Morokuma, D. K. Malick, A. D. Rabuck, K. Raghavachari, J. B. Foresman, J. Cioslowski, J. V. Ortiz, A. G. Baboul, B. B. Stefanov, G. Liu, A. Liashenko, P. Piskorz, I. Komaromi, R. Gomperts, R. L. Martin, D. J. Fox, T. Keith, M. A. Al-Laham, C. Y. Peng, A. Nanayakkara, C. Gonzalez, M. Challacombe, P. M. W. Gill, B. Johnson, W. Chen, M. W. Wong, J. L. Andres, C. Gonzalez, M. Head-Gordon, E. S. Replogle, and J. A. Pople, Gaussian, Inc., Pittsburgh, PA (1998).

[26] *MOLPRO 98.1*, H.-J. Werner, P. J. Knowles, with contributions from J. Almlöf, R. D. Amos, M. J. O. Deegan, S. T. Elbert, C. Hampel, W. Meyer, K. Peterson, R. Pitzer, A. J. Stone, P. R. Tayor, University of Birmingham (1999).

[27] *MOLCAS version 4*, K. Anderson, M. R. A. Blomberg, M. P. Fülscher, V. Kellö, R. Lindh, P.-Å. Malmqvist, J. Noga, J. Olsen, B. O. Roos, A. J. Sadlej, P. E. M. Siegbahn, M. Urban, P.-O. Widmark, University of Lund, Sweden (1998).

[28] E. Heilbronner and J. P. Maier, in: *Electron Spectroscopy, Theory, Techniques and Applications,* Ed: C. R. Brundle and D. Baker, Vol. 1, Academic Press: New York, (1977).

[29] T. Koopmans, *Physica* **7**, 104 (1937).

[30] C. C. J. Roothaan, *Rev. Mod. Phys.* **23**, 69 (1951).

[31] G. G. Hall, *Proc. Roy. Soc. (London)* **A205**, 451 (1951).

[32] S. Matzinger, *Ph. D. Dissertation Nr. 1121*, Universität Freiburg, Schweiz (1996).

[33] T. Bally, W. T. Borden, *Rev. in Comput. Chem.* **13**, 31 (1999).

[34] K. Andersson, B. O. Roos, in: *Modern Electronic Structure Theory* Vol. **1**, Ed.: D. R. Yarkony, World Scientific, Singapore, (1995).

[35] T. Ziegler, *Chem. Rev.* **91**, 651 (1991).

[36] *Density Functional Theory of Atoms and Molecules*, Ed.: R. Parr and W. Yang, Oxford University Press, (1990).

[37] *Recent Advances in Density Functional Methods* Vol. **1**, Ed.: D. P. Chong, World Scientific, Singapore (1995).

[38] W. Kohn, L. J. Sham, *Phys. Rev. A* **140**, 1133 (1965).

[39] M. E. Casida, In *Recent Advances in Density Functional Methods, part 1,* D. P. Chong, Ed.; World Scientific: Singapore, see p. 155 (1995).

[40] R. E. Stratmann, G. E. Scuseria, M. J. Frisch, *J. Chem. Phys.* **109**, 8218 (1998).

[41] A. Marcinek, J. Adamus, K. Huben, J. Gebicki, T. J. Bartczak, P. Bednarek, T. Bally, *J. Am. Chem. Soc.* **122**, 437 (2000).

[42] *Spartan* SGI Version 4, B. J. Deppmeier, A. J. Diessen, W. J. Hehre, H. C. Johnson, J. M. Leonard, J. Yu, L. Lou, J. Baker, J. E. Carpenter, R. W. Dixon, S. S. Field, S. D. Kahn, W. J. Pietro, Wavefunction Inc. (1995).

[43] D. Ginsburg, *Acc. Chem. Res.* **2**, 121 (1969).

[44] A. Greenberg, J. F. Liebmann, *"Strained Organic Molecules"*, Academic Press, New York (1978) see p. 344f.

[45] D. Ginsburg, *"Propellanes"*, Verlag Chemie, Weinheim, (1975).

[46] K. B. Wiberg, J. E. Hiatt, G. J. Burgmaier, *Tetrahedron Lett.* 5855 (1968).

[47] P. G. Gassman, A. Topp, J. W. Keller, *Tetrahedron Lett.* 1093 (1969).

[48] K. B. Wiberg, G. J. Burgmaier, K.-W. Shen, S. J. La Place, W. C. Hamilton, M. D. Newton, *J. Am Chem. Soc.* **94**, 7402 (1972).

[49] P. Chakrabarti, P. Seiler, J. P. Dunitz, A.-D. Schlüter, G. Szeimies, *J. Am. Chem. Soc.* **103**, 7378 (1981).

[50] M. D. Newton, J. M. Schulman, *J. Am. Chem. Soc.* **94**, 773 (1972).

[51] K. B. Wiberg, *J. Am. Chem. Soc.* **105**,1227 (1983).

[52] J. E. Jackson, L. C. Allen, *J. Am. Chem. Soc.* **106**, 591 (1984).

[53] F. H. Walker, K. B. Wiberg, J. Michl, *J. Am. Chem. Soc.* **104**, 2056 (1982).

[54] K. B. Wiberg, F. H. Walker, W. E. Pratt, J. Michl, *J. Am. Chem. Soc.* **105**, 3638 (1983).

[55] F. H. Walker, K. B. Wiberg, *J. Am. Chem. Soc.* **104**, 5239 (1982).

[56] D. Ginsburg, *Acc. Chem. Res.*, **2**, 121 (1969).

[57] K. Semmler, G. Szeimies, *Tetrahedron Lett.* **27**, (48) 5839 (1985).

[58] R. S. Pappas, *Ph.D. Dissertation*, University of Tennessee, Knoxville (1995)

[59] T. Bally, W. Tang, Zhang, *J. Phys. Chem.* **97**, 4373 (1993).

[60] P. Pulay, G. Fogarasi, F. Pang, J. E. Boggs, *J. Am. Chem. Soc.* **101**, 2550 (1979).

[61] W. Tang, T. Bally, *J. Am. Chem. Soc.* **97**, 4365 (1993).

[62] X.-Z. Qin, F. Williams, *J. Phys. Chem.* **90**, 2292 (1986).

[63] J. K. Kochi, P. J. Krusic, *J. Am. Chem. Soc.* **90**, 7157, (1968).

[64] A. L. J. Beckwith, R. O. C. Norman, *J. Chem. Soc. B* **1969**, 400.

[65] A.-C. Sergenton, M. Allan, *private communication*.

[66] E. Haselbach, *Helv. Chim. Acta* **54**, 2257 (1971).

[67] G. Narahari Sastry, T. Bally, V. Hrouda, P. Cársky, *J. Am. Chem. Soc.* **120**, 9323 (1998).

[68] L. Truttmann, K. R. Asmis, T. Bally, *J. Phys. Chem.* **99**, 17844 (1995).

[69] J. Belzner, U. Bunz, K. Semmler, G. Szeimies, K. Opitz, A. Schlüter, *Chem. Ber.* **122**, 397 (1989).

[70] F. Alber, G. Szeimies, *Chem. Ber.* **125**, 757 (1992).

[71] K. B. Wiberg, S. T. Waddell, *J. Am. Chem. Soc.* **112**, 2194 (1990).

[72] J. Belzner, G. Szeimies, *Tetrahedron Lett.* **27**, (48) 5839 (1986).

[73] R. Bloch, P. Perchec, J. Conia, *Angew. Chemie Internat. Ed. Engl.* **9**, 798 (1970).

[74] P. Le Perchec, J. M. Conia, *Tetrahedron Lett*. **19**, 1587 (1970).

[75] R. Köster, S. Arora, P. Binger, *Angew. Chem.* **5**, 186 (1969).

[76] K. A. Lukin, N. S. Zefirov, *Zh. Org. Khim*. **23**, 2548 (1987).

[77] C. R. Hauser, W. R. Dunnavant, *Org. Synth. Coll. Vol.* **4**, 963 (1963).

[78] H. N. Cripps, E. F. Kiefer, *Org. Synth.* **42**, 12 (1962).

[79] G. Gustavson, N. Demjanoff, *J. prakt. Chem.* **38**, 202 (1988).

[80] J. D. Roberts, C. M. Sharts, *Org. React.* **12**, 32 (1962).

[81] H. N. Cripps, J. K. Williams, W. H. Sharkey, *J. Am. Chem. Soc.* **81**, 2723 (1959).

[82] K. B. Wiberg, D. S. Connor, *J. Am. Chem. Soc.* **88**, 4437 (1966).

[83] *Organikum*, 17th Ed. VEB Deutscher Verlag der Wissenschaften: Berlin (1988) see p. 423.

[84] C. C. Wu, R. W. Lenz, *J. Polym. Sci.* **10**, 3529 (1972).

[85] J. L. Charlton, R. Agagnier, *Can, J. Chem.* **51**, 1852 (1973).

[86] P. S. Skell, A. Y. Garner, *J. Am. Chem. Soc.* **78**, 3410 (1956).

[87] L. Skattebøl, *J. Org. Chem.* **29**, 2951 (1964).

[88] L. Skattebøl, *J. Org. Chem.* **31**, 2789 (1966).

[89] J. Backes, *Meth. Org. Chem. (Houben-Weyl)*, D. Klamann Ed., Thieme: Stuttgart, **E 16c**, 370 - 677 (1992).

[90] J. A. Deyrup, in: *Small Ring Heterocycles*, A. Hassner Ed., Wiley: New York, 1 - 214 (1983).

[91] R. Huisgen, in: *1,3 Dipolar Cycloaddition Chemistry*, A. Padwa Ed., Wiley: New York, 1 - 176 (1984).

[92] J. W. Jown, *Rec. Chem. Prog.* **32**, 51 - 83 (1971).

[93] A. P. Schaap, G. Prasad, S. D. Gagnon, *Tetrahedron Lett.* **24**, 3047 (1983).

[94] V. Caer, A. Laurent, E. Laurent, R. Tardevil, Z. Cebulska, R. Bartnik, *Nouv. J. Chim.* **11**, 351 - 356 (1987).

[95] T. Brigaud, E. Laurent, R. Tardevil, Z. Cebulska, R. Bartnik, *J. Chem. Res. (S)* **8**, 330 - 331 (1994).

[96] C. Gaebert, *Diploma Thesis*, Universität Münster (1994).

[97] C. Gaebert, J. Mattay, *J. Inf. Recording* **23**, 3 (1996).

[98] C. Gaebert, J. Mattay, *Tetrahedron* **53**, (42), 14297 (1997).

[99] H. Basch, M. B. Robin, N. A. Kuebler, C. Baker, D. W. Turner, *J. Chem. Phys.* **51**, 52 (1969).

[100] P. Rademacher, G. Irsch, W. Sicking, E.-U. Würthwein, *J. Mol. Struct.* **197**, 291 (1989).

[101] J. L. Holmes, J. K. Terlouw, *Can. J. Chem.* **54**, 1007 (1976).

[102] M. H. Lien, A. C. Hopkinson, *Can. J. Chem.* **62**, 922 (1984).

[103] F. Williams, X. Qin, *J. Phys. Chem.* **90**, 2292 (1986).

[104] G. Maier, C. Schmidt, H.P. Reisenauer, E. Endlein, D. Becker, J. Eckwert, B.A. Hess Jr., L.J. Schaad, *Chem. Ber.* **126**, 2337 (1993).

[105] M.E. Jacox, *Chem. Phys.* **43**, 157 (1979).

[106] M.E. Jacox, D.E. Milligan, *J. Am. Chem. Soc.* **85**, 278 (1963).

[107] T. Shimanouchi, *Tables of Molecular Vibrational Frequencies Consolidated*, Ed.: National Bureau of Standards, 160 (1972).

[108] I. Stolkin, T.-K. Ha, H.H. Günthard, *Chem. Phys.* **21**, 327 (1977).

[109] N.P. Machara, B. S. Ault, *Chem. Phys. Lett.* **140**, 411 (1987).

[110] R. E. Carter, T. Drakenberg, N.-Å. Bergman, *J. Am Chem. Soc.* **97**, 6990 (1975).

[111] I. M. B. Nielsen, *J. Phys. Chem. A* **102**, 3193 (1998).

[112] R. J. Lichter, K. Crimaldi, D. A. Baker, *J. Org. Chem.* **47**, 3524 (1982).

[113] K. N. Houk, S. Searles, M. D. Rozeboom, S. E. Seyedrezai, *J. Am, Chem, Soc.* **104**, 3448 (1982).

[114] A.-C. Sergenton, *private communication.*

[115] T. Shida, *Electronic absorption spectra of radical ions*, Elsevier Ed.: Tokyo (1988) see p. 208.

[116] H.-G. Korth, H. Trill, R. Sustmann, *J. Am. Chem. Soc.* **103**, 4483 (1981).

Acknowledgements

Die ausgezeichnete Atmosphäre und die gute Zusammenarbeit am Institut waren wichtige Voraussetzungen für das Gelingen dieser Arbeit. Ich möchte mich bei folgenden Personen für ihre Unterstützung bedanken:

Curriculum Vitae

Personal Data:

Name:	Beat Christoph Müller
Born:	December 1, 1970 in Zofingen (AG), Switzerland
Parents:	Gottfried and Christine Müller-Vatter
Marital status:	single

Education:

1977 - 1982:	Primary School in Freiburg
1982 - 1986:	Secondary School in Freiburg
1986 - 1990:	Matura Typus C at the Kollegium St. Michael in Freiburg
1991 - 1995:	Studies of Chemistry at the University of Fribourg
	Diploma Theses: Inorganic Chemistry (Primary Branch)
	Physical Chemistry (Secondary Branch)
since 1995:	Ph.D. Thesis at the Institute for Physical Chemistry, University of Fribourg, Switzerland under the supervision of Prof. Dr. Thomas Bally and supported by the Swiss National Science Foundation
	Teaching assistant for the lecture of Prof. Dr. Michael Allan
	Assistant for practical courses for students

List of Presentations:

- B. Müller, T. Bally: "*Rearrangements of [1.1.1] Propellane on Ionization*". Poster at the "International Conference on Reactive Intermediates and Reaction Mechanisms" in Ascona, Switzerland, 1998.
- B. Müller, T. Bally: "*Ring Opening of Substituted Aziridines on Ionization*". Poster at the "International Workshop on Reactive Intermediates" in Szczyrk, Poland, 1999.
- B. Müller, T. Bally, F. Williams, R. Pappas: "*What happens to [1.1.1]Propellane on ionization?*". Talk at the "Polish Swiss Meeting on Reactive Intermediates" in Szklarska Poreba, Poland, 1996
- B. Müller, T. Bally, F. Williams, R. Pappas: "*Matrix isolation and photochemistry of C_5H_6 hydrocarbon radical cations*". Talk at the "EPA Graduate Student Symposium 2000" in Freiburg/CH, 2000.